

Abstract

Quantum Microwave Engineering for the Protection and Readout of Superconducting Qubits

Zhixin Wang

2023

The engineering of quantum information machines—at the fundamental level—relies on advancement in the control and measurement techniques of individual quantum coherent systems. In this scientific roadmap, a central challenge has been the reconciliation—in the same physical platform—of two exceptional goals: the protection from decoherence channels of pure quantum states, and their accurate and efficient readout using macroscopic measurement apparatuses, which appear to be demanding opposite experimental conditions with respect to the accessibility of quantum information from the external environment. Can near-ideal measurement be achieved in artificial quantum systems without the sacrifice of their coherence properties? This dissertation addresses this question in superconducting Josephson circuits by presenting the positive outcomes of two single-qubit experiments: First, the dephasing time of a transmon qubit embedded in the three-dimensional (3D) circuit quantum electrodynamics (QED) architecture can be reproducibly increased owing to a new type of microwave cavity attenuator that can effectively reduce the residual thermal photon population in the readout mode. Second, intra-cavity quantum readout signals in the 3D circuit QED system can be amplified by a weakly nonlinear Josephson junction array quadratically coupled to the transmon qubit; this two-step dispersive readout scheme meanwhile demonstrates a suppression of the photon-induced qubit relaxation effect, and therefore indicates a high quantum nondemolition fidelity with more than 100 microwave photons in the 3D readout cavity. The compatibility of these two

inventions—the cold cavity attenuator and the “ Π -mon” artificial molecule—suggests a promising experimental direction of integrating extra-cavity dissipation and intra-cavity amplification to simultaneously realize high-coherence superconducting qubits and their high-performance quantum-limited readout, which will be instrumental in implementing scalable, fault-tolerant quantum networks and advancing the state-of-the-art knowledge of fundamental quantum physics.

Quantum Microwave Engineering for the
Protection and Readout of Superconducting Qubits

A Dissertation
Presented to the Faculty of the Graduate School
of
Yale University
in Candidacy for the Degree of
Doctor of Philosophy

by
Zhixin Wang
(王之鑫)

Dissertation Director: Michel H. Devoret

December 2022

Copyright © by Zhixin Wang

All rights reserved.

This above all: to thine own self be true,
And it must follow, as the night the day,
Thou canst not then be false to any man.

—*Hamlet*: I.iii.78–80

Contents

Table of Contents	i
List of Figures	v
List of Tables	viii
List of Abbreviations	ix
List of Symbols	xii
Acknowledgements	xx
Scientific Overview	xxviii
0.1 Background and problems	xxviii
0.2 Summary of original contributions	xxx
0.3 Arrangement of chapters and sections	xxxii
1 Quantum Electrical Engineering: A Conceptual Primer	1
1.1 Engineering science in the quantum regime	3
1.2 Quantum information machines: principles, prospects, and challenges	5
1.3 Quantum electrical circuits: ideas and implementations	8
1.3.1 Macroscopic quantum phenomena	9

1.3.2	Superconducting artificial atoms	12
1.3.3	Circuit quantum electrodynamics (QED)	21
1.3.4	Quantum-limited amplification	26
1.3.5	A brief discourse on “quantumness”	31
1.4	Noise in quantum circuits: origins and impacts	33
2	Theoretical Models of Quantum Measurements	37
2.1	Entropy, information, and measurements	39
2.2	Basic notions of a qubit measurement	41
2.3	Realistic qubit readout: nonidealities and their quantification	45
2.3.1	Readout fidelity	46
2.3.2	Quantum nondemolition (QND) fidelity	48
2.3.3	Measurement time	53
2.3.4	Measurement efficiency	54
2.4	From projective to continuous measurements	56
3	Measurements and Decoherence in Circuit QED	66
3.1	Historical precursors	68
3.2	Circuit QED dispersive readout of superconducting qubits	73
3.2.1	Dispersive Hamiltonian	73
3.2.2	Cavity reflection and transmission measurements	76
3.2.3	Measurement setup of a circuit QED system	83
3.3	Measurement-induced qubit dephasing	89
3.4	Measurement-induced qubit-state transition	95

4	Experimental Methods of Quantum Microwave Circuits	100
4.1	Josephson circuits: design, fabrication, and test	101
4.2	Microwave cavities: geometries and materials	104
4.3	Low-temperature experimental system	106
4.3.1	Cryogenics and thermometry	106
4.3.2	Low-temperature microwave wiring	109
4.3.3	Thermalization and electromagnetic shielding	114
4.4	Room-temperature electronics	116
4.4.1	Pulsed signal generation	117
4.4.2	Microwave signal detection	118
4.5	Control and simulation software	121
5	Cavity Attenuator: Protecting Quantum Information from Thermal Electromagnetic Noise	123
5.1	Electromagnetic attenuation: lumped- vs. distributed-element circuits	125
5.2	Design and test of cavity attenuators	128
5.3	Coupling the cavity attenuator to the circuit QED system	132
5.4	Improving qubit coherence times	139
5.5	Measuring thermal photon populations	145
5.6	Conclusions and future directions	147
6	Π-mon: An Artificial Molecule for the Intra-Cavity Amplification of Qubit Readout Signals	150
6.1	Preamble: purposes of intra-cavity preamplifiers	152
6.2	Design principles of the artificial molecule	155

6.3	Π -mon circuit: classical and quantum analysis	158
6.3.1	Bright, dark, and mediator modes	159
6.3.2	Effective circuit Hamiltonian	163
6.3.3	Circuit quantization	166
6.4	Π -mon coupled to a linear readout cavity	169
6.4.1	Control and measurement interfaces	171
6.4.2	Experimental setup and parameters	172
6.5	Nonlinear spectroscopy of the bright mode	178
6.6	Suppressing photon-induced qubit-state transitions	181
6.7	Demonstrations of the intra-cavity amplification	183
6.7.1	Steady-state intra-cavity gain	185
6.7.2	Bright-mode-assisted single-shot qubit readout	187
6.8	Summary and upcoming steps	190
7	Conclusions and Outlooks	194
7.1	Qubit coherence versus measurability	195
7.2	Microwave thermalization in hybrid quantum networks	198
7.3	Multi-stage quantum measurement systems	199
	Bibliography	202

List of Figures

0	Structure of this dissertationxxxiii
1.1	Physical structure and circuit symbols of a Josephson junction	11
1.2	Macroscopic, microscopic, and mesoscopic scales	12
1.3	Circuit model of superconducting artificial atoms	14
1.4	Reduction of the Josephson nonlinearity in a junction array	21
1.5	Schematic diagram of the circuit QED system	23
1.6	Comparison of the two quantum-limited amplification schemes	30
2.1	Venn-type diagrammatic model of a physical measurement	40
2.2	Minimal conceptual model of a quantum measurement	42
2.3	Channel models of the qubit readout fidelity	47
2.4	Channel models of the QND fidelity	52
2.5	Discrete-time model of a qubit readout process	57
2.6	Simulation of repetitive weak qubit measurements.	62
2.7	Simulation of nonideal qubit measurement records	65
3.1	Stern–Gerlach experiment	69
3.2	Nuclear magnetic resonance (NMR) experiment	70
3.3	Moving-coil mirror galvanometer of the d’Arsonval type	71
3.4	Cavity reflection and transmission measurement setups	77
3.5	Comparison of reflection and transmission measurements	82

3.6	Schematic drawing of the circuit QED measurement setup in reflection	84
3.7	Readout signals at the input and output of an amplifier chain	85
4.1	Drawing of a transmon artificial atom for 3D circuit QED systems . .	102
4.2	Drawing of a 3D microwave readout cavity	105
4.3	Thermal cycle diagram of the cryogen-free dilution refrigerator	107
4.4	Cryogenic microwave setup for a standard circuit QED experiment . .	111
4.5	Microwave pulse generation through IQ modulation	116
4.6	Superheterodyne microwave interferometer and digitization circuits .	120
5.1	Comparison of a lumped-element resistor and a dissipative waveguide	127
5.2	A dissipative cavity capacitively coupled to two transmission lines . .	128
5.3	Drawing of a resonant cavity attenuator	129
5.4	Room-temperature transmission spectroscopy of the cavity attenuator	131
5.5	Cryogenic wiring diagram of the cavity attenuator experiment	134
5.6	Drawing of the cavity attenuator coupled to a circuit QED module .	135
5.7	Circuit model of a cavity attenuator coupled to a circuit QED module	136
5.8	Spectroscopy of a cavity attenuator coupled to a circuit QED module	139
5.9	Qubit coherence times with and without cavity attenuators	140
5.10	Repeatability test for qubit coherence time improvements	144
5.11	Noise-induced qubit dephasing measurements	146
6.1	Combining extra-cavity dissipation and intra-cavity attenuation in the circuit QED measurement setup	153
6.2	Qubit readout scheme assisted by an intra-cavity preamplifier	156
6.3	Π -mon artificial molecule	158
6.4	Uncoupled linear modes in the Π -mon	159

6.5	Lumped-element circuit model of the Π -mon	160
6.6	Even-odd mode analysis of the Π -mon circuit	161
6.7	Π -mon coupled to a 3D readout cavity	170
6.8	Optical and scanning electron micrographs of the Π -mon sample . . .	172
6.9	Cryogenic wiring diagram of the Π -mon experiment	174
6.10	Continuous-wave bright mode two-tone spectroscopy with variable drive powers	180
6.11	Photon-induced qubit relaxation measurement on the dark mode . . .	182
6.12	Principles of the intra-cavity dispersive gain	184
6.13	Intra-cavity gain measured using the three-tone continuous-wave spectroscopy method	187
6.14	Bright-mode-assisted single-shot readout of the dark mode	189
6.15	Illustration of the dark-mode-selective bright-mode drive	191
6.16	Single-shot readout of the dark mode assisted by the bright mode 0–2 transition	193
7.1	Modular diagram of a microwave–optical quantum transduction setup	199
7.2	Multi-stage model for quantum measurements	200

List of Tables

3.1	Summary of key features of Stern–Gerlach, NMR, and mirror galvanometer experiments as compared to the circuit QED setup . . .	72
3.2	Selected single-shot qubit readout experiments with circuit QED systems in the linear dispersive regime	88
3.3	Two circuit QED measurement systems using transmon–cavity couplings of the longitudinal and cross-Kerr forms	97
5.1	Resonant frequencies and bandwidths of cavity attenuators	132
5.2	Transmon frequencies and anharmonicities in the cavity attenuator experiment	141
5.3	Summary of experimental parameters and results with different cavity attenuators	142
6.1	Frequencies of the Π -mon modes and the readout cavity	176
6.2	Kerr matrix of the Π -mon coupled to a linear readout cavity	176
6.3	Numerical simulation of the Kerr matrix	177
6.4	Coherence times of the dark and bright modes	177

List of Abbreviations

1D	One-dimensional
2D	Two-dimensional
3D	Three-dimensional
AC	Alternating current
ADC	Analog-to-digital converter
API	Application programming interface
AWG	Arbitrary waveform generator
BBQ	Black-box quantization
BCS	Bardeen–Copper–Schieffer (theory)
BoPET	biaxially-oriented polyethylene terephthalate
CLNA	Cryogenic low-noise amplifier
CW	Continuous wave
DAC	Digital-to-analog converter
DC	Direct current
DR	dilution refrigerator
EDM	Electrical discharge machining
EF	Eccosorb filter
EPR	Energy-participation ratio
FDT	Fluctuation–dissipation theorem
FEM	Finite element method
FPGA	Field-programmable gate array
HEMT	High-electron-mobility transistor
IAP	Intermediate anchoring plate

IF	Intermediate frequency
IPA	Isopropyl alcohol
IQ	In-phase and quadrature
JPA	Josephson parametric amplifier
JPC	Josephson parametric converter
JPD	Josephson parametric dimer
JTWPA	Josephson traveling-wave parametric amplifier
LC	Inductor–capacitor
LO	Local oscillator
LSB	Lower sideband
MOSFET	Metal–oxide–semiconductor field-effect transistor
MC	Mixing chamber
NMR	Nuclear magnetic resonance
OFHC	Oxygen-free high-conductivity (copper)
OVC	Outer vacuum can
PC	Personal computer
PP	Phase-preserving (amplification)
PS	Phase-sensitive (amplification)
PT	Pulse tube (cryocooler)
QED	Quantum electrodyamics
QLA	Quantum-limited amplifier
QND	Quantum nondemolition (measurement)
QPA	Qubit parametric amplifier
RF	Radio frequency
RRR	Residual-resistivity ratio
RTA	Room-temperature amplifier
RTP	Room-temperature plate

RWA	Rotating wave approximation
SEM	Scanning electron microscope
SIMBA	Superconducting isolating modular bifurcation amplifier
SIS	Superconductor–insulator–superconductor (junction)
SLUG	Superconducting low-inductance undulatory galvanometer
SMA	Subminiature version A
SNAIL	Superconducting nonlinear asymmetric inductive element
SNR	Signal-to-noise ratio
SPA	SNAIL parametric amplifier
SQL	Standard quantum limit
SSB	Single-sideband (modulation)
SQUID	Superconducting quantum interference device
TE	Transverse electric (mode)
USB	Upper sideband
VNA	Vector network analyzer
ZPF	Zero-point fluctuations

List of Symbols

Physical constants

c	Speed of light in vacuum
e	Elementary charge
k_B	Boltzmann constant
h	Planck constant
\hbar	Reduced Planck constant
Φ_0	Magnetic flux quantum
ϕ_0	Reduced magnetic flux quantum
R_q	Superconducting resistance quantum
ϵ_0	Vacuum electric permittivity
m_e	Electron mass
a_0	Bohr radius
R_∞	Rydberg constant
α	Fine-structure constant

Basic quantum operators

$\hat{\mathbb{I}}$	Identity operator
$\hat{\sigma}_x, \hat{\sigma}_y, \hat{\sigma}_z$	Pauli x, y, z operators
$\hat{\sigma}$	Pauli operator vector $(\hat{\sigma}_x, \hat{\sigma}_y, \hat{\sigma}_z)$
$\hat{\rho}$	Density operator
$\hat{\rho}'$	Post-measurement density operator, result recorded
$\hat{\rho}'_{\text{NR}}$	Post-measurement density operator, result not recorded
\hat{U}	Unitary evolution operator

$\hat{\Pi}$	Projection operator
\hat{M}	Generalized (non-projective) measurement operator
\hat{O}_q	Quantum system operator (generic measurement model)
\hat{O}_m	Meter operator (generic measurement model)
$\hat{\varphi}$	Gauge-invariant superconducting phase
\hat{n}	Cooper-pair number
\hat{I}	In-phase component (sinusoidal signal)
\hat{Q}	Quadrature component (sinusoidal signal)

Annihilation and creation operators

\hat{t}, \hat{t}^\dagger	Transmon
\hat{c}, \hat{c}^\dagger	Readout cavity
\hat{a}, \hat{a}^\dagger	Cavity attenuator
$\hat{a}_{\text{in}}, \hat{a}_{\text{in}}^\dagger$	Cavity attenuator input
$\hat{a}_{\text{out}}, \hat{a}_{\text{out}}^\dagger$	Cavity attenuator output
\hat{r}, \hat{r}^\dagger	Hybridized readout mode: cavity attenuator–readout cavity
\hat{b}, \hat{b}^\dagger	Π -mon bright mode
\hat{d}, \hat{d}^\dagger	Π -mon dark mode
\hat{m}, \hat{m}^\dagger	Π -mon mediator mode
\hat{i}, \hat{i}^\dagger	Idler mode (phase-preserving amplification)
$\hat{e}_{\vec{k}\uparrow,\downarrow}, \hat{e}_{\vec{k}\uparrow,\downarrow}^\dagger$	Electron with momentum \vec{k} and spin \uparrow, \downarrow

Hamiltonian operators

\hat{H}_q	Qubit
\hat{H}_m	Meter
\hat{H}_{int}	Qubit–meter/ancilla interaction
\hat{H}_{q-m}	Qubit coupled to the meter
\hat{H}_t	Transmon

\hat{H}_{t-c}	Transmon coupled to the readout cavity
\hat{H}_{disp}	Dispersive coupling
\hat{H}_{long}	Longitudinal (displacement) coupling
\hat{H}_{Π}	Π -mon
$\hat{H}_{\Pi-c}$	Π -mon coupled to the readout cavity

Quantum states

$ 0\rangle, 1\rangle$	Qubit eigenstates (of $\hat{\sigma}_z$)
$ \pm x\rangle, \pm y\rangle$	Eigenstates of $\hat{\sigma}_x, \hat{\sigma}_y$
$ +\rangle, -\rangle$	Meter states
$ \emptyset\rangle$	Meter null states
$ \nu \geq 2\rangle$	ν -th excited states (of transmon or Π -mon)
$ q_\nu\rangle$	Quantum system eigenstates (generic measurement model)
$ m_\mu\rangle$	Meter states (generic measurement model)
$ \Psi_{\text{BCS}}\rangle$	BCS ground state

Electromagnetic fields and signals

\vec{E}	Electric field
I	In-phase component (sinusoidal signal)
Q	Quadrature component (sinusoidal signal)
$C_{nn}[\omega]$	Photon-number correlation function
$S_{nn}[\omega]$	Photon-number spectral density
$C_{VV}[\omega]$	Voltage correlation function
$S_{VV}[\omega]$	Voltage spectral density

Superconductivity

Δ	Superconducting energy gap
T_c	Superconducting critical temperature

Josephson junction

φ	Gauge-invariant phase
I_c	Critical current
L_J	Josephson inductance
L_{NL}	Josephson nonlinear inductance
C_J	Junction capacitance
R_n	Normal resistance

Superconducting artificial atom

E_J	Josephson energy
E_C	Coulomb energy
E_L	Linear inductive energy
L	External linear inductance
C_s	External shunting capacitance
C_g	External gate capacitance
C	Total capacitance (including the junction capacitance)
Z_c	Characteristic impedance
q	Electric charge
Φ	Magnetic flux
n	Cooper-pair number
φ_{ZPF}	Zero-point fluctuations: superconducting phase
n_{ZPF}	Zero-point fluctuations: Cooper-pair number

Π -mon artificial molecule

$L_{J,t}$	Josephson inductance, transmon junction
$L_{J,a}$	Josephson inductance, array junctions
C_t	Shunting capacitance, transmon mode
C_a	Shunting capacitance, junction array mode

$C_{g,t}$	Ground capacitance, transmon mode
C_c	Coupling capacitance, transmon–junction array
N_J	Number of Josephson junctions per arm of the array

Resonant frequencies and detunings

$\omega_t^{\nu,\nu'}, f_t^{\nu,\nu'}$	Transmon: $ \nu\rangle \rightarrow \nu'\rangle$ transition
$\omega_b^{\nu,\nu'}, f_b^{\nu,\nu'}$	Π -mon bright mode: $ \nu\rangle \rightarrow \nu'\rangle$ transition
$\omega_d^{\nu,\nu'}, f_d^{\nu,\nu'}$	Π -mon dark mode: $ \nu\rangle \rightarrow \nu'\rangle$ transition
$\omega_m^{\nu,\nu'}, f_m^{\nu,\nu'}$	Π -mon mediator mode: $ \nu\rangle \rightarrow \nu'\rangle$ transition
ω_c, f_c	Readout cavity
ω_a, f_a	Cavity attenuator
ω_r, f_r	Hybridized readout mode (cavity attenuator–readout cavity)
Δ_{tc}	Transmon–readout cavity
Δ_{bc}	Π -mon bright mode–readout cavity
Δ_{mb}	Π -mon mediator mode–bright mode
Δ_{dm}	Π -mon dark mode–mediator mode

“Atom”–photon coupling strengths

g_{tc}	Transmon–readout cavity, linear coupling
g_{long}	Transmon–readout cavity, longitudinal coupling
g_{CK}	Transmon–readout cavity, cross-Kerr coupling

Linear modes: energy decay rates

κ_c	Readout cavity
κ_a	Cavity attenuator
κ_r	Hybridized readout mode
$\kappa_{r,i}, \kappa_{r,c}$	Hybridized readout mode: internal and coupling loss

Nonlinearities: self-Kerr anharmonicities

K_t	Transmon
K_b	Π -mon: bright mode
K_d	Π -mon: dark mode
K_m	Π -mon: mediator mode
K_c	Readout cavity (hybridized with the transmon or Π -mon)

Nonlinearities: cross-Kerr coupling strengths

χ_{tc}	Transmon–readout cavity
χ_{tr}	Transmon–hybridized readout mode
χ_{bc}	Π -mon bright mode–readout cavity
χ_{dc}	Π -mon dark mode–readout cavity
χ_{mc}	Π -mon mediator mode–readout cavity
χ_{bd}	Π -mon bright mode–dark mode
χ_{bm}	Π -mon bright mode–mediator mode
χ_{dm}	Π -mon dark mode–mediator mode

Qubit coherence times and rates

T_1, Γ_1	Energy relaxation
T_{1P}, Γ_{1P}	Energy relaxation: Purcell limit
T_ϕ, Γ_ϕ	Dephasing
T_2, Γ_2	Decoherence
T_{2R}, Γ_{2R}	Decoherence, measured with the Ramsey experiment
T_{2H}, Γ_{2H}	Decoherence, measured with the Hahn echo experiment

State and mode populations

P_0, P_1	Qubit $ 0\rangle$ and $ 1\rangle$
\bar{n}_c	Readout cavity

\bar{n}_{th}	Thermal-photon population
\bar{n}_{b}	Π -mon bright mode

Spectroscopy and external drives

$\omega_{\text{spec}}, f_{\text{spec}}$	Spectroscopic drive frequency
P_{spec}	Spectroscopic drive power
$\omega_{\text{d}}, f_{\text{d}}$	Parametric drive frequency
P_{d}	Parametric drive power

Qubit measurements

$P(A)$	Probability
$P(A B)$	Conditional probability: $P(A \cap B)/P(B)$
$\mathcal{F}_0, \mathcal{F}_1$	Readout fidelity, with the qubit initialized in $ 0\rangle, 1\rangle$
\mathcal{F}_{tot}	Total readout fidelity
$\mathcal{Q}_0, \mathcal{Q}_1$	QND fidelity, with the qubit initialized in $ 0\rangle, 1\rangle$
\mathcal{Q}_{tot}	Total QND fidelity
$\mathcal{Q}'_{\text{tot}}$	Apparent total QND fidelity
S, S'	System entropies prior and posterior to the measurement
J	Information gain
J_{meas}	Information collected in the measurement
J_{env}	Information lost into the environment
η_{m}	Measurement/information efficiency
τ_{m}	Minimal measurement time (SNR = 1)
T_{m}	Measurement/data-acquisition time

Weak measurement model

\vec{v}	Bloch vector
x, y, z	Bloch vector: Cartesian components

r, θ, ϕ	Bloch vector: modulus, polar angle, and azimuthal angle
χ	Qubit–ancilla coupling strength
ϵ	Qubit–ancilla dimensionless coupling strength
Δt	Interaction time interval
k	Number of weak measurement steps

Quantum-limited amplification

G	Amplifier gain
G_{PP}	Linear phase-preserving gain
G_{PS}	Linear phase-sensitive gain
n_{add}	Added noise, measured in photon number

Acknowledgements

Science *on paper* is supposed to be a growing body of impersonal knowledge, whereas science *in action* is an organized human activity. This dissertation, while investigating superconducting circuits and quantum information, has been a product of fruitful interactions with many people during a long and rewarding intellectual journey. It is therefore most appropriate to begin by acknowledging their contributions to the scientific works reported in the following chapters, as well as their influences on my professional and personal characters in many different ways.

First and foremost, I want to thank my doctoral adviser Michel Devoret, who has over the past years established a role model to me in science and education. Among the many lessons I learned from Michel, I would like to list three by way of the guiding principles for this dissertation: First, at the very core of sophisticated scientific expeditions is the simple pleasure of discovering how things work—namely, pure knowledge beneath the apparent technological progress. Second, one should not claim a solid understanding of any natural phenomenon until they can connect abstract theories to intuitive pictures and interpret the same picture from multiple complementary perspectives. Third, scientific ideas and results should always be reported in the clearest and most responsible way, both to communicate our findings and to expose our limitations. Michel has been teaching these principles mostly through demonstrations, as all effective teaching should be. The pleasure of studying and working with Michel also arises from his broad knowledge and endless curiosity in science, his Flaubertian attentiveness to the detail, his open but principled mindset toward new ideas, his appreciation for art and humanities, and the most important of all, his unquestion-

able genuineness toward people and things. Many of these influences are going to last throughout my future career.

During the first four years of my doctoral research, Shyam Shankar was the other important mentor to whom I owed the majority of my practical knowledge in a superconducting quantum circuit laboratory. In particular, it was under Shyam’s close guidance that I moved forward along the line of inquiry that has eventually become the topic of this dissertation. Similar to Michel, Shyam possesses a meticulous scientific attitude and at the same time a gentle and encouraging personality. The depth of his knowledge in quantum physics can only be matched by his supportiveness to his colleagues, his patience when supervising junior team members, and his responsibility when it comes to research planning and laboratory management. This spirit of collaboration and knowledge sharing is what makes QuLab a correlated many-body system in which everyone benefits from everyone else.

Besides Michel and Shyam, I want to thank several QuLab alumni for their crucial help in the beginning stage of my Ph.D. adventure: Gijs de Lange was my first postdoc mentor in the group, who taught me—through a Special Investigation (SI) project on nanowire microwave circuits—the mindset and methodology of an experimentalist facing a physics question. Anirudh Narla was the senior master of the dilution refrigerator *Dreadnought*¹ when I started our cold cavity attenuator project, to whom I owed a long list of techniques for designing, constructing, and operating low-temperature measurement systems. Uri Vool belongs to the small group of physicists with balanced expertise in experiment and theory; besides his many other influences, Uri introduced me to the theory of the photon-induced qubit dephasing effect, which was the starting point of almost one half of my doctoral research activities. Zlakto Mineev is exemplary in being an outstanding scientist and communicator,

¹A few years later, the II-mon artificial molecule was measured in the same dilution refrigerator.

who was generous with his time to teach me a number of useful skills, ranging from spectroscopy analysis to scientific writing; I also had the privilege to become one of the earliest users of his quantum circuit simulation package, now openly available to our entire community [Mineev *et al.*, 2021b].

Moreover, I can hardly imagine a Ph.D. journey as productive and inspiring without the inputs from many other QuLab members: During his participation in the cold cavity attenuator project, Philippe Campagne-Ibarcq instructed me to measure the AC-Stark shift and raised my understanding of qubit dephasing and measurements to a new level. Later, I had the pleasure of collaborating with Ioannis Tsioutsios on testing transmon qubits from novel fabrication protocols, who has since been a supportive colleague and friend. During our many overlap years, I could almost stop by Shantanu Mundhada's desk any time to discuss any questions, from quantum optics, FPGA electronics, to his visiting experience in France. Apart from being an excellent physicist, Evan Zalys-Geller was our local authority in mechanical arts and electronic technology, who is constantly willing to share his machining and wiring tips together with his enthusiasm for solving hands-on challenges. The majority of qubit measurements I performed were assisted by parametric amplifiers designed and fabricated by Nicholas Frattini and Volodymyr Sivak. I would also like to thank Nick for his in-house technical help on dilution refrigeration, and I have been frequently learning from Vlad since we started sharing the same cryostat to conduct our dissertation research in parallel. Discussions with Jayameenakshi Venkatraman and Xu Xiao on parametric phenomena in driven nonlinear oscillators have always been inspiring, and I only wish we could have more opportunities to implement those ideas. Finally, I want to thank Wei Dai for his deep participation in the Π -mon project over the past 18 months. Wei is another exemplary researcher capable of combining technical pursuits with deep inquiries into fundamental problems. It will be safe to expect more fruitful results arising from this line of experiments in his charge.

I would like to thank other QuLab postdocs and graduate students from whom I have learned in various aspects during my Ph.D. years: Benjamin Brock, Tom Connolly, Rodrigo Cortiñas, Andy Ding, Spencer Diamond, Alec Eickbusch, Valla Fatemi, Sumita Ghosh, Alex Grimm, Max Hays, Sumeru Hazra, Vidul Joshi, Akshay Koottandavida, Angela Kou, Pavel Kurilovich, Gangqiang Liu, Alessandro Miano, Ananda Roy, Kyle Serniak, Katrina Sliwa, Clarke Smith, and Steven Touzard. I also want to thank our undergraduate interns, who often possess the most energetic and inquisitive minds in both classrooms and laboratories: Shoumik Chowdhury, Chunyang Ding, Owen Duke, Alvin Gao, Shantanu Jha, Andrew Lingenfelter, Henry Liu, and Andrew Saydjari. Finally, I cannot conclude this section without acknowledging Luigi Frunzio, who has been offering constant support and unconditional positivity toward scientific research, laboratory management, and virtually everything occurring around us.

Apart from QuLab, I also wish to thank our partner laboratory headed by Robert Schoelkopf. Among RSL members, Philip Reinhold and Kevin Chou provided immense help with control electronics and software platforms when I was learning to operate the two generations of home-assembled quantum control and measurement systems.² Luke Burkhart generously shared his knowledge of vacuum technology when we were maintaining pump carts and leak checkers for both groups. I have also been enjoying my interactions with Vijay Jain, Chan U Lei, and Serge Rosenblum both inside and outside the department. Finally, I want to thank other RSL members over the many years for everything I have learned from them: Chris Axline, Jacob Blumoff, Teresa Brecht, Benjamin Chapman, Yiwen Chu, Nathanael Cottet, Jacob Curtis, Yanni Dahmani, Sal Elder, Christa Flümamm, Suhas Ganjam, Yvonne Gao, John Garmon, Stijn de Graaf, Parker Henry, Vijay Jain, Lev Krayzman, Brian Lester,

²See Sections 4.4 and 4.5.

Kaicheng Li, Yao Lu, Aniket Maiti, Nissim Ofek, Alex Read, James Teoh, Taekwan Yoon, Wolfgang Pfaff, Neel Thakur, Chen Wang, Chris Wang, Patrick Winkel, Sophia Xue, and Yaxing Zhang.

In the middle stage of my doctoral research, I had the opportunities to collaborate with a few theory and engineering groups at the Yale Quantum Institute for several stimulating projects. First, I want to thank Steven Girvin and Shruti Puri for their deep insights when we were attempting to formulate and understand the general noise-induced qubit dephasing problem, which eventually produced a fitting-parameter-free quantitative match between theory and experimental data.³ In particular, Steve has influenced me both by his exceptional scientific rigor in theorization, calculation, and writing, and by his “bilingual fluency” in both theoretical and experimental languages. Second, it was also a pleasure to work with Liang Jiang, Changchun Zhong, and Mengzhen Zhang on the entanglement generation and verification protocols between microwave and optical photons; since then I have been impressed by Liang’s broad and accurate vision in almost every frontier of quantum information science. Finally, when performing the quantum microwave radiometry experiment, I received great help—from device fabrication to cryogenic setup—from Xu Han, Mingrui Xu, Wei Fu, Sihao Wang, and Yuntao Xu in the laboratory of Hong Tang. I also want to thank Hong for leading the collaborative investigations on microwave–optical quantum transduction, which has gathered researchers from different backgrounds to tackle the outstanding technological challenges of building expandable hybrid quantum networks.

In addition to research collaborations, I am indebted to several Yale faculty members in Physics and Applied Physics for their pedagogical influences. David DeMille, Sohrab Ismail-Beigi, Leonid Glazman, Liang Jiang, and Robert Schoelkopf taught me

³Personally, I would like to recall this episode as the peak moment of intellectual satisfaction among all my research experiences in physics so far.

the physical pictures of atoms, solids, quantum many-body systems, quantized light, and microwave circuits, all with great clarity. These concepts form the backbone of the physical ideas discussed in this dissertation. One year following our first encounter in his classroom, Sohrab further showed me the art of undergraduate teaching with full attentiveness and passion. Moreover, the administrative staff members have been playing an essential role in all academic and research activities at both the Department of Applied Physics and the Yale Quantum Institute. I want to thank Alexander Bozzi, Florian Carle, Theresa Evangeliste, Nuch Graves, Giselle Maillet, Racquel Miller, Maria Rao, Jessica Tefft, and Melissa Wojciechowski for their time and efforts in creating a productive and pleasant environment for students and researchers over many years. Moreover, the progress of our experimental works would not be possible without the support of various research facilities on campus. I would like to specially thank David Johnson, Vincent Bernardo, and Nick Bernardo for teaching me elementary machining techniques and managing the Wright Lab, the Gibbs, and the School of Engineering and Applied Science (SEAS) machine shops, which were instrumental to the hardware setup of our low-temperature experimental systems.

In July 2019, I had the opportunity to join the summer school on quantum information machines at the École de Physique des Houches in France, where I rediscovered a simple but precious spirit that is not always present in elite American universities: everyone enjoys what they are doing for their own sake and does them admirably well. I want to thank Michel, Benjamin Huard, and Ioan Pop for organizing the program and bringing together the most passionate students and researchers in this field. At Les Houches, our manuscript on quantum microwave radiometry benefited from discussions with Patrice Bertet, Aashish Clerk, Konrad Lehnert, and Andreas Wallraff. I also want to thank Andreas, Patrice, and Leonardo DiCarlo for inviting me to visit their laboratories and universities/institutes. These visits will have a lasting influence on my career vision in the future.

The next group of people from the Yale community I am going to acknowledge are not directly connected to quantum physics, but have all influenced the contents and stylization of this dissertation in one way or another: First, I want to thank Verlyn Klinkenborg for his seminar on general-nonfiction writing, which was essentially about taming the structure and dynamics of a language to express facts and ideas in the most concise and clear manner;⁴ through his instructions, Verlyn effectively reshaped my conception of writing, which has since become a major interest of mine outside science. Maryam Sanjabi and Susan Morrow introduced me to the French and German languages, respectively, as new origins to explore the cultural diversity of the world. Deborah Coen, Chitra Ramalingam, and Paola Bertucci from the Yale Program in the History of Science and Medicine inspired me to look into the complexity and subtlety of human factors in modern science. Finally, it was a unique and enjoyable experience to be a teaching fellow⁵ for the general education course on film and physics co-created by Michel and Francesco Casetti, which was a bold pedagogical experiment aimed at demonstrating the interconnection of human creativities.

Furthermore, I want to thank Michel Devoret, Steven Girvin, Jack Harris, Douglas Stone, and Benjamin Huard for their careful reading of this work and many insightful questions. It is particularly fortunate to have Doug in my committee, who has witnessed my entire trajectory at Yale since my undergraduate research internship with his group back in Summer 2014; he has been another role model of mine for his deep knowledge in physics, his genuine support for young students, and his humanitarian perspective on the evolution of science.

This dissertation would not be completed without the constant support from my

⁴Unfortunately, due to the technicality of its contents, this dissertation cannot be fully aligned with Verlyn's minimalism language style.

⁵Together with Jacob Curtis, Carolyn Jacobs, and Joseph Lap.

friends both in and outside the Yale community, with whom I can freely exchange our intellectual ideas and life experiences. In particular, I want to thank Zhan Liu and Lev Krayzman for sharing apartments since the beginning of the pandemic. A special thank goes to Mingrui Zhang, my long-time neighbor in graduate dormitories, whose sincerity and wit are responsible for many memorable episodes in our friendship.

Last, I want to thank my parents Yan Wang and Lin Song for their unconditional love. Not being scholars themselves, they nevertheless understand the value of pure knowledge and have been supportive in every phase of my academic adventure. I would like to reserve the final acknowledgement to my grandpa Zhenglian Wang for being the exemplar of open-mindedness, professionalism, modesty, benevolence, and social responsibility in our family. His stories have been continually reinforcing my belief in lifelong learning and the promise of the common good in modern societies.

Scientific Overview

Naturally, it is of foremost importance for the researcher to establish a correct understanding of the significance of their work, as it steers their quest.⁶

Pyotr Leonidovich Kapitsa [1940]

This dissertation contributes to the field of quantum information physics by presenting the conceptual backgrounds, theoretical principles, experimental methods, and measurement results of two original experiments performed with superconducting Josephson circuits and microwave photons in the quantum mechanical regime. Together they provide inventive solutions to improving the protection and measurement of quantum coherent states in the superconducting circuit quantum electrodynamics (QED) architecture, and are demonstrating the potentialities of quantum microwave engineering methods in exploring the fundamental relations of physics and information with novel artificial quantum systems.

0.1 Background and problems

The methodical construction and operation of an information machine are necessarily based on the natural laws that are governing the processes of information preservation and acquisition on relevant physical scales. While the development of classical

⁶Original text (in Russian): “Естественно, что правильное понимание значения работы наиболее важно установить самому исследователю, так как это направляет его искания.”

analog and digital information systems has been supported by the sophistication of electromagnetism in vacuum and material media, advances in quantum information technology are relying on the exploratory experimentation with matter and radiation exhibiting distinct quantum mechanical behaviors. Researchers aspiring to build scalable and fault-tolerant information machines in the realm of quantum physics are facing two outstanding challenges: First, in real experimental setups, individual quantum states are inevitably subject to unwanted interactions with environmental degrees of freedom, to which a pure quantum coherent system will eventually lose its information—a process known as **decoherence**. Second, individual quantum degrees of freedom merely produce diminutive signals when directly detected by most classical apparatuses, which are also prone to exert excessive **measurement back-actions** on the quantum object under observation. Moreover, the practical difficulties in protecting and accessing information stored in quantum systems are often intercoupled: optimal coherence times can be expected when a quantum object is maximally isolated from its environment, whereas improving its measurability apparently demands the opposite experimental condition—the system should be strongly coupled to an external readout channel. The reconciliation of these two competing requirements is the primary motivation for the line of research reported in this dissertation.

We have been searching for solutions to this problem in an engineerable experimental platform known as the circuit QED system wherein **superconducting artificial atoms** are coupled to **microwave photons** through a quantum coherent interface. In a circuit QED module in the dispersive coupling regime, the readout resonator provides a filtered electromagnetic environment that suppresses off-resonance decoherence channels for the superconducting qubit, and meanwhile establishes a near-quantum-nondemolition (QND) readout scheme through bi-directionally mapping the state of the qubit onto the resonator frequency without direct energy exchange. However, the performance of linear circuit QED systems is being limited by

several parasitic mechanisms, two of which deserve special concern: First, residual electromagnetic radiation, a significant part of which originates from the nonideal thermalization of microwave circuitry on the base stage of the dilution refrigerator, produces an effect known as **measurement-induced qubit dephasing** through the same readout channel linking the superconducting qubit and the microwave resonator. Second, higher-order corrections to the linear dispersive readout model are responsible for **measurement-induced qubit-state transitions** during a microwave readout process, particularly when the resonator is populated with a large number of photons; high-speed qubit readouts thus cannot be performed above a power or photon-number threshold without a noticeable increase in measurement error and non-QND events. Can one implement modifications on the standard single-resonator, linear circuit QED architecture such that the qubit can be effectively protected from residual thermal electromagnetic noise, and be read out with close-to-ideal fidelities under a high measurement strength? This dissertation presents an affirmative answer to the former question and provides positive evidence for realizing the latter goal.

0.2 Summary of original contributions

During the course of research, we reached these answers through two separate and yet compatible experimental inventions—the **resonant cavity attenuator** and the **Π -mon artificial molecule**. The first project modifies the external microwave environment of the superconducting qubit in a linear circuit QED module. The second project redesigns the interface between the qubit and microwave photons by implementing an intra-cavity, on-chip Josephson amplifier that nonlinearly mediates and assists the qubit–photon interaction. Both innovations assemble state-of-the-art quantum electrical engineering techniques for the preparation, control and measurement of quantum states in superconducting microwave circuits.

In the first experiment, in order to reduce qubit dephasing induced by residual thermal photons in the readout resonator, we designed and tested a new type of band-pass microwave attenuator that consists of a dissipative cavity well thermalized to the mixing chamber stage of a dilution refrigerator. By adding such a cavity attenuator in-line with a three-dimensional (3D) superconducting readout cavity housing a superconducting transmon artificial atom, we have reproducibly measured increased qubit coherence times. At the base temperature, through a Hahn echo experiment, we measured $T_{2H}/2T_1 = 1.0^{+0.0}_{-0.1}$ for two transmon qubits over multiple cooldowns. Through noise-induced dephasing measurements, we obtained an upper bound of 2×10^{-4} on the residual photon population in the fundamental mode of the readout cavity, which to our knowledge is the lowest value reported so far. These results validate an effective method for protecting qubits against photon noise, which can be developed into a standard technology for quantum circuit experiments.

In the second experiment, we designed and implemented a multi-mode superconducting Josephson circuit named the “II-mon,” which contains a transmon artificial atom capacitively coupled to two galvanically connected Josephson-junction-array oscillators, which serve as an on-chip parametric amplifier. The electric dipole moments of the transmon and the amplifier are perpendicular, and hence the two modes are quadratically coupled with avoided linear interaction. The on-chip amplifier mode is linearly coupled to a 3D superconducting readout cavity. In this two-step readout scheme, the qubit state—hosted primarily in the transmon—is first mapped onto the amplifier mode frequency or its average population under a parametric drive, which then causes a dispersive shift on the readout cavity frequency that can be detected in a reflection measurement setup. The transmon displayed no observable measurement-induced qubit-relaxation effect up to 200 microwave photons in the readout cavity. Qubit readouts assisted by a qubit-state-selective single-excitation parametric drive for the amplifier mode showed a sevenfold increase in the measurement strength or a

17 dB intra-cavity signal gain, with single-shot readouts demonstrated using 80 cavity photons. We expect an improved readout fidelity and speed be achieved by selectively populating the amplifier oscillator with a larger excitation number conditioned on the qubit state, and plan to examine the QND fidelity of this readout protocol with more than 100 cavity photons.

The cavity attenuator and Π -mon experiments, although separately executed, jointly contribute to a revised quantum architecture in which high-coherence physical qubits are designed to be accurately and efficiently read out with suppressed parasitic measurement back-actions: The qubit has a reduced static coupling rate to the microwave readout mode, which is realized either by adding extra-cavity cold dissipations or by reorienting the electric dipole moment of the qubit such that it is decoupled from the cavity at the linear order. In principle, these two strategies can also be implemented simultaneously. In the latter arrangement, the qubit readout is enabled by an intra-cavity parametric amplifier, through which the qubit-cavity interaction is only turned on when a frequency-selective parametric drive is applied. The combination of the on-chip geometric layout, intra-cavity parametric amplification, and extra-cavity dissipation engineering will collectively improve the protection of quantum information relative to its accessibility from external measurement channels, so as to alleviate the apparent conflict between information preservation and acquisition in a physical unit and prepare reliable elementary building blocks for scalable quantum information machines.

0.3 Arrangement of chapters and sections

The main body of this dissertation contains seven chapters. Their high-level organization is indicated by the flow chart in Figure 0.

As the opening introduction, Chapter 1 is aimed at preparing the readers with the

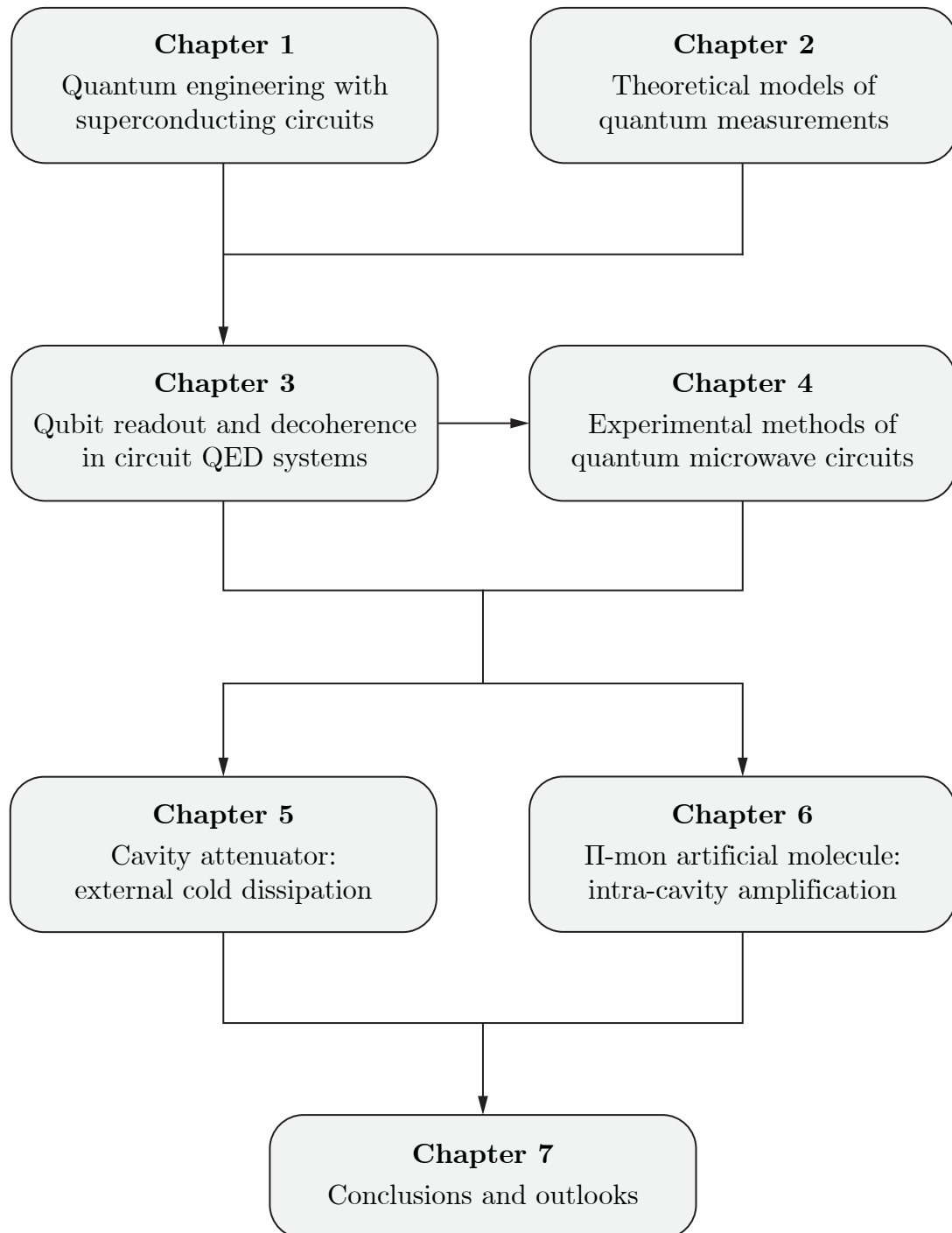


Figure 0: Chapter-level structure of this dissertation.

core concepts, methodology, problems, and knowledge on the experimental platform of the research topics addressed by this dissertation. The focus is placed on the quantum engineering method toward fundamental physics and information science (Sections 1.1 and 1.2), definition and elementary requirements of quantum information machines (Section 1.2), the emergence of mesoscopic quantum phenomena (Section 1.3.1), the principles of superconducting artificial atoms and circuit QED (Sections 1.3.2 and 1.3.3), as well as the basic notions of noise in quantum limited amplifications and dissipative quantum systems (Sections 1.3.4 and 1.4). Meanwhile, this chapter also contains a few technical points that will be revisited in the following chapters, such as the reduction of Josephson nonlinearity in a junction array (Section 1.3.2) and the radiative limit of qubit relaxation time (Section 1.3.3). These ideas and tools are foundational to the more specialized contents in the rest of this dissertation.

Chapter 2 consists of selected topical discussions on the rudimentary theoretical framework for describing and analyzing quantum measurements in both the ideal and nonideal situations, starting from perceiving general physical measurements from the information perspective (Section 2.1) and presenting the minimal conceptual model of a quantum measurement setup (Section 2.2). Section 2.3 defines the four important figures of merit that quantify the ideality of a realistic qubit readout scheme from different and yet interrelated angles—readout fidelity, QND fidelity, measurement time, and measurement efficiency. This chapter closes with the full analysis on a discrete-time, conveyor-belt model for continuous quantum measurements (Section 2.4), which, despite its simplicity, has unique values for visualizing the physical process of information acquisition and understanding the origin of measurement back-actions in real quantum systems.

Combining the background knowledge and the theoretical models in the previous two chapters, Chapter 3 reviews the physics of circuit QED measurements. Following the sketches of three relevant precursory experiments (Section 3.1), the principle of

the dispersive readout based on the linear qubit–cavity coupling in a circuit QED module is examined in detail in Section 3.2. The two accompanying effects—namely, qubit dephasing and state-transition effects induced by microwave photons in the measurement channel are discussed in Sections 3.3 and 3.4, respectively. One central message from this chapter is that measurements and dephasing in a quantum coherent system are the two sides of the same coin, which is proved by the agreement between the measurement rate and the dephasing rate during the qubit–photon interaction process (Section 3.3). Moreover, one is encouraged to engineer novel types of qubit–cavity coupling beyond the linear dispersive model in search for higher QND fidelities and lower measurement back-actions in fast readout protocols (Section 3.4). These principles and issues are directly motivating our original experiments to be reported in the following chapters.

Chapter 4 summarizes the essential laboratory techniques for conducting superconducting quantum circuit experiments, including the preparation of Josephson circuit samples (Section 4.1), the design of superconducting microwave readout cavities (Section 4.2), the cryogenics and thermometry of the dilution refrigerator (Section 4.3.1), the low-temperature microwave measurement setup (Section 4.3.2), the thermalization and electromagnetic shielding of cryogenic experimental components (Section 4.3.3), the room-temperature electronics for microwave pulse generation (Section 4.4.1) and detection (Section 4.4.2), and the software tools for experimental control and simulation (Section 4.5). In the meantime, this chapter exposes the practical problems in the standard circuit QED measurement system that are going to be addressed by our experimental inventions—in particular, the issues of residual thermal electromagnetic radiation and parasitic dissipations in the low-temperature microwave circuitry (Section 4.3). These engineering methods and practical knowledge complement the preceding theoretical chapters and elucidate the specific context of our original works.

Chapter 5 reports the resonant cavity attenuator experiment.⁷ I will first explain the advantage of distributed over lumped-element resistive circuits in their thermalization properties for low-temperature applications (Section 5.1), and argue for using a high-surface-to-volume-ratio dissipative resonant cavity made of high-thermal-conductivity materials as the reliable cold thermal reservoir for microwave quantum circuits (Section 5.2). I will then provide the test results of the cavity attenuator devices designed following these principles (Section 5.2) and analyze its coupling scheme with a standard superconducting circuit QED module to form hybridized dissipative readout modes for the qubit (Section 5.3). The effectiveness of these cavity attenuators are proved by the measurement data on qubit coherence times and residual thermal photon population in the readout mode (Sections 5.4 and 5.5). The reproducibility of these results has been confirmed in control experiments. This chapter is concluded by Section 5.6, which confirms the necessity of thermal radiative protection for superconducting qubits and proposes a few directions for improving the versatility of cavity attenuators in circuit QED experiments.

Chapter 6 presents the design and preliminary experimental results of the Π -mon artificial molecule.⁸ The chapter is opened with the basic mechanisms, examples, and advantages of incorporating intra-cavity amplification schemes into the circuit QED measurement system (Section 6.1), and continues with the two desired features in our implementation—the two-step mediated readout and the cross-Kerr qubit–amplifier coupling (Section 6.2). The multi-mode design of the Π -mon artificial molecule is presented in Section 6.3, which is analyzed using both the even–odd circuit diagram method (Section 6.3.1) and the Lagrangian–Hamiltonian formulation (Section 6.3.2).

⁷The experimental results in Chapter 5 have been previously published in Wang *et al.* [2019].

⁸The works reported in Chapter 6 have not been published as of the time when this dissertation was completed.

These two approaches yield equivalent coupled mode analysis results, with the latter leading to the canonical circuit quantization (Section 6.3.3). The coupling scheme between the Π -mon and the linear readout cavity is explained in Section 6.4, with the experimental setup and parameters introduced in the same section. The nonlinear responses of the on-chip amplifier oscillator in the two-tone spectroscopy measurements are reported in Section 6.5. The suppression of photon-induced qubit-state transition events are shown in Section 6.6. Most importantly, clear evidence of intra-cavity parametric amplification in both the continuous-wave and pulsed measurement sequences are presented in Section 6.7, with the preliminary demonstration and characterization of single-shot qubit readouts reported in the end. Methods for improving the readout performances are proposed in the final Section 6.8.

While both Chapters 5 and 6 contain their own conclusion-and-prospect section, Chapter 7 summarizes the merits of combining extra-cavity cold dissipation and intra-cavity parametric amplification for improving qubit coherence times relative its measurability, and discusses the chances and challenges for the implementation of this revised circuit QED architecture. This chapter ends with remarks on the extended implications of our experimental results for the thermalization of hybrid quantum networks and the modeling of multi-stage quantum measurement systems.

Chapter 1

Quantum Electrical Engineering: A Conceptual Primer

... In this sense, strictly speaking, physics with respect to its method (not its aim) is not at all a natural science like astronomy, geology, botany, etc.; it deals with no natural phenomena, but phenomena artificially and intentionally produced by the researcher; and in this sense it can be called a technical science.¹

Felix Auerbach [1923]

The essence of *engineering*—as both a branch of empirical knowledge and a unique form of human activity—is the methodical construction and manipulation of artificial systems based on received natural principles. By this definition, the scientific studies being presented in this dissertation are primarily affiliated to an emerging field entitled **quantum engineering**² in which researchers endeavor to develop novel tools,

¹Original text (in German): “... In diesem Sinne ist die Physik der Methode (nicht dem Ziele) nach streng genommen überhaupt keine Naturwissenschaft, wie es die Astronomie, die Geologie, die Botanik usw. sind; sie behandelt gar keine Naturerscheinungen, sondern künstlich und nach Willkür des Forschers hergestellte Phänomene; und in diesem Sinne kann man sie geradezu als eine technische Wissenschaft bezeichnen.”

²Although it is not easy to identify in the scientific literature the exact coinage of this phrase, one of its early appearances was remembered as a famous confession by John Stewart Bell in 1983, quoted in Gisin [2002]: “I am a quantum engineer, but on Sundays I have principles.” However, to Bell the

machines, and their networks by exploiting fundamental laws of quantum mechanics. Evidently, a quantum engineer is obliged to be fluent in quantum theory—not merely its mathematical formulation, but more importantly, its application to describe states and motions of physical matter and radiation. Meanwhile, quantum engineers are not satisfied with observing physical objects in their most natural states or surroundings; they instead actively employ engineering techniques to create experimental systems that would not exist in nature by default. In the laboratory, a quantum engineering experiment must contain two major parts—the selection and preparation of quantum coherent systems, and their control and measurement instruments that behave like classical objects. The efforts spent to resolve these outstanding technical challenges can only be justified by the intellectual or practical rewards that those exceptional engineering projects are to bring about.

This introductory chapter is aimed at reviewing a selected list of ideas, objects, and phenomena that prepare the conceptual foundation for this dissertation. Its four sections are devoted to the central “methodology,” “goal,” “platform,” and “problem” respectively that define the represented line of research—the *protection and measurement of quantum states in superconducting electrical circuits*. Clarity and accessibility are placed above comprehensiveness with respect to the style of presentation. For each topic, a small number of pedagogical references are grouped in footnotes for further reading and reflection.

“engineering” aspect of quantum physics chiefly refers to the operation of its theoretical machinery for computational purposes as opposed to the critical contemplation of its conceptual and philosophical basis, which is therefore different from the subject of this dissertation. In fact, “quantum engineering” as a contemporary field of research has provided essential tools for the experimental examination of quantum foundations, including Bell’s theorem. For a historical inquiry into the fundamentalism–pragmatism struggle among the quantum physics community in the postwar United States, together with its scientific and cultural impacts, see Kaiser [2011].

1.1 Engineering science in the quantum regime

While originally referring to the discreteness of energy or action in early phenomenological models for resolving the fundamental difficulties of applying classical theories to atoms and radiation, “quantum” as a modifier has since then been employed to denote a collection of natural phenomena and laws first emerging on the scale of atoms, photons, and subatomic particles, such as the discontinuity of state transitions (quantum jumps), the invasiveness of observation (quantum measurement back-action), and the existence of nonlocal correlations (quantum entanglement), and many others, which were generally perceived as “counterintuitive” or “incomprehensible” even by some of the leading contributors to this revolutionary field.³

Contrary to certain predictions that an excessive level of alienness would estrange a scientific theory from human culture,⁴ over the decades physicists have never ceased their attempts to examine the peculiarities of quantum mechanics in more direct and objective ways: For this purpose, incoherent ensembles of microscopic particles have been replaced by individual atoms, photons, electrons, or collective excitations in condensed matter and atomic gases for the demonstration of quantum coherence and measurement *in vivo*.⁵ In these experiments, single quantum degrees of freedom can

³A particularly publicized example is Albert Einstein, who during his career has left a number of memorable remarks including “Gott würfelt nicht!” (“God does not play dice!”) and “spukhafte Fernwirkungen” (“spooky actions at a distance”). In spite of these critical comments, Einstein’s role in the early history of quantum physics was overall more revolutionary than reactionary [Stone, 2013]. For monograph-length technical discussions on the conceptual perplexities of quantum theory, see Aharonov and Rohrlich [2005] and Laloë [2012].

⁴For instance, such view was expressed by Erwin Schrödinger during mid-century [Schrödinger, 1952a]. The sequel article [Schrödinger, 1952b], which assumed it would be impossible to experiment with single quantum mechanical particles, is now frequently cited to show the limitation of even the most pioneering minds. Nevertheless, Schrödinger’s central argument in these two articles that a scientific discipline should not be disconnected from its cultural context is not entirely unreasonable.

⁵For an introduction to this field, see Haroche and Raimond [2006], which has a central focus on the control and measurement of microwave cavity photons using circular Rydberg atoms. Three

only be observed in *artificial* environments—for instance, high-finesse optical or microwave cavities, electromagnetic fields in vacuum chambers, or nanostructures on solid-state substrates—and meanwhile under stringent physical conditions, often including low temperatures and carefully filtered radiation backgrounds. In the meantime, classical optical or electrical signals are applied to control and interrogate those quantum objects, manipulating their states and carrying their information back to the experimenters. Furthermore, in certain experimental platforms such as superconducting Josephson circuits (see Section 1.3), engineering methods are present not only in the *environments* and the *control, measurement, and communication tools* for the quantum degrees of freedom, but in the *design* and *fabrication* of these quantum objects as well. In this example, one can compare the degree of artificiality of a quantum circuit experiment to that of a steam engine or a radiowave receiver. The term “quantum engineering” can thus be fully justified.

However, the elevated level of human involvement in the construction and operation of quantum machines by no means implies these artificial systems are distanced from nature, or quantum engineering is purely an applied field that is distinct from basic science. On the contrary, engineered quantum systems have assisted their inventors to depict the properties and behaviors of single or many quantum mechanical particles with unprecedented lucidity: Once a new quantum machine prototype is created, researchers must immediately calibrate its performance with reference to basic physics principles; and if the reliability of this type of machines is confirmed, they are often applied to test predictions of quantum theory or to detect radiation or materi-

more recommended textbooks are Cohen-Tannoudji and Guéry-Odelin [2011], Nazarov and Blanter [2009], and Zagoskin [2011], with the first covering atomic systems and the latter two on solid-state platforms. More up-to-date pedagogical materials are available from proceedings of topical summer schools, such as Esteve *et al.* [2004], Devoret *et al.* [2011], Inguscio *et al.* [2016], and Cohadon *et al.* [2020].

als of unexplored categories. The research work of a quantum engineer is therefore hardly distinguishable from that of a physicist; and in reality, this distinction may not exist at all, because in quantum engineering, scientific inquiries and engineering techniques are more concerted than exclusive. A quantum engineer is a scientist and an engineer at the same time.

1.2 Quantum information machines: principles, prospects, and challenges

Up to the present, most engineered quantum systems have been designed and operated as *information* machines. This trend can be partially attributed to the leading external impetus since the 1980s—namely, the quest for the physical implementation of quantum algorithms that are capable of demonstrating computational advantages beyond the limitation of classical digital logic, especially in certain problems with practical implications [de Wolf, 2019; Mermin, 2007; Nielsen and Chuang, 2000]. Nevertheless, quantum machines have their intrinsic connections to information science even without being assigned explicit computational tasks by their designers, which can be understood from the perspective of information transmission or communication: As a general principle, the execution of any physical measurement leads to an entropy reduction of the system under observation and simultaneously, an information gain of the observer (see Chapter 2 for details). This information channel linking the physical system and the experimenter is of particular interest if the former exhibits quantum behaviors, and in this situation, an efficient measurement chain serves as a sensitive probe for examining the dynamics of those quantum degrees of freedom and their interactions with the external environment. In summary, *a measurement system with quantum coherent objects under observation is by default a quantum information machine*; consequently, engineering efforts in inventing and improving these experi-

mental systems constitute valuable contributions to quantum information science.

How can a quantum information machine be distinguished from a classical one? The primary criterion is less about its microscopic material constitution, but whether human experimenters are able to *interact* with it through control and measurement channels that manifest distinct quantum features, including but not limited to indeterministic outcomes of identical measurements, the incompatibility of noncommuting observables (or quantum measurement back-action), vacuum fluctuations in measurement signals, et cetera [Devoret, 2008; Devoret *et al.*, 2011]. By this definition, the core constituent of a quantum (information) machine can be as tiny as single electrons on a liquid or solid noble-gas surface [Koolstra *et al.*, 2019; Platzman and Dykman, 1999; Schuster *et al.*, 2010; Zhou *et al.*, 2022], or as massive as fused silica mirrors weighing tens of kilograms in a gravitational wave interferometer [Whittle *et al.*, 2021; Yu *et al.*, 2020].⁶ The crucial requirement is whether these natural or artificial entities can be configured using experimental methods into a regime where quantum laws overrule their classical counterparts.

Although a wide range of physical objects can display quantum behaviors under appropriate conditions, higher standards ought to be imposed if one wishes to declare a quantum engineering system to be a reasonable candidate for scalable, fault-tolerant quantum information machines. At the turn of the new millennium, driven by a reductionist viewpoint, DiVincenzo [2000] discussed the physical realization of quantum computation by proposing a set of requirements on the elementary unit of quantum information—**quantum bit**, usually abbreviated as **qubit**, namely, quantum coher-

⁶On the contrary, semiconductor transistors, such as the metal–oxide–semiconductor field-effect transistor (MOSFET) in integrated circuits, despite approaching the nanometer scale in state-of-the-art manufacturing processes, are still classical information devices because their voltage and current signals are well-observed classical quantities, which is necessary for the operation of classical digital logic.

ent (either mathematical or physical) object with a Hilbert space identical to that of a spin-1/2 system. For clarity, DiVincenzo’s criteria can be regrouped in four major aspects and be rephrased as

- (i) **Coherence:** Qubit coherence times should be—preferably by several orders of magnitude—longer than the time scale of control and measurement operations.
- (ii) **Controllability:** High-fidelity initialization protocols and universal quantum gate sets should be available for qubit state manipulation.
- (iii) **Measurability:** High-quality (to be defined in Section 2.3) qubit readout protocols should exist for information output and quantum error correction.
- (iv) **Connectivity/scalability:** Individual qubits should be able to couple locally or remotely so as to form quantum processors or networks on larger scales.

Concise and clear as these requisites are, any conceptual breakdown of a holistic problem must always be complemented with a reminder that in reality, the multiple dimensions of a practical challenge are often not orthogonal and thus may not be optimized independently. Such is the case of DiVincenzo’s criteria, in which the different requirements are intercorrelated at the physical level.⁷ For instance, the reconciliation of “coherence” with “controllability” and “measurability” requests nontrivial strategies, because their improvements apparently demand opposite experimental

⁷More than one decade later, Devoret and Schoelkopf [2013] proposed an updated, stepwise research roadmap, which supplied DiVincenzo’s classic criteria with up-to-date experimental considerations: for instance, the quantum nondemolition (QND) property of readout protocols was emphasized; the implementation of error-corrected logical qubits was recognized as the key step toward achieving fault-tolerant quantum computation; modular architectures were promoted in regard to building quantum information systems with greater complexity and scalability; and very importantly, the improvement of elementary components and operations—such as qubit coherence and measurement—remains a continuing endeavor in parallel with progress occurring at higher logical levels.

conditions: longer coherence times are more achievable when qubits are further isolated from their surroundings and therefore immune to environmental perturbations, whereas fast control and readout have to be implemented through external electromagnetic channels to which the qubits are strongly coupled. Moreover, we are going to encounter in Section 2.3 that different figures of merit for “measurability” are not all positively correlated either. The lesson is that real experimental progress in quantum information processing cannot merely feature an isolated improvement in any single category. Instead, one is obliged to show that this improvement is implemented not—at least not in principle—simply at the expense of other performance metrics.

The central goal of the series of projects reported in this dissertation is the optimization of the “coherence” and “measurability” of superconducting qubits in the circuit quantum electrodynamics (QED) architecture, by understanding and engineering the interactions between artificial atoms (molecules) and microwave photons in an open, dissipative environment. Prior to more technical discussions, our introduction should benefit from a succinct review of the concepts and experimental platforms of quantum electrical engineering, with a focus on its realization using superconducting Josephson circuits.

1.3 Quantum electrical circuits: ideas and implementations

Electrical circuits should be no strange to citizens of our “electrified” modern world. And yet those macroscopic engineering constructions, which confine electromagnetic fields for power or information purposes, are not intuitively associated with the realm of atoms and photons.⁸ How can electrical circuits be quantum mechanical? Why do

⁸An extremely clear and intuitive derivation of circuit notations from electromagnetic field theory were presented by Feynman *et al.* [1964]. A similar derivation from Maxwell’s field equations to

researchers study quantum phenomena in these artificial devices, as opposed to using natural atoms and molecules? What are the unique tools and architectures they have provided for quantum engineering? This section will address these questions in the logical order, which happens to be chronological as well.

1.3.1 Macroscopic quantum phenomena

In 1935, Erwin Schrödinger raised the famous “cat paradox” trying to showcase the absurdity of applying quantum theory to macroscopic living beings [Schrödinger, 1935]. This paradox has nevertheless sparked the interest among contemporary physicists to search for quantum phenomena in objects much larger than atoms and molecules. A few lines of work have been remarkable: First, several classes of condensed matter, for example, superconductors, superfluids, and Bose–Einstein condensates, manifest the *macroscopic accumulation of microscopic quantum effects* [Annett, 2004; Leggett, 2006].⁹ Second, *quantum transport* phenomena, such as the quantized conductance and the quantum Hall effect, can emerge in low dimensional, high-purity solid-state samples where the electron coherence length is comparable to the sample size [Datta, 1995]. Third and the most relevant to this dissertation, in certain physical systems, *collective degrees of freedom* arising from the participation of a macroscopic number of microscopic particles, when thermalized at sufficiently low temperatures and carefully isolated from their external environment, can contain no more than a few quanta of excitation and thus exhibit clear quantum dynamics. One of the first ob-

Kirchhoff’s circuit laws can be found in Appendix A of Agarwal and Lang [2005].

⁹Take the BCS ground-state wave function $|\Psi_{\text{BCS}}\rangle = \prod_{\vec{k}} \left(u_{\vec{k}} + v_{\vec{k}} \hat{e}_{\vec{k}\uparrow}^\dagger \hat{e}_{-\vec{k}\downarrow}^\dagger \right) |0\rangle$ as an example, in which \hat{e}^\dagger stands for the electron creation operator; \vec{k} for the spatial momentum; $\uparrow\downarrow$ for the spins; $u_{\vec{k}}$ and $v_{\vec{k}}$ as in the Bogoliubov transformation; and $|0\rangle$ for the vacuum state [Bardeen *et al.*, 1957]. Quantum entanglement is generated and only generated between each electron pair with opposite momenta and spins, whereas $|\Psi_{\text{BCS}}\rangle$ is simply the product state of a macroscopic number of entangled Cooper pairs.

served macroscopic quantum variable is the gauge-invariant phase difference across a superconductor–insulator–superconductor (SIS) tunnel junction, commonly known as the **Josephson junction** [Anderson and Rowell, 1963; Josephson, 1962, 1964] (see Figure 1.1).¹⁰ It was discovered in mid-1980s that at sub-hundred-millikelvin temperatures, in a current-biased Josephson junction, the escape rate of its macroscopic phase variable in the washboard potential deviates from the classical calculation and obeys the distinct quantum mechanical prediction due to the quantum tunneling effect [Clarke *et al.*, 1988; Devoret *et al.*, 1985; Martinis *et al.*, 1985, 2020]. In these experiments, quantum fluctuations of a single collective degree of freedom emerged to be comparable to thermal excitations, and had caused nonclassical measurement outcomes. More recently, the Josephson phase variable across tunnel junctions has been joined by quantized vibrational modes—phonons—in mechanical oscillators [O’Connell *et al.*, 2010] and quantized spin waves—magnons—in ferromagnetic crystals [Tabuchi *et al.*, 2014, 2015] to form a growing list of experimental systems wherein single macroscopic quantum variables can be observed and manipulated *in vivo*. These solid-state platforms have therefore offered unique opportunities for researchers to design novel artificial quantum systems using available engineering tools.

The subfield of modern physics studying the aforementioned macroscopic quantum

¹⁰As it was discovered later, the Josephson effect can be observed in several classes of mesoscopic heterostructures consisting of two pieces of superconductor interrupted by a “weak link,” which can be either short or long compared to the superconducting coherence length [Likharev, 1979]. The thin insulator layer in an SIS tunnel junction—as depicted in Figure 1.1—is one example of weak links, which allows a supercurrent to flow across the junction due to the coherent quantum tunneling effect of Cooper pairs. Microscopic mechanisms other than quantum tunneling are present in other types of weak links such as quantum point contacts and semiconductor nanowires, in which supercurrents are conducted by localized fermionic modes known as Andreev bound states [Andreev, 1964; Beenakker and van Houten, 1991; Furusaki and Tsukada, 1991]. In this light, the theory of Andreev reflection and Andreev bound states provides a unified picture for understanding the Josephson effect: for instance, the supercurrents across an SIS tunnel junction (or simply, Josephson junction) can be thought as being carried by millions of sub-gap Andreev levels due to the presence of a large number of conduction channels in the weak link. See Hays [2021] for further discussions.

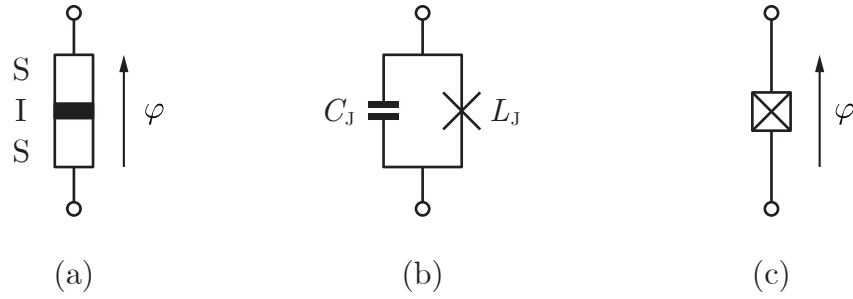


Figure 1.1: Physical structure and circuit symbols of a Josephson junction. (a) Cross-section sketch of the tunnel junction: a Josephson junction is a single-port electrical device consisting of two pieces of superconductor (S) separated by a nanometer-thin insulator layer (I). The gauge-invariant phase variable φ is the time integral of the voltage V across the junction: $\varphi(t) = \phi_0^{-1} \int_{-\infty}^t V(t') dt'$, where $\phi_0 = \hbar/2e$ is the reduced magnetic flux quantum. (b) Using the lumped-element circuit language, a Josephson junction can be represented as a junction capacitor C_J shunting an ideal Josephson element (cross), which possesses a nonlinear inductance $L_{NL}(\varphi) = L_J / \cos \varphi$, with $L_J = \phi_0 / I_c$ defined as the Josephson inductance and I_c being the critical current of the junction. (c) Circuit symbol of a Josephson junction equivalent to the parallel circuit in (b). For the physics of the Josephson effect, see de Gennes [1966], Tinkham [1996], Rose-Innes and Rhoderick [1978], and Orlando and Delin [1991].

phenomena has been called **mesoscopic physics**, for these physical objects of interest are neither *macroscopic* systems in the conventional definition where laws of classical mechanics reign, nor *microscopic* systems in the strict sense that are only composed of a small number of atomic or subatomic particles.¹¹ The central reason underlying this unique “intermediate” category is illustrated in Figure 1.2: in nature, there is no necessary correlation between the *number of particles* in a physical system and its

¹¹Besides Datta [1995] and Nazarov and Blanter [2009], also see Imry [1997], Akkermans [2010], Grabert and Devoret [1992], and Sohn *et al.* [1997] for an overview of mesoscopic physics. References on macroscopic quantum coherence overlaps those about quantum machines in Footnote 5 of this chapter. In practice, mesoscopic physics also includes the studies of low-dimensional quantum structures such as quantum dots, nanowires, and carbon nanotubes, although quantum variables in these systems (for instance, single electron spins) are often microscopic in their nature.

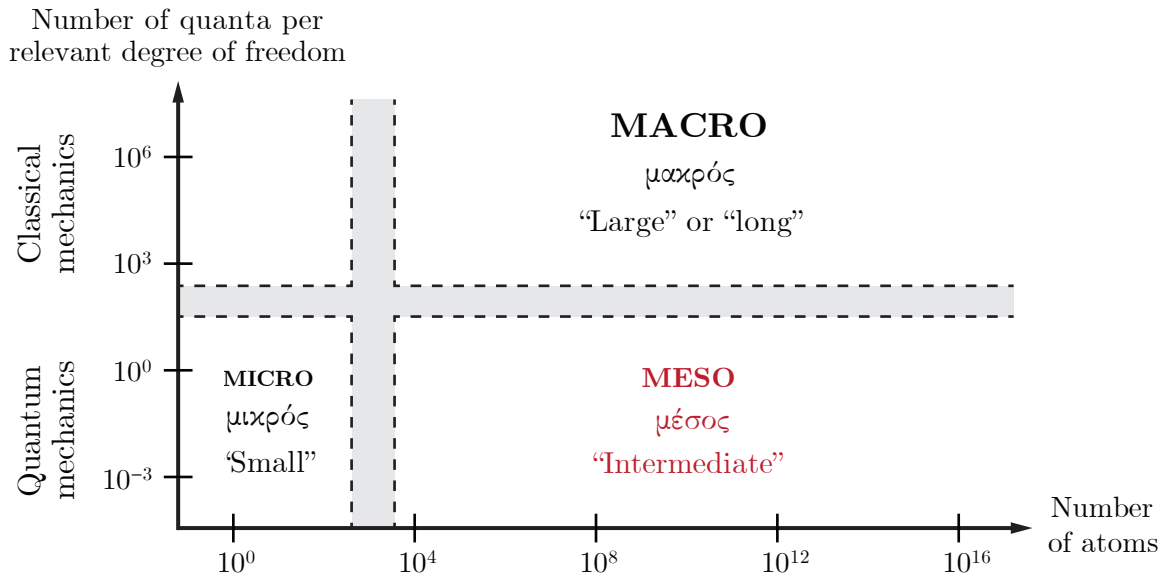


Figure 1.2: Illustration of the macroscopic, microscopic, and mesoscopic scales. The horizontal and vertical axes represent the structural complexity and the information complexity of a physical system, respectively. Mesoscopic phenomena arise when the system contains a large number of atoms but at the same time, only a very small number of excitation quanta per degree of freedom. The Latin prefixes of these three scales are annotated with their ancient Greek roots and their literal translations.

number of excitation quanta per degree of freedom; and it is the excitation number, rather than the particle number, that distinguishes the quantum regime from the classical one.

1.3.2 Superconducting artificial atoms

Following the observations of macroscopic quantum phenomena, the next important step toward engineering a “Schrödinger’s cat” was to demonstrate the quantum superposition and coherent dynamics of classical states that are macroscopically dis-

tinguishable.¹² Such idea was first proposed as a crucial test for the applicability of quantum theory to the macroscopic realm [Leggett, 1980, 1987], and were then realized around the turn of the century in several superconducting microwave devices containing one or more Josephson junctions [Chiorescu *et al.*, 2003; Martinis *et al.*, 2002; Nakamura *et al.*, 1999; Vion *et al.*, 2002; Yu *et al.*, 2002]. These mesoscopic electrical circuits have been generically named **superconducting artificial atoms** because one can coherently manipulate their quantum state just like in natural atoms. A superconducting artificial atom is reduced to a **superconducting qubit** if only two levels in its energy spectrum are of practical interest—for instance, being used as computational basis states for quantum information processing.¹³

Experimentally, an “atom” is characterized by a discrete set of energy levels in its low-energy spectrum; but besides that, it must have two additional properties in order to display quantum coherent dynamics in the time domain:

- (i) *Low dissipation*: The linewidths of those energy levels should be small compared to their level separations, which is essential for quantum systems to have long intrinsic coherence times.
- (ii) *Nonlinearity*: Those energy levels must not be equally spaced as in a quantum harmonic oscillator, which would otherwise prohibit the selective excitation of individual levels using electromagnetic drives.

¹²At the theoretical level, the measure of “macroscopic distinguishability” between different mesoscopic classical states in quantum coherent experiments has been a subtle topic of discussion. See Fröwis *et al.* [2018] for an updated review.

¹³A few recommended introductions to the basic physics of superconducting qubits are Makhlin *et al.* [2001], Devoret and Martinis [2004], Martinis [2004], Wendin and Shumeiko [2007], Clarke and Wilhelm [2008], Girvin [2014], Wendin [2017], and Krantz *et al.* [2019]. Also see Kjaergaard *et al.* [2020] and Siddiqi [2021] for reviews on recent experimental advances.

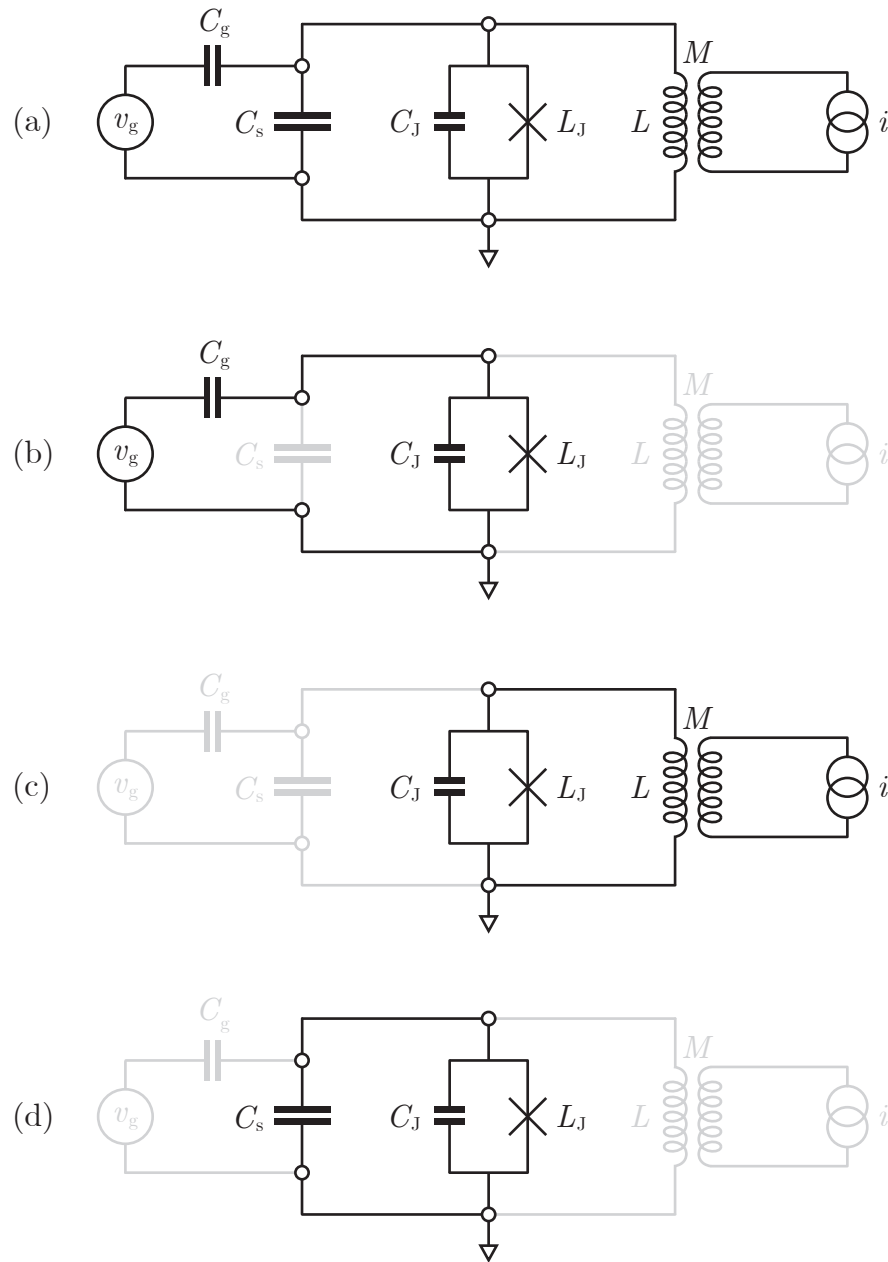


Figure 1.3: (a) Generic circuit model of a superconducting artificial atom. The triangular symbol denotes a radio-frequency (RF) ground. (b) Cooper-pair box: prototype of the charge qubit family [Bouchiat *et al.*, 1998; Nakamura *et al.*, 1999]. (c) RF superconducting quantum interference device (SQUID): prototype of the flux qubit family [Friedman *et al.*, 2000]. (d) Transmon: a variation of the charge qubit, wherein the Josephson junction is shunted by an external capacitor [Koch *et al.*, 2007; Paik *et al.*, 2011; Schreier *et al.*, 2008].

Electrical signals in superconductors have near-zero dissipation if the photon energies associated with those signals are far below the superconducting energy gap—typically corresponding to microwave or far-infrared frequencies for conventional BCS superconductors [Tinkham, 1996]; resonant electromagnetic modes in superconducting circuits should therefore have high quality factors, in practice mainly limited by their coupling to the environment. Furthermore, the Josephson junction (Figure 1.1) provides a nonlinear inductive element, which breaks the harmonic energy-level structure of a linear resonant circuit mode. Hence researchers have been implementing varieties of superconducting artificial atoms using Josephson junctions connected to a linear reactive circuit network.

The circuit model of a prototypal superconducting artificial atom is presented in Figure 1.3, where the Josephson junction in the center is coupled to external shunting and biasing circuitry on both sides. The variation among different classes of artificial atoms arises from the competition of three energy scales [Smith, 2019]:

- (i) Josephson energy, defined as the energy gain per single electron when a Cooper pair tunnels across the Josephson junction, and phenomenologically equal to

$$E_J = \frac{\phi_0^2}{L_J}, \quad (1.1)$$

in which $\phi_0 = \hbar/2e$ is the reduced magnetic flux quantum, and $L_J = \phi_0/I_c$ is the Josephson inductance. Alternatively, I_c and E_J can be predicted using the microscopic BCS theory [Ambegaokar and Baratoff, 1963a,b],

$$I_c = \frac{\pi\phi_0}{\hbar} \frac{\Delta}{R_n}, \quad (1.2)$$

$$E_J = \frac{\pi\phi_0^2}{\hbar} \frac{\Delta}{R_n}, \quad (1.3)$$

where Δ denotes the superconducting energy gap, and R_n is the junction resis-

tance in the normal (non-superconducting) state.

- (ii) Coulomb energy, defined as the charging energy of transferring one single electron to the top electrode,

$$E_C = \frac{e^2}{2C}, \quad (1.4)$$

in which $C = C_J + C_s + C_g$ is the total capacitance between the junction electrodes.

- (iii) Linear inductive energy

$$E_L = \frac{\phi_0^2}{L}. \quad (1.5)$$

The specific type of artificial atom that will be investigated in this dissertation is the **transmon**, which is schematically a nonlinear LC oscillator consisting of—as depicted in Figure 1.3(d)—a Josephson junction, an external shunting capacitor $C_s \gg C_J$, and no external linear inductor ($E_L = 0$). Concerning the energy scales, the circuit is in a regime of $E_J/E_C \sim 50\text{--}100$, which is designed to suppress unwanted energy-level dispersions caused by gate charge fluctuations in the Cooper-pair box [Figure 1.3(b)], and meanwhile, to maintain a reasonable anharmonicity for fast qubit control operations [Koch *et al.*, 2007]. Mathematically, the classical Hamiltonian of a transmon circuit can be written using the magnetic flux and electric charge variables on its top electrode,

$$H_t = \frac{q^2}{2C} - E_J \cos\left(\frac{\Phi}{\phi_0}\right), \quad (1.6)$$

or alternatively using the dimensionless superconducting phase $\varphi = \Phi/\phi_0$ and Cooper-

pair number $n = q/2e$,

$$H_t = 4E_C n^2 - E_J \cos(\varphi). \quad (1.7)$$

Note that the above two equations have the same form as the Hamiltonian of a one-dimensional rigid rotor in the gravitational field. In the transmon regime ($E_J \gg E_C$), the dynamics of the system is confined to the vicinity of $\varphi = 0$, and hence¹⁴

$$H_t = 4E_C n^2 + \frac{E_J}{2} \varphi^2 - \frac{E_J}{24} \varphi^4 + O(\varphi^6). \quad (1.8)$$

The canonical circuit quantization protocol¹⁵ yields

$$\varphi \rightarrow \hat{\varphi} = \varphi_{\text{ZPF}}(\hat{t}^\dagger + \hat{t}), \quad (1.9)$$

$$n \rightarrow \hat{n} = in_{\text{ZPF}}(\hat{t}^\dagger - \hat{t}), \quad (1.10)$$

in which the quantum operators obey their commutation relations

$$[\hat{\varphi}, \hat{n}] = i \quad (1.11)$$

$$[\hat{t}, \hat{t}^\dagger] = 1. \quad (1.12)$$

¹⁴Note that we have dropped the constant term $-E_J$ in this Hamiltonian expansion. Another type of constant term that will be dropped in this dissertation is the zero-point energy of a harmonic oscillator mode in quantized Hamiltonians.

¹⁵For the Lagrangian and Hamiltonian representations of electrical circuits and their canonical quantization protocol, see Devoret [1997] and Vool and Devoret [2017]. For a general treatment on the quantization of electromagnetic fields, see Cohen-Tannoudji *et al.* [1987].

Moreover, zero-point fluctuations of φ and n are given by

$$\varphi_{\text{ZPF}} = \frac{1}{\sqrt{2}} \left(\frac{8E_C}{E_J} \right)^{\frac{1}{4}} = \frac{1}{\sqrt{2}} \sqrt{\frac{2\pi Z_c}{R_q}}, \quad (1.13)$$

$$n_{\text{ZPF}} = \frac{1}{\sqrt{2}} \left(\frac{E_J}{8E_C} \right)^{\frac{1}{4}} = \frac{1}{\sqrt{2}} \sqrt{\frac{R_q}{2\pi Z_c}}, \quad (1.14)$$

in which $Z_c = \sqrt{L_J/C}$ is the characteristic impedance of the oscillator, and $R_Q = h/(2e)^2$ is the superconducting resistance quantum. These values of zero-point fluctuations obey the Heisenberg uncertainty principle,

$$\varphi_{\text{ZPF}} n_{\text{ZPF}} = \frac{1}{2}. \quad (1.15)$$

With the above relations, we can then write down the quantized Hamiltonian of the transmon using bosonic creation and annihilation operators

$$\hat{H}_t = \sqrt{8E_J E_C} \hat{t}^\dagger \hat{t} - \frac{E_C}{12} (\hat{t}^\dagger + \hat{t})^4 + O[(\hat{t}^\dagger + \hat{t})^6]. \quad (1.16)$$

After dropping energy non-conserving terms (also known as the rotating wave approximation, RWA) and normal-ordering the bosonic operators [Louisell, 1973; Scully and Zubairy, 1997], we obtain

$$\hat{H}_t = \left(\sqrt{8E_J E_C} - E_C \right) \hat{t}^\dagger \hat{t} - \frac{E_C}{2} \hat{t}^{\dagger 2} \hat{t}^2 + O[(\hat{t}^\dagger + \hat{t})^6]. \quad (1.17)$$

Now we arrive at the conclusion that the transmon Hamiltonian including its lowest-order nonlinearity has the form of a **quantum Kerr oscillator**, in which transition frequencies between its ν -th and $(\nu + 1)$ -th levels are given by

$$f_t^{\nu, \nu+1} = f_t^{01} - \frac{\nu E_C}{h} = \frac{\sqrt{8E_J E_C} - (\nu + 1)E_C}{h}. \quad (1.18)$$

The Coulomb energy E_C is therefore referred to as the transmon **anharmonicity** (or self-Kerr nonlinearity), which will be denoted by K_t in the rest of this dissertation.

In reality, the fundamental transition frequency f_t^{01} is commonly designed to be on the order of a few gigahertz, and E_C/h to be around 150–250 MHz. These conventions are mostly derived from practicality: In superconducting quantum devices, accessible transition frequencies must be below the energy gap such that superconductivity can be preserved during the coherent manipulation of their quantum state between those levels. For example, thin-film aluminum—the most frequently used superconducting material in artificial atoms—has a critical temperature $T_c \approx 1.3$ K under zero external magnetic field, corresponding to an energy gap $\Delta \approx 1.76k_B T_c \approx 200$ μ eV [Tinkham, 1996]. Electromagnetic radiation with a frequency above $2\Delta/h \approx 96$ GHz would then break Cooper pairs and drive the material back to its normal state.¹⁶ On the other hand, thermal excitations in the quantum system can only be sufficiently suppressed when $k_B T \ll hf_t^{01}$. The technology of dilution refrigeration is capable of providing continuous cooling power at $T \sim 10$ – 20 mK, which requires f_t^{01} to be preferably by one order of magnitude above $k_B T/h \sim 200$ – 400 MHz. Considering these restrictions on both sides, transmons with f_t^{01} between 4–8 GHz are most commonly implemented in laboratories; meanwhile, the control and measurement of these artificial atoms can be reliably supported by commercial microwave generation and analysis equipment at gigahertz frequencies.¹⁷

Given f_t^{01} , the value of E_C can be determined according to the ratio E_J/E_C . In practice, $E_C \sim 150$ – 250 MHz allows qubit gate operations to be completed on the

¹⁶The sensitivity of superconductivity to high-frequency radiation provides the principle for Josephson-junction-based millimeter-wave detectors. See Tucker and Feldman [1985] for a review.

¹⁷Note that temperature T , voltage V , and frequency f can all be related an energy scale after the multiplication of a fundamental constant— $k_B T$, eV , and hf , which represent thermal excitations, electrostatic energy, and photon energy, respectively. The conversion and comparison of these physical quantities are frequently encountered in low-temperature electromagnetic measurements.

10 ns time scale without significant population leakage out of the two-level computational subspace, usually chosen to be spanned by the ground state $|0\rangle$ and first excited state $|1\rangle$ of a transmon. Yet in addition, there are other application scenarios where a superconducting nonlinear oscillator with a lower anharmonicity is desired—for instance, to provide a weakly nonlinear mode with low intrinsic dissipation for quantum-limited microwave amplification. A transmon-style circuit with a lower E_C , or equivalently, a higher E_J/E_C ratio can in principle fulfill the requirement. But in reality, the fabrication of Josephson junctions with a very large E_J —or a very large junction area, according to Equation (1.3)—posts practical difficulties. One solution is to use a junction array in place of a single junction, as shown in Figure 1.4: Consider the model of an array of N identical junctions, each having a Josephson energy E'_J . In its lowest-energy configuration, the Josephson phase φ across the junction array will be equally distributed on each junction [Sivak *et al.*, 2020].¹⁸ The potential energy term in the circuit Hamiltonian can thus be written as

$$-N_J E'_J \cos\left(\frac{\varphi}{N_J}\right) \rightarrow \frac{E'_J}{2N_J} \varphi^2 - \frac{E'_J}{24N_J^3} \varphi^4 + O(\varphi^6). \quad (1.19)$$

Comparing Equations (1.8) and (1.19), it can be found that by setting $E'_J = N_J E_J$, one obtains a junction array mode that has the same linear inductance as a single-junction transmon. Given their shunting capacitance or E_C to be the same, the two oscillators then have the same linear resonant frequency, but the one with the junction array has a lower anharmonicity suppressed by a factor of N_J^2 . This method of engineering weakly nonlinear quantum oscillators is applied to the design of the Π -mon artificial molecule, as will be reported in Chapter 6.

¹⁸A more rigorous treatment of the energy spectrum of Josephson junction arrays, taking junction capacitors and ground capacitors into consideration, can be found in Masluk *et al.* [2012].

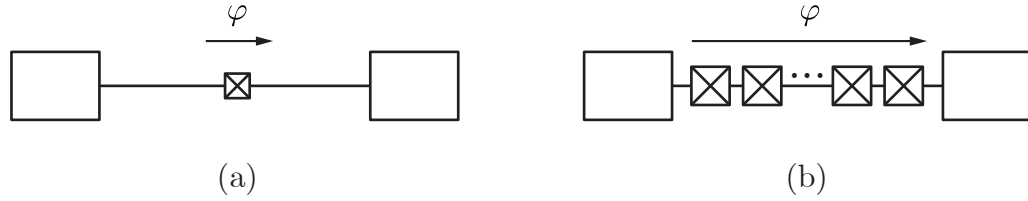


Figure 1.4: Reduction of the Josephson nonlinearity in a junction array: Replacing a single Josephson junction (with a Josephson energy E_J) with an array of N_J junctions, each having a Josephson energy $N_J E_J$, leads to a quantum Kerr oscillator with the same fundamental transition frequency but a reduced anharmonicity by a factor of N_J^2 . The junction or junction array is shunted by the external capacitance formed by a pair of coplanar electrode pads. This specific physical layout is compatible with the three-dimensional circuit QED architecture [Paik *et al.*, 2011].

To sum up, like natural atoms, superconducting artificial atoms have anharmonic energy levels that allow the coherent manipulation of their quantum state; but unlike natural atoms, whose energy levels are determined only by their subatomic-particle composition and fundamental scientific constants, the *artificiality* of superconducting circuits grants researchers the possibility to design “atoms” using engineering methods: in reality, each artificial atom has its own unique characters depending on the circuit topology, device parameters, material properties, and fabrication procedures. As will be seen in the next section, artificial atoms can also interact with microwave photons through an *engineerable*, coherent interface, which brings atomic physics and quantum optics to mesoscopic solid-state circuits.

1.3.3 Circuit quantum electrodynamics

Photons are the elementary excitations of electromagnetic fields. Atoms absorb and emit photons at the leading order, if present, through their electric dipole interaction [Cohen-Tannoudji *et al.*, 1987; Grynberg *et al.*, 2010]. The atom–photon interaction can be enhanced if the photons are confined in a high-finesse cavity—an experimen-

tal system known as cavity quantum electrodynamics, abbreviated as **cavity QED** [Haroche and Raimond, 2006; Miller *et al.*, 2005; Walther *et al.*, 2006]. Parallel to the derivation of artificial atoms from natural atoms [Haroche *et al.*, 2020], the electrical circuit counterpart of cavity QED was first proposed and achieved with a Cooper-pair box coupled to a superconducting coplanar waveguide resonator [Blais *et al.*, 2004; Wallraff *et al.*, 2004], and subsequently using transmons [Houck *et al.*, 2007; Paik *et al.*, 2011; Schuster *et al.*, 2007], fluxoniums [Manucharyan *et al.*, 2009a; Pop *et al.*, 2014], and standard and modified flux qubits [Stern *et al.*, 2014; Yan *et al.*, 2016] coupled to either two-dimensional (2D) or three-dimensional (3D) microwave cavities. The field has been since named **circuit quantum electrodynamics**, abbreviated as **circuit QED**.¹⁹

The circuit QED architecture is essentially about engineering the electromagnetic environment of superconducting artificial atoms [Devoret *et al.*, 2003; Esteve *et al.*, 1986], and as a result, it has significantly improved the coherence, measurability, and connectivity of superconducting quantum circuits (see Section 1.2):

- (i) The enhancement of qubit coherence times by coupling the artificial atom to a resonator can be understood from a classical microwave engineering viewpoint [Pozar, 2012]: as described in Figure 1.5(b), the linear cavity mode serves as a resonant bandpass filter between the transmon and the semi-infinite transmission line, the latter hosting a broadband continuum of electromagnetic modes that would otherwise cause the energy decay of the transmon without the filter-

¹⁹For pedagogical introductions to circuit QED, see Girvin [2014], Blais *et al.* [2021], and Gao *et al.* [2021]. Also see Schoelkopf and Girvin [2008], Girvin *et al.* [2009], and Blais *et al.* [2020] for more succinct reviews. Moreover, in addition to superconducting qubits, the circuit QED architecture has been applied to couple microwave photons to a variety of microscopic or macroscopic quantum degrees of freedom to form hybrid quantum systems; see Clerk *et al.* [2020] for progress on this forefront.

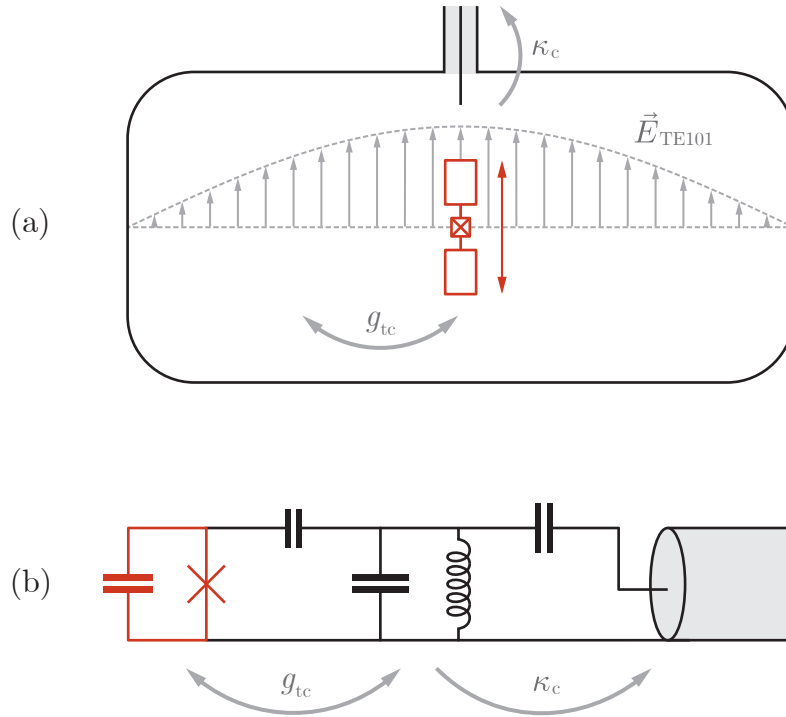


Figure 1.5: Schematic diagram of the circuit QED system. (a) Cross-section drawing of one specific (and structurally the simplest) physical layout: a fixed-frequency transmon (red) capacitively coupled to a 3D rectangular microwave cavity [Paik *et al.*, 2011]. The electric field profile of the fundamental cavity mode—TE₁₀₁—is depicted in the background (gray arrows with a sinusoidal envelope), which is parallel to the electric dipole moment of the transmon (red arrow). The cavity TE₁₀₁ mode is coupled to a microwave coaxial cable through a pin coupler (top center, gray). From the perspective of antennas, the transmon carries a vertical short electric dipole, and the coaxial pin can be regarded as a vertical monopole due to the ground effect of the cavity ceiling [Balanis, 2016]. The alignment of their dipole moments provides the geometric basis for the linear coupling between the transmon, the cavity, and the coaxial line. (b) Circuit model of (a). Different from the symbols in Figure 1.3, here the junction capacitor and the external shunting capacitor of the transmon are combined into one (dominated by the latter). Note that the linear LC oscillator in the center is a faithful representation of the cavity only near one of its resonant frequencies.

ing protection from the cavity. In atomic physics, this was originally predicted as the **Purcell effect**: the spontaneous emission of an atom can be enhanced if it is coupled to a cavity *on resonance*, and suppressed if the cavity and the atomic transition are *detuned* [Purcell, 1946]. Such effect was also observed in superconducting circuits [Houck *et al.*, 2008], and has been motivating the operation of circuit QED systems in their **dispersive regime** wherein the frequency separation between the artificial atom and the microwave resonator is large compared to their linear coupling strength such that they have no direct energy exchange at the leading order. Mathematically, the quantized Hamiltonian of the transmon–cavity system can be written as

$$\frac{\hat{H}_{t-c}}{\hbar} = \omega_c \hat{c}^\dagger \hat{c} + \omega_t^{01} \hat{t}^\dagger \hat{t} - \frac{K_t}{2} \hat{t}^{\dagger 2} \hat{t}^2 + g_{tc} (\hat{t}^\dagger + \hat{t}) (\hat{c}^\dagger + \hat{c}), \quad (1.20)$$

in which “c” denotes the cavity and “t” denotes the transmon; the creation and annihilation operators of the cavity mode obey the bosonic commutation relation $[\hat{c}, \hat{c}^\dagger] = 1$; the transmon anharmonicity is denoted by $K_t = E_C/\hbar$. The dispersive regime is characterized by $\Delta_{tc} = |\omega_c - \omega_t^{01}| \gg g_{tc}$, in which the off-resonance coupling between the transmon and the cavity results in a cavity-photon-induced qubit decay rate—also called the “Purcell limit”:

$$\Gamma_{1P} = \frac{1}{T_{1P}} = \left(\frac{g_{tc}}{\Delta_{tc}} \right)^2 \kappa_c, \quad (1.21)$$

in which κ_c is the cavity decay rate primarily through its coupling to the transmission line [Koch *et al.*, 2007; Schuster, 2007]. In practice, T_{1P} sets an upper bound of qubit T_1 in a circuit QED system.

Experimentally, when $T_{1P} \gtrsim 0.1\text{--}1$ ms is achieved, the qubit T_1 is no longer constrained by radiative decay channels, but mostly by intrinsic mechanisms

such as dielectric material losses [Dunsworth *et al.*, 2017; Read *et al.*, 2022; Wang *et al.*, 2015] and nonequilibrium quasiparticles in Josephson junctions [Catelani *et al.*, 2011; Martinis *et al.*, 2009; Serniak *et al.*, 2019, 2018; Wang *et al.*, 2014]. In other circuit QED setups where a large κ_c is specially wanted for fast qubit readout (see Section 2.3.3), the Purcell limit of qubit energy decay can be further extended by reducing the electromagnetic mode density near the qubit frequency using, for instance, a quarter-wave impedance transformer [Reed *et al.*, 2010b], a quarter-wave bandpass filter [Jeffrey *et al.*, 2014; Sete *et al.*, 2015; Walter *et al.*, 2017], a rectangular waveguide section [Narla, 2017; Narla *et al.*, 2016], or a resonant cavity attenuator [Wang *et al.*, 2019], which have been collectively called “Purcell filters.” With these cautions, measurement values of $T_1 \gtrsim 10\text{--}100\ \mu\text{s}$ are now being regularly reported from transmons embedded in the circuit QED architecture.

The impact of cavity photons on qubit dephasing time, together with its methods of prevention, will be addressed in Section 3.3 and Chapter 5.

- (ii) The circuit QED system in the dispersive regime provides a near *quantum non-demolition* microwave readout channel for superconducting qubits [Blais *et al.*, 2004; Wallraff *et al.*, 2005]. I will review its basic concepts in Section 3.2, its general experimental implementation in Chapter 4, and present a novel qubit readout scheme in Chapter 6.
- (iii) Through the conversion of quantum information from its standing (material) to flying (photonic) carriers, the interaction between artificial atoms can be extended beyond their nearest physical neighbors. Progress on this forefront includes entanglement generation, quantum state transfer, and quantum gate protocols both inside the same circuit QED unit [Chow *et al.*, 2011, 2013; DiCarlo *et al.*, 2009; Majer *et al.*, 2007; Paik *et al.*, 2016; Ristè *et al.*, 2013]

and between *separate* or *remote* transmon–cavity modules [Axline *et al.*, 2018; Burkhardt *et al.*, 2021; Campagne-Ibarcq *et al.*, 2018; Chou *et al.*, 2018; Gao *et al.*, 2019, 2018; Kurpiers *et al.*, 2018, 2019; Leung *et al.*, 2019; Narla *et al.*, 2016; Roch *et al.*, 2014; Rosenblum *et al.*, 2018]. In Chapter 7, I will briefly discuss how the innovations in single-qubit experiments reported in this dissertation is able to contribute to the realization of a modular, scalable quantum network.

1.3.4 Quantum-limited amplification

In the circuit QED architecture, microwave photons in a readout resonator are entangled with artificial atoms and are subsequently released into the output transmission line, carrying information of the qubit state under observation. Qubit readout is therefore converted to the problem of microwave signal processing near the quantum limit, which has been notably empowered by the new development of quantum-limited microwave parametric amplifiers—typically also implemented with superconducting Josephson circuits thanks to the low-dissipation (ideally, dissipation-free) nonlinearity provided by the Josephson effect [Roy and Devoret, 2016]. The operation of Josephson parametric amplifiers is free from the large number of microscopic degrees of freedom that would participate and cause extra dissipation in conventional analog electronic devices. With careful circuit engineering, the amount of added noise in these amplification processes can approach its minimal level imposed by the fundamental laws of quantum mechanics [Caves, 1982; Haus and Mullen, 1962; Shimoda *et al.*, 1957].

Based on their different physical mechanisms, linear analog amplifiers can be divided into the *phase-preserving* (PP) and *phase-sensitive* (PS) categories: The former amplifies both the in-phase (I) and the quadrature (Q) components²⁰ of a sinusoidal

²⁰In this dissertation, we use the complex *phasor* representation of analog sinusoidal signals

signal with the same gain factor,

$$I_{\text{out}}^{\text{PP}} = \sqrt{G_{\text{PP}}} I_{\text{in}}, \quad (1.22)$$

$$Q_{\text{out}}^{\text{PP}} = \sqrt{G_{\text{PP}}} Q_{\text{in}}. \quad (1.23)$$

The latter amplifies one quadrature component (assuming it being Q) while de-amplifying the other one with the same factor,

$$I_{\text{out}}^{\text{PS}} = \frac{1}{\sqrt{G_{\text{PS}}}} I_{\text{in}}, \quad (1.24)$$

$$Q_{\text{out}}^{\text{PS}} = \sqrt{G_{\text{PS}}} Q_{\text{in}}. \quad (1.25)$$

The noise properties of these two classes of linear amplifiers are nevertheless different in their **quantum limit**: The minimal added noise of a phase-preserving amplifier in the high-gain limit ($G_{\text{PP}} \gg 1$) is equal to *one half* of the energy of a single photon at the signal frequency; this lower limit is however not present for phase-sensitive amplifiers [Caves, 1982; Clerk *et al.*, 2010]. These two distinct results originate from the Heisenberg uncertainty principle, or quantum back-action during the measurement of *incompatible* observables: In phase-preserving amplification, both quadrature components of the signal—analogue to the position and momentum of a quantum mechanical particle—are amplified simultaneously, and hence the output signal is subject to additional quantum noise, which is also linked to the **standard**

oscillating at a given angular frequency ω :

$$A \sin(\omega t + \theta) = I \sin(\omega t) + Q \cos(\omega t) \rightarrow \tilde{A} = A e^{i\theta} \in \mathbb{C},$$

in which $I = A \cos \theta$ and $Q = A \sin \theta$ are the in-phase and quadrature (IQ) components of the signal, respectively. A single-frequency alternating signal is therefore denoted by (I, Q) in the complex plane, analogue to the position and momentum (x, p) of a one-dimensional particle in its phase space.

quantum limit (SQL) in interferometric measurements with classical sources of light [Braginsky, 1970; Caves, 1980; Caves *et al.*, 1980; Schawlow and Townes, 1958]. On the other hand, phase-sensitive amplification, which only amplifies one quadrature component of the input signal, is analogous to monitoring only the position or the momentum of the particle, or breaking the standard quantum limit by using squeezed states of light in interferometry experiments [Caves, 1981]. The de-amplification or erasure of information in the conjugate quadrature is dictated by quantum mechanics as the state of a particle in its phase space cannot be determined with infinite precision.

Mathematically, these results can be expressed by writing the quantum operators of I and Q using bosonic creation and annihilation operators,

$$I_\beta \rightarrow \hat{I}_\beta = \frac{1}{2} (\hat{c}_\beta^\dagger + \hat{c}_\beta), \quad (1.26)$$

$$Q_\beta \rightarrow \hat{Q}_\beta = \frac{i}{2} (\hat{c}_\beta^\dagger - \hat{c}_\beta), \quad (1.27)$$

in which $\beta \in \{\text{in}, \text{out}\}$. From $[\hat{c}_\beta, \hat{c}_\beta^\dagger] = 1$, one can obtain the canonical commutation relation

$$[\hat{I}_\beta, \hat{Q}_\beta] = \frac{i}{2}. \quad (1.28)$$

The input–output relations for the two types of parametric amplifiers can then be written as

$$\hat{I}_{\text{out}} = \sqrt{G_{\text{PP}}} \hat{I}_{\text{in}} + \sqrt{G_{\text{PP}} - 1} \hat{I}_{\text{in}}^{\text{id}}, \quad (1.29)$$

$$\hat{Q}_{\text{out}} = \sqrt{G_{\text{PP}}} \hat{Q}_{\text{in}} - \sqrt{G_{\text{PP}} - 1} \hat{Q}_{\text{in}}^{\text{id}}, \quad (1.30)$$

and

$$\hat{I}_{\text{out}} = \frac{1}{\sqrt{G_{\text{PS}}}} \hat{I}_{\text{in}}, \quad (1.31)$$

$$\hat{Q}_{\text{out}} = \sqrt{G_{\text{PS}}} \hat{Q}_{\text{in}}, \quad (1.32)$$

respectively, such that the canonical commutation relation—Equation (1.28) is preserved. For the phase-preserving amplifier, $\hat{I}_{\text{in}}^{\text{id}}$ and $\hat{Q}_{\text{in}}^{\text{id}}$ are quadrature operators—similar to \hat{I}_{in} and \hat{Q}_{in} —of an *idler* input mode,²¹ which is responsible for the minimal added noise to the output signal,

$$(\Delta \hat{I}_{\text{out}})^2 = G_{\text{PP}} (\Delta \hat{I}_{\text{in}})^2 + (G_{\text{PP}} - 1) (\Delta \hat{I}_{\text{in}}^{\text{id}})^2, \quad (1.33)$$

$$(\Delta \hat{Q}_{\text{out}})^2 = G_{\text{PP}} (\Delta \hat{Q}_{\text{in}})^2 + (G_{\text{PP}} - 1) (\Delta \hat{Q}_{\text{in}}^{\text{id}})^2. \quad (1.34)$$

The quantum limit of phase-preserving amplification is achieved when the idler input is in the vacuum state ($\Delta \hat{I}_{\text{in}}^{\text{id}} = \Delta \hat{Q}_{\text{in}}^{\text{id}} = 1/2$),

$$\frac{(\Delta \hat{I}_{\text{out}})_{\text{min}}^2}{G_{\text{PP}}} = (\Delta \hat{I}_{\text{in}})^2 + \frac{1}{4} \left(1 - \frac{1}{G_{\text{PP}}}\right) \xrightarrow{G_{\text{PP}} \gg 1} (\Delta \hat{I}_{\text{in}})^2 + \frac{1}{4}, \quad (1.35)$$

$$\frac{(\Delta \hat{Q}_{\text{out}})_{\text{min}}^2}{G_{\text{PP}}} = (\Delta \hat{Q}_{\text{in}})^2 + \frac{1}{4} \left(1 - \frac{1}{G_{\text{PP}}}\right) \xrightarrow{G_{\text{PP}} \gg 1} (\Delta \hat{Q}_{\text{in}})^2 + \frac{1}{4}. \quad (1.36)$$

²¹The input–output relation for a phase-preserving amplifier is more often written as

$$\begin{aligned} \hat{c}_{\text{out}} &= \sqrt{G_{\text{PP}}} \hat{c}_{\text{in}} + \sqrt{G_{\text{PP}} - 1} \hat{c}_{\text{in}}^{\dagger}, \\ \hat{c}_{\text{out}}^{\dagger} &= \sqrt{G_{\text{PP}}} \hat{c}_{\text{in}}^{\dagger} + \sqrt{G_{\text{PP}} - 1} \hat{c}_{\text{in}}, \end{aligned}$$

where \hat{c}_{in} and $\hat{c}_{\text{in}}^{\dagger}$ are bosonic operators of the idler mode. Then $\hat{I}_{\text{in}}^{\text{id}}$ and $\hat{Q}_{\text{in}}^{\text{id}}$ are defined in the same way as Equations (1.26) and (1.27).

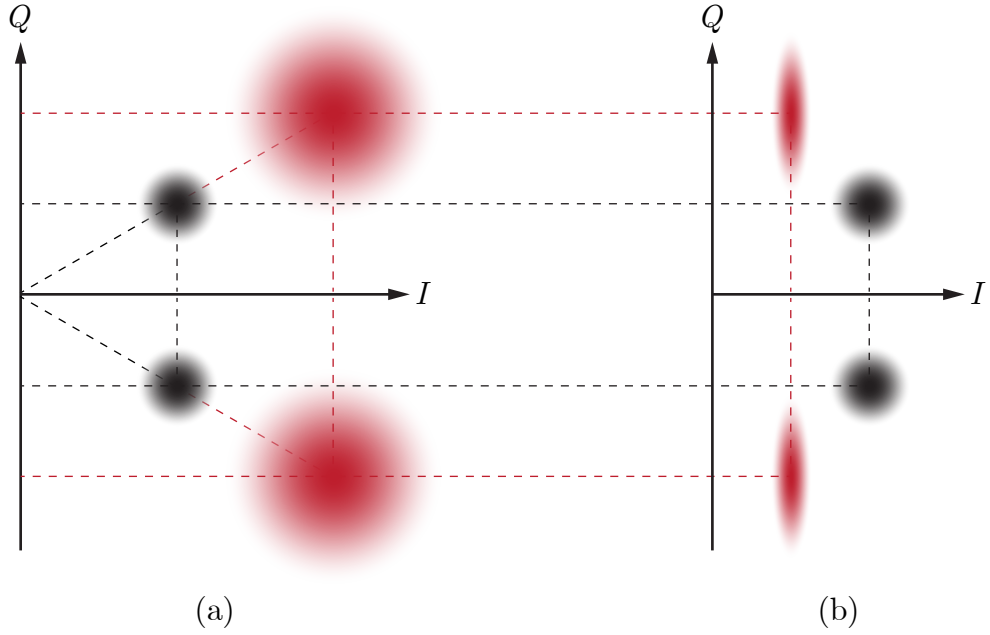


Figure 1.6: Comparison of the (a) phase-preserving and (b) phase-sensitive quantum-limited linear amplification schemes. The input states—colored in black—are chosen to be coherent states with the minimal quadrature uncertainties, $\Delta\hat{I}_{\text{in}} = \Delta\hat{Q}_{\text{in}} = 1/2$. The different output states are colored in red. The “signal” is defined to be along the quadrature component (Q axis). The same gain factor along the signal axis is adopted in all three situations: $G = G_{\text{PP}} = G_{\text{PS}}$. The ratio of their output quadrature noise is $\Delta Q_{\text{PP}} : \Delta Q_{\text{PS}} = \sqrt{2G-1} : \sqrt{G}$, which are inversely proportional to their quadrature signal-to-noise ratios. As an example, the case of $G = 4$ is plotted here.

On the other hand, for an ideal phase-sensitive amplifier, along its signal axis,

$$\frac{(\Delta\hat{Q}_{\text{out}})^2}{G_{\text{PS}}} = (\Delta\hat{Q}_{\text{in}})^2, \quad (1.37)$$

where no added noise is present. A true-to-scale numerical comparison between the two situations can be found in Figures 1.6(a) and 1.6(b).

Josephson parametric amplifiers with quantum-limited or near-quantum-limited noise properties in both the phase-sensitive [Castellanos-Beltran *et al.*, 2008; Hatridge *et al.*, 2011; Yamamoto *et al.*, 2008; Yurke *et al.*, 1989, 1988] or the phase-preserving

mode [Bergeal *et al.*, 2010a,b; Roch *et al.*, 2012] had enabled the first generation of experiments that demonstrated the high-fidelity single-shot readout of qubit states in linear circuit QED setups [Hatridge *et al.*, 2011; Johnson *et al.*, 2012; Lin *et al.*, 2013; Ristè *et al.*, 2012; Vijay *et al.*, 2011]. Since then, boosting qubit readout has been a major motivation for a number of innovative designs of microwave amplifiers based on Josephson junctions [Abdo *et al.*, 2018, 2013; Bell and Samolov, 2015; Eichler *et al.*, 2014; Frattini *et al.*, 2018, 2017; Kamal *et al.*, 2011, 2012; Lecocq *et al.*, 2017; Macklin *et al.*, 2015; Mutus *et al.*, 2014; O’Brien *et al.*, 2014; Planat *et al.*, 2020; Rosenthal *et al.*, 2021; Sivak *et al.*, 2019, 2020; Sliwa *et al.*, 2015; Zorin, 2016] or high-kinetic-inductance materials [Chaudhuri *et al.*, 2017; Ho Eom *et al.*, 2012; Ranzani *et al.*, 2018; Vissers *et al.*, 2016], which are optimized for bandwidth, dynamic range, or signal directionality.²²

1.3.5 A brief discourse on “quantumness”

After reviewing the key ideas and implementations of superconducting quantum circuits, I wish to conclude this section with a short remark on their “quantumness”—by what definitions are these engineered systems quantum mechanical? The answer should at least contain the following four aspects:

- (i) Superconductivity and the Josephson effect (Section 1.3.1) are *macroscopic* phenomena explained by a quantum theory of electrons and phonons at the *microscopic* level (the BCS theory). However, the physical measurement quantities characterizing these phenomena—for instance, the current and voltage in the constitutive equations of a Josephson junction obtained from a conventional

²²Besides their applications in circuit QED systems, Josephson amplifiers have also advanced the frontier of quantum-limited radiometry—for instance, microwave-cavity-based experiments in search of the hypothetical particle—axion—of dark matter [Asztalos *et al.*, 2010; Backes *et al.*, 2021; Brubaker *et al.*, 2017; Du *et al.*, 2018; Zhong *et al.*, 2018].

electrical transport experiment—are strictly classical variables with no observable quantum fluctuations or measurement back-action, not different from those in the I – V relations of an Ohmic resistor or a semiconductor transistor. People thus categorize superconductors as “quantum materials”—in spite of their microscopic quantum mechanical constituents, quantum coherent dynamics—like Rabi oscillation or Ramsey interference—does not unfold itself on the macroscopic scale.

- (ii) Superconducting artificial atoms (Section 1.3.2) and their interactions with microwave photons (Section 1.3.3) exhibit the coherent dynamics of *single* quantum degrees of freedom in condensed matter with the participation of a large number of microscopic particles. These mesoscopic devices are employed as physical units of information—qubits, which are to be controlled using the quantum logic. They are candidate components of quantum information machines whose algorithmic operation is distinct from that of classical computers.
- (iii) The *quantum limit* of linear analog amplification (Section 1.3.4) is a direct manifestation of the quantum back-action in the measurement of electromagnetic fields, although Josephson parametric amplifiers typically work in the weakly nonlinear, semiclassical regime and thus do not display quantum coherent dynamics between classical states like artificial atoms.
- (iv) The Josephson nonlinearity in parametric amplifiers can also be used to prepare squeezed states of microwave radiation from coherent or vacuum fields [Eddins *et al.*, 2018; Flurin *et al.*, 2012; Liu *et al.*, 2020; Murch *et al.*, 2013; Toyli *et al.*, 2016], because they possess a quantum optical interface like artificial atoms, which due to their strong nonlinearity can absorb and emit single microwave photons—the most “quantum” state of electromagnetic radiation

among all [Campagne-Ibarcq *et al.*, 2018; Houck *et al.*, 2007; Inomata *et al.*, 2016; Lescanne *et al.*, 2020; Narla *et al.*, 2016].²³

In summary, the Josephson nonlinearity, combined with the suppression of electromagnetic dissipation in superconductors,²⁴ is the foundation of all the following aspects of quantumness—macroscopic quantum coherence, quantum-limited measurement, and nonclassical states of radiation—in superconducting quantum circuits. In a broader sense, low-dissipation nonlinear elements with a coherent electromagnetic interface are the core of quantum engineering systems. Josephson junctions are among a very short list of macroscopic engineerable objects that can fulfill this requirement. Their macroscopicity, however, raises the outstanding challenge of protecting quantum states from various sources of environmental perturbations, which is to be discussed in the next section.

1.4 Noise in quantum circuits: origins and impacts

In natural science, *noise* is the collective name of stochastic physical quantities in an experimental system that escape deterministic predictions by the researcher using a feasible amount of time and resources. It reflects the limitation of interrogation and control power over the system under investigation, and usually causes negative impacts by deteriorating useful signals and thus prohibiting the accessibility of complete knowledge about the problems of interest. Fundamentally, noise arises from the large number of *unmonitored* degrees of freedom—aggregatively referred to as the *reservoir* or *environment*—that are present in all realistic physical systems and their control and measurement apparatuses. The central quantitative relation predicting the level

²³According to the quantum theory of optical coherence [Glauber, 1963], a single-photon source is at the extreme of antibunching with $g^{(2)}(0) = 0$.

²⁴Or equivalently, the high-quality-factor modes in resonant superconducting electrical circuits.

of noise on a physical quantity in an open system given the *dynamical susceptibility* or *response function* is the **fluctuation–dissipation theorem** (FDT), which links the fluctuations of an observable to the irreversible energy decay or information loss into the dissipative environment [Callen and Welton, 1951; Kubo, 1966].²⁵

Where is the leading source of dissipation in the circuit of superconducting artificial atoms—in particular, those embedded in a circuit QED system as shown in Figure 1.5(b), in which the electrical response of a semi-infinite transmission line with a characteristic impedance Z_c is equivalent to a resistor $R = Z_c$? Using the FDT theorem in the quantum regime, one can derive the power spectral density of its electrical resistive noise at temperature T ,

$$S_{VV}[\omega] = \int \langle \hat{V}_n(t) \hat{V}_n(0) \rangle e^{i\omega t} dt = \left[\coth \left(\frac{\hbar\omega}{2k_B T} \right) + 1 \right] \hbar\omega Z_c, \quad (1.38)$$

in which V_n is the voltage noise across its port. In the high-temperature (classical) limit,

$$S_{VV}[\omega] \xrightarrow{k_B T \gg \hbar|\omega|} 2k_B T Z_c, \quad (1.39)$$

which is known as the **Johnson–Nyquist noise** originating from the *thermal agitation* of charge carriers in an electrical conductor at thermal equilibrium [Johnson, 1928; Nyquist, 1928]. Oppositely, in the low-temperature (quantum) limit,

$$S_{VV}[\omega] \xrightarrow{k_B T \ll \hbar|\omega|} \begin{cases} 2\hbar\omega Z_c, & \omega > 0, \\ 0, & \omega < 0, \end{cases} \quad (1.40)$$

²⁵A number of useful textbook resources are available as introductions to the linear response theory and the fluctuation–dissipation theorem in statistical mechanics and condensed matter physics. Mazenko [2006] and Sólyom [2003] are recommended here for their clarity.

which represents the **quantum noise** due to vacuum fluctuations of electric fields. We have therefore proved the necessity of dilution refrigeration as argued in Section 1.3.2 in order to suppress thermal noise in quantum microwave circuits. The essence of cooling in low-temperature physics is to remove extra entropy from uncontrolled physical degrees of freedom so as to increase the amount of information in measurement signals that reveal the quantum mechanical properties of matter. As I will show in Section 3.3 (theory) and Chapter 5 (experiment), reducing thermal excitations in the electromagnetic environment of artificial atoms is crucial for improving the qubit dephasing time. Methods and considerations of thermalization in the circuit QED experimental setup will be addressed in Section 4.3.

Quantum noise, fortunately, does not cause additional qubit dephasing in a circuit QED module in its dispersive regime because the vacuum state $|0\rangle$ has a definite photon number and thus does not induce fluctuations of the qubit transition frequency (see Sections 3.2 and 3.3). However, it will be detected and amplified by the measurement chain and sets the ultimate limit of SNR given a certain number of microwave photons in the readout cavity drive (see Section 3.2.3). This limit can only be achieved if the measurement chain has perfect efficiency—namely, all photons used to interrogate the target are collected and no information is lost to the dissipative environment. The key strategy to mitigate the impact of unavoidable readout loss is to amplify signals before those dissipative sources. This is the central idea behind quantum-limited amplification (Section 1.3.4), and moreover, intra-cavity amplification, which is to be reported and discussed in Chapter 6.

Thermal noise and quantum noise are the two components of a fluctuating electromagnetic field at finite temperatures. In quantum microwave circuit experiments, they are *intrinsic* forms of noise that are naturally contained in a circuit QED system in thermal equilibrium. In addition, electromagnetic radiation *exterior* to the ideal circuit QED model (Figure 1.5) in practice can also cause damage to the experiment—

for instance, infrared photons that excite nonequilibrium quasiparticles across the Josephson junction [Diamond *et al.*, 2022; Houzet *et al.*, 2019] or fluctuating charges across the transmon capacitor that lead to the energy-level dispersion of qubits [Seraniak *et al.*, 2019, 2018]. The former demands careful electromagnetic filtering in the experimental setup, and the latter can be addressed by reconsidering the parameters and topology of the quantum circuit.²⁶ We will come back to these points in Chapters 4 and 6.

So far, I have briefly reviewed the preliminary concepts and knowledge on which the rest of this dissertation will be founded. This central aim has been to direct our attention to the problems of noise mitigation and information acquisition in artificial quantum systems—superconducting Josephson circuits in particular. In Chapter 2, I will introduce the theoretical framework for understanding quantum measurement and decoherence in the circuit QED architecture, in order to guide our experimental efforts in improving qubit protection and readout protocols using quantum microwave engineering techniques.

²⁶Note that the insensitivities to gate charge and external flux fluctuations are among the main motivations for the design of the fixed-frequency transmon.

Chapter 2

Theoretical Models of Quantum Measurements

Through measuring to knowing—I would like to write as a motto above every physics laboratory.¹

Heike Kamerlingh Onnes [1882]

The scientific laws we formulate mathematically in quantum theory no longer deal with elementary particles themselves, but with our knowledge of elementary particles.²

Werner Heisenberg [1955]

As the true origin of objective knowledge, measurements have been promoted to a critical position in modern systems of natural science. Empirically speaking, scientific concepts have ultimately to be defined at the operational level by their measurement protocols and actions [Bridgman, 1927; Poincaré, 1905]. In the realm of atoms and quanta, the microscopicity of physical objects, the weakness of experimental signals, and the scarcity of obtainable information designate measurement as the essential

¹Original text (in Dutch): “Door meten tot weten, zou ik als zinspreuk boven elk fysisch laboratorium willen schrijven.”

²Original text (in German): “Die Naturgesetze, die wir in der Quantentheorie mathematisch formulieren, nicht mehr von den Elementarteilchen an sich handeln, sondern von unserer KENNTNIS der Elementarteilchen.”

art “to explain visible complications through the invisible simplicity” [Perrin, 1913].³ Nowhere is the centrality of measurement more conspicuous than in quantum mechanics, where the action of information acquisition intermediates between the deterministic and the stochastic, the continuous and the discrete, the reversible and the irreversible, the observed and the observer [Heisenberg, 1930]. In contrast to our intuition adapted to the classical world, in quantum physics the natural object and the experimenter are not strictly separable any more: “One can no longer speak of the behavior of the particle independently of the process of observation” [Heisenberg, 1955].⁴ Conceptual difficulties concerning the emergence of post-measurement outcomes, the correlation between microscopic and macroscopic states, and the quantum–classical boundary—collectively known as the “measurement problem”—have prompted continual reexaminations of the foundations of quantum theory [d’Espagnat, 1976; Griffiths, 2002; Jammer, 1966; Lamb, 1969; Wheeler and Zurek, 1983; Zurek, 1990].

This chapter will provide rudimentary theoretical tools for describing and understanding quantum measurements in the ideal and nonideal situations. In particular, I will discuss both *strong projective* and *weak continuous* measurements in order to explain how measurement outcomes and their figures of merit emerge from the underlying physical processes. Elementary languages of information theory will be used to elaborate the connection between physical measurements and information acquisition. In the end, we will have developed some useful intuitions on key concepts such as measurement strength, SNR, quantum back-action, and information efficiency, which will be frequently encountered in the design and implementation of quantum measurement experiments.

³Original text (in French): “expliquer du visible compliqué par de l’invisible simple.”

⁴Original text (in German): “man kann gar nicht mehr vom Verhalten der Teilchen, losgelöst vom Beobachtungsvorgang sprechen.”

2.1 Entropy, information, and measurements

“Information is physical.”⁵ While it is apparent that in the real world, information has always to be associated with a physical carrier so as to be received and recognized by human or nonhuman agents, contemporary interpretations of the physicality of information further emphasize that not merely those physical carriers, but elementary steps of information processing are also subject to the fundamental laws of physics. A conceptual milestone toward this understanding was the linkage of information to the statistical entropy of a physical system for resolving the paradox of Maxwell’s demon without violating the second law of thermodynamics [Brillouin, 1951a,b; Szilard, 1929].⁶ Meanwhile, information was assigned an operational definition as the *entropy reduction* of a physical system before and after a measurement event [Brillouin, 1953, 1956],

$$J = S - S', \quad (2.1)$$

in which S and S' stand for the initial and final entropy of the system under observation, and J denotes the increase of information from the viewpoint of the observer acquired after an ideal measurement.⁷ In reality, any physical instrument can only collect and record a limited portion of information carriers during a measurement, whereas the rest are lost irreversibly into the unmonitored environment, as illustrated

⁵This exact phrase is known to have been coined and popularized by Rolf Landauer in a series of articles published in the 1990s [Landauer, 1991, 1996, 1999], although studies on the relationship between physics and information (or intelligence) can be traced back at least to Laplace [1814].

⁶The unification of statistical mechanics and information theory was further established through the principle of maximum entropy in Jaynes [1957a,b]; also see Balian [1982].

⁷Information gain (or mutual information) is more frequently denoted by I in the literature; but in this dissertation, I has been reserved for the in-phase component of a sinusoidal signal (see Section 1.3.4).

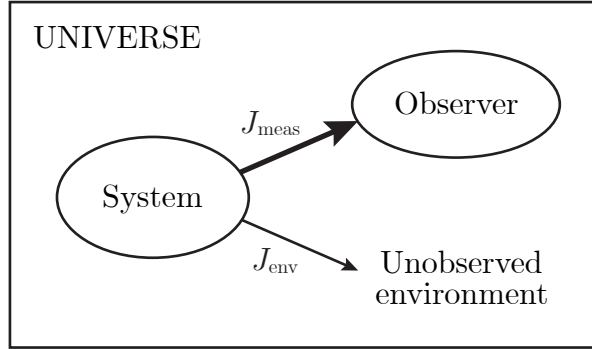


Figure 2.1: Venn-type diagrammatic model of a physical measurement, in which the universe is divided into the “system” under observation and its environment, which further consists of an observed subspace (the “observer”) and the unobserved environment. The monitored and unmonitored information flows—from the viewpoint of the observer—are denoted by J_{meas} and J_{env} , respectively. The ratio ($J_{\text{meas}}/J_{\text{env}}$) should be maximized in a measurement operation with near-ideal efficiency.

in Figure 2.1. One can thus specify the “collectable” part of information from the total entropy reduction of the system as

$$J_{\text{meas}} < S - S' = J_{\text{meas}} + J_{\text{env}}, \quad (2.2)$$

and define the **information efficiency** of a nonideal physical measurement as

$$\eta_{\text{m}} = \frac{J_{\text{meas}}}{J_{\text{meas}} + J_{\text{env}}} < 1. \quad (2.3)$$

Maximizing η_{m} has been a persistent task for experimental physicists who wish to acquire more complete knowledge of the natural object or phenomena under investigation.

Isolated quantum systems containing only a small number of internal degrees of freedom and external communication channels offer the ideal platform for examining

the connection between information and physical measurement at the fundamental level. More particularly, in the quantum realm, information loss out of the observed experimental subspace is the essential cause of *decoherence*—the degradation of quantum coherent properties when a previously closed quantum system is brought in contact with the open environment, which—according to contemporary views—provides the key to understanding the quantum-to-classical transition from the microscopic to the macroscopic scale [Joos *et al.*, 2003; Schlosshauer, 2005, 2007; Zurek, 1991, 2003]. In the following sections, I will present how quantum measurements are implemented and characterized using simplified theoretical models, which is the prerequisite knowledge for understanding the qubit readout protocols and decoherence channels in circuit QED experiments.

2.2 Basic notions of a qubit measurement

By its nature, a quantum coherent system—regardless of its physical size or number of microscopic particles—only contains a small number of excitation quanta (see Section 1.3.1). In most cases, its orthogonal quantum states $\{|q_\nu\rangle\}$ are not sufficiently distanced—in either the energy spectrum or the phase space—to be directly differentiated by human sensations or classical measurement devices. Consequently, most quantum measurements in reality have to be implemented with the assistance of an ancillary physical system denoted as the “meter,” whose state is correlated with that of the quantum system under observation due to their interaction during the measurement process. Unlike signals at the single-quantum level, the meter states $\{|m_\mu\rangle\}$ are supposed to be macroscopic and robust against environmental perturbations—in other words, they are able to be analyzed by the experimenter or their classical electronic equipment. Moreover, if the mapping $\{|q_\nu\rangle\} \mapsto \{|m_\mu\rangle\}$ is injective and the

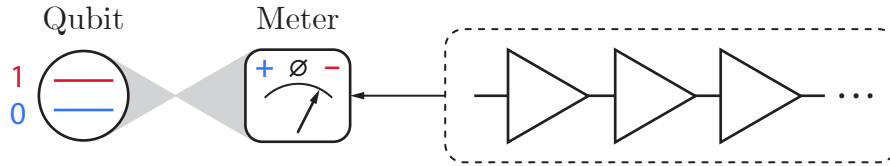


Figure 2.2: Minimal conceptual model of a quantum measurement. A qubit with eigenstates $|0\rangle$ and $|1\rangle$ is used as an example of a quantum object under observation. The meter was initialized at $|\emptyset\rangle$ in the absence of the qubit–meter interaction, and will be eventually projected onto either $|+\rangle$ or $|-\rangle$ depending on whether the qubit is left in $|0\rangle$ or $|1\rangle$. The meter states $|\pm\rangle$ are supposed to be quasi-orthogonal and macroscopically distinguishable. The internal structure of the meter can be abstracted as a multi-stage amplifier chain for magnifying input quantum signals to the classical scale that are robust against ambient noise and resolvable by standard measurement equipment—for instance, classical electronic devices, if the meter output has the form of electrical signals. Posterior to a projective measurement, the qubit state should be reduced to and recorded as a classical bit. It will be made clear in Section 3.2 that in a standard circuit QED experimental system, the “qubit” lives in a selected two-level subspace of a superconducting artificial atom, and the “meter” consists of microwave photons and their amplification circuits.

meter states are quasi-orthogonal—

$$|\langle m_\mu | m_{\mu'} \rangle| \ll 1, \text{ if } \nu \neq \nu', \quad (2.4)$$

such an observation process is known a **strong projective measurement**, in which the qubit state can almost be *unambiguously* determined after a single measurement event.

As the simplest and most relevant example, the high-level conceptual picture of a qubit readout experiment is illustrated in Figure 2.2. In a strong projective measurement, the qubit states $|0\rangle$ and $|1\rangle$ ought to be unambiguously projected onto the meter states $|+\rangle$ and $|-\rangle$ after a controllable interaction process that generates

quantum entanglement between the two subsystems. Assuming the qubit was initially prepared in a pure superposition state $(c_0 |0\rangle + c_1 |1\rangle)$ and the meter was in a null state $|\emptyset\rangle$, the measurement process can be described by the following transformations [von Neumann, 1932; Zurek, 1981]:

$$(c_0 |0\rangle + c_1 |1\rangle) |\emptyset\rangle \xrightarrow{\text{entanglement}} c_0 |0\rangle |+\rangle + c_1 |1\rangle |-\rangle \xrightarrow{\text{projection}} \begin{cases} |0\rangle |+\rangle, & P_0 = |c_0|^2, \\ |1\rangle |-\rangle, & P_1 = |c_1|^2, \end{cases}$$

with $P_{q=0,1}$ denoting the probabilities associated with the measurement outcome $|q\rangle$. Eventually, it is the macroscopic, quasi-orthogonal meter states $|\pm\rangle$ that are detected and recorded, which have been maximally entangled with the qubit and thus brings its information to the observer.

The protocol described above can be rewritten using the density operator formalism [Haroche and Raimond, 2006; Nielsen and Chuang, 2000; Wiseman and Milburn, 2009], according to which a strong projective measurement can be defined through a set of *projection operators* corresponding to each measurement outcome,

$$\hat{\Pi}_q = |q\rangle\langle q|, \quad (2.5)$$

which satisfy

$$\hat{\Pi}_q^\dagger = \hat{\Pi}_q, \quad (2.6)$$

$$\hat{\Pi}_q^2 = \hat{\Pi}_q, \quad (2.7)$$

$$\hat{\Pi}_q \hat{\Pi}_{q'} = \delta_{qq'}, \quad (2.8)$$

$$\sum_q \hat{\Pi}_q = \hat{\mathbb{I}}. \quad (2.9)$$

Here $\delta_{qq'}$ is the Kronecker delta, and $\hat{\mathbb{I}}$ is the identity operator. Given the qubit was

prepared at an arbitrary initial state denoted by its density operator $\hat{\rho}$, the probability of having the measurement outcome $|q\rangle$ and the associated post-measurement qubit density operator $\hat{\rho}'(q)$ are given by

$$P(q) = \text{tr}(\hat{\rho}\hat{\Pi}_q), \quad (2.10)$$

$$\hat{\rho}'(q) = \frac{\hat{\Pi}_q\hat{\rho}\hat{\Pi}_q}{\text{tr}(\hat{\rho}\hat{\Pi}_q)} = \hat{\Pi}_q. \quad (2.11)$$

Otherwise, if the measurement outcome is not recorded, the post-measurement qubit density operator will instead be

$$\hat{\rho}'_{\text{NR}} = \sum_q \hat{\Pi}_q\hat{\rho}\hat{\Pi}_q. \quad (2.12)$$

Besides its compatibility with qubits in arbitrary mixed states, the density operator formalism of quantum measurement also has the advantage of being capable of representing *non-projective* measurements, if one replaces the projectors $\{\hat{\Pi}_q\}$ in Equations (2.10)–(2.12) with a set of *generalized measurement operators* $\{\hat{M}_j\}$ (with j indexing each possible outcome) that obey the normalization condition

$$\sum_j \hat{M}_j^\dagger \hat{M}_j = \hat{\mathbb{I}}, \quad (2.13)$$

and yet do not need to be Hermitian or orthogonal. The probability and state-update formulae will then be

$$P(j) = \text{tr}(\hat{M}_j\hat{\rho}\hat{M}_j^\dagger), \quad (2.14)$$

$$\hat{\rho}'(j) = \frac{\hat{M}_j\hat{\rho}\hat{M}_j^\dagger}{\text{tr}(\hat{M}_j\hat{\rho}\hat{M}_j^\dagger)}, \quad (2.15)$$

if a measurement outcome j has been recorded, or

$$\hat{\rho}'_{\text{NR}} = \sum_j \hat{M}_j \hat{\rho} \hat{M}_j^\dagger, \quad (2.16)$$

if no measurement outcome is recorded. As an example, this generalized measurement formalism will be employed to describe the incremental steps of a weak continuous measurement in Section 2.4.

2.3 Realistic qubit readout: nonidealities and their quantification

As can be derived from the conceptual model presented in the previous section, an *ideal* strong projective measurement implemented with a qubit–meter system apparently demands

- (i) Perfect correlation between the qubit state and the meter state;
- (ii) Perfect distinguishability of the meter states at the macroscopic level.

Moreover, the model also assumes that the meter does not alter the qubit state during the measurement process, which is another nontrivial task in real experiments. A set of quantitative measures should therefore be proposed to evaluate the performance of realistic quantum measurement schemes: how accurate and efficient can the state of a quantum object be read out in a given experimental setup?

In the following subsections, I will address this question by introducing four figures of merit to quantify the ideality of a qubit readout scheme—

1. **Readout fidelity:** the correlation between the pre-measurement *qubit* state and the post-measurement *meter* state,

2. **Quantum nondemolition fidelity:** the correlation between the pre-measurement and post-measurement *qubit* states,
3. **Measurement time:** the minimal time duration for the meter to yield sufficiently distinguishable measurement outcomes, and
4. **Measurement efficiency:** the percentage of total measurement signals that are collected and amplified by the meter.

In this section I will focus on the concepts and mathematical modeling of the listed performance metrics. Although we are mainly concerned with the qubit measurements within the scope of this dissertation, the following discussion can be straightforwardly generalized to multi-level quantum systems.

2.3.1 Readout fidelity

What is the probability for the pre-measurement qubit state to be projected onto the corresponding post-measurement meter state? In the language of information theory, this mapping can be modeled as a *binary channel*,⁸ as depicted in Figure 2.3:

- (a) In the ideal situation, the $|0\rangle \rightarrow |+\rangle$ and $|1\rangle \rightarrow |-\rangle$ projections both have a unit probability.
- (b) In a realistic measurement setup, the $|0\rangle \rightarrow |-\rangle$ and $|1\rangle \rightarrow |+\rangle$ crossovers cannot be neglected. The readout process should be accordingly modeled as a binary *asymmetric* channel, in which the transmission probabilities $P(+|0)$ and $P(-|1)$ quantify the faithfulness of the measurement outcome with the qubit initialized in $|0\rangle$ and $|1\rangle$, respectively. Mathematically, the **readout fidelities** are defined

⁸The binary channel is a communication channel model whose input and output are binary numbers [Cover and Thomas, 2005].

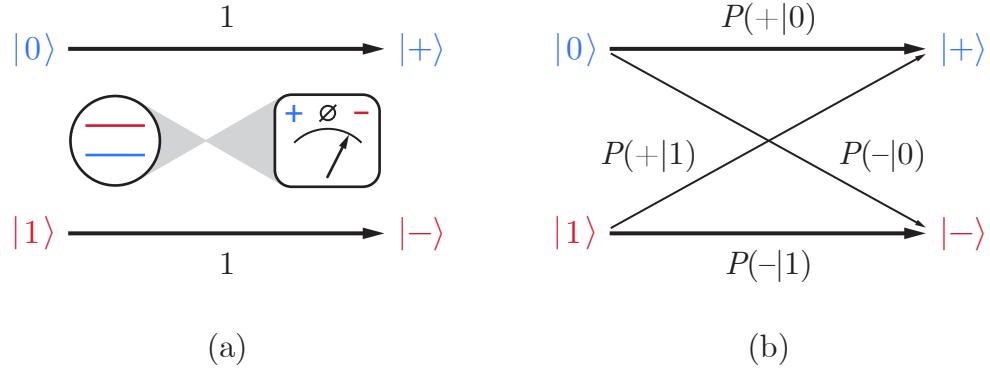


Figure 2.3: Binary channel models of the qubit readout fidelity, with the qubit state $|0\rangle$, $|1\rangle$ and the meter state $|\pm\rangle$ as the input and output, respectively. (a) Ideal qubit readout represented as a noiseless binary channel, in which $P(+|0) = P(-|1) = 1$. (b) Non-ideal qubit readout as a binary asymmetric channel, with nonnegligible crossover probabilities $P(-|0)$ and $P(+|1)$. The branch probabilities are subject to the normalization condition: $\sum_{m=\pm} P(m|0) = \sum_{m=\pm} P(m|1) = 1$.

as the difference between the transmission and crossover probabilities [Devoret and Schoelkopf, 2013],

$$\mathcal{F}_0 = P(+|0) - P(-|0) = 2P(+|0) - 1 = 1 - 2P(-|0), \quad (2.17)$$

$$\mathcal{F}_1 = P(-|1) - P(+|1) = 2P(-|1) - 1 = 1 - 2P(+|1). \quad (2.18)$$

Note that \mathcal{F}_0 or \mathcal{F}_1 will be zero when $P(+|0)$ or $P(-|1)$ equals $1/2$ —that is, when the readout outcome is completely uncorrelated with the qubit state. The binary channel capacity in this extreme situation becomes zero, meaning that no information about the qubit can be extracted from the meter state [Shannon, 1948].

Finally, one can define the *total* readout fidelity as

$$\mathcal{F}_{\text{tot}} = \frac{\mathcal{F}_0 + \mathcal{F}_1}{2} = 1 - P(-|0) - P(+|1), \quad (2.19)$$

which reaches one for an ideal readout and equals zero when the state of the qubit and that of the meter are completely uncorrelated [Gambetta *et al.*, 2007].

2.3.2 Quantum nondemolition fidelity

In entry-level textbooks,⁹ the *measurement postulate* of quantum mechanics is typically introduced using the language of wave-function “collapse” or “reduction” [Dirac, 1930; Heisenberg, 1930; von Neumann, 1932], which breaks the unitarity of the dynamical evolution of quantum states as governed by the Schrödinger equation, and randomly selects a measurement outcome from the eigenvalues of the observable. Despite being successful in predicting a wide range of experimental results, this postulate nevertheless assumes the measurement can be completed infinitely fast,¹⁰ which is apparently *unphysical* since in reality, the accumulation of information during any scientific observation must be a continuous process over time.¹¹ As a matter of fact, the finite strength or time duration of quantum measurement is crucial for understanding a list of nonidealities emerging in realistic qubit readout experiments.

For instance, the dynamics of the coupled qubit–meter system may perturb the

⁹For example, Cohen-Tannoudji *et al.* [1973] and Sakurai and Napolitano [2021].

¹⁰More precisely, it assumes the interaction between the quantum system and the meter is sufficiently strong such that the measurement can be completed much faster than any other time-evolution processes in the system. Although this presumption was generally true during the early years of experimental quantum physics, later implementations of repetitive or continuous measurement protocols have brought those experiments into a regime where unitary evolution and measurement occur concurrently and are in directly competition. One such example is the *quantum Zeno effect* in which the coherent dynamics of a quantum system is partially “frozen” under continuous observation [Bernu *et al.*, 2008; Itano *et al.*, 1990; Misra and Sudarshan, 1977; Slichter *et al.*, 2016] or confined to a multi-dimensional eigen-subspace [Facchi *et al.*, 2000; Facchi and Pascazio, 2002; Gleyzes and Raimond, 2016; Touzard *et al.*, 2018]; see Facchi and Pascazio [2008] for a topical review.

¹¹To quote Lamb [1986]: “The structure of quantum mechanics makes it very natural to pretend that some (if not all) of the observables that characterize a dynamical system can be “measured” experimentally at least in principle. . . . Unfortunately, the founders of the theory did not tell us much about how such measurements . . . could be made.”

qubit state in the midst of the measurement process. Readout data collected at later times will then become incompatible with those collected at prior moments. After a finite time window of data acquisition, a standard quantum limit (SQL) is imposed on the measurement accuracy of the quantum variable, as a result of the fundamental quantum measurement back-action derived from the Heisenberg uncertainty principle. To formalize this issue, one can write down the composite Hamiltonian of the quantum measurement system as

$$\hat{H}_{\text{q-m}} = \hat{H}_{\text{q}} + \hat{H}_{\text{m}} + \hat{H}_{\text{int}}, \quad (2.20)$$

in which \hat{H}_{q} and \hat{H}_{m} stand for the uncoupled Hamiltonians of the qubit and the meter, respectively; their interaction Hamiltonian is denoted by \hat{H}_{int} . If the qubit state and the meter state as described in Section 2.2 are associated with observables \hat{O}_{q} and \hat{O}_{m} , then the *measurability condition* can be represented by

$$[\hat{O}_{\text{m}}, \hat{H}_{\text{int}}] \neq 0, \quad (2.21)$$

which is to say, the meter must be able to evolve under the qubit–meter interaction so as to be entangled with the qubit and record its state information. In the meantime, the qubit may also evolve under \hat{H}_{q} and \hat{H}_{int} between incremental measurement steps, gradually deviating from its original state and producing a lower measurement precision. A readout scheme free from such measurement-induced qubit-state evolution is known as a **quantum nondemolition** (QND) measurement [Braginsky and Khalili, 1992, 1996; Caves *et al.*, 1980; Peres, 1993], in which higher precision can be achieved by repeating the measurement in series and integrating individual outcomes

afterwards.¹² Mathematically, the QND measurement can be realized—sufficiently but not necessarily—if the observable is a constant of motion with respect to \hat{H}_q and \hat{H}_{int} ,

$$[\hat{O}_q, \hat{H}_q] = 0, \quad (2.22)$$

$$[\hat{O}_q, \hat{H}_{\text{int}}] = 0. \quad (2.23)$$

To quantify the “QND-ness” of a qubit readout scheme, one can define its **QND fidelity**—conditioned on the qubit being initialized in $|0\rangle$ or $|1\rangle$ —by the correlation between the qubit states before and after a measurement,

$$\mathcal{Q}_0 = P(0|0), \quad (2.24)$$

$$\mathcal{Q}_1 = P(1|1). \quad (2.25)$$

By this definition, the QND fidelity reaches one when the qubit state remains unaltered over consecutive measurement steps, and equals zero when the pre-measurement and post-measurement states are orthogonal. Analogous to Equation (2.19), the *total* QND fidelity can be defined as

$$\mathcal{Q}_{\text{tot}} = \frac{\mathcal{Q}_0 + \mathcal{Q}_1}{2} = \frac{P(0|0) + P(1|1)}{2}. \quad (2.26)$$

¹²Historically, the detailed analysis of QND measurement was first prompted by the mission of detecting the mechanical vibration of macroscopic gravitational-wave antennas [Braginsky and Vorontsov, 1975; Braginsky *et al.*, 1980; Meystre and Scully, 1983]. The QND principles had subsequently been imported to the study of microscopic and mesoscopic quantum systems, including superconducting circuits [Boulant *et al.*, 2007; Johnson *et al.*, 2010; Lupaşcu *et al.*, 2007; Ristè *et al.*, 2012]. As will be shown in Section 3.2, the circuit QED architecture has offered multiple realizations of QND schemes for qubit readout under certain approximations; and yet in reality, unwanted mechanisms still occasionally flip the qubit state during the measurement process and thus cause additional measurement back-action above the minimal value predicted by quantum mechanics.

Given these definitions, how can the QND fidelity of a readout scheme be experimentally extracted? Unfortunately, a straightforward solution is not provided by Equations (2.24) and (2.26), because $P(0|0)$ and $P(1|1)$ do not involve the meter state and thus cannot be measured directly. Additional assumptions are needed if one wish to reconstruct $P(0|0)$ and $P(1|1)$ from measurable correlations. Two channel models for this purpose are shown in Figure 2.4:

- (a) In this cascaded binary-channel model with four free parameters, each complete measurement contains a “readout” mapping from the initial qubit state to the post-measurement meter state—the same as the channel model of the readout fidelity in Figure 2.3—followed by a second “projection” mapping from the post-measurement meter state to the post-measurement qubit state [Lupaşcu *et al.*, 2007]. One can verify that in this model,

$$P(+|+) + P(-|-) = P(0|0) + P(1|1), \quad (2.27)$$

and hence \mathcal{Q}_{tot} as defined in Equation (2.26) is equal to an *apparent* total QND fidelity defined as

$$\mathcal{Q}'_{\text{tot}} = \frac{P(+|+) + P(-|-)}{2}, \quad (2.28)$$

in which the meter state correlations $P(+|+)$ and $P(-|-)$ are directly measurable. Simple and convenient as it is, this model has the drawback of intermingling the readout fidelity and the QND fidelity by setting $\mathcal{Q}_{\text{tot}} \leq (\mathcal{F}_{\text{tot}} + 1)/2$. This constraint is purely due to the cascade of “readout” and “projection” steps in a single measurement cycle, which has no obvious physical basis.

- (b) The artificial restriction in model (a) can be removed in a six-parameter channel model in which the initial state of the qubit is mapped onto the joint state of the qubit–meter system posterior to the measurement. In this model, Equation

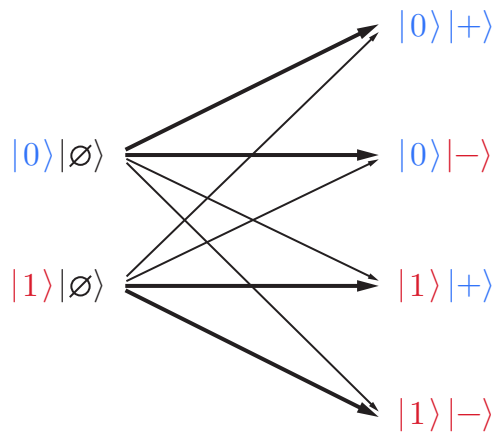
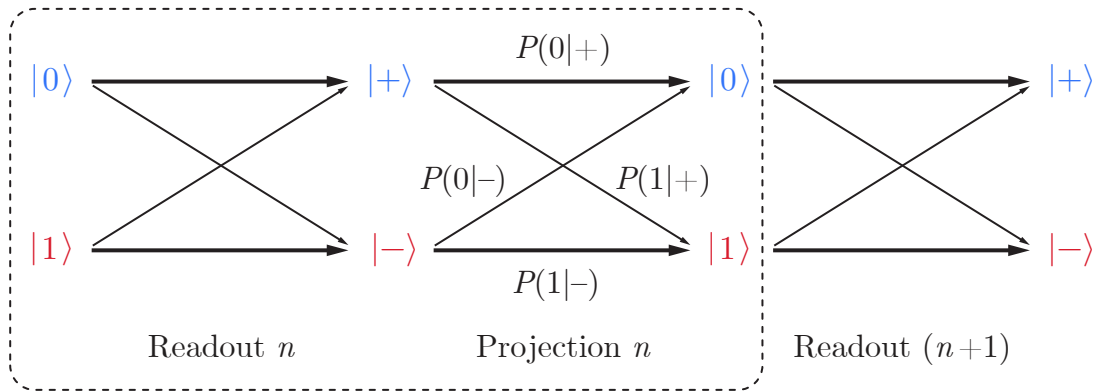


Figure 2.4: Channel models of the QND fidelity. (a) Four-parameter channel model of consecutive qubit measurements. The dashed box represents a single measurement event (labeled as the n -th in a succession), in which a “readout” mapping (as modeled in Figure 2.3) is followed by a “projection” mapping that measures the correlation between the readout outcome (meter state) and the post-measurement qubit state. (b) Six-parameter channel model projecting the pre-measurement qubit state—with the meter in a pre-measurement null state $|\emptyset\rangle$ —to the post-measurement qubit–meter joint state. Note that although there are eight branch probabilities in each channel model, four of them in (a) and two of them in (b) are not free parameters because of the normalization conditions: the probabilities out of a given node must sum to one.

(2.27) no longer holds and therefore \mathcal{Q}_{tot} and $\mathcal{Q}'_{\text{tot}}$ are not equivalent; $P(+|+)$ and $P(-|-)$ become functions of the initial probabilities of the qubit being prepared in $|0\rangle$ and $|1\rangle$, denoted as P_0 and P_1 , respectively:

$$P(\pm|\pm) = \frac{\sum_{q_1, q_2=0,1} P(\pm|q_1)P(q_1 \pm |q_2)P_{q_2}}{\sum_{q=0,1} P(\pm|q)P_q}. \quad (2.29)$$

The dependence of $P(\pm|\pm)$ on $P_{q=0,1}$ has been experimentally verified in Ristè *et al.* [2012], which also provided a direct support for the validity of this single-stage mapping model (b) over the cascaded model (a).

To sum up, model (b) has the advantage of producing \mathcal{F}_{tot} and \mathcal{Q}_{tot} as independent quantities, each ranging from 0 to 1; on the other hand, it requests a more complicated protocol to determine the channel parameters before \mathcal{Q}_{tot} (rather than $\mathcal{Q}'_{\text{tot}}$) can be extracted. In fact, $\mathcal{Q}'_{\text{tot}}$ has been more frequently reported in superconducting qubit experiments when their QND fidelity was concerned. However, it is worth remarking that $\mathcal{Q}'_{\text{tot}}$ is not strictly the definition of the QND fidelity and thus should not be used interchangeably with \mathcal{Q}_{tot} . Distinct notations are therefore recommended for these two characteristic quantities. Testing their difference will provide valuable information for those interested in the detailed physics of QND measurements.

2.3.3 Measurement time

Besides raising the issue of non-ideal QND fidelity, the finite strength of qubit–meter interaction in any realistic measurement model also requires a minimal time duration τ_m for the meter to produce discriminable outcomes with a certain signal-to-noise ratio (SNR). In an experiment, the data-acquisition time T_m should be at least equal to τ_m for the majority of qubit information to be collected by the measurement apparatus.

Together with the readout fidelity and the QND fidelity, the measurement time is another important performance metric of a qubit readout protocol. To achieve a

strong projective measurement, T_m should be short compared to the time scales of other physical processes occurring simultaneously with the measurement. For example, a qubit readout is sufficiently QND only when $T_m \ll T_1$, and sufficiently efficient only when $T_m \ll T_2$. Hence in order to reduce T_m , a strong qubit–meter coupling is generally desirable, and yet increasing their coupling strength beyond an optimal value will introduce parasitic mechanisms that lower \mathcal{F}_{tot} and \mathcal{Q}_{tot} , before the measurement scheme eventually breaks down (see Section 3.4). Moreover, the bandwidth of measurement apparatuses and the sampling rates of pulse-generation and data-acquisition electronics set other hardware limits of T_m . For superconducting qubits, high-fidelity single-shot readout with $T_m \sim 10^2$ ns has been routinely achieved with the assistance of quantum-limited amplifiers in the past decade (see Table 3.2).

2.3.4 Measurement efficiency

From the entropy or information perspective, the efficiency η_m of a physical measurement is generally defined by Equation (2.3) in the opening paragraph of this chapter; and yet its physical meaning depends on the specific measurement scheme adopted in an experiment:

- (i) The concept of measurement efficiency in the quantum regime¹³ was originally associated with *destructive* particle counters such as the Geiger–Müller counter or the photomultiplier tube, which feature single-particle sensitivity but nevertheless absorb those particles after the detection. The efficiency of these passive measurement devices has been defined as the number of detected events divided by the total number of incident particles [Fox, 2006].

¹³Also called “quantum efficiency” or “quantum measurement efficiency” in the literature. However, it is worth noting that the core definition of measurement efficiency—the collectable percentage of signals or information—is not exclusively associated with quantum measurements.

- (ii) Whereas in *nondestructive* measurement protocols,¹⁴ the experimenter is capable of “seeing a particle without destroying it” using a “probe” on which the information of the “target” particle is imprinted [Haroche and Raimond, 2006]. In this situation, η_m is equal to the number of probe particles collected by the meter divided by the total number of probe particles that have interacted with the “target” during the measurement process; on the other hand, inefficiency indicates a loss of post-interaction probe particles together with the information they carry about the “target.”¹⁵ For example, if the meter consists of a chain of linear microwave amplifiers as in the circuit QED readout of superconducting qubits, η_m is then equal to the percentage of signal photons that are eventually able to reach the classical domain.

The efficiency and the fidelity are separate aspects of a quantum measurement: By its mere definition, a high-fidelity qubit readout does not explicitly demand the measurement signals to be processed in a highly efficient way, as long as the collectable portion of signals has already provided enough information about the qubit state such that a sufficient SNR is obtainable at the classical level. Nevertheless, for a practical experimental setup with a finite measurement strength, a higher efficiency becomes critical for improving the readout fidelity and reducing the measurement time. As an example, considering a chain of linear amplifiers, given other experimental parameters being the same, the SNR of a field quadrature component is proportional to $\sqrt{\eta_m}$,

¹⁴Note that a *nondestructive* measurement should not be confused with a quantum *nondemolition* (QND) measurement as defined in Section 2.3.2. The former merely requires the particle under detection is not absorbed by the detector after the measurement process; the latter further demands the quantum state of the particle (or any single quantum degree of freedom) is not perturbed during repetitive measurements. In summary, a QND measurement should at least be nondestructive; but the reverse is not true.

¹⁵Note that this definition of the measurement efficiency is consistent with its general entropy definition in Equation (2.3), assuming signal photons all have the same loss rate in the output circuits regardless of the amount of information they carry.

and the minimal measurement time τ_m to achieve a certain SNR is proportional to η_m^{-1} . Generally speaking, optimizing η_m in an experimental setup requires

- (i) A physical configuration in which readout signals can be maximally collected;
- (ii) A low-loss environment where unwanted dissipations are minimized;
- (iii) An efficient amplification mechanism in which the lowest level of noise is added to the measurement signals.

In superconducting circuits, high-fidelity single-shot circuit QED readout is typically realized with $\eta_m \gtrsim 0.1$ (see Table 3.2). The pursuit of higher measurement efficiencies has been the chief motivation for intra-cavity quantum amplification schemes, which will be topic of Chapter 6.

2.4 From projective to continuous measurements

While examining the nonidealities of qubit readout protocols in the previous section, we have been reminded of quantum measurements as continuous physical processes of qubit–meter interaction and information accumulation. Key parameters of a projective measurement—such as its strength, back-action, time, SNR, and efficiency—have to be essentially understood in the continuous-time picture. To further develop these insights, I will present in this section a discrete-time qubit readout model through which the languages of projective and continuous quantum measurements can be unified.¹⁶ In the end, it will be demonstrated through numerical simulations how nonideal effects during the measurement process, such as signal dissipations (measurement inefficiency) and measurement-induced qubit-state transitions (non-QND events), can influence qubit readout results in real experiments.

¹⁶This discrete model of weak continuous measurements was originally analyzed in Brun [2002], with a different and yet equivalent form of qubit–ancilla interaction.

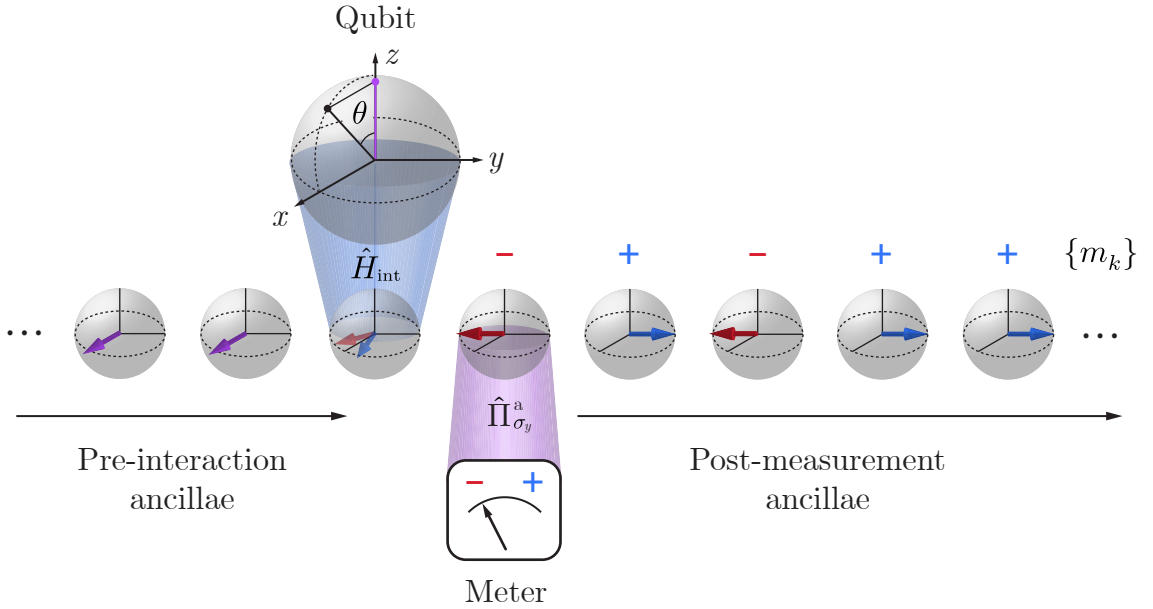


Figure 2.5: Discrete-time model of a qubit readout process. The Bloch sphere representation $|\psi\rangle = \cos(\theta/2)|0\rangle + e^{i\phi}\sin(\theta/2)|1\rangle$ is used to denote the states of two-level systems. The qubit is represented by the large Bloch sphere and remains fixed in space. An array of ancillae—initially prepared in $|+x\rangle_a$ —are shown as small Bloch spheres, moving from left to right in series as if on a conveyor belt. When approaching the qubit, the k -th ancilla interacts with it for a time interval Δt under the interaction Hamiltonian \hat{H}_{int} . Immediately afterwards, the ancilla is projectively read out by a meter onto $|\pm y\rangle_a$, which producing a random binary number $m_k = \pm$. During the successive qubit–ancilla interactions, $\{m_k\}$ are recorded and plugged into the quantum state-update (Bayesian) model to trace the state of the qubit in real time.

The model is depicted in Figure 2.5. A qubit to be measured—represented by the large Bloch sphere, fixed in the drawing space as a target—is successively interrogated by a linear chain of two-level ancillae, each for a time duration Δt . Their interaction Hamiltonian has the form of

$$\frac{\hat{H}_{\text{int}}}{\hbar} = \frac{\chi}{2} \hat{\sigma}_z^{\text{q}} \otimes \hat{\sigma}_z^{\text{a}}, \quad (2.30)$$

where $\hat{\sigma}_z^q$ and $\hat{\sigma}_z^a$ denote the Pauli- z operators of the qubit and the ancilla, respectively.

The unitary time evolution operator should thus be

$$\hat{U}_{\text{int}}(\Delta t) = \exp\left(-\frac{i\hat{H}_{\text{int}}\Delta t}{\hbar}\right) = \exp\left(-\frac{i\epsilon}{2}\hat{\sigma}_z^q \otimes \hat{\sigma}_z^a\right), \quad (2.31)$$

in which $\epsilon = \chi\Delta t$ is a dimensionless variable measuring the strength of the qubit–ancilla interaction. The qubit was prepared in an arbitrary initial state, denoted by its density operator

$$\hat{\rho}_q = \frac{\hat{\mathbb{I}}_q + \vec{v}_q \cdot \hat{\vec{\sigma}}_q}{2}. \quad (2.32)$$

In this expression, “ \cdot ” stands for the inner product of two vectors: $\hat{\vec{\sigma}}_q = (\hat{\sigma}_x^q, \hat{\sigma}_y^q, \hat{\sigma}_z^q)$ is the Pauli-operator vector, and \vec{v}_q is the 3D Bloch state vector with a modulus $|\vec{v}_q| \leq 1$. Without losing generality, one can choose the orientation of the reference frame such that $\vec{v}_q = (x_q, 0, z_q) = (r_q \sin \theta_q, 0, r_q \cos \theta_q)$, with $r_q = 1$ representing a pure state and $r_q < 1$ representing a mixed state. Before the interaction, the ancilla was prepared in

$$|+x\rangle_a = \frac{|0\rangle_a + |1\rangle_a}{\sqrt{2}}, \quad (2.33)$$

or equivalently,

$$\hat{\rho}_a = \frac{\hat{\mathbb{I}}_a + \hat{\sigma}_x^a}{2}. \quad (2.34)$$

The joint qubit–ancilla state after time Δt should then be

$$\hat{\rho}_{\text{int}}(\Delta t) = \hat{U}_{\text{int}}(\Delta t)(\hat{\rho}_s \otimes \hat{\rho}_a)\hat{U}_{\text{int}}^\dagger(\Delta t). \quad (2.35)$$

Immediately after their interaction, the ancilla is projectively measured onto the basis

$$|\pm y\rangle_a = \frac{|0\rangle_a \pm i|1\rangle_a}{\sqrt{2}}, \quad (2.36)$$

or equivalently, by the projection operators

$$\hat{\Pi}_{\sigma_y=\pm 1}^a = \frac{\hat{\mathbb{I}}_a \pm \hat{\sigma}_y^a}{2}. \quad (2.37)$$

Using Equations (2.10) and (2.11), one can obtain the probabilities corresponding to the two measurement outcomes—

$$P(m_k = \pm 1) = \frac{1 - m_k z_s \sin \epsilon}{2} = \frac{1 - m_k r_s \cos \theta_s \sin \epsilon}{2}, \quad (2.38)$$

together with the qubit state update, expressed with the pre-measurement and post-measurement Bloch vector components (with k being the ancilla index)—

$$x'_q = \frac{x_q \cos \epsilon}{1 - m_k z_q \sin \epsilon} = \frac{r_q \sin \theta_q \cos \epsilon}{1 - m_k r_q \cos \theta_q \sin \epsilon}, \quad (2.39)$$

$$y'_q = y_q = 0, \quad (2.40)$$

$$z'_q = \frac{z_q - m_k \sin \epsilon}{1 - m_k z_q \sin \epsilon} = \frac{r_q \cos \theta_q - m_k \sin \epsilon}{1 - m_k r_q \cos \theta_q \sin \epsilon}. \quad (2.41)$$

These results can also be derived using the generalized measurement formalism introduced in last paragraph of Section 2.2. Two *non-projective* measurement operators acting on the qubit should be defined as

$$\hat{M}_{\pm}^q = \sqrt{\frac{1 \mp \sin \epsilon}{2}} |0\rangle\langle 0|_q + \sqrt{\frac{1 \pm \sin \epsilon}{2}} |1\rangle\langle 1|_q, \quad (2.42)$$

in association with the two measurement outcomes $m_k = \pm 1$. Their normalization

condition can be easily verified—

$$\sum_{\pm} \hat{M}_{\pm}^{q\dagger} \hat{M}_{\pm}^q = \hat{\mathbb{I}}_q. \quad (2.43)$$

Equations (2.38)–(2.41) can then be obtained from Equations (2.14) and (2.15). It is also easy to find that \hat{M}_{\pm}^q represent the projective measurement when $\epsilon = \pi/2$.

In the limit of $\epsilon \ll 1$, the procedure described above exemplifies a **weak measurement** of the qubit through the projective measurement of the ancilla, which has been weakly entangled with the qubit after their interaction during the time window Δt . According to Equations (2.39)–(2.41), the measurement back-action drives the qubit toward $|0\rangle_q$ or $|1\rangle_q$ only by an incremental step away from its original state, whose direction depends on the projective measurement outcome m_k of the ancilla—a weakly biased stochastic binary variable given by Equation (2.38).¹⁷ In particular, if the qubit started in the north/south hemisphere of its Bloch sphere, the small bias quantity in $P(m_k)$ —proportional to ϵ in the first-order approximation—tends to steer the qubit *toward* the north/south pole. Consequently, after a large number of weak measurement steps, the qubit will end up close to one of the two poles, indicating the completion of a strong projective measurement. In the meantime, the sum of all the ancilla projective readout outcomes—

$$R = \sum_k m_k \quad (2.44)$$

¹⁷If the qubit started from a pure state ($r_q = 1$), Equations (2.39)–(2.41) can be rewritten as a single formula,

$$\tan\left(\frac{\theta'_q}{2}\right) = \tan\left(\frac{\theta_q}{2}\right) \tan\left(\frac{\pi}{4} + m_k \frac{\epsilon}{2}\right).$$

The stochastic movement of the qubit Bloch vector due to the measurement back-action can be mapped onto a biased random walk on a unit hyperbola. See Mineev [2018] for details.

constitute the *cumulative measurement records*, which eventually point to the same direction as the post-measurement state of the qubit. The trajectory $\{\vec{v}_q(t_0 + k\Delta t)\}$ computed using the qubit initial state $\vec{v}_q(t_0)$ and the incremental measurement records $\{m_k\}$ is known as the discrete-time **quantum trajectory** of the qubit under repetitive weak measurements, representing the subjective knowledge of the experimenter about the qubit state during the observation process [Carmichael, 1993; Weber *et al.*, 2016]. A numerical simulation of the quantum trajectories and measurement records of a qubit starting from the equator of its Bloch sphere—

$$|+x\rangle_q = \frac{|0\rangle_q + |1\rangle_q}{\sqrt{2}} \quad (2.45)$$

is shown in Figure 2.6, in which the emergence of strong projective measurements after $k \gg \epsilon^{-2}$ repetitive weak measurements can be clearly seen.

The threshold $k \sim \epsilon^{-2}$ between strong and weak measurements can be understood as follows: Assuming the qubit was initialized in the vicinity of one of its eigenstates, the measurement records in a first-order approximation can be regarded as realizations of a binary (± 1) random variable following the Bernoulli distribution

$$P_{\pm} = \frac{1 \pm \epsilon}{2}, \quad (2.46)$$

which an expected value $P_+ - P_- = \epsilon$ and a standard deviation $\sqrt{1 - \epsilon^2} = 1 + O(\epsilon^2)$. Now consider the sum of k such identical Bernoulli variables. When $k = \epsilon^{-2} \gg 1$, following the central limit theorem, both the mean and the standard deviation of the cumulative measurement records are approximately equal to ϵ^{-1} , indicating a measurement SNR ≈ 1 . Therefore, in this system, the minimal measurement time

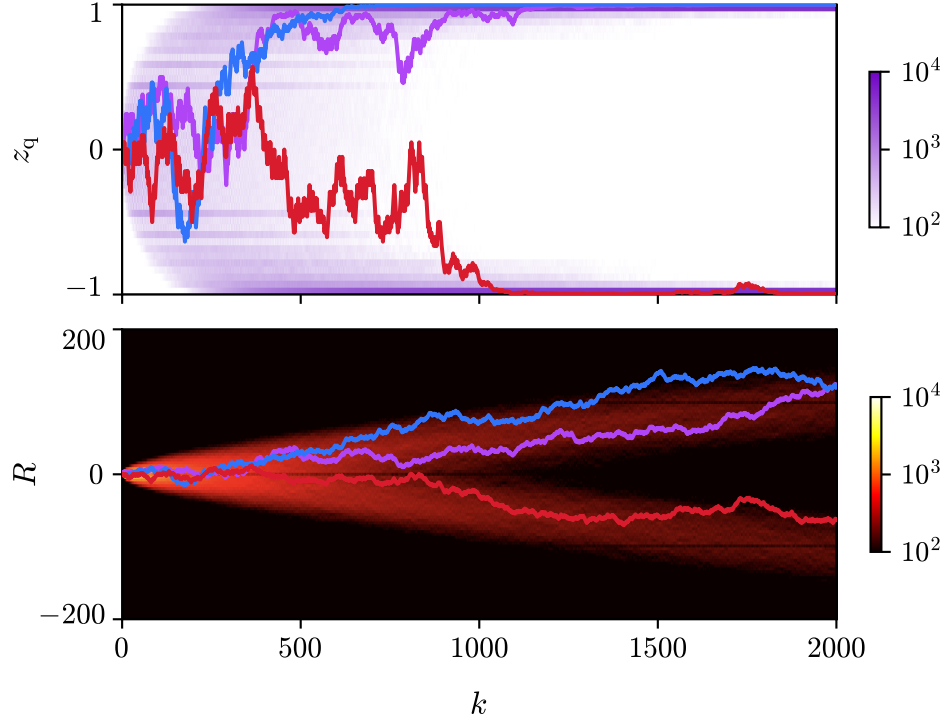


Figure 2.6: Numerical simulation of repetitive weak qubit measurements, following the protocol described in the text. The qubit–ancilla interaction strength is chosen to be $\epsilon = \chi\Delta t = 0.05$; the qubit was initialized in $|+x\rangle_{\text{q}}$ at $t = t_0$. Upper panel: The blue, purple, and red traces are three simulated stochastic quantum trajectories $\{z_{\text{q}}(t_0 + k\Delta t)\}$ over 2×10^3 measurement steps. Lower panel: the corresponding cumulative measurement records $R = \sum_{k'=0}^k m_{k'}$ are plotted using the same colors. The logarithmic histograms of 1×10^4 quantum trajectories and cumulative measurement records are shown in the backgrounds. The discontinuities of the quantum trajectory distribution in the upper subfigure are numerical artifacts due to the discrete measurement steps or the finite value of ϵ . It can be seen that when $k \gg \epsilon^{-2}$, the quantum measurement back-action is projecting the qubit close to $|0\rangle_{\text{q}}$ or $|1\rangle_{\text{q}}$, and meanwhile the measurement records show a clear bimodal distribution; the post-measurement qubit state is then able to be deduced from the measurement records with an increasingly high fidelity. Strong projective measurements are thus recovered from the succession of weak measurement steps.

can be defined as

$$\tau_m = \frac{\Delta t}{\epsilon^2}. \quad (2.47)$$

Alternatively, viewed from information theory, the transformation of each ancilla from a unbiased to a biased random bit indicates a reduction of its Shannon entropy, or equivalently an information gain equal to

$$1 + \sum_{\pm} P_{\pm} \ln P_{\pm} = \frac{\epsilon^2}{2 \ln 2} + O(\epsilon^4). \quad (2.48)$$

Therefore, a series of $k = \epsilon^{-2}$ measurements will collectively produce $(2 \ln 2)^{-1} \approx 0.72$ bit of information, which is close to 1 bit—the information gain in a projective qubit measurement.

Furthermore, this measurement model demonstrates two other ideal properties: It is both fully QND and fully efficient—

- (i) Since $[\hat{\sigma}_z^q, \hat{H}_{\text{int}}] = 0$, the qubit state does not evolve along the measurement axis during its interaction with the ancillae.¹⁸
- (ii) Equations (2.39)–(2.41) indicate that the modulus of the qubit Bloch vector is preserved over incremental measurement steps, provided that the measurement outcomes are all collected and recorded. This result is expected because *a fully efficient measurement does not reduce the purity of a quantum state*. On the contrary, it can be checked that if measurement outcome of an ancilla is not recorded, according to Equation (2.12) or (2.16), the qubit state-update

¹⁸In the meantime, $[\hat{\sigma}_y^a, \hat{H}_{\text{int}}] \neq 0$; the measurability condition is thus satisfied. Review Equations (2.21)–(2.23) for a sufficient but not necessary set of criteria for QND measurements.

formulae will instead become

$$x'_{\text{q,NR}} = x_{\text{q}} \cos \epsilon = r_{\text{q}} \sin \theta_{\text{q}} \cos \epsilon, \quad (2.49)$$

$$y'_{\text{q,NR}} = y_{\text{q}} = 0, \quad (2.50)$$

$$z'_{\text{q,NR}} = z_{\text{q}} = r_{\text{q}} \cos \theta_{\text{q}}. \quad (2.51)$$

The loss of readout information is consistent with the absence of measurement back-action along the z_{q} axis. However, the Bloch vector component within the x - y plane is reduced by a factor of $\cos \epsilon \approx e^{-\epsilon^2/2}$ in the limit of $\epsilon \ll 1$, which is known as the **measurement-induced qubit dephasing**—a fundamental phenomenon connecting information efficiency with quantum coherence (to be further explored in Section 3.3 and Chapter 5).

Finally, by adding nonlinearities into the model, one can simulate how significantly the measurement records can be impacted by qubit-state transitions and measurement inefficiencies (Figure 2.7). Many more intriguing quantum processes can be explained using this pedagogical model, such as the concurrent measurements of two incompatible quantum observables [Arthurs and Kelly, 1965; Hacoheh-Gourgy *et al.*, 2016] and the competition between continuous quantum measurements and coherent qubit drives [Minev *et al.*, 2019]. And yet it is time to move on to the next topic as so far we have been equipped with enough theories and intuitions to understand the quantum measurements and decoherence in circuit QED systems, which will be discussed in the coming chapter. There I will link concrete physical meanings to the conceptual and mathematical models introduced in the past sections, such that they will be guiding our experimental works on this frontier.

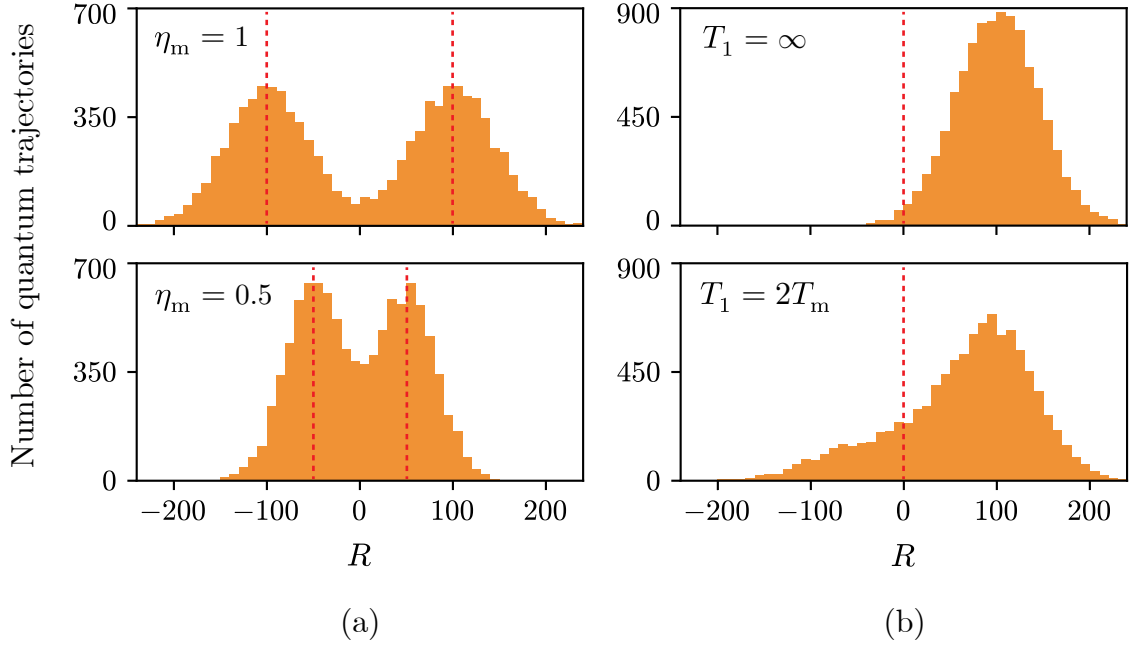


Figure 2.7: Numerical simulation of qubit measurement records considering measurement inefficiency and qubit-state transition events. Histograms: distributions of 1×10^4 cumulative measurement records $R = \sum_{k'=0}^k m_{k'}$ after $k = 2 \times 10^3$ weak measurement steps with $\epsilon = \chi \Delta t = 0.05$. (a) The qubit was initialized in $|+x\rangle_q$. Measurement efficiencies $\eta_m = 1$ and $\eta_m = 0.5$ are used in the top and bottom panels, respectively. The measurement records display bimodal normal distributions. The two peaks have opposite mean values $\pm \eta_m k \epsilon$ and the same standard deviation $\sqrt{\eta_m k}$; the SNR is therefore equal to $\epsilon \sqrt{\eta_m k}$. (b) The qubit was initialized in $|0\rangle_q$. The upper panel depicts ideal measurements; in the lower panel, a bit-flip probability $0.1\epsilon^2$ is assigned during every weak measurement step, corresponding to a qubit relaxation time $T_1 = 10\epsilon^{-2}\Delta t = 4 \times 10^3 \Delta t$, which is twice the measurement time $T_m = 2 \times 10^3 \Delta t$. The probability of obtaining measurement records $R < 0$ is noticeably increased, reducing the SNR and the readout fidelity, if $R = 0$ is employed as the demarcation to distinguish $|0\rangle_q$ from $|1\rangle_q$ from the measurement outcome. In other words, if $R > 0$ and $R < 0$ correspond to the $|\pm\rangle$ meter states in the binary channel model of Figure 2.3(b), qubit-state transition events during the measurement process can have visible impacts on \mathcal{Q}_{tot} by increasing $P(-|0)$ and $P(+|1)$ beyond the ideal normal distribution tails.

Chapter 3

Measurements and Decoherence in Circuit Quantum Electrodynamics

In general, illuminating an inert object in order to be able to observe it does not disturb it any more than what the astronomer does when looking at a star . . . In the old physics, . . . no minimum action limited the necessary intervention for the measurement. It is otherwise in the new physics, due to the existence of the quantum h below which no action can go.¹

Paul Langevin [1935]

As has been briefly introduced in Section 1.3.3, circuit QED is concerned with the engineerable interaction of photons with solid-state artificial atoms in the quantum regime. It has provided quantum physicists and engineers with a versatile experimental platform to study atomic physics and quantum optics using microwave electrical circuits, and meanwhile a scalable architecture to explore prototypes of quantum information processors and networks. The basic physics of circuit QED is grounded in the quantum theory of light–matter interaction [Cohen-Tannoudji *et al.*, 1988; Gryn-

¹Original text (in French): “Le fait d’éclairer un objet inerte pour pouvoir l’observer ne le trouble pas plus, en général, que ne le fait pour une étoile l’astronome qui la regarde . . . Dans l’ancienne physique, . . . aucun minimum d’action ne limitait l’intervention nécessaire à la mesure. Il en est autrement dans la physique nouvelle, du fait de l’existence du quantum h au-dessous duquel aucune action ne peut descendre.”

berg *et al.*, 2010].² Nevertheless, the artificiality of the energy spectra and coupling parameters³ in quantum electrical circuits has allowed quantum optics, quantum control, and quantum simulation experiments to be performed in new regimes that have not yet been accessed with natural atoms and molecules [Gu *et al.*, 2017; Houck *et al.*, 2012; Ma *et al.*, 2021; Terhal *et al.*, 2020]. Moreover, circuit QED modules have been configured as microwave radiometers [Scigliuzzo *et al.*, 2020; Wang *et al.*, 2022, 2021] or itinerant single-photon counters [Besse *et al.*, 2018; Campagne-Ibarcq *et al.*, 2018; Inomata *et al.*, 2016; Kono *et al.*, 2018; Lescanne *et al.*, 2020; Narla *et al.*, 2016], which are being applied to detecting quantum microwave signals for fundamental research purposes, such as electron spin fluorescence [Albertinale *et al.*, 2021] and hidden photon dark matter [Dixit *et al.*, 2021].

In this chapter, I will discuss two complementary aspects of the coherent “atom”–

²See the references in Footnote 19 of Chapter 1.

³In atomic physics, atoms interact with photons whose energies are close to atomic transitions, which is of the same order of magnitude as the ionization energy. In order to increase the coupling strength between the atom and the field, physicists trap photons in high-quality-factor resonant cavities, whose geometric scale cannot be smaller than the photon wavelength λ . Therefore, the electric field induced by a single photon in the cavity cannot exceed

$$\frac{1}{2}\epsilon_0 |\mathbf{E}|^2 \lambda^3 \sim \frac{hc}{\lambda} \quad \Rightarrow \quad |\mathbf{E}| \sim \frac{1}{\lambda^2} \sqrt{\frac{hc}{\epsilon_0}}.$$

The atom–photon coupling energy is of the order $ea_0|\mathbf{E}|$, in which ea_0 is an estimation of the atomic electric dipole (a_0 being the Bohr radius). As a result, the ratio between the coupling and the photon energy is approximately

$$\frac{ea_0|\mathbf{E}|}{hc/\lambda} \sim \alpha^{3/2} \sim 10^{-3},$$

with α denoting the fine structure constant. Stronger atom–photon couplings need to be achieved by increasing the electric dipole moment beyond the ea_0 level. In atomic cavity QED experiments, this is realized by using *Rydberg atoms* whose the outer electron is excited to a high orbit, resulting in an effective atomic radius by several orders of magnitude larger than a_0 . In circuit QED experiments, the electric dipoles of superconducting artificial atoms are not directly determined by natural constants, and “atom”–photon couplings have been observed in the *ultrastrong* [Forn-Díaz *et al.*, 2010; Niemczyk *et al.*, 2010] and the *deep strong* regimes [Yoshihara *et al.*, 2017]. See Frisk Kockum *et al.* [2019] for a review.

photon interface in the circuit QED architecture—how the qubit state is measured with microwave radiation, and how the cavity-assisted measurement channel introduces parasitic photon-induced decoherence mechanisms to the embedded qubit. We will see the theoretical models of quantum measurements—introduced in Chapter 2—are materialized using elements of superconducting quantum circuits reviewed in Chapter 1, and in particular, the leading physical factors responsible for the readout nonidealities and accordingly, how a qubit readout scheme can potentially be improved. The conclusions will be instructional for our experimental innovations in search for an improved single-qubit protection and measurement scheme, which is to be reported in Chapters 5 and 6.

3.1 Historical precursors

What are the key ideas behind the experimental methods of circuit QED? First and foremost, as its name indicates, the influence from atomic cavity QED has been widely acknowledged [Blais *et al.*, 2004; Haroche *et al.*, 2020]. Nevertheless, the intellectual precursors of the circuit QED measurement techniques can be traced back to a few pioneering experiments much earlier than the era of the “second quantum revolution” [Dowling and Milburn, 2003].

- (i) The central task of the circuit QED readout protocol—like any quantum measurement experiment—is to faithfully map those fragile quantum states separated from each other by no more than a few elementary quanta onto robust meter states that are macroscopically recordable and distinguishable. Such a mapping was first achieved one century ago by the **Stern–Gerlach experiment** based on the atomic or molecular beam technique [Dunoyer, 1913; Gerlach and Stern, 1922; Ramsey, 1956; Schmidt-Böcking *et al.*, 2016], in which the two electron-spin states were projected onto opposite transverse momenta of the

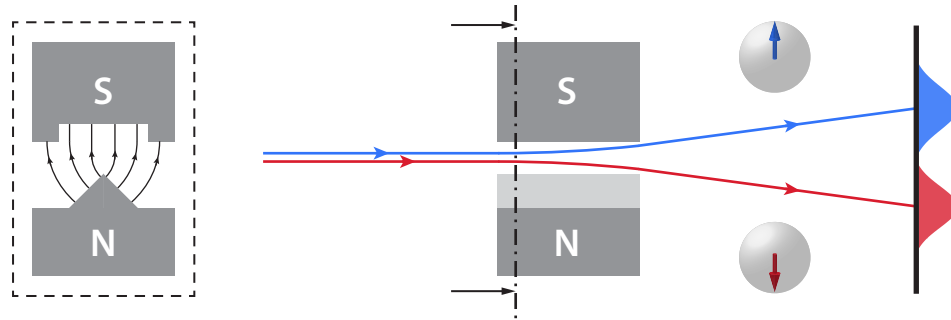


Figure 3.1: Simplified drawing of the Stern–Gerlach experiment: an inhomogeneous static magnetic field, whose profile is shown in the dashed box on the left, exerts a spin-dependent force along the field gradient on the atom mid-flight, whose spin degree of freedom is thus coupled to its spatial movement and can be distinguished on a macroscopic scale.

silver atom (Figure 3.1). In their original report, the center-to-center distance between the two deposits on the glass plate is 0.20 mm, clearly resolvable under an optical microscope. The deposition process typically took several hours to yield a discernible pattern, which was caused by the insensitivity of the “imaging” system. In an imaginary situation where the positions of silver atoms on the glass plate can be individually recorded—like single electrons in a double-slit experiment [Merli *et al.*, 1976; Tonomura *et al.*, 1989]—the Stern–Gerlach setup would then be able to demonstrate the single-shot readout of electron spin states.

- (ii) Despite its success, the Stern–Gerlach experiment lacks the flexibility of being a versatile platform for quantum measurements, mostly limited by the atomic beam method: The spin state and the meter variable (transverse motion) are materially associated with the same atom, whose detection is eventually through

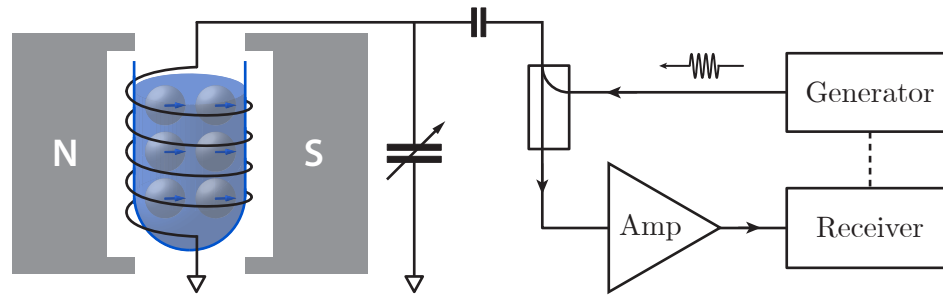


Figure 3.2: Nuclear magnetic resonance (NMR) experiment. When the input radio-frequency (RF) radiation is on resonance with the spin ensemble in a static magnetic field, the collective spin polarization can be determined by detecting the RF energy absorption using a lock-in amplifier.

a destructive mechanism.⁴ Repeated measurements of the same quantum state are therefore forbidden. Furthermore, the mechanical nature of the meter variable is only compatible very elementary signal processing techniques in the form of spatial maneuver. These problems were overcome by the invention of the **nuclear magnetic resonance** (NMR) technique [Bloch, 1946; Bloch *et al.*, 1946; Bloembergen *et al.*, 1948; Purcell *et al.*, 1946], in which the state information of the spin ensemble is reflected on a resonant probe generated and analyzed by radio-frequency (RF) or microwave electronics (Figure 3.2). Electromagnetic waves can be processed in the classical end with little additional back-action to the spin system. However, the coupling between RF/microwave radiation with individual nuclear magnetic moments is so weak that a macroscopic number of spins are needed to produce a discernible signal [Abragam, 1961]. Unlike the Stern–Gerlach experiment, in which the distance between split atomic beams gradually accumulates in the midst of their flight, the absence of any intrinsic

⁴See Footnote 14 of Chapter 2.

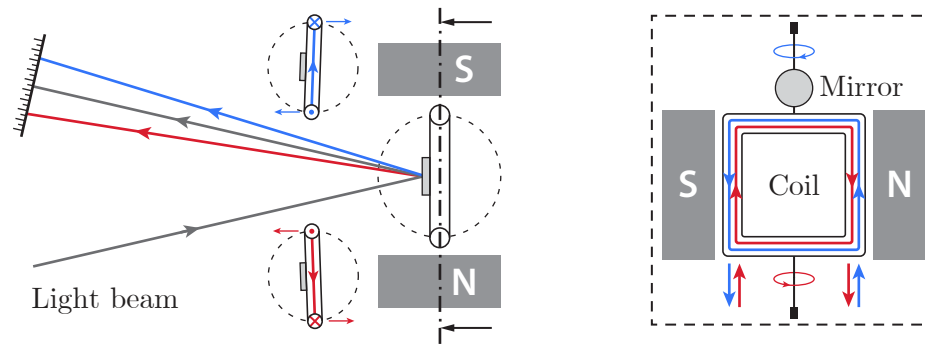


Figure 3.3: Moving-coil mirror galvanometer of the d'Arsonval type: top view (left) and profile of the coil, magnet, and mirror (right). The Laplace force on the current-carrying coil produces a small angular displacement of the mirror, which is then amplified by the optical lever and detected through the measurable shift of the reflected light beam.

amplification mechanism in the NMR setup prevents it from directly detecting individual quantum degrees of freedom.

- (iii) Can one build a measurement setup that combines the advantages of the two complementary approaches by employing electromagnetic signals to resolve single quantum states? The NMR detection method of spin ensembles relies on the resonant absorption of RF energy stored in the standing electromagnetic field of the tunable resonator. Higher sensitivity and lower back-action can in principle be achieved if traveling waves are used as probes to interact with the target in a *non-absorptive* manner. A classic design illustrating this idea is the **mirror galvanometer** for indicating the direction and magnitude of weak electric currents. Figure 3.3 describes the working mechanism of an improved moving-coil model invented by Arsène d'Arsonval, in which the electric current is first quasi-linearly projected to the angular displacement of the suspended coil–mirror rotor and then quasi-linearly measured in reflection by a light beam received by a

Experiment	Object	Meter	Single-quantum resolution
Stern–Gerlach	Quantum	Mechanical	Yes
NMR	Quantum	Electromagnetic	No
Mirror galvanometer	Classical	Electromagnetic	—
Circuit QED	Quantum	Electromagnetic	Yes

Table 3.1: Stern–Gerlach, NMR, and mirror galvanometer experiments demonstrated different aspects of the circuit QED measurement setup—the electromagnetic readout of a quantum mechanical object with single-quantum resolution.

moving telescope, represented as a ruler in the drawing [d’Arsonval, 1888]. From a system point of view, this classical electromagnetic meter already possesses two crucial elements of a typical quantum measurement setup: an intermediate *ancilla* (coil–mirror) between the system under detection (electric current) and the readout signal sent by the experimenter (light beam), and an *amplification circuit* (optical lever) mapping the small deflection of the ancilla onto a visible quantity. In the end, the linear shift of the telescope from its zero-current position constitutes the *signal*, while the *noise* is determined by the intrinsic Gaussian beam profile [Yariv and Yeh, 2006]. The readout SNR can be maximized through techniques of optical signal processing until it approaches the standard quantum limit.

From a general quantum measurement perspective, Table 3.1 summarizes the key features of these three experiments as compared to the circuit QED setup, which has realized the high-fidelity microwave readout of superconducting qubits in a nondestructive and near QND manner. This comparison is intended to display a continuity among the ideas and methods of precise measurement protocols in physics, where the strong object–meter coupling and the efficient amplification and analysis of meter sig-

nals are always desired. In the following section, we will examine the implementation of these two central points in the microwave measurement of superconducting qubits.

3.2 Circuit QED dispersive readout of superconducting qubits

In the Stern–Gerlach experiment or the NMR measurement, the interaction Hamiltonian can be directly expressed through the magnetic dipole coupling between the spins and the external magnetic fields. However, the visualization of the spin–photon coupling model in circuit QED is less straightforward, where the physical system needs to be formalized using appropriate mathematical languages through several layers of abstraction. The first step—from solid-state devices and electromagnetic fields in the three-dimensional (3D) space to the one-dimensional (1D) circuit diagram—has been shown in Figure 1.5, in which the readout cavity is modeled as an LC resonator at the fundamental mode (TE_{101}) frequency of the cavity, and capacitively coupled to the transmon represented by an ideal Josephson element shunted by a coplanar capacitor. In practice, the single-mode resonator model is a reasonable simplification unless higher cavity resonant modes can produce non-negligible effects within the parameter range of interest [Filipp *et al.*, 2011; Houck *et al.*, 2008; Sears *et al.*, 2012].

3.2.1 Dispersive Hamiltonian

The standard procedure of circuit quantization yields the quantum Hamiltonian as given by Equation (1.20):

$$\frac{\hat{H}_{t-c}}{\hbar} = \omega_c \hat{c}^\dagger \hat{c} + \omega_t^{01} \hat{t}^\dagger \hat{t} - \frac{K_t}{2} \hat{t}^{\dagger 2} \hat{t}^2 + g_{tc} (\hat{t}^\dagger + \hat{t}) (\hat{c}^\dagger + \hat{c}). \quad (3.1)$$

Next, one can express the *linear* part of the Hamiltonian above using annihilation

and creation operators of the uncoupled eigenmodes

$$\begin{pmatrix} \hat{\tilde{c}} \\ \hat{\tilde{t}} \end{pmatrix} = \begin{pmatrix} \cos \zeta & \sin \zeta \\ -\sin \zeta & \cos \zeta \end{pmatrix} \begin{pmatrix} \hat{c} \\ \hat{t} \end{pmatrix}, \quad (3.2)$$

in which

$$\zeta = \frac{1}{2} \arctan \left(\frac{2g_{tc}}{\omega_t^{01} - \omega_c} \right) = \frac{1}{2} \arctan \left(\frac{2g_{tc}}{\Delta_{tc}} \right). \quad (3.3)$$

The dispersive regime is characterized by $g \ll |\Delta_{tc}|$ or $|\zeta| \ll 1$. Following the rotating wave approximation (RWA), Equation (1.20) can be rewritten as

$$\frac{\hat{H}_{t-c}}{\hbar} = \tilde{\omega}_c \hat{c}^\dagger \hat{c} + \tilde{\omega}_t^{01} \hat{t}^\dagger \hat{t} - \frac{\tilde{K}_t}{2} \hat{t}^\dagger \hat{t}^2 - \frac{\tilde{K}_c}{2} \hat{c}^\dagger \hat{c}^2 - \tilde{\chi}_{tc} \hat{t}^\dagger \hat{t} \hat{c}^\dagger \hat{c}, \quad (3.4)$$

in which $\tilde{\omega}_c = \omega_c + O(\zeta^2)$ and $\tilde{\omega}_t^{01} = \omega_t^{01} + O(\zeta^2)$ are the modified cavity resonance and transmon 0–1 transition frequencies, respectively; $\tilde{K}_t = K_t + O(\zeta^2)$ is the modified transmon anharmonicity; and

$$\tilde{\chi}_{tc} = 2K_t \zeta^2 + O(\zeta^4) \approx 2K_t \left(\frac{g_{tc}}{\Delta_{tc}} \right)^2, \quad (3.5)$$

$$\tilde{K}_c = K_t \zeta^4 + O(\zeta^6) \approx K_t \left(\frac{g_{tc}}{\Delta_{tc}} \right)^4, \quad (3.6)$$

with $\tilde{\chi}_{tc}$ being the **dispersive coupling strength** (or cross-Kerr nonlinearity) between the cavity and the transmon,⁵ and \tilde{K}_c being the anharmonicity of the readout

⁵A more accurate approximation of the dispersive coupling strength has been derived in Koch *et al.* [2007]:

$$\tilde{\chi}_{tc} \approx 2K_t \frac{g_{tc}^2}{\Delta_{tc}(\Delta_{tc} + K_t)}.$$

cavity [Nigg *et al.*, 2012; Sears *et al.*, 2012]. These two terms are both proportional to K_t and thus originate from the nonlinearity of the Josephson junction due to the off-resonance transmon–cavity coupling. For simplicity, from now on I will drop the tildes (\sim) in Equation (3.4) and concentrate on the dispersive coupling term

$$\frac{\hat{H}_{\text{disp}}}{\hbar} = -\chi_{\text{tc}} \hat{t}^\dagger \hat{t} \hat{c}^\dagger \hat{c}. \quad (3.7)$$

If the transmon dynamics is confined to its lowest two levels $|0\rangle$ and $|1\rangle$, then $\hat{t}^\dagger \hat{t}$ can be replaced by the qubit Pauli- z operator $(\hat{\sigma}_z + 1)/2$:

$$\frac{\hat{H}_{\text{disp}}}{\hbar} = -\frac{\chi_{\text{tc}}}{2} \hat{\sigma}_z \hat{c}^\dagger \hat{c} - \frac{\chi_{\text{tc}}}{2} \hat{c}^\dagger \hat{c}. \quad (3.8)$$

The two-level truncation of the Hilbert space of the transmon will be valid if single-qubit operations are no faster than the time scale $1/K_t$. Equation (3.8) is the effective Hamiltonian of the spin–photon coupling model that the dispersive scheme of qubit readout relies upon.

In the dispersive regime, the energy exchange between the transmon and the cavity is prohibited at the leading order due to their large frequency separation. The interaction Hamiltonian \hat{H}_{disp} merely exerts a qubit-state-dependent frequency shift on the readout cavity,

$$\frac{\hat{H}_c}{\hbar} + \frac{\hat{H}_{\text{disp}}}{\hbar} = \left(\omega_c - \frac{\hat{\sigma}_z + 1}{2} \chi_{\text{tc}} \right) \hat{c}^\dagger \hat{c}. \quad (3.9)$$

Here $\hat{H}_c = \hbar\omega_c \hat{c}^\dagger \hat{c}$ denotes the Hamiltonian of the linear cavity mode. Consequently,

$$\omega_c^0 = \omega_c, \quad \text{if the qubit is in } |0\rangle, \quad (3.10)$$

$$\omega_c^1 = \omega_c - \chi_{\text{tc}}, \quad \text{if the qubit is in } |1\rangle. \quad (3.11)$$

Define the *symmetric* readout frequency

$$\omega_{\text{RO}} = \frac{\omega_c^0 + \omega_c^1}{2}. \quad (3.12)$$

Equations (3.10) and (3.11) can then be rewritten as

$$\omega_c^0 = \omega_{\text{RO}} + \frac{\chi_{\text{tc}}}{2}, \quad (3.13)$$

$$\omega_c^1 = \omega_{\text{RO}} - \frac{\chi_{\text{tc}}}{2}. \quad (3.14)$$

3.2.2 Cavity reflection and transmission measurements

The dependence of the cavity resonant frequency on the qubit state can be measured through the **cavity spectroscopy**, which can be arranged in two possible ways—the **reflection** measurement and the **transmission** measurement: As illustrated in Figure 3.4, if one sends a microwave readout pulse at frequency ω_{RO} , the qubit-state-dependent cavity frequency shift will be mapped onto a phase shift of either (a) the reflected signal from the same cavity port, or (b) the transmitted signal from a second cavity port, both of which can be recorded as the readout signal to encode the state information of the qubit [Vool, 2017]. The cavity responses in the spectroscopy measurements for both configurations can be computed using the input–output formalism [Walls and Milburn, 2008] of the coupled qubit–cavity system.

We start from the circuit QED Hamiltonian under the two-level approximation

$$\frac{\hat{H}_{\text{q-c}}}{\hbar} = \frac{\hat{H}_c}{\hbar} + \frac{\hat{H}_q}{\hbar} + \frac{\hat{H}_{\text{disp}}}{\hbar} = \omega_c \hat{c}^\dagger \hat{c} + (\omega_t^{01} - \chi_{\text{tc}} \hat{c}^\dagger \hat{c}) \frac{\hat{\sigma}_z + 1}{2}. \quad (3.15)$$

(a) For reflection measurements, the Heisenberg–Langevin equation of the cavity

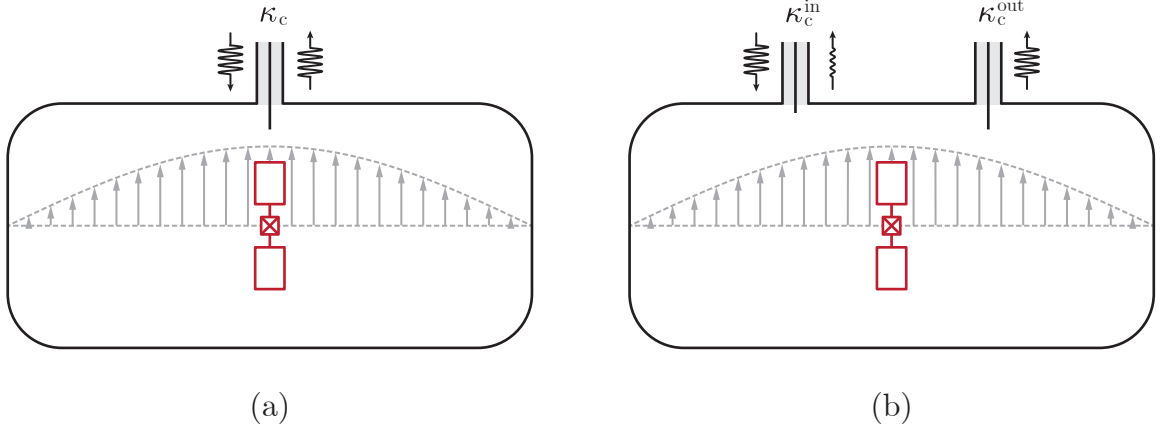


Figure 3.4: Cavity reflection and transmission measurement setups in circuit QED experiments. Similar to Figure 1.5, without loss of generality, a fixed-frequency transmon coupled to a 3D readout cavity is used as an example. The pin couplers can also be replaced by other resonator–transmission line coupling mechanisms, such as the capacitor coupling between 2D coplanar waveguides [Hatridge *et al.*, 2013; Wallraff *et al.*, 2005] and the aperture coupling between 3D waveguide sections [Narla *et al.*, 2016; Wang *et al.*, 2019]. (a) In the reflection measurement, κ_c denotes the cavity linewidth due to its coupling to the external transmission line. (b) In the transmission measurement, $\kappa_c = \kappa_c^{\text{in}} + \kappa_c^{\text{out}}$ is the total coupling linewidth of the input and output ports, and $\kappa_c^{\text{out}} \gg \kappa_c^{\text{in}}$ is to ensure the majority of readout signals can be collected by the output circuitry. In both situations, we assume that the intrinsic linewidth of the readout cavity is much smaller than its coupling linewidth and is therefore taken to be zero in the calculation. This is a reasonable approximation in reality when the cavity is made of or coated with superconducting materials.

mode can be written as

$$\dot{\hat{c}} = \frac{1}{i\hbar} [\hat{c}, \hat{H}_{\text{q-c}}] - \frac{\kappa_c}{2} \hat{c} + \sqrt{\kappa_c} \hat{c}_{\text{in}} = \frac{1}{i\hbar} [\hat{c}, \hat{H}_{\text{q-c}}] + \frac{\kappa_c}{2} \hat{c} + \sqrt{\kappa_c} \hat{c}_{\text{out}}, \quad (3.16)$$

in which \hat{c}_{in} and \hat{c}_{out} denotes the input and output mode operators of the readout cavity from its single port. Define the readout mode operator conditioned on

the qubit state as

$$\hat{c}_q = \langle q | \hat{c} | q \rangle, \quad q = 0, 1. \quad (3.17)$$

Here we disregard the energy relaxation of the qubit, so that $\hat{\sigma}_z$ is a constant of motion during the qubit–photon interaction process. Equation (3.16) can thus be rewritten as

$$\dot{\hat{c}}_q = - \left(i\omega_c^q + \frac{\kappa_c}{2} \right) \hat{c}_q + \sqrt{\kappa_c} \hat{c}_{\text{in}}, \quad (3.18)$$

in which the qubit-state-dependent cavity resonant frequencies ω_c^0 and ω_c^1 have been given by Equations (3.13) and (3.14). The formal solution of the above dynamical equation is

$$\hat{c}_q(t) = \hat{c}_q(0)e^{-\left(i\omega_c^q + \frac{\kappa_c}{2}\right)t} + \sqrt{\kappa_c} \int_0^t \hat{c}_{\text{in}}(t')e^{-\left(i\omega_c^q + \frac{\kappa_c}{2}\right)(t-t')} dt'. \quad (3.19)$$

Consider a steady-state coherent cavity drive at the symmetric readout frequency $\omega_d = \omega_{\text{RO}}$ with an average amplitude

$$\langle \hat{c}_{\text{in}}(t) \rangle = \alpha_{\text{in}} e^{-i\omega_{\text{RO}}t}. \quad (3.20)$$

In the absence of the initial cavity population

$$\langle \hat{c}_q(0) \rangle = 0, \quad (3.21)$$

the steady-state cavity amplitude conditioned on the qubit state can be com-

puted from Equation (3.19)—

$$\alpha_q(t) = \langle \hat{c}_q(t) \rangle = \frac{\sqrt{\kappa_c} \alpha_{\text{in}}}{\frac{\kappa_c}{2} - i(\omega_{\text{RO}} - \omega_c^q)} e^{-i\omega_{\text{RO}}t} = \frac{\sqrt{\kappa_c} \alpha_{\text{in}}}{\frac{\kappa_c}{2} \pm \frac{i\chi_{\text{tc}}}{2}} e^{-i\omega_{\text{RO}}t}. \quad (3.22)$$

According to the input–output relation

$$\hat{c}_{\text{in}} - \hat{c}_{\text{out}} = \sqrt{\kappa_c} \hat{c}, \quad (3.23)$$

one can write down the steady-state average amplitude of the output mode $\alpha_{\text{out}} = \langle \hat{c}_{\text{out}} \rangle$ conditioned on the qubit state—

$$\alpha_{\text{out}}^q(t) = -\frac{\kappa_c \mp i\chi_{\text{tc}}}{\kappa_c \pm i\chi_{\text{tc}}} \alpha_{\text{in}} e^{-i\omega_{\text{RO}}t}. \quad (3.24)$$

Define the *reflection* phase shift

$$\theta_r = 2 \arctan \left(\frac{\chi_{\text{tc}}}{\kappa_c} \right). \quad (3.25)$$

Equation (3.24) can then be rewritten as

$$\alpha_{\text{out}}^q(t) = -(\cos \theta_r \mp i \sin \theta_r) \alpha_{\text{in}} e^{-i\omega_{\text{RO}}t} = -\alpha_{\text{in}} e^{-i(\omega_{\text{RO}}t \pm \theta_r)}, \quad (3.26)$$

In this equation, $\pm\theta_r$ denotes the phase shift of the reflected signal from the readout cavity due to its qubit-state-dependent dispersive frequency shift, compared to the reflected signal from an imaginary cavity with resonant frequency ω_{RO} . Experimentally, the cavity reflection spectrum is measured by varying the drive frequency ω_d of the probe tone and recording the phase shift θ of the reflected signal, which will be $\pm\theta_r$ when $\omega_d = \omega_{\text{RO}}$, conditioned on the qubit being in $|0\rangle$ and $|1\rangle$, respectively.

- (b) For transmission measurements, the Heisenberg–Langevin equation of the cavity mode should include the operators of both cavity ports—

$$\dot{\hat{c}} = \frac{1}{i\hbar} [\hat{c}, \hat{H}_{q-c}] - \frac{\kappa_c}{2} \hat{c} + \sqrt{\kappa_c^{\text{in}}} \hat{c}_{\text{in}}^{\text{in}} + \sqrt{\kappa_c^{\text{out}}} \hat{c}_{\text{in}}^{\text{out}}, \quad (3.27)$$

in which $\hat{c}_{\text{in}}^{\text{in}}$ and $\hat{c}_{\text{in}}^{\text{out}}$ denote the input mode operators of the “input” and “output” ports, with coupling rates κ_c^{in} and κ_c^{out} , respectively (see Figure 3.4). Similar to Equation (3.20), one can write the average amplitude of the input mode operators as

$$\langle \hat{c}_{\text{in}}^{\text{in}}(t) \rangle = \alpha_{\text{in}} e^{-i\omega_{\text{RO}} t}, \quad (3.28)$$

$$\langle \hat{c}_{\text{in}}^{\text{out}}(t) \rangle = 0. \quad (3.29)$$

In the absence of the initial cavity population, the steady-state cavity amplitude conditioned on the qubit state is given by

$$\alpha_q(t) = \frac{\sqrt{\kappa_c^{\text{in}}} \alpha_{\text{in}}}{\frac{\kappa_c}{2} - i(\omega_{\text{RO}} - \omega_c^q)} e^{-i\omega_{\text{RO}} t} = \frac{\sqrt{\kappa_c^{\text{in}}} \alpha_{\text{in}}}{\frac{\kappa_c}{2} \pm \frac{i\chi_{tc}}{2}} e^{-i\omega_{\text{RO}} t}. \quad (3.30)$$

Then the output mode operator from the “output” port, following the relation

$$\hat{c}_{\text{in}}^{\text{out}} - \hat{c}_{\text{out}}^{\text{out}} = \sqrt{\kappa_c^{\text{out}}} \hat{c}, \quad (3.31)$$

has a steady-state average amplitude

$$\alpha_{\text{out}}^{\text{out},q}(t) = -\frac{\sqrt{\kappa_c^{\text{in}} \kappa_c^{\text{out}}} \alpha_{\text{in}}}{\frac{\kappa_c}{2} \pm \frac{i\chi_{tc}}{2}} e^{-i\omega_{\text{RO}} t}. \quad (3.32)$$

Define the *transmission* phase shift

$$\theta_t = \arctan\left(\frac{\chi_{tc}}{\kappa_c}\right). \quad (3.33)$$

Equation (3.32) can then be rewritten as

$$\begin{aligned} \alpha_{\text{out}}^{\text{out},q}(t) &= -2\sqrt{\frac{\kappa_c^{\text{in}}\kappa_c^{\text{out}}}{\kappa_c^2 + \chi_{tc}^2}}(\cos\theta_t \mp i\sin\theta_t)\alpha_{\text{in}}e^{-i\omega_{\text{RO}}t} \\ &= -\frac{2\sqrt{\kappa_c^{\text{in}}\kappa_c^{\text{out}}}}{\kappa_c}\alpha_{\text{in}}\cos\theta_t e^{-i(\omega_{\text{RO}}t \pm \theta_t)}. \end{aligned} \quad (3.34)$$

Experimentally, the phase shift of the transmitted signal is measured using the similar method to that of the reflected signal, as previously described.

The results of Equations (3.26) and (3.34) are graphically shown in Figure 3.5. Given the same χ_{tc} and κ_c , the phase shift θ_r of the readout signal in the reflection measurement is by a factor of two larger than the phase shift θ_t in the transmission measurement. Given a constant cavity input power, the optimal parameter setting for both schemes to yield the largest output-state separation is thus $\chi_{tc} = \kappa_c$, corresponding to $\theta_r = \pi$ and $\theta_t = \pi/2$.

Define the separation between the two qubit-state-dependent cavity states as

$$D = |\alpha_0 - \alpha_1|, \quad (3.35)$$

and similarly, the separation of the two cavity output states

$$D_{\text{out},r} = |\alpha_{\text{out}}^0 - \alpha_{\text{out}}^1| = \sqrt{\kappa_c}D, \quad (3.36)$$

$$D_{\text{out},t} = |\alpha_{\text{out}}^{\text{out},0} - \alpha_{\text{out}}^{\text{out},1}| = \sqrt{\kappa_c^{\text{out}}}D \quad (3.37)$$

for reflection and transmission measurements, respectively. An interesting result can

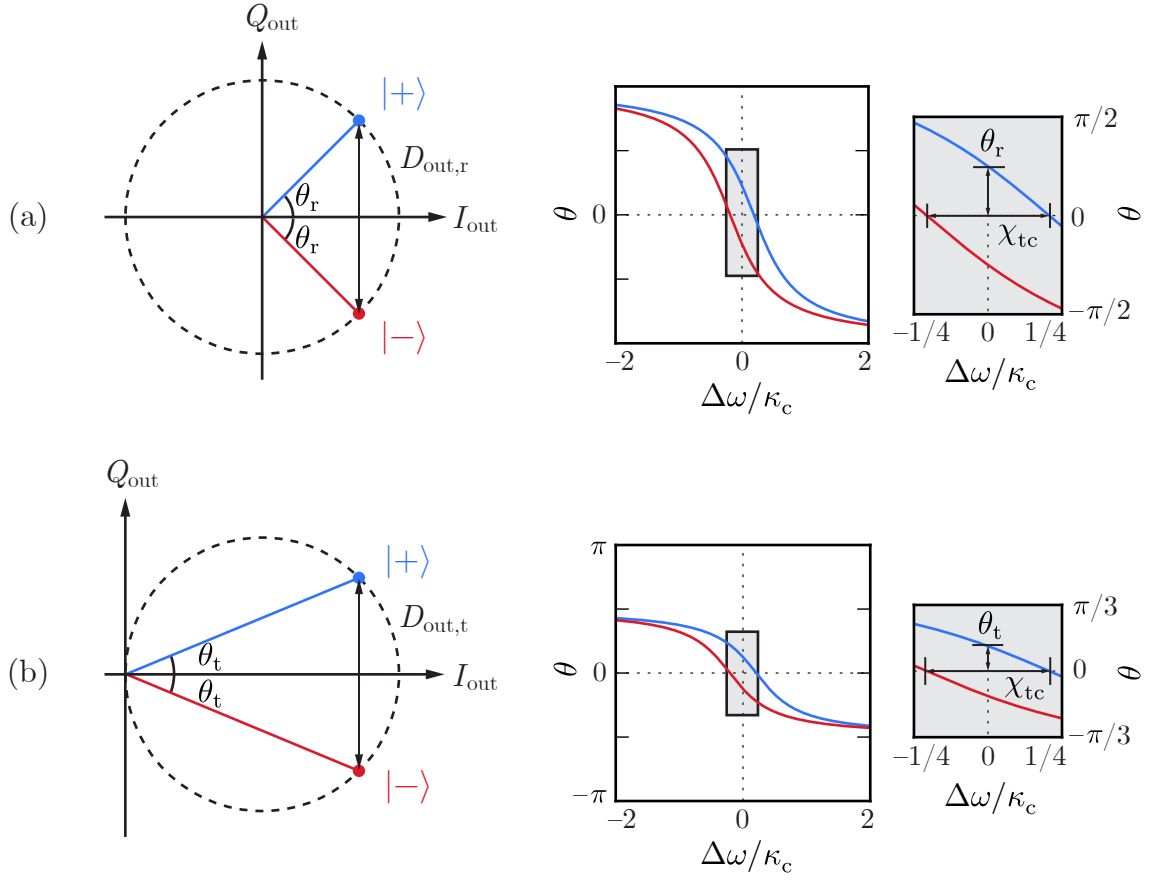


Figure 3.5: Comparison of the (a) reflection and (b) transmission measurement schemes of the readout cavity. Plotted in the left panels is the *average* cavity output field in its in-phase and quadrature (IQ) plane, defined as $\hat{I}_{out} = (\hat{c}_{out} + \hat{c}_{out}^\dagger)/2$ and $\hat{Q}_{out} = (\hat{c}_{out} - \hat{c}_{out}^\dagger)/2i$ for the reflection measurement setup, and $\hat{I}_{out} = (\hat{c}_{out}^{out} + \hat{c}_{out}^{out\dagger})/2$ and $\hat{Q}_{out} = (\hat{c}_{out}^{out} - \hat{c}_{out}^{out\dagger})/2i$ for the transmission measurement setup. Blue and red colors are linked to the meter states $|+\rangle$ and $|-\rangle$ that are associated with the cavity frequencies ω_c^0 and ω_c^1 or qubit states $|0\rangle$ and $|1\rangle$. The dashed circles stand for trajectories of the average cavity response ($\langle \hat{I}_{out} \rangle, \langle \hat{Q}_{out} \rangle$) with a constant *input* drive power and varying cavity resonant frequencies. The radii of the circles are $|\alpha_{in}|$ in (a) and $|\alpha_{in}| \sqrt{\kappa_c^{in} \kappa_c^{out}} / \kappa_c$ in (b). The separations between the output states are labeled by $D_{out,r}$ and $D_{out,t}$ as defined in Equations (3.36) and (3.37). Plotted in the right panels are the phase responses of the cavity spectra. The horizontal axes are $\Delta\omega = \omega_d - \omega_{RO}$ divided by the cavity linewidth κ_c . In both (a) and (b), the dispersive coupling strength is chosen to be $\chi_{tc} = (\sqrt{2} - 1)\kappa_c$, resulting in $\theta_r = 2\theta_t = \pi/4$.

be obtained if we write D using the *intra-cavity* photon number $\bar{n}_c = |\alpha_q|^2$. The expression is the same for *both* measurement configurations—

$$D = 2\sqrt{\bar{n}_c} \sin \theta_t. \quad (3.38)$$

This result implies that given fixed values of κ_c , χ_{tc} and \bar{n}_c , the cavity measurement will yield the same SNR given ideal coherent input states, regardless of how the measurement is arranged (either in reflection or transmission). However, as is shown in Figure 3.5, when $\chi_{tc} < \sqrt{3}\kappa_c$, a lower output power is needed in the reflection setup for it to yield the same SNR as the transmission setup. This is particularly desirable when the output amplifier chain has a limited dynamical range. Meanwhile, a higher measurement efficiency, *ceteris paribus*, should also be expected, because the amplitude response of a lossless cavity in a reflection measurement is unitary, which minimizes photon dissipations through unwanted channels. By contrast, in the transmission measurement scheme, a fraction of intra-cavity photons carrying qubit-state information are lost by way of the input port. Experimentally, whenever the transmission measurement setup is adopted, $\kappa_c^{\text{out}} \gg \kappa_c^{\text{in}}$ is chosen by default such that the majority of readout signals can be collected by the output amplifier chain, and the measurement efficiency is thus maximized (see Section 2.3.4).

3.2.3 Measurement setup of a circuit QED system

Figure 3.6 depicts a minimal circuit diagram for the reflection measurement setup of the circuit QED experiment, in which the qubit–cavity module is interrogated by microwave pulses attenuated and filtered through the input line. Directly connected to the only port readout cavity is a microwave circulator that imposes the directionality of the input and output signals. The readout pulses are subsequently amplified by a multi-stage amplifier chain, typically consisting of one quantum-limited

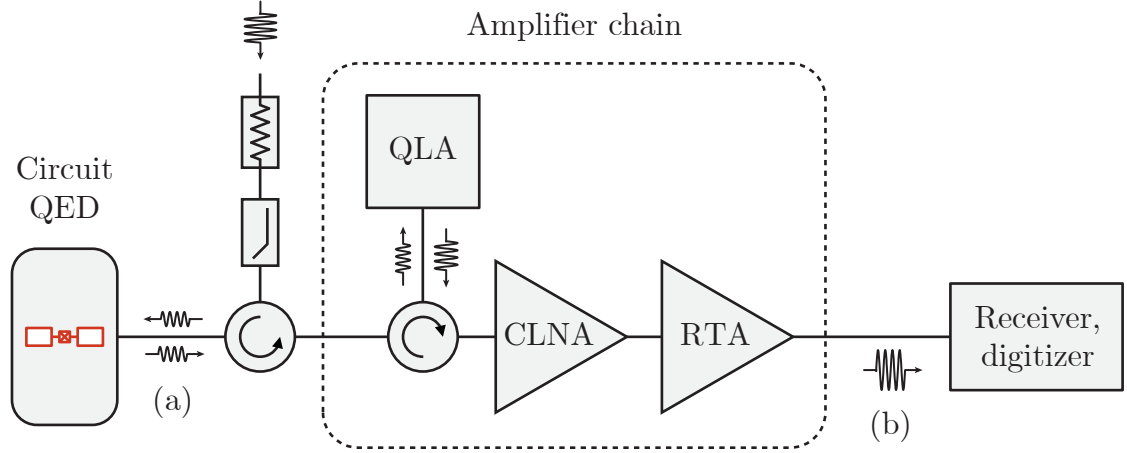


Figure 3.6: Schematic drawing of the circuit QED measurement setup in reflection. QLA: quantum-limited amplifier. CLNA: cryogenic low-noise amplifier, typically realized with high-electron-mobility transistors (HEMT). RTA: room-temperature amplifiers. The IQ-plane representations of the readout signals at (a) the output of the readout cavity and (b) the output of the amplifier chain are shown in Figure 3.7.

Josephson parametric amplifier (QLA), one semiconductor cryogenic low-noise amplifier (CLNA), and one or more room-temperature semiconductor amplifiers (RTA), until the output readout signals can be unambiguously distinguished and recorded by classical electronic devices. Due to the added noise of the amplifier chain, the SNR of the output quadrature signals is reduced by a factor of $\sqrt{\eta_m}$ compared to the ideal SNR, with η_m again denoting the measurement efficiency. The relation is illustrated in Figure 3.7.

Define the in-phase (I) and quadrature (Q) components of the *intra-cavity* field as

$$\hat{I} = \frac{1}{2} (\hat{c}^\dagger + \hat{c}), \quad (3.39)$$

$$\hat{Q} = \frac{i}{2} (\hat{c}^\dagger - \hat{c}). \quad (3.40)$$

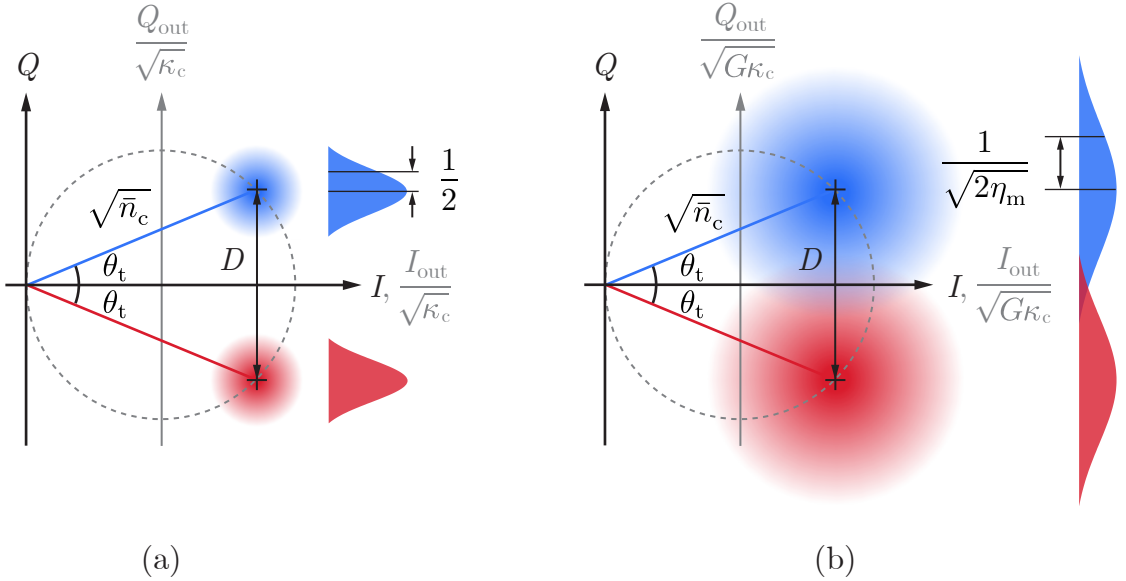


Figure 3.7: IQ-plane representations of readout signals in a reflection measurement setup at the (a) input and (b) output of a phase-preserving amplifier chain with a total gain G and a measurement efficiency η_m . The measurement (data acquisition) time is chosen to be $T_m = 1/\kappa_c$ such that the SNR of the output field is equal to that of the intra-cavity field. The coordinates $(I_{\text{out}}, Q_{\text{out}})$ are rescaled differently in (a) and (b) such that the distance between the output states—as defined in Equation (3.36)—matches that of the intra-cavity states—as defined in Equation (3.35)—represented using the coordinates (I, Q) . For an arbitrary measurement time T_m , the quadrature uncertainties of the output field would be reduced by a factor of $\sqrt{\kappa_c T_m}$ due to statistical averaging. In this situation, $\bar{n}_m = \bar{n}_c \kappa_c T_m$ is often used to denote the total number of photons that have interrogated the qubit during the measurement process. Note that according to Equation (3.38), the azimuthal angles of the frequency-shifted cavity states in the intra-cavity (I, Q) coordinates is $\pm\theta_t = \pm\arctan(\chi_{tc}/\kappa_c)$ instead of $\pm\theta_r = \pm 2\arctan(\chi_{tc}/\kappa_c)$ as in the $(I_{\text{out}}, Q_{\text{out}})$ coordinates. For transmission measurements, the origins of the (I, Q) and $(I_{\text{out}}, Q_{\text{out}})$ coordinates overlap, and the azimuthal angles would be $\pm\theta_t$ for both the intra-cavity and the output fields. For a phase-sensitive amplifier chain with the same measurement efficiency, the signal quadrature (Q) uncertainty of the post-measurement field (b) would be reduced by a factor of $\sqrt{2}$. The difference comes from the vacuum fluctuations of the idler mode in the phase-preserving amplification scheme, which is absent in phase-sensitive amplifiers (see Section 1.3.4).

By this definition, a coherent state with average photon number \bar{n}_c is represented in the IQ plane—as shown in Figure 3.7(a)—by a 2D symmetric Gaussian distribution with a central distance $\sqrt{\bar{n}_c}$ from the origin and standard deviations $1/2$ along both axes, indicating the statistical outcomes of field component measurements performed by an imaginary device inside the cavity.⁶ If the amplifier chain provides a power gain $G \gg 1$ along the signal axis, the standard deviation of the amplified output field after a measurement (data acquisition) time T_m will be $\sqrt{G/4\eta_m T_m}$ for phase-sensitive amplification, and $\sqrt{G/2\eta_m T_m}$ for phase-preserving amplification.⁷ The latter case is shown in Figure 3.7(b).

In practice, given the amplifiers are able to provide sufficient gains, η_m is mainly limited by the added noise of the quantum-limited amplifier as well as the residual dissipations between the readout cavity and the amplifier chain.⁸ We will return to this issue and examine the physical causes of the measurement inefficiencies after presenting the detailed experimental setup in Sections 4.3.2 and 6.1.

Finally, it is worth remarking that if the cavity state is confined to its zero-or-one-photon subspace, \hat{H}_{disp} is reduced to \hat{H}_{int} in the qubit–ancillae model of weak

⁶Note that this IQ representation of a coherent cavity state is different from the phase-space representations of the quantum state of a harmonic oscillator, such as the Glauber–Sudarshan P , Husimi Q , or the Wigner W functions [Haroche and Raimond, 2006; Scully and Zubairy, 1997; Walls and Milburn, 2008].

⁷The input and output operators \hat{c}_{in} , \hat{c}_{out} in the input–output formulation have the dimension of $[\text{T}]^{-1/2}$ (T for time as in the SI standard).

⁸For an N -stage amplifier chain with gains G_1, G_2, \dots, G_N and added noise in photon numbers n_1, n_2, \dots, n_N , the total added noise referred to the input of the first amplifier is

$$n_{\text{add}} = n_1 + \sum_{k=2}^N \frac{n_k}{\prod_{j=1}^{k-1} G_j} \gtrsim n_1, \quad \text{if } G_1, G_2, \dots, G_N \gg 1. \quad (3.41)$$

The derivation of this relation can be found in Pozar [2012], where the added noise of an amplifier is expressed using its noise temperature, which is proportional to the photon number in the classical regime.

Experiment [year]	$\kappa_c/2\pi$ [MHz]	$\chi_{tc}/2\pi$ [MHz]	T_1 [μ s]	$T_{2R(H)}$ [μ s]	Amplifier	\mathcal{F}_{tot} [0–1]	$\mathcal{Q}'_{\text{tot}}$ [0–1]	T_m [ms]	η_m [0–1]
Vijay <i>et al.</i> [2011]	4.9	4.3	0.32	0.29	JPA	PS	—	200	0.19
Johnson <i>et al.</i> [2012]	9	−7.4	1.8	0.055	JPA	PS	—	10	—
Ristè <i>et al.</i> [2012]	0.43	3.7, 2.6	23, 27	0.45, 4.2	JPA	PS	0.94 [†]	300	—
Lin <i>et al.</i> [2013]	16	80	0.6	—	JPA	PS	—	100	0.35
Hatridge <i>et al.</i> [2013]	5.8	5.4	2.8	0.7–2.0	JPC	PP	—	240	0.2–0.4
Liu <i>et al.</i> [2014]	10	3	2.8	2	SLUG	PP	0.947	(200)	0.27
Jeffrey <i>et al.</i> [2014]	4.3	—	10–12	—	JPA	PP	—	(150)	0.25
Magesan <i>et al.</i> [2015]	1.21	2.8	29	(22)	JPA	—	—	1200	—
							0.9642	2600	—
Macklin <i>et al.</i> [2015]	8.7	4.4	—	—	JTWPA	PP	—	100	0.49
Bultink <i>et al.</i> [2016]	0.64	2.6	25	(39)	JPA	PP	—	400	—
Walter <i>et al.</i> [2017]	37.5	7.9	7.6	2 (6)	JPD	PS	—	48	0.66
							0.992	88	0.75
Heinsoo <i>et al.</i> [2018]	3.1–14.3	1.7–2.4	4.9–6.0	0.7–7.8	JTWPA	PP	0.872–0.976	220	0.43–0.52
Andersen <i>et al.</i> [2019]	1.7–3.0	1.6–3.9	13.7–23.4	11.2–12.5	JTWPA	PP	0.974–0.984	400	0.24
Andersen <i>et al.</i> [2020b]	6.0–17.3	0.75–2.5	5.7–16.8	4.3–21.5	JTWPA	PP	0.956–0.988	300–400	0.15–0.30
Rosenthal <i>et al.</i> [2021]	0.44	1.93	9	15	SIMBA	PS	0.955	100	0.70

* Reported in Slichter [2011]. A higher readout fidelity $\mathcal{F}_{\text{tot}} = 0.81$ was achieved on a different transmon with $T_1 = 0.91 \mu\text{s}$.

[†] Both \mathcal{F}_{tot} and $\mathcal{Q}'_{\text{tot}}$ were limited by the qubit-state transition during the waiting time $T_w = 2.4 \mu\text{s}$ between the successive measurement pulse. In the limit of $T_w = 0$, the authors inferred $\mathcal{Q}'_{\text{tot}} \approx \mathcal{F}_{\text{tot}} = 0.981$ through extrapolation, implying close-to-ideal correlation between readout outcomes and post-measurement qubit states in the model of Figure 2.4(b).

[‡] Intrinsic readout fidelity or qubit-state discriminability computed from a quadrature SNR = 2.4. Data not reported are noted by —.

Table 3.2: Selected experiments that demonstrated and characterized high-fidelity single-shot qubit readout with circuit QED systems in the linear dispersive regime, $\hat{H}_{\text{disp}} = -\hbar\chi_{\text{tc}}\hat{t}^\dagger\hat{t}\hat{c}^\dagger\hat{c}$. The values of the reported figures of merit have been converted according to the conventions of the present article. $T_{2\text{R}}$: Ramsey dephasing time. $T_{2\text{H}}$: Hahn echo dephasing time. Quantum-limited amplifiers (QLA), operated in either the phase-preserving (PP) or the phase-sensitive (PS) mode, are referred to by their acronyms—JPA: Josephson parametric amplifier [Castellanos-Beltran *et al.*, 2008; Hatridge *et al.*, 2011; Yamamoto *et al.*, 2008; Yurke *et al.*, 1989, 1988]. JPC: Josephson parametric converter [Bergeal *et al.*, 2010a,b; Roch *et al.*, 2012]. SLUG: Superconducting low-inductance undulatory galvanometer [Hover *et al.*, 2012; Ribeill *et al.*, 2011]. JTWPA: Josephson traveling-wave parametric amplifier [Macklin *et al.*, 2015; O’Brien *et al.*, 2014]. JPD: Josephson parametric dimer Eichler *et al.* [2014]. SIMBA: Superconducting isolating modular bifurcation amplifier Rosenthal *et al.* [2021]. The apparent total QND fidelity $\mathcal{Q}'_{\text{tot}}$ —defined in Equation (2.28)—is reported in these experiments instead of \mathcal{Q}_{tot} . Listed under T_{m} are by default the durations of the data integration window. If the integration time is not reported, the lengths of the microwave measurement pulse are enclosed in parentheses. Efforts on reducing T_{m} include shaping the readout pulse to actively populate and/or deplete the readout resonator faster than its time constant of free decay [Bultink *et al.*, 2016, 2018; Jeffrey *et al.*, 2014; Liu *et al.*, 2014; McClure *et al.*, 2016].

measurements—Equation (2.31). In Section 2.4, the chain of ancillae were initialized in $|+x\rangle$ and projectively measured onto the $|\pm y\rangle$ basis after their finite-strength interaction with the qubit. Analogously, in the dispersive qubit readout protocol, the cavity should be initialized in the coherent state centered at $(\sqrt{n_c}, 0)$ in the IQ plane (see Section 1.3.4), and subsequently measured along the Q axis after the qubit–photon interaction (see Figures 3.5 and 3.6). In this way, the parallelism between the two-level pedagogical model and the circuit QED dispersive readout scheme can be clearly visualized.

Table 3.2 summarizes key parameters and performance metrics of selected single-

shot qubit readout experiments employing qubit–cavity interactions in the linear dispersive regime. Attempts to achieve improvements beyond the state-of-the-art values of \mathcal{F}_{tot} , \mathcal{Q}_{tot} , T_{m} , and η_{m} are motivating researchers to explore variations of qubit–cavity couplings beyond the simple linear form (see Section 3.4).

3.3 Measurement-induced qubit dephasing

As has been shown in the previous section, the microwave readout of superconducting qubits is based on cross-Kerr dispersive coupling between the cavity and the qubit in the circuit QED system. The same coupling Hamiltonian \hat{H}_{disp} , which is responsible for the qubit-state-dependent shift of the cavity resonant frequency, can in the meantime cause a cavity-state-dependent shift of the qubit transition frequency,

$$\frac{\hat{H}_{\text{q}}}{\hbar} + \frac{\hat{H}_{\text{disp}}}{\hbar} = (\omega_{\text{t}}^{01} - \chi_{\text{tc}} \hat{c}^\dagger \hat{c}) \frac{\hat{\sigma}_z + 1}{2}, \quad (3.42)$$

in which $\hat{H}_{\text{q}} = \hbar\omega_{\text{t}}^{01}\hat{\sigma}_z/2$ denotes the two-level Hamiltonian of the transmon qubit. Therefore, fluctuations of the cavity photon number operator $\hat{c}^\dagger\hat{c}$ lead to the fluctuations of the qubit 0–1 frequency, resulting in a channel of cavity-photon-induced qubit dephasing [Bertet *et al.*, 2005a,b; Clerk and Utami, 2007; Gambetta *et al.*, 2008, 2006; Schuster *et al.*, 2005]. In this section, I will present an analytical theory of the measurement-induced-qubit dephasing effect based on the input–output formalism of the coupled cavity–qubit system. A more complete version of this theory in the context of quantum microwave radiometry has been published in the Supplemental Material of Wang *et al.* [2021].

We start from Equation (3.16)—the Heisenberg–Langevin equation of the cavity mode in the reflection measurement setup, whose formal solution is given by Equation (3.19). The convention of notations is the same as that in Section 3.2.2.

- (i) If the readout cavity is subject to coherent-state drives, the total cavity-induced qubit dephasing effect—namely, the off-diagonal element of the qubit density matrix after the cavity reaches a steady state—is given by $e^{-\int \Gamma_\phi^{\text{coh}}(t) dt}$, in which the dephasing rate is given by

$$\Gamma_\phi^{\text{coh}} = \frac{\kappa_c}{2} |\alpha_0 - \alpha_1|^2, \quad (3.43)$$

in which $\alpha_0 = \langle \hat{c}_0 \rangle$ and $\alpha_1 = \langle \hat{c}_1 \rangle$ are the steady-state complex coherent-state amplitudes of the readout cavity given the qubit being in $|0\rangle$ and $|1\rangle$, respectively [Bultink *et al.*, 2018; Gambetta *et al.*, 2008, 2006; Silveri *et al.*, 2016]. Considering the special case of a symmetric readout drive at the frequency $\omega_{\text{RO}} = (\omega_c^0 + \omega_c^1)/2$, one can find

$$\alpha_0(t) = \frac{\sqrt{\kappa_c} \alpha_{\text{in}}}{\frac{\kappa_c}{2} + i \frac{\chi_{\text{tc}}}{2}} e^{-i\omega_{\text{RO}} t}, \quad (3.44)$$

$$\alpha_1(t) = \frac{\sqrt{\kappa_c} \alpha_{\text{in}}}{\frac{\kappa_c}{2} - i \frac{\chi_{\text{tc}}}{2}} e^{-i\omega_{\text{RO}} t}, \quad (3.45)$$

and

$$\Gamma_\phi^{\text{coh}} = \frac{1}{2} \left(\frac{4\kappa_c \chi_{\text{tc}} |\alpha_{\text{in}}|}{\kappa_c^2 + \chi_{\text{tc}}^2} \right)^2. \quad (3.46)$$

If one denotes the average cavity photon number using

$$\bar{n}_c = |\alpha_0|^2 = |\alpha_1|^2 = \frac{4\kappa_c |\alpha_{\text{in}}|^2}{\kappa_c^2 + \chi_{\text{tc}}^2}, \quad (3.47)$$

Equation (3.46) can be rewritten as

$$\Gamma_\phi^{\text{coh}} = \frac{2\bar{n}_c \kappa_c \chi_{\text{tc}}^2}{\kappa_c^2 + \chi_{\text{tc}}^2}. \quad (3.48)$$

Therefore, the coherent-photon-induced qubit dephasing rate is proportional to the average intra-cavity photon population \bar{n}_c .

Equation (3.43) is an important identity as it links the qubit dephasing rate and the SNR of an ideal circuit QED measurement setup. For instance, for a practical phase-preserving amplifier chain with a total measurement efficiency η_m , the SNR of the steady-state output signal after a measurement time window T_m is

$$\text{SNR} = \sqrt{2\eta_m \bar{n}_c \kappa_c T_m} \sin \theta_t. \quad (3.49)$$

Define the **measurement rate** as

$$\Gamma_{\text{meas}} = \frac{\text{SNR}^2}{T_m} \quad (3.50)$$

The measurement efficiency can be expressed as the ratio of the measurement rate and the dephasing rate—

$$\eta_m = \frac{\Gamma_{\text{meas}}}{\Gamma_{\phi}^{\text{coh}}}. \quad (3.51)$$

Experimentally, with κ_c and χ_{tc} measured using spectroscopy methods, Equation (3.48) can be used to calibrate the intra-cavity photon number \bar{n}_c of a circuit QED system, and Equation (3.51) to extract its measurement efficiency [Bultink *et al.*, 2018].⁹ With an overall reduction factor $\kappa_c^{\text{out}}/\kappa_c$ in η_m , the same

⁹Here the SNR is defined as the average amplitude of the output quadrature signal divided by its standard deviation. If the “signal” is defined as the separation between the two meter states, then a factor of two should be added on the right hand side of Equation (3.49) and a factor of 1/4 on the right hand side of Equation (3.50). For a phase-sensitive amplifier chain, the expression of SNR should be multiplied by a factor of $\sqrt{2}$ and hence the right hand side of Equation (3.51) should be divided by two [Eddins *et al.*, 2019].

relation applies to transmission measurements as well.

- (ii) If the readout cavity is subject to steady-state, broadband (white) thermal drives,

$$\langle \hat{c}_{\text{in}}^\dagger(t) \hat{c}_{\text{in}}(t') \rangle = \bar{n}_{\text{th}} \delta(t - t'), \quad (3.52)$$

in which $\delta(t)$ is the Dirac delta function in the time domain. The above correlation function indicates that broadband thermal noise has a zero correlation time and a white power spectral density. The steady-state cavity population—calculated using Equation (3.19)—is then

$$\langle \hat{c}_q^\dagger \hat{c}_q \rangle = \lim_{t \rightarrow \infty} \kappa_c \iint_0^t \langle \hat{c}_{\text{in}}^\dagger(t') \hat{c}_{\text{in}}(t'') \rangle e^{(i\omega_c^q - \frac{\kappa_c}{2})(t-t')} e^{-(i\omega_c^q + \frac{\kappa_c}{2})(t-t'')} dt' dt'' = \bar{n}_{\text{th}}. \quad (3.53)$$

A thermal drive can be considered as an incoherent mixture of coherent drives. Accordingly, the dephasing effect can be computed by averaging over all possible realizations of qubit dephasing induced by input coherent states, which can be simplified through the cumulant expansion of averages,

$$\left\langle e^{-\int \Gamma_\phi^{\text{coh}}(t) dt} \right\rangle = \exp \left[-\int \langle \Gamma_\phi^{\text{coh}}(t) \rangle dt + \frac{1}{2} \iint \langle \Gamma_\phi^{\text{coh}}(t) \Gamma_\phi^{\text{coh}}(t') \rangle dt dt' + \dots \right]. \quad (3.54)$$

Higher-order cumulants can be neglected in the limit of small input thermal photon numbers, namely, $\bar{n}_{\text{th}} \ll 1$. Under this approximation, the thermal-noise-induced qubit dephasing rate is given by

$$\Gamma_\phi^{\text{th}} = \langle \Gamma_\phi^{\text{coh}} \rangle = \frac{\kappa_c}{2} \langle |\alpha_0 - \alpha_1|^2 \rangle. \quad (3.55)$$

Define the distance of the two qubit-state-dependent cavity states—

$$\hat{D} = \hat{c}_0 - \hat{c}_1, \quad (3.56)$$

which is the quantized version of Equation (3.35). We can then rewrite Equation (3.55) as

$$\Gamma_\phi^{\text{th}} = \frac{\kappa_c}{2} \langle \hat{D}^\dagger \hat{D} \rangle = \frac{\kappa_c}{2} \langle \hat{c}_0^\dagger \hat{c}_0 + \hat{c}_1^\dagger \hat{c}_1 - \hat{c}_0^\dagger \hat{c}_1 - \hat{c}_1^\dagger \hat{c}_0 \rangle. \quad (3.57)$$

Since

$$\begin{aligned} \langle \hat{c}_0^\dagger \hat{c}_1 \rangle &= \lim_{t \rightarrow \infty} \kappa_c \iint_0^t \langle \hat{c}_{\text{in}}^\dagger(t') \hat{c}_{\text{in}}(t'') \rangle e^{(i\omega_c^0 - \frac{\kappa_c}{2})(t-t')} e^{-(i\omega_c^1 + \frac{\kappa_c}{2})(t-t'')} dt' dt'' \\ &= \bar{n}_{\text{th}} \kappa_c \lim_{t \rightarrow \infty} \int_0^t e^{(i\chi_{\text{tc}} - \kappa_c)(t-t')} dt' = \frac{\bar{n}_{\text{th}} \kappa_c}{\kappa_c - i\chi_{\text{tc}}} = \langle \hat{c}_1^\dagger \hat{c}_0 \rangle^*, \end{aligned} \quad (3.58)$$

one can obtain

$$\Gamma_\phi^{\text{th}} = \frac{\bar{n}_{\text{th}} \kappa_c \chi_{\text{tc}}^2}{\kappa_c^2 + \chi_{\text{tc}}^2}. \quad (3.59)$$

A general solution of the thermal-photon-induced qubit dephasing rate beyond the small-thermal-photon-number limit ($\bar{n}_{\text{th}} \ll 1$) has been calculated by Clerk and Utami [2007]:

$$\Gamma_\phi^{\text{th}} = \frac{\kappa_c}{2} \text{Re} \left[\sqrt{\left(1 + \frac{i\chi_{\text{tc}}}{\kappa_c}\right)^2 + \frac{4i\chi_{\text{tc}}\bar{n}_{\text{th}}}{\kappa_c}} - 1 \right]. \quad (3.60)$$

Equations (3.59) and (3.60) have important implications on the upper bound of the qubit dephasing time T_ϕ in the absence of external drives. Assuming

κ_c and χ_{tc} have comparable values¹⁰ and are both on the order of megahertz, one average thermal photon can give raise to a dephasing rate on the order of 10^{-6} s^{-1} . In practical experimental systems, a residual thermal population $\bar{n}_{\text{th}} \sim 10^{-2}$ – 10^{-3} then limits T_ϕ under 10 – $100 \text{ } \mu\text{s} \lesssim T_1$. According to the relation [Abragam, 1961]

$$\frac{1}{T_2} = \frac{1}{2T_1} + \frac{1}{T_\phi}, \quad (3.61)$$

the decoherence time T_2 is thus much shorter than its upper limit $2T_1$. I will demonstrate in Chapter 5 that this limit is attainable by coupling the readout cavity to cold electromagnetic dissipations that can effectively suppress \bar{n}_{th} to the level of 10^{-4} .

A couple of remarks before we conclude this section: First, Equations (3.48) and (3.59) have the similar form, but a steady-state coherent cavity field leads to a factor-of-two higher qubit dephasing rate than a steady-state thermal cavity field with the same average photon number. That is to say, photon statistics plays a role in determining the cavity-photon-induced qubit dephasing rate.¹¹ Second, the above derivations of the exponential decay model of qubit dephasing over time is only valid

¹⁰For the maximization of the readout SNR given a fixed power of the input coherent drive. See Figure 3.5.

¹¹A similar factor-of-two difference can be found in the correlation times of the coherent and thermal drives as filtered by the cavity. This is shown by the correlation functions of the fluctuating cavity photon number, which is

$$\langle \delta \bar{n}(t) \delta \bar{n}(t') \rangle_{\text{coh}} = \bar{n}_c e^{-\frac{\kappa_c}{2} |t-t'|}$$

for an on-resonance coherent cavity drive, and

$$\langle \delta \bar{n}(t) \delta \bar{n}(t') \rangle_{\text{th}} = \bar{n}_{\text{th}} (\bar{n}_{\text{th}} + 1) e^{-\kappa_c |t-t'|}$$

for a broadband thermal drive.

on a time scale longer than $1/\kappa_c$; in the opposite limit, a Gaussian decay model dominates [Gambetta *et al.*, 2006; Schuster *et al.*, 2005], and a qubit dephasing time is thus not well defined. This is also shown by the two-level measurement model in Section 2.4 that the reduction of the transverse component of the Bloch vector after an unrecorded measurement event is proportional to $e^{-(\Delta t)^2}$ instead of $e^{-\Delta t}$, with the dimensionless incremental interaction strength $\epsilon = \chi\Delta t \ll 1$.

3.4 Measurement-induced qubit-state transition

While presenting the theory of measurement-induced qubit dephasing in the previous section, we have assumed that the qubit state is not altered during its interaction with cavity photons, which is equivalent to an ideal QND fidelity as defined in Section 2.3.2. This is a reasonable approximation when the two-level dispersive coupling Hamiltonian \hat{H}_{disp} as given by Equation (3.8) is considered, which implies the commutation relation

$$[\hat{\sigma}_z, \hat{H}_{\text{disp}}] = 0. \quad (3.62)$$

Therefore, the dispersive qubit–cavity coupling under the RWA provides a QND measurement channel that allows repetitive qubit readouts in pursuit of higher measurement precision. Nevertheless, \hat{H}_{disp} is the result of perturbative transformations from the linear transmon–cavity coupling in Equation (3.1),

$$\frac{\hat{H}_{\text{lin}}}{\hbar} = g_{\text{tc}}(\hat{t}^\dagger + \hat{t})(\hat{c}^\dagger + \hat{c}). \quad (3.63)$$

The dropping of higher-order terms in the perturbative approximations is responsible for qubit-state-transition events during the qubit–photon interaction processes. In reality, it has been predicted and observed that additional qubit relaxations and

excitations, including transitions out of the two-level subspace, can be induced by microwave photons in the readout resonator [Boissonneault *et al.*, 2008, 2009; Lescanne *et al.*, 2019; Picot *et al.*, 2008; Sank *et al.*, 2016; Slichter *et al.*, 2012; Verney *et al.*, 2019]. Experimentally, this is typically reflected as the decrease of qubit T_1 in the presence of a high number of intra-cavity photons \bar{n}_c . These findings have encouraged the usage of a moderate level of microwave drive power—more specifically, an intra-cavity photon number on the order of 10^0 to 10^1 —in the qubit readout, which again boosts the demand for a higher measurement efficiency to maintain a sufficient SNR.

Unlike the photon-induced qubit dephasing effect, which can be explained using the linear model of qubit–cavity coupling, the photon-induced qubit relaxation is essentially a nonlinear phenomenon originating from higher-order Hamiltonian terms neglected in the RWA. These parasitic effects can in principle be suppressed by engineering new forms of qubit–photon couplings that are intrinsically compatible with QND measurements, without further perturbative approximations.

- (i) For instance, ideas have been proposed to replace the *transverse* field–field coupling in Equation (3.63) with a *longitudinal* coupling of the form

$$\frac{\hat{H}_{\text{long}}}{\hbar} = g_{\text{long}} \hat{t}^\dagger \hat{t} (\hat{c}^\dagger + \hat{c}), \quad (3.64)$$

which directly commutes with $\hat{\sigma}_z$ after the two-level truncation [Billangeon *et al.*, 2015; Didier *et al.*, 2015; Kerman, 2013]. Such a longitudinal interaction Hamiltonian has been experimentally realized by adding a parametric qubit drive at the cavity frequency to a linearly coupled circuit QED system in the weak dispersive regime [Touzard *et al.*, 2019].

Experiment [year]	$\kappa_c/2\pi$ [MHz]	$g/2\pi$ [MHz]	$\chi_{tc}/2\pi$ [MHz]	T_1 [μ s]	$T_{2R(H)}$ [μ s]	Amplifier	\mathcal{F}_{tot} [0–1]	$\mathcal{Q}'_{\text{tot}}$ [0–1]	T_m [ns]	η_m [0–1]	\bar{n}_c
Touzard <i>et al.</i> [2019]	1.6	1.28	0.1	90–190	(30–170)	SPA PS	0.989	0.984	(870)	0.6	2.6
Dassonneville <i>et al.</i> [2020]	12.7	9	0.18	3.3	3.2	JPA PS	0.974	0.99	(50)	> 0.6	2

Table 3.3: Comparison of the experimental parameters and results of two circuit QED measurement systems using transmon–cavity couplings of the longitudinal and cross-Kerr forms. The coupling coefficient g stands for g_{long} in Equation (3.64) for the longitudinal-coupling system Touzard *et al.* [2019] and g_{CK} in Equation (3.65) for the cross-Kerr-coupling system [Dassonneville *et al.*, 2020]. Note that in the second experiment, g_{CK} denotes the cross-Kerr coupling strength between the transmon qubit and the hybridized ancilla–cavity polariton readout mode, instead of that between the qubit and the on-chip ancilla, which is denoted by g_z by the authors. The *residual* dispersive coupling between the transmon and the cavity is listed under χ_{tc} . In both experiments, the values of T_m in parentheses are the durations of microwave measurement pulses. The measurement efficiency of the second experiment was reported in Dassonneville [2019] as a less-than 2 dB calibrated signal attenuation on the output line between the JPA and the HEMT amplifier. The intra-cavity measurement photon number is denoted by \bar{n}_c . The rest of the notations are consistent with those in Table 3.2.

(ii) Alternatively, the QND qubit–cavity coupling of the cross-Kerr form

$$\frac{\hat{H}_{\text{CK}}}{\hbar} = g_{\text{CK}}(\hat{t}^\dagger + \hat{t})^2(\hat{c}^\dagger + \hat{c})^2 \quad (3.65)$$

has also been proposed [Diniz *et al.*, 2013] and demonstrated [Dassonneville, 2019; Dassonneville *et al.*, 2020] using a readout cavity coupled to a superconducting artificial molecule in which the linear coupling between the qubit and cavity modes is avoided.

The key parameters and results of the two experiments are summarized in Table 3.3. In Chapter 6, I will further elaborate on the design method (ii) and present our experimental work on the Π -mon artificial molecule, which is aimed at achieving high-power dispersive qubit measurements in the 3D circuit QED architecture with a near-ideal QND fidelity.

The discussions on the qubit dephasing and relaxation effects induced by photons in the readout cavity conclude the theoretical preparation part of this dissertation. We have encountered two parasitic issues in the circuit QED measurement setup that are to be addressed with novel quantum circuit designs:

1. The residual thermal photon population in the readout cavity limiting the qubit dephasing time;
2. The increase of qubit-state transition events induced by cavity photon at strong measurement powers.

After a short Chapter 4 summarizing the key experimental techniques, I will devote Chapters 5 and 6 to the two problems respectively by introducing the resonant cavity attenuator and the Π -mon artificial molecule. These original works are the preliminary steps toward the simultaneous realization of high-coherence superconduct-

ing qubits and their high-performance quantum-limited readout, for tackling more demanding quantum information processing tasks and fundamental investigations in quantum dynamics and measurements.

Chapter 4

Experimental Methods of Quantum Microwave Circuits

An experimentalist wishing to pursue research at millikelvin temperatures faces four technical difficulties: how to reach the low temperature, how to measure it, how to reduce the external heat leak so that the low temperature can be maintained for a sufficiently long time, and how to transfer cold from one place to another.

Olli Viktor Lounasmaa [1974]

Thus each ‘resonant’ experiment involves two steps: (a) induce, or ‘drive’ the resonance, (b) detect its occurrence. The problem of detection, by far the more difficult of the two, has been solved in a large (and still growing) number of ways, each best adapted to the special features of the system studied.

Anatole Abragam [1961]

In the first three chapters, using a variety of mathematical and physical models, we have presented the central questions of the current dissertation research. After introducing the motivations and tools of superconducting quantum circuit engineering, as well as the rudimentary theories of projective and quasi-continuous quantum measurements, we reviewed the standard schemes of qubit-state readouts in the circuit QED architecture, and highlighted the cavity-photon-induced qubit dephasing

and relaxation effects, which have to be alleviated in more ideal artificial quantum systems. In this chapter, I will redirect our discussions into the physics laboratory and overview the techniques of preparations and low-temperature microwave measurements of superconducting electrical circuits involved in our original experiments.

The experimental methods of circuit QED are naturally divided into five parts—

- (i) The design, fabrication, and room-temperature selection of superconducting Josephson circuits on dielectric substrates;
- (ii) The design and machining of microwave readout cavities coupled to superconducting Josephson circuits and external microwave transmission lines;
- (iii) The electromagnetic wiring and thermal installation of the low-temperature microwave measurement setup in a dilution refrigerator;
- (iv) The arrangement and tuning of electronic equipment and the preparation of the ambient electromagnetic environment at the room temperature;
- (v) The control software for the room-temperature electronics as well as the data acquisition and processing system.

I will cover one part in each following section. Special designs beyond the standard circuit QED toolkit appearing in our original experiments will be introduced in Chapters 5 and 6 separately.

4.1 Josephson circuits: design, fabrication, and test

As has been illustrated in Section 1.3.3, the transmon design compatible with 3D circuit QED systems features a minimal complexity. The drawing in Figure highlights the three key geometric parameters of the external coplanar capacitor: the width and the length of the electrode pads, and their separation. While the capacitance

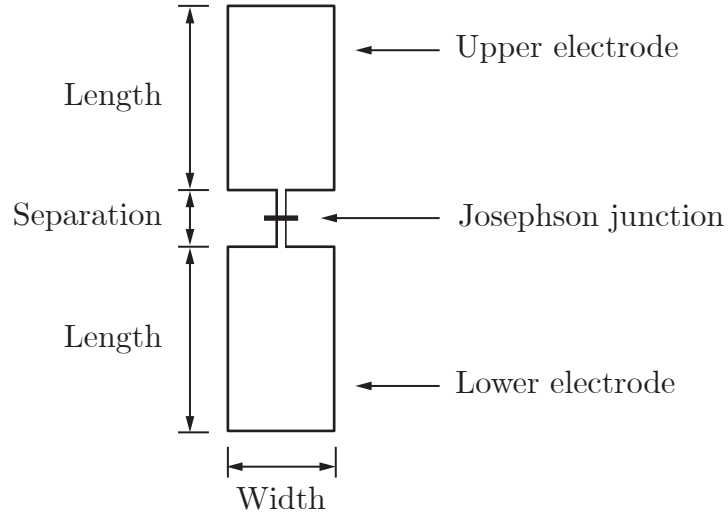


Figure 4.1: Drawing of a transmon artificial atom for 3D circuit QED systems. The geometric scale of the SIS tunnel junction area (sub-micrometer) is much smaller than that of the coplanar capacitor electrodes (typically, hundred-micrometer). In the circuit simulation, the Josephson junction can thus be modeled as a nonlinear lumped-element inductor.

between the two symmetric electrodes is proportional to their width, the electric dipole coupling between the transmon and the readout cavity is mainly determined by the length and the separation—along the direction parallel to the cavity electric field. The Josephson junction is centered in the link between the two electrode pads, whose geometric scale is small enough such that the junction can be treated as a lumped-element device.

Thin-film aluminum ($T_c \approx 1.3$ K under zero external magnetic field) is the most common superconducting material that standard Josephson junctions are made of. The thin insulator layer in the SIS sandwich structure can then be grown through the oxidation of aluminum. Superconductors with higher critical temperatures and magnetic fields, such as niobium nitride (NbN) [Niepce *et al.*, 2019], niobium titanium nitride (NbTiN) [Samkharadze *et al.*, 2016], titanium nitride (TiN) [Shearrow *et al.*,

2018], granular aluminum (grAl) [Winkel *et al.*, 2020], and tantalum (Ta) [Place *et al.*, 2021] also find their applications in transmon circuits, for improved qubit coherence properties or high-field experiments with hybrid quantum systems.

The preparation of superconducting circuit chips is compatible with the micro-fabrication techniques originally developed in the modern semiconductor industry [Campbell, 2001]. The experiments reported in the following two chapters were performed with aluminum-based transmon qubits fabricated using the standard bridge-free, double-angle evaporation protocol [Lecocq *et al.*, 2011; Pop *et al.*, 2012]. The circuit pattern is defined on 2 inch-diameter, 430 um-thick, double-side-polished C-plane sapphire wafers using the electron-beam lithography technique, facilitated by a 100 kV electron-beam pattern generator (Raith EBPG 5000+). The thin-film aluminum in these Josephson junctions is deposited and oxidized in a combined electron-beam evaporation and oxidation system (Plassys UMS300 UHV). The readers are invited to consult Mineev [2018] and Serniak [2019] for detailed descriptions of the transmon fabrication process.

Posterior to dicing and cleaning, individual samples are selected from the wafer through measuring the room-temperature DC resistance R_n of the Josephson junction.¹ Following Equations (1.2) and (1.3), the Josephson inductance can be inferred using the formula

$$L_J = \frac{\hbar}{\pi\Delta} R_n, \quad (4.1)$$

in which Δ is the superconducting energy gap [Ambegaokar and Baratoff, 1963a,b]. In reality, a correction factor γ should be multiplied on the right-hand side of the

¹A DC link is patterned on the lithography mask to short the two electrode pads so as to prevent the accumulation of electrostatic charge during the fabrication and storage. The DC link is to be broken by the probe needle before the room-temperature junction resistance test.

formula to account for the increase of the normal resistance of Josephson junctions when cooled down to low temperatures,

$$L_J = \frac{\gamma \hbar}{\pi \Delta} R_n. \quad (4.2)$$

In our experiments, $\gamma \approx 1.15\text{--}1.20$ is typically consistent with low-temperature sample characterizations.

The aluminum Josephson junctions in the SNAIL² parametric amplifiers (SPA) are fabricated following the Niemeyer–Dolan-bridge process [Dolan, 1977; Niemeyer and Kose, 1976] on 300 μm -thick silicon substrates.

4.2 Microwave cavities: geometries and materials

A transmon sample, after passing the room-temperature junction resistance test, is to be loaded into one of the chip slots in a 3D microwave readout cavity, as shown in the upper panel of Figure 4.2. To implement the simple linear qubit–cavity coupling as in Equation (3.63), the electric dipole moment of the transmon should be aligned with the electric field of the TE_{101} mode (between 7.4–7.9 GHz in our experimental systems), which is along the shortest dimension of cavity. The two asymmetric chip slots coincide with the nodes of the electric field of the cavity TE_{103} mode—the second lowest mode that can be excited through a symmetric coaxial pin or a waveguide aperture coupler. The alignment of the two half-cavity parts is assisted by a pairs of Dowel pins. One circle of thin indium wire is placed inside the sealing grove to reduce the seam loss of the cavity [Brecht *et al.*, 2017, 2015].³ A long screw can be inserted

²Abbreviation of the superconducting nonlinear asymmetric inductive element [Frattini *et al.*, 2018, 2017; Sivak *et al.*, 2019].

³The seam loss can be further minimized by suppressing the electromagnetic field at the cavity seam, for instance, with a waveguide section whose cutoff frequency is above the frequency

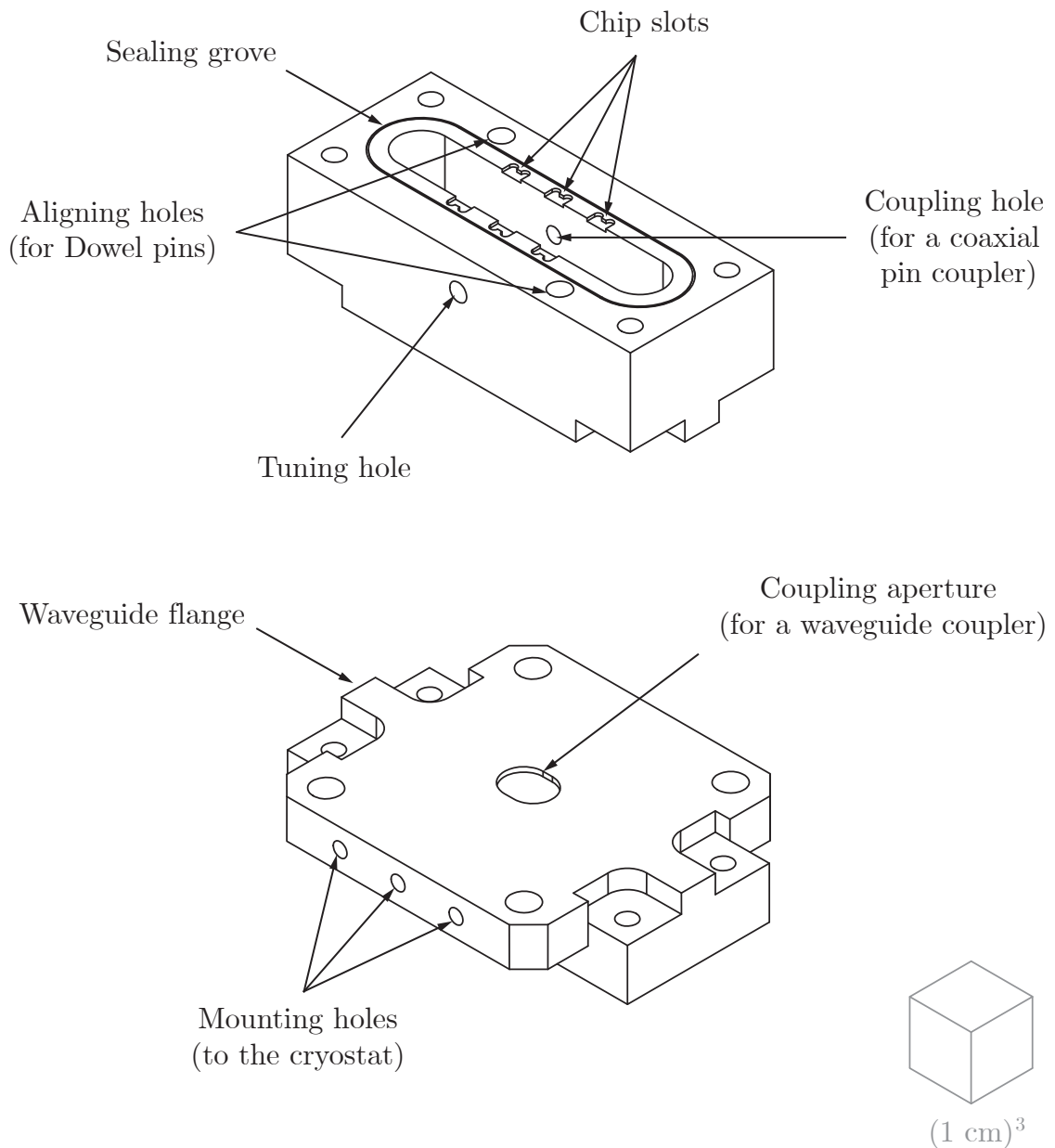


Figure 4.2: Drawing of a 3D microwave readout cavity used in the following experiments. The round shape of the inner side walls is designed to ease the machining process compared to a rectangular design with sharp internal angles. The upper cavity half can be paired with a mirrored copy of itself, or its variation depicted in the lower panel, which is designed to be coupled to a waveguide section or a waveguide-to-coaxial-cable coupler.

through the tuning hole to lower the cavity resonant frequency within the range of ~ 200 MHz.

The most common material choice of the 3D cavities is the 6061 aluminum alloy, which is superconducting at sub-kelvin temperatures and thus minimizes the intrinsic conductive loss. Oxygen-free high-conductivity (OFHC) copper with an aluminum coating layer is also often adopted for an improved bulk thermal conductivity combined with low surface electrical dissipations—the latter is due to the *skin effect* of the distribution of electromagnetic fields inside a conductor at microwave frequencies [Pozar, 2012].

4.3 Low-temperature experimental system

The circuit QED module, as described in the previous two sections, is installed in an environment around 20 mK and measured using a microwave electronic system. In this section, I will briefly discuss how the low temperatures are maintained and calibrated, how microwave circuit elements are arranged to assist electromagnetic measurements at the single quantum level, and what special cautions are exercised to improve the thermalization and electromagnetic shielding of the sample.

4.3.1 Cryogenics and thermometry

The low temperature environment of our quantum circuit experiments is provided by an Oxford TritonTM 200 cryogen-free dilution refrigerator, whose basic thermal circuit diagram⁴ is drawn in Figure 4.3. The cryostat consists of five gold-plated

of the fundamental cavity mode [Reagor *et al.*, 2016]. Such design offers an attractive solution for superconducting-cavity quantum memories, where high intrinsic quality factors are particularly desired.

⁴Further details, such as cold traps and the room-temperature gas handling system, are not represented in this diagram.

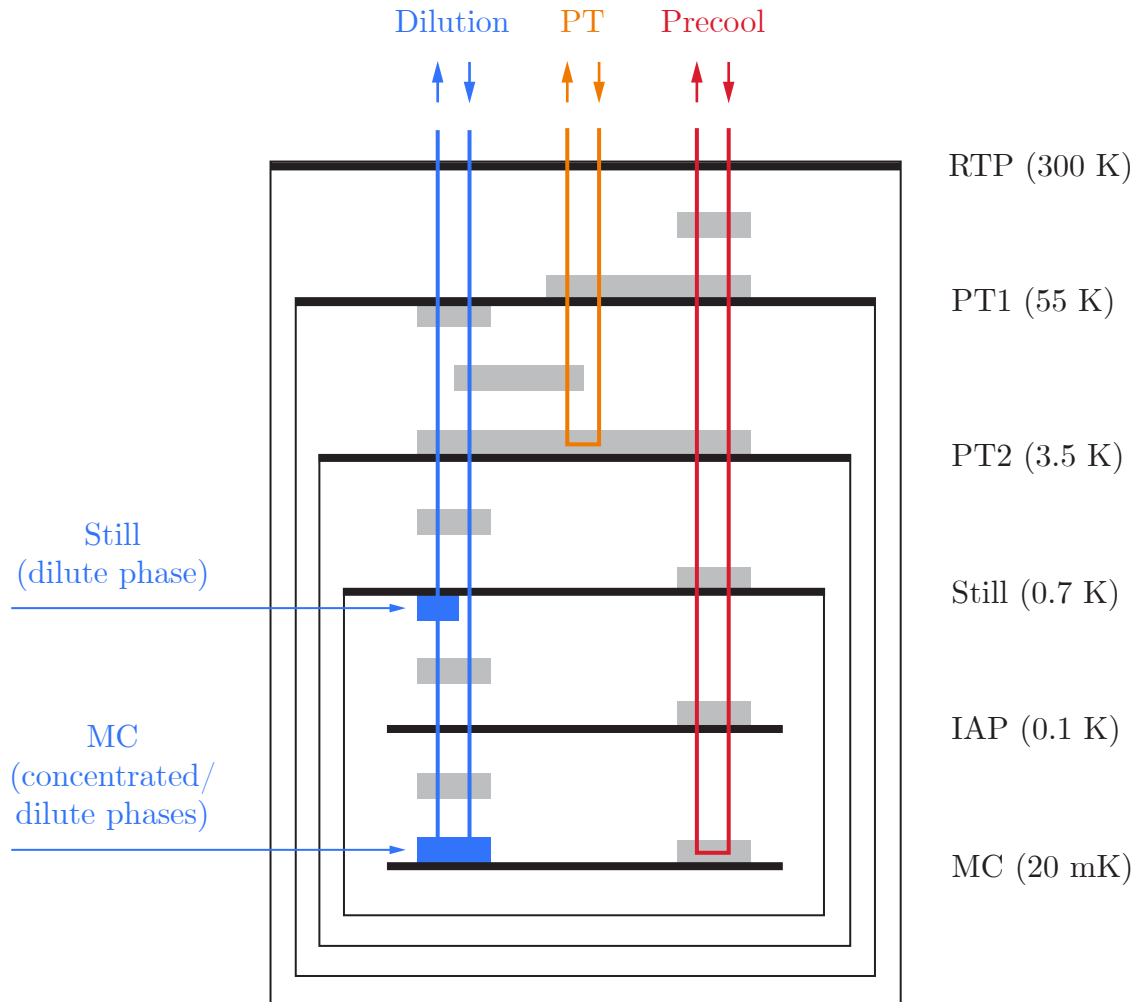


Figure 4.3: Simplified thermal cycle diagram of the cryogen-free dilution refrigerator. From left to right, the blue, orange, and red lines stand for the dilution refrigeration, pulse tube, and precool cycles, respectively. The still and mixing chamber in the dilution unit are colored in blue. Annotations on the right label the six plates and their typical temperatures. RTP: room-temperature plate. PT: pulse-tube. IAP: intermediate anchoring plate. MC: mixing chamber. The RTP, PT1, and PT2 stages are paired with aluminum shields, while the still stage is each paired with a light-tight copper shield. Only the room-temperature shield, also named the outer vacuum can (OVC) is hermetic and sealed with O-rings. Gray boxes represent heat exchangers of various types. In reality, the PT1 and PT2 heat exchangers are not anchored but thermal connected through copper thermal straps to the cryostat stages, in order to reduce the impact of vibrations caused by the pulse tube cryocooler.

temperature stages below the room temperature, and three closed-loop refrigeration cycles—a two-stage pulse tube (PT) cryocooler, a dilution unit, and a precool circuit. The stages are mechanically supported but thermally isolated from each other. The entire cryostat is loaded on three passive vibration isolators for suppressing mechanical noise during the experiments. In a standard cooldown process, the PT first lowers the temperature of the lowest stage to 10 K after 24–30 hours, while a small amount of helium-3 and helium-4 (^3He – ^4He) mixture is circulated in the precool circuit to assist the thermalization of lower cryostat stages to the PT cooler. After the precool circuit is evacuated, the dilution unit is turned on and all the stages will reach their expected temperatures as labeled in the diagram after another few hours.⁵ These low temperatures can be maintained for an extended period of time set by the experimental schedule of the research team. The ^3He – ^4He dilution refrigeration mechanism is the only *continuous* cooling method capable of reaching temperatures below 0.3 K—the low-pressure limit of the evaporative cooling temperature with ^3He .

Three types of low temperature sensors are employed to monitor different parts of the cryostat in real time—

- (a) PT1: Platinum resistance thermometer (PT100)
- (b) PT2: Zirconium oxynitride resistance thermometer (Cernox)
- (c) Still and intermediate anchoring plate (IAP): Ruthenium oxide (RuO_2) resistance thermometer
- (d) Mixing chamber (MC) plate: the Cernox and RuO_2 thermometers are used as the primary temperature sensors above and below 1 K, respectively.

⁵For basic principles of the ^3He – ^4He dilution refrigeration method, see Lounasmaa [1974] and Pobell [2007].

In selected experimental rounds, a cobalt-60 (^{60}Co) nuclear-orientation thermometer [Lounasmaa, 1974; Marshak, 1983] was installed on the MC stage for reliable absolute temperature measurements below 100 mK.

While these sensors—after calibrations—are usually reliable in reporting the temperature of their immediate surroundings, it should be emphasized that due to the limited thermal conductivities of various components in the cryogenic experimental installation, the thermometer readouts do not directly reflect the effective temperatures of the quantum circuit sample and the microwave modes.

4.3.2 Low-temperature microwave wiring

The design of a quantum-limited microwave measurement system is essentially about manipulating electromagnetic signals at various finite levels of noise temperature. The major tasks include attenuation, filtering, directional circulation, and amplification. Figure 4.4 displays a simplified wiring diagram for the standard reflection measurement of a single circuit QED module consisting of one transmon qubit linearly coupled to one readout cavity. This diagram offers more concrete descriptions of the high-level schematic drawing in Figure 3.6.

Microwave readout pulses at frequency f_{RO} are generated at the room temperature and delivered to the circuit QED module through an input transmission line, shown vertically on the left. The typical Johnson–Nyquist noise temperature associated with those passive room-temperature electronic devices is on the order of 300 K, which corresponds to the energy of 10^3 microwave photons around 7 GHz.⁶ The measurement signals in the circuit QED readout cavity—usually between 1–10 microwave photons—would be overwhelmed by thermal fluctuations from the room

⁶See Footnote 17 in Chapter 1 for the conversion between thermal excitations and photon energies frequently encountered in low-temperature electromagnetic measurements.

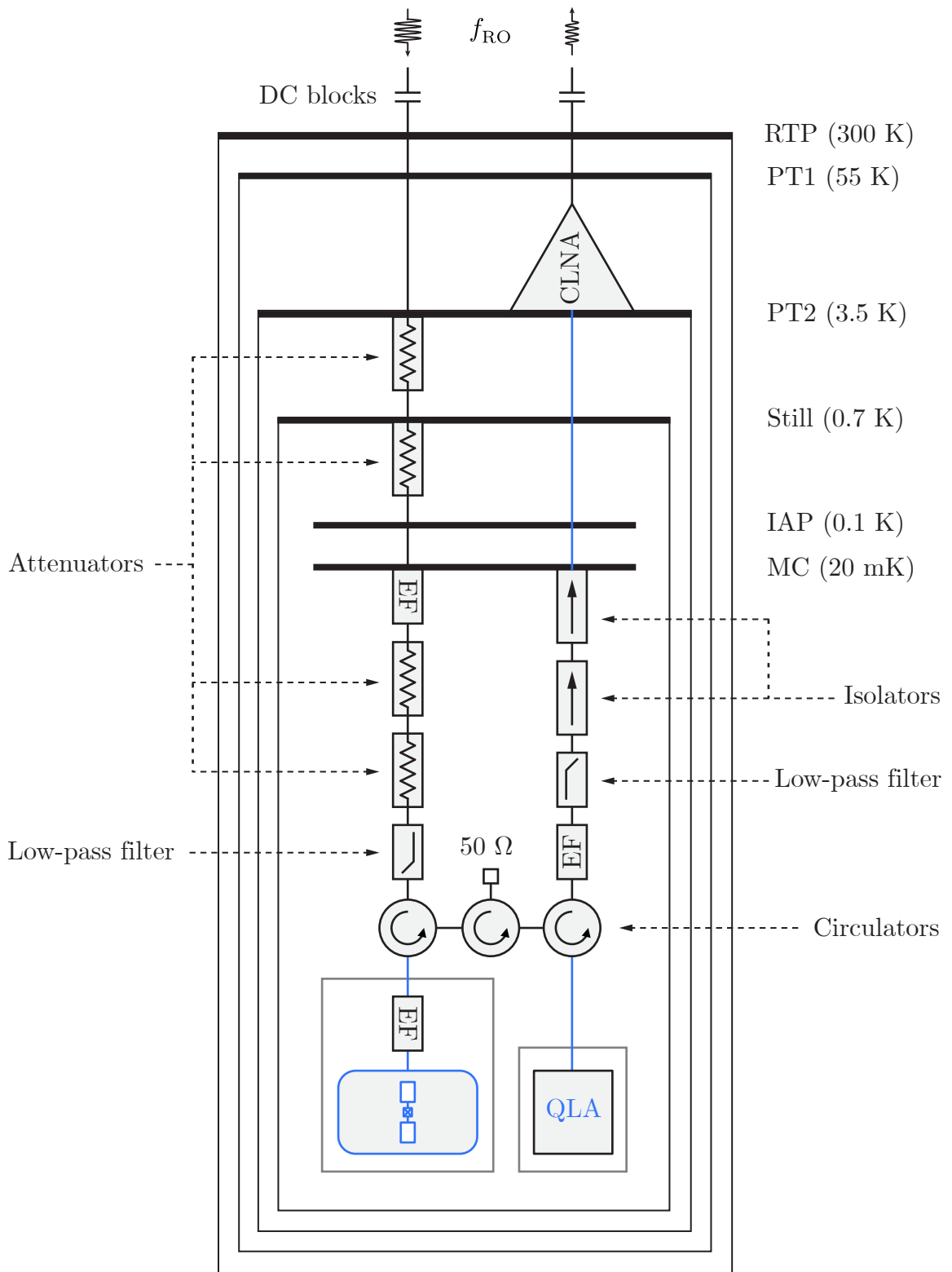


Figure 4.4: Cryogenic microwave setup for a standard circuit QED experiment in a dilution refrigerator. The low-temperature system consists of three essential parts: (i) an input line with cryogenic microwave attenuators and filters; (ii) the circuit QED system—here exemplified by a transmon linearly coupled to a 3D rectangular readout cavity measured in reflection; (iii) the output amplifier chain consisting of a quantum-limited amplifier (QLA) realized with Josephson microwave circuits, and a semiconductor cryogenic low-noise amplifier (CLNA) typically realized using the high-electron-mobility transistor (HEMT) technology. The microwave pump of the QLA and the DC bias of the CLNA are not represented. EF stands for Eccosorb filters. Blue lines represent niobium–titanium (Nb–Ti) superconducting microwave coaxial cables. Following this color code, other superconducting circuit elements—the transmon, the readout cavity, and the Josephson amplifier are also colored in blue. The gray blocks stand for the electromagnetic shields of the circuit QED module and the QLA. The names and abbreviations of the temperature stages are the same as in Figure 4.3. DC blocks are installed on both the input and output lines at the top of the cryostat to prevent the formation of DC ground loops. Copies of the input line can be added as the qubit drive lines. Pump lines of the QLA is constructed similarly but with less attenuation.

temperature, unless the noise is dissipated into the cold reservoirs inside the cryostat. Therefore, a series of cryogenic microwave attenuators are installed on the input line at different temperature stages. Mathematically, the output thermal fluctuations an attenuator—measured in the photon number—are given by the relation

$$\bar{n}_{\text{th}}^{\text{out}} = \eta_a \bar{n}_{\text{th}}^{\text{in}} + (1 - \eta_a) \bar{n}_{\text{th}}^{\text{res}}, \quad (4.3)$$

in which η_a stands for the attenuation; $\bar{n}_{\text{th}}^{\text{in}}$, $\bar{n}_{\text{th}}^{\text{out}}$, and $\bar{n}_{\text{th}}^{\text{res}}$ measure the thermal fluctuations of the input signal, the output signal and the thermal reservoir of the attenuator, respectively. When $\bar{n}_{\text{th}}^{\text{in}}, \bar{n}_{\text{th}}^{\text{out}}, \bar{n}_{\text{th}}^{\text{res}} \gg 1$, the above relation can also be written using

temperatures,

$$T_{\text{out}} = \eta_a T_{\text{in}} + (1 - \eta_a) T_{\text{res}}. \quad (4.4)$$

The temperatures and photon numbers can be converted using the Bose–Einstein distribution function [Pathria and Beale, 2021],

$$\bar{n}_{\text{th}} = \frac{1}{e^{\frac{hf}{k_{\text{B}}T}} - 1}, \quad (4.5)$$

in which f is the frequency of the radiation mode. The value of input attenuation on each stage should be chosen such that the attenuated input noise— $\eta_a \bar{n}_{\text{th}}^{\text{in}}$ —should be comparable to $\bar{n}_{\text{th}}^{\text{res}}$. As a practical example, given an input signal with $T_{\text{in}} = 300$ K passing a 20 dB attenuator ($\eta_a = 0.01$) on the PT2 stage ($T_{\text{res}} = 3.5$ K), then $T_{\text{out}} \approx T_{\text{in}}/100 + T_{\text{res}} = 6.5$ K. A typical arrangement of attenuator along a readout input line is 20 dB on the PT2 stage, 10 dB on the Still stage, and 40 dB on the MC stage. These attenuators are made of nichrome (NiCr) thin-film resistors and provide broadband attenuation below 18 GHz at low temperatures. The MC attenuation is often separated into multiple stages in series for reduced heat dissipations on each element. The stainless-steel coaxial cables, which can maintain the thermal isolation between different stages, add another ~ 10 dB attenuation along the input line.

On top of the broadband attenuation, the input line is also equipped with two types of low-pass filters—a homemade Eccosorb CR-110 filter (EF) that is absorptive in the far-infrared frequency band [Halpern *et al.*, 1986] but has a matched impedance between 2–10 GHz [Pop *et al.*, 2014], and a commercial low-pass filter with a cutoff frequency at 10 GHz. It has also been proved that an EF inside the electromagnetic shield of the circuit QED module can improve the charge-parity lifetime of the qubit by potentially suppressing the photon-assisted quasiparticle tunneling events

[Diamond *et al.*, 2022; Serniak *et al.*, 2019].

On the MC stage, cryogenic ferrite circulators with a directional passband between 4–8 GHz are used to separate input and output signals for the reflection cavity measurement and the reflection quantum-limited amplifier. One or more additional circulators—with the third port terminated by a $50\ \Omega$ resistive load—between the ones connected to the cavity and the amplifier ports can enhance the directionality of readout signals.

Circuit elements on the MC stage are typically connected by semi-rigid copper coaxial cables, for their low insertion loss and flexibility for wiring. Residual dissipations occurring along the microwave cables, connectors, and cryogenic circulators between the circuit QED module and the quantum-limited Josephson amplifier are often the limiting factor of the overall measurement efficiency of the readout system. Niobium–titanium (Nb–Ti) superconducting cables are often used in this range to minimize the added noise and improve the measurement efficiency.

After the Josephson amplifier on the base stage, the output line is equipped on the PT2 stage with a broadband semiconductor cryogenic low-noise amplifier (CLNA) based on high-electron-mobility transistors (HEMT) [Weinreb, 1980]. Specific models used in the following experiments are fabricated by Low Noise Factory and Cosmic Microwave Technology, which provide 35–45 dB gain within various gigahertz bandwidths in the range of 1–12 GHz. Their noise temperatures—tested by the manufacturers around 10 K—are between 2–8 K, comparable to the PT2 stage temperature. The DC power dissipation of these semiconductor amplifiers is on the order of 10 mW, which is below the optimal cooling power of the PT2 stage.

A straight section of Nb–Ti superconducting coaxial cable directly connects the MC stage and the PT2 stage on the output line to minimize added noise in readout signals before the CLNA/HEMT amplifier. Two cryogenic ferrite insulators with a directional passband between 3–12 GHz are installed in series at the input of the

superconducting cable on the MC stage to prevent thermal radiation at higher temperatures from moving downward and contaminating the quantum signals.

4.3.3 Thermalization and electromagnetic shielding

One key challenge in circuit QED experiments is the coupling between the cryogenic system and the microwave circuitry explained in the previous two subsections, since quantum-limited microwave measurements essentially depend on the effective thermalization of the electromagnetic environment of superconducting circuits. In practice, the temperature of the MC stage—as monitored by the RuO₂ sensor anchored on the cryostat plate—does not directly reflect the physical temperature immediately surrounding the circuit QED module, or the effective temperature of the electromagnetic field inside the measurement circuits. Special cautions are ought to be taken to minimize the temperature gradients between different parts of the experimental system that are ideally expected to be thermalized to the MC of the dilution refrigerator at 20 mK.

The cryostat plates and the mechanical holders of quantum circuit modules below the MC stage are made of OFHC copper—a reliable high-thermal-conductivity metal at millikelvin temperatures. Gold plating of a few micrometers thick is generally preferred, thanks to the softness of the gold–gold interface to form larger contact areas for more efficient heat conduction [Dillon *et al.*, 2017]. If gold plating is not available, the surface oxide layer of copper should be removed with a scouring pad and a fine sandpaper. To eliminate organic residues attached to the surfaces, the sample holders and 3D cavities are subsequently cleaned with an anionic detergent (Alconox), acetone, and isopropyl alcohol (IPA) through sonication and dried with compressed nitrogen gas. The tightness of all mechanical fasteners should be frequently examined because the contact thermal conductance is proportional to the interfacial force. Molybdenum (Mo) washers are paired with screws of all sorts due to the small con-

tractivity/expansivity of Mo at low temperatures. The mechanical joints will thus remain tight when the cryostat is cooled down.

Nevertheless, materials with low thermal conductivities at millikelvin temperatures are also present in the experimental system. Two notable examples are aluminum as in superconducting cavities and waveguides, and stainless steel, which is widely used in the packages for commercial cryogenic attenuators and ferrite circulators/isolators. OFHC copper blocks, clamps and strips are employed as additional thermal links to assist the thermalization of these circuit components to the MC stage of the cryostat. Residual thermal radiation with effective temperatures in the 50–70 mK range is commonly observed in experiment setups of the same type. Novel home-made lumped-element broadband attenuators [Yeh *et al.*, 2017] and resonant cavity attenuators [Wang *et al.*, 2019] can be invented to address this issue, which will be discussed in detail in Chapter 5.

Due to the sensitivity of superconducting quantum circuits to external electromagnetic perturbations, extra layers of protection are applied around the sample to further screen ambient magnetic fields and infrared radiation in the dilution refrigerator. Both the circuit QED module and the Josephson quantum-limited amplifier are housed in high-magnetic-permeability mu-metal (Amumetal A4K) shields thermally anchored to the OFHC copper mechanical holders below the MC stage. In selected experimental rounds, a copper wrap coated with a mixture of epoxy (Stycast 2850) and fine carbon powder is placed inside the circuit QED shield for infrared absorption [Barends *et al.*, 2011]. The circuit QED module is also wrapped with three layers of aluminized biaxially-oriented polyethylene terephthalate (boPET) films. The copper sample holder of the Josephson amplifier is paired with an aluminum shield inside its mu-metal can for improved magnetic screening.

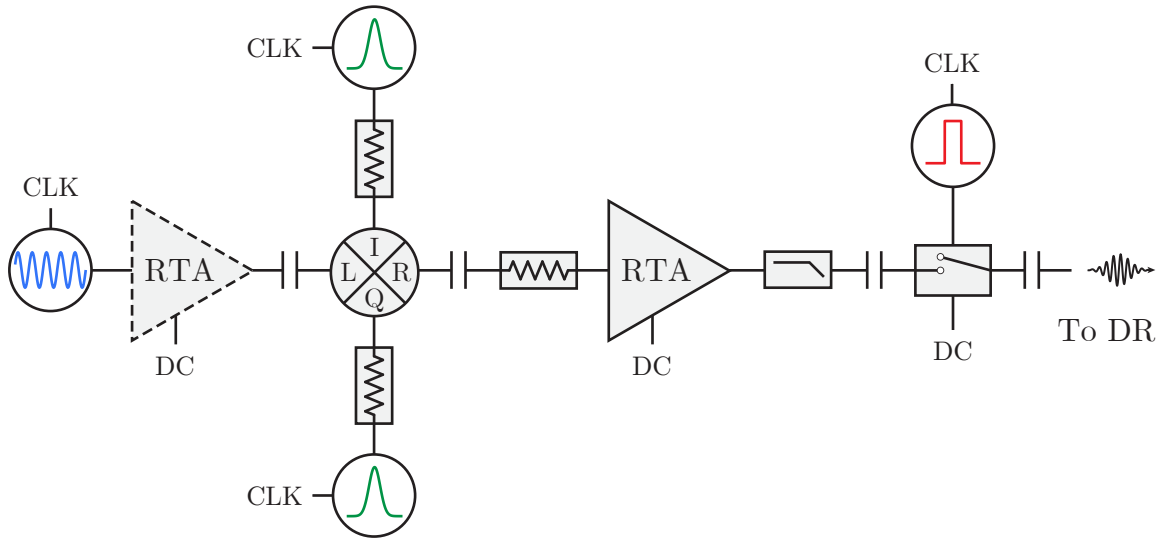


Figure 4.5: Microwave circuit for arbitrary-shape pulsed signal generation through IQ modulation. Signal sources: blue—microwave carrier signal; green—IQ modulation signals; red—digital marker signal. All these signal generators are synchronized through a 10 MHz reference clock signal from the rubidium (Rb) atomic frequency standard (CLK). The L and R ports of the double-balanced IQ mixer are the local oscillator (LO) input and radio-frequency (RF) output. DR: dilution refrigerator. RTA: room-temperature amplifier. The RTA on the left (dashed outline) is needed when the maximum output power of the microwave generator is below minimum required LO input power of the IQ mixer. Circuit symbols for the attenuators, the microwave low-pass filter, and the DC blocks are the same as Figure 4.4.

4.4 Room-temperature electronics

The electronic system above the room-temperature plate of the dilution refrigerator is assembled with commercial devices and cables, for generating and analyzing pulsed microwave signals.

4.4.1 Pulsed signal generation

The circuit diagram for arbitrary-shape microwave pulse generation used in our experiments is shown in Figure 4.5. Four different models of microwave generators—Vaunix Lab Bricks LMS, SignalCore SC5511A, Agilent N5183A MXG, and Agilent E8267D PSG—have been used to generate the continuous-wave (CW) microwave carrier signals with various frequency ranges, power ranges, and noise levels. Two generations of equipment were employed to generate the arbitrary-shape analog modulator signals and their synchronized digital marker signals—

- (i) In the cavity attenuator experiment, they were produced by a Tektronix 5014C arbitrary waveform generator (AWG) with 14-bit digital-to-analog converters (DAC) and sample rates up to 1.2 giga-samples per second (GS/s).
- (ii) In the Π -mon experiment, we used an Innovative Integration X6-1000M field-programmable gate array (FPGA) board (12-bit DAC with sample rates up to 1 GS/s) connected to a VPXI-ePC controller.⁷

The signals generators are synchronized through a 10 MHz external clock, provided by a rubidium (Rb) atomic frequency standard (Stanford Research Systems FS725).

The analog modulation occurs in a double-balanced IQ mixer. Small attenuators (typically 3 dB) are connected to the mixer ports to suppress reflected signals due to impedance mismatch. The output noise of the room-temperature semiconductor microwave amplifier is first suppressed by a low-pass filter and then by a high-speed microwave switch controlled by the digital marker signal. Finally, the power of the pulsed signals can be monitored by a spectrum analyzer (Signal Hound SA124B or

⁷See Appendix D of Reinhold [2019] for a high-level introduction to the hardware and software of the FPGA quantum controller.

Agilent EXA N9010A) after a directional coupler (not shown in the diagram), before sent to an input line of the dilution refrigerator (see Figure 4.4).

When it comes to power efficiency, the method of single-sideband (SSB) modulation displays the advantage of concentrating the drive power at one single frequency. This is achieved by fine-tuning the DC offset of the IQ signals as well as their amplitude ratio and phase difference to suppress the residual output signals at the frequencies of the carrier and the opposite sideband. In practice, the lower sideband (LSB) is used to drive the qubit such that the carrier and upper sideband (USB) leakages are far detuned from the higher transitions of the transmon. By default, the sideband detuning is set to be 50 MHz in our following experiments.

IQ modulator signals with Gaussian envelopes are used to produce qubit control pulses. Moreover, the pulse-shaping technique also found its application in accelerating the photon population and depletion of the readout cavity for optimized qubit measurement times [Bultink *et al.*, 2016, 2018; Jeffrey *et al.*, 2014; Liu *et al.*, 2014; McClure *et al.*, 2016; Touzard *et al.*, 2019].

4.4.2 Microwave signal detection

The analysis of output readout signals from the cryostat is assisted by a superheterodyne microwave interferometer as depicted in Figure 4.6. A microwave generator is fixed at the readout frequency f_{RO} , whose output after the same type of high-speed microwave switch used in the pulse generation circuit (Figure 4.5) is delivered to the cryogenic input line as the square microwave readout pulse to interrogate the transmon. In the meantime, the continuous-wave (CW) output from a second microwave generator—set at the frequency $f_{\text{RO}} + f_{\text{IF}}$ —is mixed with the f_{RO} to yield an

intermediate-frequency (IF) reference signal at f_{IF} .⁸ On the other arm, measurement signals from the cryostat is first amplified by a (chain of) room-temperature low-noise amplifier(s),⁹ and then mixed with the CW signal at $f_{\text{RO}} + f_{\text{IF}}$ to down-convert the measurement signals to the IF band. The IF measurement and reference signals are sent to band-pass filters, IF amplifiers (Stanford Research Systems SR445A), and analog-to-digital converters (ADC) for demodulation and processing in the digital domain.

Two generations of ADCs were paired with the DACs mentioned in the previous subsection—

- (i) The cavity attenuator experiment employed an AlazarTech ATS9870 two-channel 8-bit digitizer with a sampling rate at 1 GS/s (input peak-to-peak voltage range between 200 mV to 4 V).
- (ii) In the Π -mon experiment, the two ADC channels are integrated into the Innovative Integration X6-1000M FPGA card (12-bit, 1 GS/s sampling rate, and 1 V peak-to-peak voltage at maximum).

Hence in these measurement systems, 1 V is the typical scale for voltage signals showing “classical distinguishability.” The experimental setup described in Figures 4.4 and 4.6 constitute the “meter” as in the qubit–meter model of quantum measurements explained in Chapter 2.

⁸By default, $f_{\text{IF}} = 50$ MHz is fixed in our experiments. Accordingly, the frequency span of the IF band-pass filters is 41–58 MHz.

⁹In our setup, we use a MITEQ AMF-5F low-noise amplifier with a 39 dB gain between 4–12 GHz and a noise temperature $T_{\text{n}} = 124$ K.

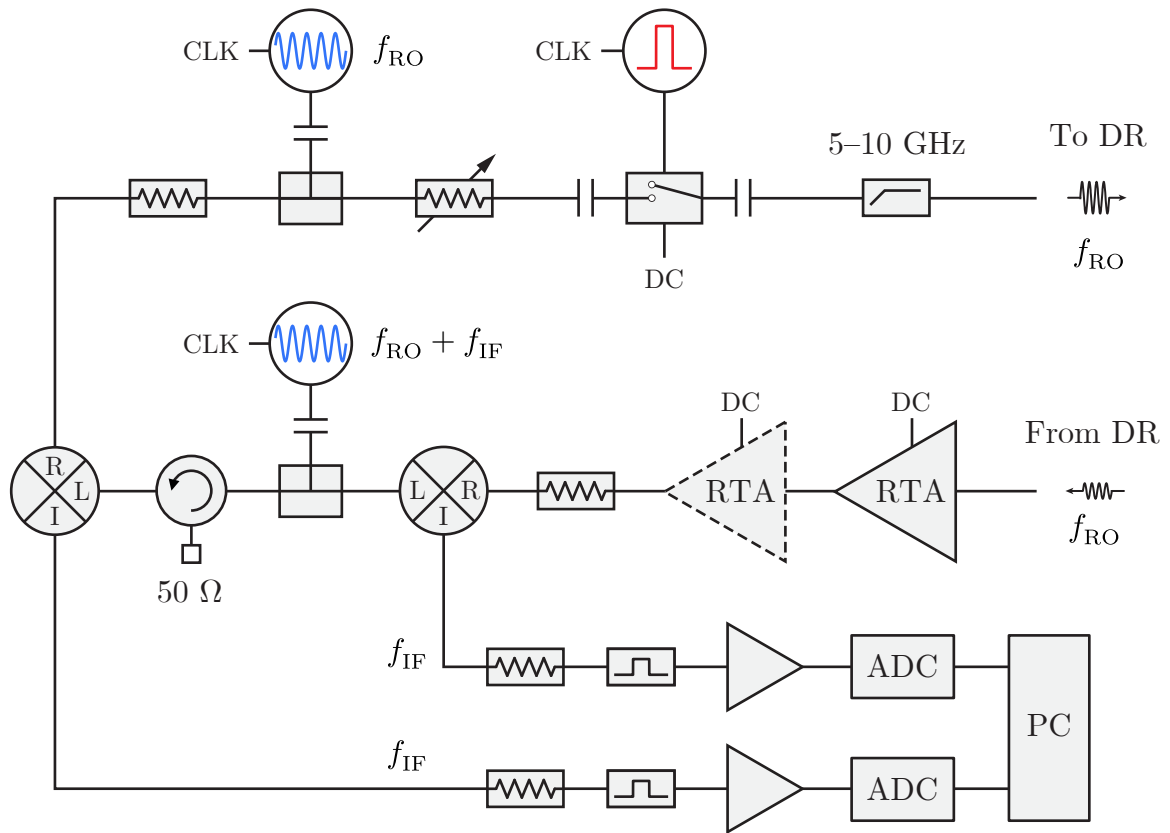


Figure 4.6: Superheterodyne microwave interferometer and digitization circuits. The signal generator, attenuator, filter, switch, clock, and DC block symbols are the same as in Figure 4.5. The two microwave generators (blue) at the frequencies f_{RO} and $f_{RO} + f_{IF}$ respectively are each connected to a two-way (50/50) Wilkinson power divider [Wilkinson, 1960]. Besides “L” and “R”, the “I” in the mixer symbol stands for its intermediate frequency (IF) port. The room-temperature circulator with a 50 Ohm resistive terminator on its third port imposes the directionality of the signal flow. DR: dilution refrigerator. RTA: room-temperature amplifier at microwave frequencies. A second RTA (dashed outline) is needed only when the gain of the first RTA is not sufficient for the demodulation of the measurement signals. The two small triangular symbols without text represent IF amplifiers. ADC: analog-to-digital converter. PC: personal computer.

4.5 Control and simulation software

The room-temperature electronic instruments mentioned in the previous section are controlled through their application programming interface (API) using the Python programming language. For the measurement system based on the Tektronics AWG and the AlazarTech digitizer, the software package `qrlab` is employed to control the pulsed signal generation and detection. The Innovative Integration FPGA system is loaded with the Yngwie quantum controller [Reinhold, 2019]. The integration of signal generators and digitizers has enabled more versatile control operations, especially concerning high-speed feedback that is central to active qubit-state preparation and measurement-based quantum error correction.

In the design phase of a circuit QED experiment, the 3D electromagnetic simulation software based on the finite element method (FEM)—Ansys HFSS and Maxwell—is used for the linear eigenmode and driven modal analysis of the superconducting artificial atoms/molecules and microwave cavities. AWR Microwave Office is used for analyzing linear lumped-element circuit models in the design of Josephson quantum-limited amplifiers.

The nonlinear simulation of circuit QED modules given their linear simulation results and Josephson junction parameters is assisted by the Python-based software package `pyEPR` in which the energy-participation ratios (EPR) of nonlinear circuit elements—Josephson junctions—are employed to numerically compute the effective quantum Hamiltonian of the Josephson circuits [Minev, 2018; Minev *et al.*, 2021a].

In this chapter, I have presented a concise introduction to the essential elements for performing a circuit QED experiment in a low-temperature physics laboratory. Notably, the experimental system features a hybridization of knowledge and methods from a number of different disciplines of physical science and engineering. Moreover,

the combination of homemade and commercial devices, equipment, and software exemplifies the need for technological creativity—in addition to fundamental physics insights—in quantum engineering research. In the end, it is worth remarking on the highly *empirical* and *technical* nature of these experimental methods—rather than having been cast into a stable system of knowledge, the frontier of quantum technology is being known for its high-frequency updates thanks to expanding research and development activities from both the academic and industrial communities. Certain fragments of this chapter—at both the hardware and software levels—are going to be modified or replaced in the arriving years by the new standards. With these being said, the basic principles of microfabrication, cryogenic engineering, electromagnetic design, microwave signal processing, and high-level system control will remain instructional to quantum electrical engineering as well as related research fields.

Chapter 5

Cavity Attenuator: Protecting Quantum Information from Thermal Electromagnetic Noise

And first, we desire that the Instances we have given you of the Contingency of Experiments may make you think your self oblig'd to try those Experiments very carefully, and more than once, upon which you mean to build considerable Superstructures either theoretical or practical, and to think it unsafe to rely too much upon single Experiments . . .

Robert Boyle [1661]

The past two decades have witnessed an exponential increase in the coherence times of superconducting qubits [Devoret and Schoelkopf, 2013; Kjaergaard *et al.*, 2020]. Major breakthroughs have been driven by novel circuit designs and operations such as biasing a charge qubit at its charge-noise-insensitive point [Cottet, 2002; Vion *et al.*, 2002], shunting the Josephson junction with a capacitance to suppress noise in charge-based [Koch *et al.*, 2007; Schreier *et al.*, 2008] and flux-based qubits [Steffen *et al.*, 2010; You *et al.*, 2007], and shunting the Josephson junction with a superinductance to eliminate offset charge fluctuations in a fluxonium qubit [Manucharyan *et al.*, 2009b]. Moreover, in the circuit QED architecture [Blais *et al.*, 2004; Wallraff *et al.*, 2004], it has been well understood that the readout cavity modifies the

electromagnetic environment of the qubit and can thus affect qubit coherence [Esteve *et al.*, 1986; Houck *et al.*, 2008]. In recent years, for transmon qubits embedded in 3D microwave cavities [Paik *et al.*, 2011], energy relaxation times $T_1 > 100 \mu\text{s}$ have been frequently observed [Dial *et al.*, 2016; Mineev *et al.*, 2019; Narla *et al.*, 2016; Ristè *et al.*, 2013]. However, in these experiments, transmon coherence times T_2 are often much shorter than $2T_1$, indicating qubit coherence is predominantly limited by pure dephasing. An outstanding question in this field is whether the upper limit $T_2 \rightarrow 2T_1$ can be reproducibly obtained in long-lifetime superconducting qubits.¹

In this chapter, I will report the design and implementation of a new type of resonant microwave attenuator based on a cavity realized by a section of dissipative waveguide, which aims at reducing the residual thermal photon population in circuit QED systems such that the limit of $T_2 \rightarrow 2T_1$ can be approached in practice. The non-superconducting metal cavity is seamless and machined by conventional techniques without any material growth or microfabrication processes. By coupling it to a transmon-cavity system, we consistently measured enhanced coherence times on two qubits in multiple cooldowns, and obtained record-breaking pure dephasing time T_ϕ and \bar{n}_{th} at the base temperature, leaving qubit coherence solely limited by energy relaxation. Given its simple design and reliable performance, this cold cavity attenuator will provide a useful addition to the state-of-the-art quantum circuit toolbox.

The materials in the following sections are organized in the logical order: I will first explain, in Section 5.1, the advantage of *distributed-element* resistive systems over lumped-element ones with respect to the realization of well-thermalized dissipative reservoirs at low temperatures. Based on this idea, in Section 5.2, I will introduce the design principles, material selections, machining techniques, and test results of

¹See Equation (3.61) from Section 3.3.

the resonant cavity attenuators. Then I will analyze the measurement system of a cold cavity attenuator coupled to a standard circuit QED module in Section 5.3. The experimental data of qubit coherence times and the cavity thermal population measurements will be presented in Sections 5.4 and 5.5. I will conclude in Section 5.6 with the implications of these measurement results and discuss a few proposed methods to improve the versatility of cavity attenuators in superconducting quantum circuit experiments.

5.1 Electromagnetic attenuation: lumped-element versus distributed-element circuits

One of the main dephasing channels that limit T_2 in the circuit QED system is the residual thermal photon population in the readout cavity [Bertet *et al.*, 2005a,b; Clerk and Utami, 2007; Sears *et al.*, 2012; Yan *et al.*, 2018, 2016; Yeh *et al.*, 2017]. In the dispersive coupling regime, due to the AC Stark effect, fluctuations in the thermal photon number of the cavity cause random shifts of the qubit transition frequency and thus contribute to qubit dephasing [Gambetta *et al.*, 2006; Schuster *et al.*, 2005]. In the limit of average thermal photon number $\bar{n}_{\text{th}} \ll 1$, the induced dephasing rate is proportional to \bar{n}_{th} as given by Equation (3.59):

$$\Gamma_{\phi}^{\text{th}} = \frac{\bar{n}_{\text{th}} \kappa_c \chi_{\text{tc}}^2}{\kappa_c^2 + \chi_{\text{tc}}^2}, \quad (5.1)$$

where κ_c is the cavity linewidth, and χ_{tc} is the dispersive shift of the qubit frequency per cavity photon. Theoretically, for a 7.5 GHz cavity mode at 20 mK, \bar{n}_{th} is expected to be on the order of 10^{-8} . However, the values of \bar{n}_{th} estimated from measurements of $\Gamma_{\phi}^{\text{th}}$ in recent experiments range from 6×10^{-4} to 1.5×10^{-1} , corresponding to effective mode temperatures between 55 mK and 140 mK [Goetz *et al.*, 2017; Rigetti *et al.*,

2012; Suri *et al.*, 2013; Yan *et al.*, 2018, 2016; Yeh *et al.*, 2017]. Understanding the origin of excess thermal photons and reducing \bar{n}_{th} are therefore crucial to enhancing the qubit coherence times and reliably achieving $T_2 \rightarrow 2T_1$.

One major source of the excess \bar{n}_{th} is the coupling of the cavity mode to the input and output ports. This coupling opens a channel for low-temperature components in the microwave wiring to affect the thermal population of the cavity mode. Examples include commercial cryogenic attenuators, filters, and isolators. These components and the Teflon insulator in the coaxial cables are difficult to thermalize to the mixing chamber stage of the dilution fridge. Attenuators are particularly important in this regard since they are the dominant dissipation sources in the wiring of a cryostat and ideally form the bath that thermalizes the readout cavity modes. Insulators inside commercial cryogenic attenuators have poor thermal conductivities at low temperatures as do their stainless-steel packages. Lately, thermal anchoring of attenuators has been improved by replacing these materials with better thermal conductors and redesigning the circuit layout [Yeh *et al.*, 2017]. Nevertheless, a fundamental restriction in performance arises from the lumped element thin-film resistive network that these attenuators are made of.

An explanation of this challenge and its solution are shown in Figure 5.1. In a lumped element resistor, the electric and heat currents are parallel to each other, as presented in Figure 5.1(a). Given a certain electrical resistance, the order of magnitude of its thermal resistance due to electronic degrees of freedom is subject to the constraint imposed by the **Wiedemann–Franz law** [Ashcroft and Mermin, 1976]. For instance, a 50Ω resistor at 20 mK should have an electronic thermal resistance on the order of $10^8 \text{ mK}/\mu\text{W}$. Therefore, microwave attenuators at low temperatures are primarily thermalized through electron–phonon interaction and phonon transport [Roukes *et al.*, 1985; Wellstood *et al.*, 1994]. However, this phonon mechanism suffers from a bottleneck since very few phonons are present at millikelvin temperatures.

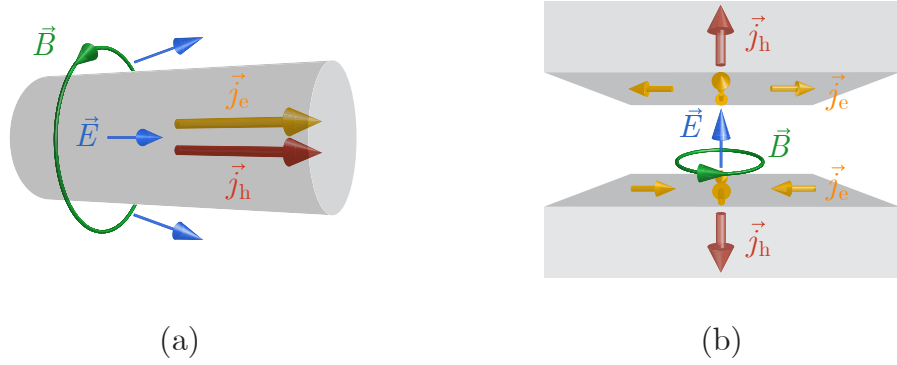


Figure 5.1: Comparison of the electromagnetic fields outside and currents inside (a) a lumped element resistor and (b) a dissipative waveguide section (TE mode). Blue and green arrows indicate electric field \vec{E} and \vec{B} magnetic field lines, while yellow and red arrows indicate electric current \vec{j}_e and heat current \vec{j}_h .

Numerical simulations show that under microwatt input powers, the temperature difference inside the resistive network of the attenuator can easily reach 100 mK [Yeh *et al.*, 2017]. Whereas it may be reduced by proper choice of materials and circuit layout, thermalizing all materials to 20 mK may be fundamentally impossible, since some thermal gradient is necessary to produce a sufficient phonon heat current.

To overcome this fundamental challenge, we would prefer to use electrons in a Fermi degenerate system to conduct heat, since electronic excitations are always present at low temperatures. We thus consider an alternative dissipation source for microwave radiation—the normal metal walls of a waveguide section. As shown in Figure 5.1(b), in a dissipative waveguide, electric current mainly flows within the skin depth of the wall, while heat is conducted by electrons into the bulk metal, perpendicular to the electric current. In principle, such a distributed structure, if made of a good thermal conductor, can realize an improved cold black body radiation environment at microwave frequencies, which is the goal of our work.

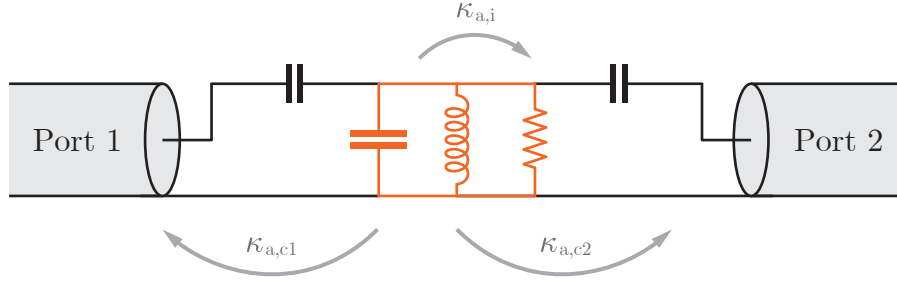


Figure 5.2: Near-resonant circuit model of a dissipative cavity (orange) capacitively coupled to two transmission lines (Ports 1 and 2). Parameters $\kappa_{a,i}$, $\kappa_{a,c1}$, and $\kappa_{a,c2}$ stand for the intrinsic dissipation and the external coupling linewidths through the two ports, respectively.

5.2 Design and test of cavity attenuators

Most commercial cryogenic attenuators have more than 10 GHz bandwidth. However, microwave pulses for qubit control and measurement are centered only around certain frequencies, and thus only narrowband attenuation is required. This forms the basis for the idea of attenuating quantum signals with a dissipative cavity. For instance, to protect a readout cavity at frequency f_r with ~ 1 MHz linewidth from excess photon noise, we would like to supplement commercial attenuators with a cavity attenuator. Such a cavity attenuator should: (i) be centered around f_r , (ii) provide 10–20 dB attenuation on resonance, and (iii) have 10–50 MHz bandwidth, which is an order of magnitude broader than the linewidth of the readout cavity (1–5 MHz). In addition, it should be made of a low-temperature-compatible normal metal, such as brass or, what is even better, oxygen-free high-thermal-conductivity (OFHC) copper.

Designing a microwave cavity that can be well thermalized to millikelvin temperatures and has a 10–50 MHz internal dissipation rate (internal quality factor $Q_{a,i} \sim 500$) is a challenging task, since good thermal conductors also have low electrical conductive loss. In general, the quality factor of an electromagnetic resonator

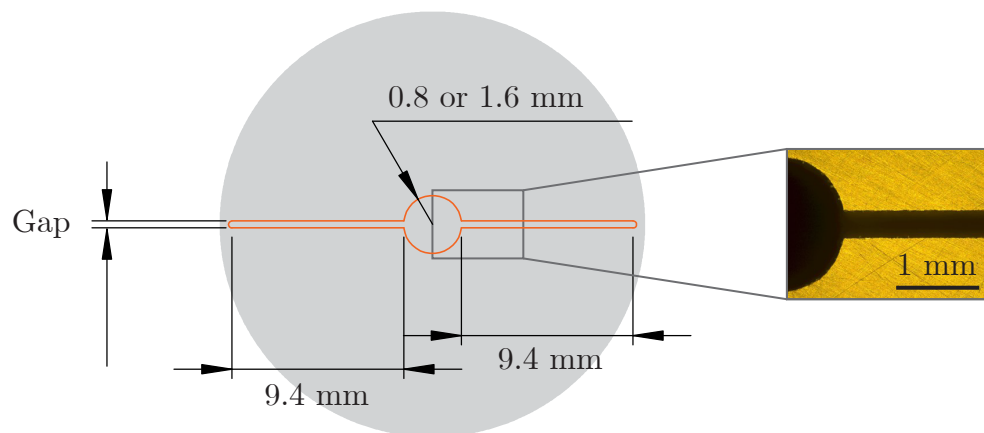
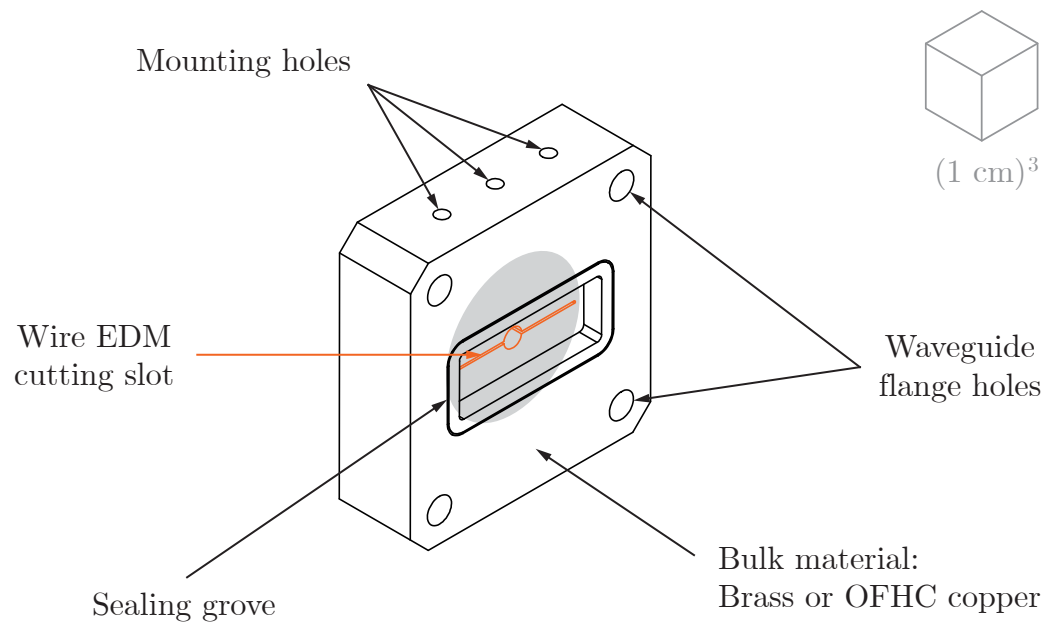


Figure 5.3: Drawing of a resonant cavity attenuator. The wire electrical discharge machining (EDM) cutting slot is highlighted in orange. A sealing groove—similar to that in Figure 4.2—is reserved for a circle of thin indium wire. The lower panel depicts a zoomed-in profile view of the thin-gap seamless cavity area (gray shadow), on the right of which is an enlarged, real-color optical micrograph. In this example, the cavity attenuator is made of brass (alloy 260) with a 0.3 mm gap.

is proportional to the average electromagnetic field energy stored in the resonator divided by the energy dissipation per cycle—

$$Q_{a,i} = 2\pi \frac{E_{\text{store}}}{E_{i,\text{loss}}} = \omega_a \frac{E_{\text{store}}}{P_{i,\text{loss}}}, \quad (5.2)$$

in which $E_{i,\text{loss}}$ and $P_{i,\text{loss}}$ denotes the energy per cycle and power of internal dissipations, respectively [Pozar, 2012]. Therefore, given the resistivity of the material, the quality factor due to the conductive loss of a 3D cavity resonator is approximately inversely proportional to its surface-to-volume ratio. An order-of-magnitude estimate shows that the smallest dimension of our brass or OHFC copper dissipative cavity must be in the submillimeter range. Furthermore, as illustrated in Figure 5.2, when the dissipative cavity is coupled to two microwave ports, its on-resonance power transmission is given by

$$|S_{21}|^2 = \frac{4\kappa_{a,c1}\kappa_{a,c2}}{(\kappa_{a,i} + \kappa_{a,c1} + \kappa_{a,c2})^2}, \quad (5.3)$$

where $\kappa_{a,i}$ and $\kappa_{a,c1,2}$ are the internal dissipation and external coupling rates. An attenuation around 10–20 dB requires $\kappa_{a,i}/10 \sim \kappa_{a,c1}, \kappa_{a,c2}$, which means the cavity is under-coupled to its external couplers.

Figure 5.3 shows a particular physical realization satisfying all these requirements. It is a single-piece brass (260 alloy) block fabricated using wire electrical discharge machining (EDM) [Ho *et al.*, 2004].² Such a design eliminates seams and therefore their associated loss [Brecht *et al.*, 2017, 2015]. Its external dimensions match those of the commercial WR-102 waveguides. In addition, it can be directly thermalized to the mixing chamber of a dilution refrigerator through copper braids. As sketched

²The wire EDM cutting of the cavity attenuator devices used in this experiment was performed by the Gibbs Machine Shop at Yale University and the Advanced Research Corporation (ARC).

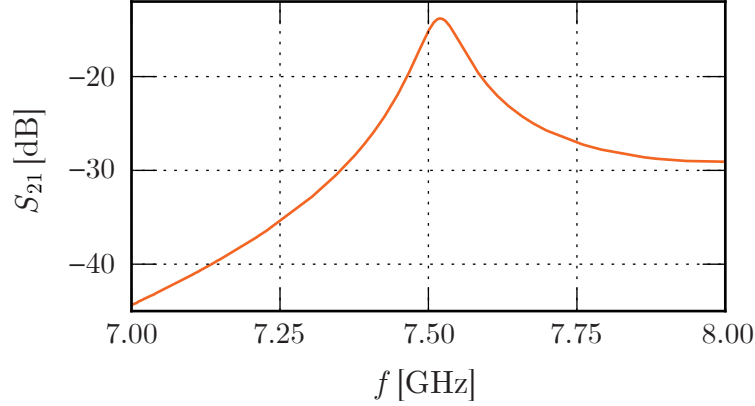


Figure 5.4: Transmission spectroscopy of the cavity attenuator measured with a vector network analyzer (VNA) at the room temperature. The waveguide couplers on both sides have $\kappa_{a,c1}, \kappa_{a,c2} \approx \kappa_{a,i}/10$. The transmission peak centers at 7.52 GHz with a 14 dB insertion loss. The reflection loss of the cavity attenuator is 2 dB on resonance (not shown in the figure). Combining transmission and reflection measurements, we extracted $\kappa_{a,i}/2\pi = 54$ MHz.

in the lower panel of Figure 5.3, the cavity is rectangular, apart from a cylindrical hole in the middle for initializing the wire EDM cutting. Due to the open boundary condition at both coupling ports, the electromagnetic field in the fundamental mode is non-uniform only in the longest dimension that is 22 mm in this device and sets the mode frequency. The 0.3 mm gap sets the internal dissipation rate of the cavity due to conductive loss. The room-temperature characterization of the cavity with a calibrated vector network analyzer (VNA) is shown in Figure 5.4.

Based on this design, we fabricated cavity attenuators with different materials and gap sizes. Parameters of three representative devices are listed in Table 5.1. For cryogenic measurements, the temperature of the attenuator block reached 15 mK as verified by ^{60}Co nuclear orientation thermometry. As can be seen in the table, cavity frequencies increase due to the thermal contraction of metal materials at low temperatures; in the meantime, phonon vibrations freeze out, which increases the

Material		Brass	Copper	Copper
Gap (mm)		0.3	0.13	0.08
$T = 296$ K	f_a [GHz]	7.52	7.68	7.68
	$\kappa_{a,i}/2\pi$ [MHz]	54	62	69
$T = 15$ mK	f_a [GHz]	7.67	7.75	7.79
	$\kappa_{a,i}/2\pi$ [MHz]	44	24	19

Table 5.1: Resonant frequency f_a and internal dissipation rate $\kappa_{a,i}$ of three cavity attenuators measured through reflection and transmission spectroscopies at the room temperature (296 K) and 15 mK, respectively.

metal conductivities and reduces the cavity dissipation rates. For brass—a copper–zinc (Cu–Zn) alloy material— $\kappa_{a,i}$ is reduced by about 20%. For OFHC copper, $\kappa_{a,i}$ is reduced by around a factor of three, indicating a ten-fold increase in electrical conductivity. Note that this value is smaller than the DC residual resistivity ratio (RRR) of OFHC copper because of the **anomalous skin effect**, which appears when the mean free path of the metal is longer than the wavelength of the RF probe signal [Chambers, 1950; Pippard, 1947, 1954]. The dissipation rates of copper cavity attenuators are limited by the smallest diameter of the EDM cutting wires that our machine shops had access to.

5.3 Coupling the cavity attenuator to the circuit QED system

The cavity attenuator is designed to be installed at the signal port of the standard circuit QED module in the dispersive regime. The detailed low-temperature wiring diagram is shown in Figure 5.5. The assembly drawing of the coupled system is shown in Figure 5.6, whose corresponding near-resonant circuit model is depicted

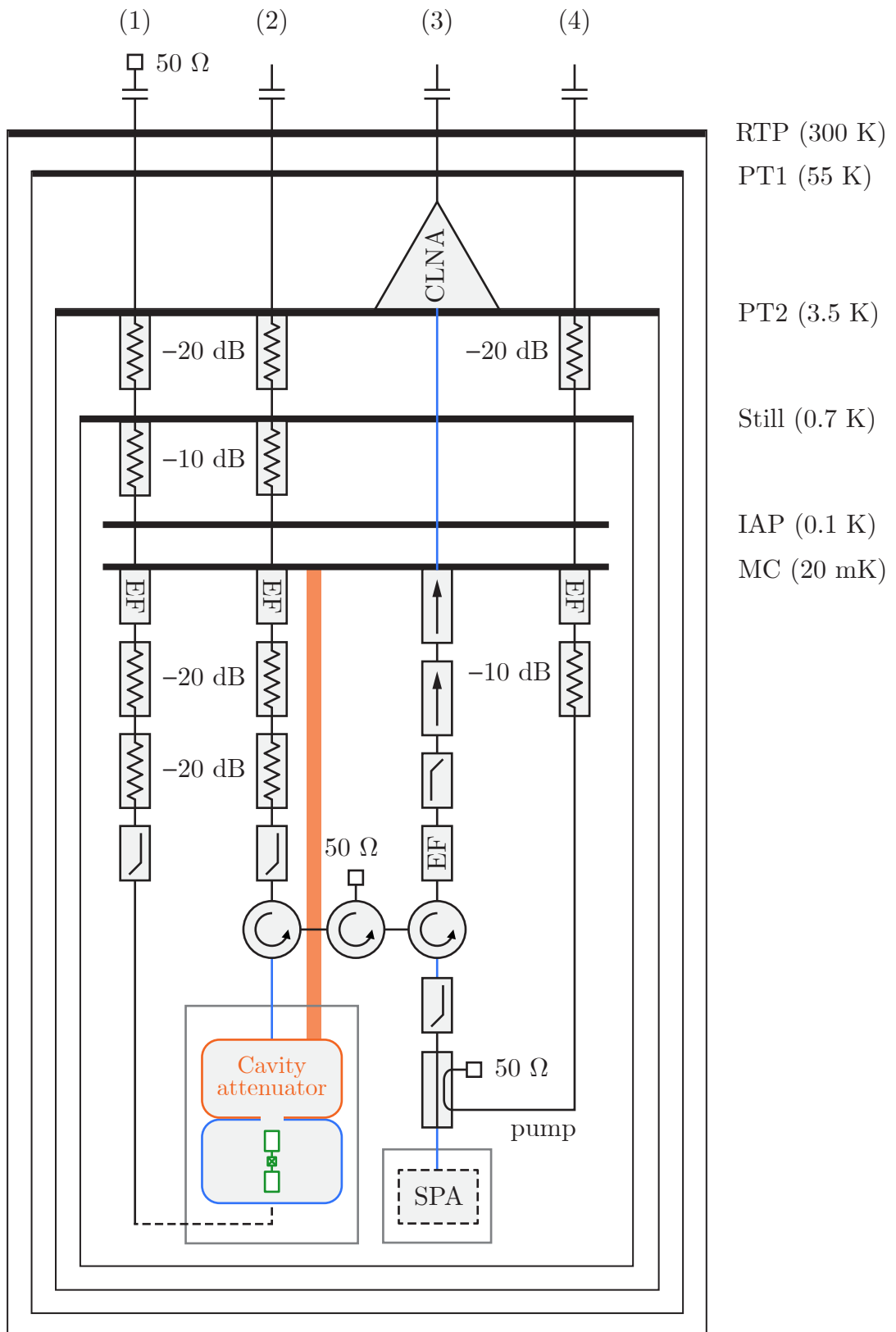


Figure 5.5: Cryogenic wiring diagram of the cavity attenuator experiment. Here the basic circuit symbols are the same as those in Figure 4.4. The coupled cavities—wrapped by three layers of aluminized boPET (Mylar) films—are housed in a high-magnetic-permeability mu-metal magnetic shield with an epoxy-and-carbon-coated copper wrap attached inside. The color codes for the cavity attenuator, readout cavity, and transmon artificial atom are the same as in Figure 5.7. The orange belt stands for the direct thermal link between the mixing chamber (MC) plate and the cavity attenuator. Nb–Ti superconducting coaxial cables are colored in blue. The four lines at the top of the dilution refrigerator, from left to right, are for (1) ancillary transmon drive, (2) readout input and transmon drive, (3) readout output, and (4) parametric amplifier pump. The leftmost input line—terminated by a $50\ \Omega$ load at the room temperature—is weakly coupled to the aluminum readout cavity (with a coupling quality factor on the order of 10^6), and is connected only in the control experiment described in Section 5.4. Its connection to the readout cavity is thus represented using a dashed line. The SNAL parametric amplifier (SPA)—also shown in a dashed box—was installed in selected data-collecting cycles and operated in the phase-preserving mode. The parametric pump of the SPA was delivered through a 20 dB directional coupler to the same port as readout signals. The DC current line for the SPA magnet is not shown in this diagram.

in Figure 5.7. A cavity attenuator is connected to the coupling aperture of the aluminum readout cavity housing a transmon qubit. Microwave measurement of the coupled cavities can be performed in reflection. This configuration provides maximum protection against incident photon noise—the transmon is not directly exposed to any excess radiation coming from the transmission lines. Consequently, thermal-photon-induced qubit dephasing can be studied in detail. However, this configuration also degrades the measurement signal-to-noise ratio because the readout signal has been attenuated before being amplified by the output chain. For instance, a dissipative cavity with a 10 dB on-resonance attenuation at the readout port necessarily imposes a factor of ten reduction on the total measurement efficiency, given other conditions

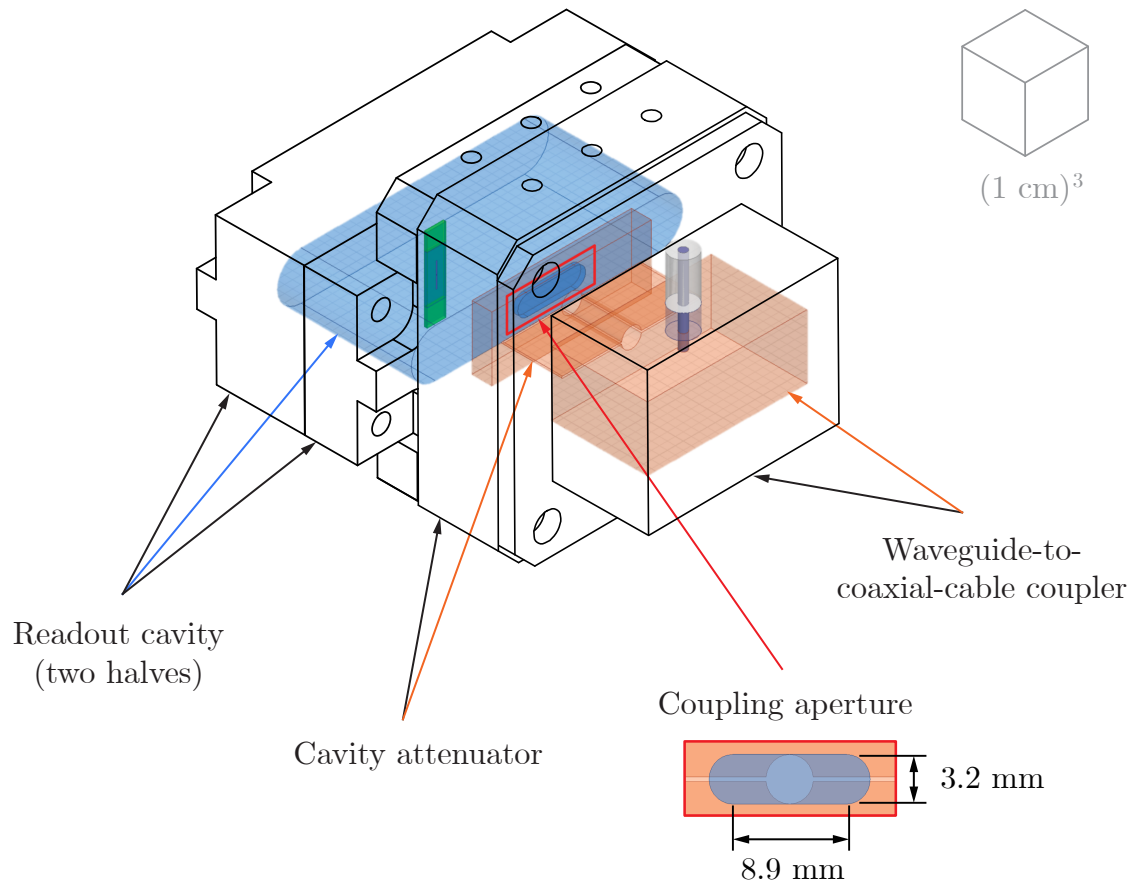


Figure 5.6: Assembly drawing of the cavity attenuator coupled to a 3D circuit QED module. The external dimensions of the system are delineated by the black lines, while the colored drawing displays the internal structure as used in the finite-element-method based (FEM) electromagnetic simulation software (Ansys HFSS). Blue: aluminum readout cavity. Orange: brass or copper cavity attenuator and the waveguide-to-coaxial-cable coupler, home-designed with a cross-section matching that of the WR-90 waveguide ($22.86 \text{ mm} \times 10.16 \text{ mm}$). The coupling aperture between the readout cavity and the cavity attenuator is depicted in the zoomed-in cross-section drawing in the upper-left corner (enclosed by the red box). The dimensions of the wire EDM cavity (partly shown in the background of this profile drawing) has been described in Figure 5.3. The sapphire chip is colored in green, on which sits a standard transmon sample (see Figure 4.1). The system is measured in reflection through the subminiature version A (SMA) coaxial transmission line connected to the pin coupler on the waveguide adapter.

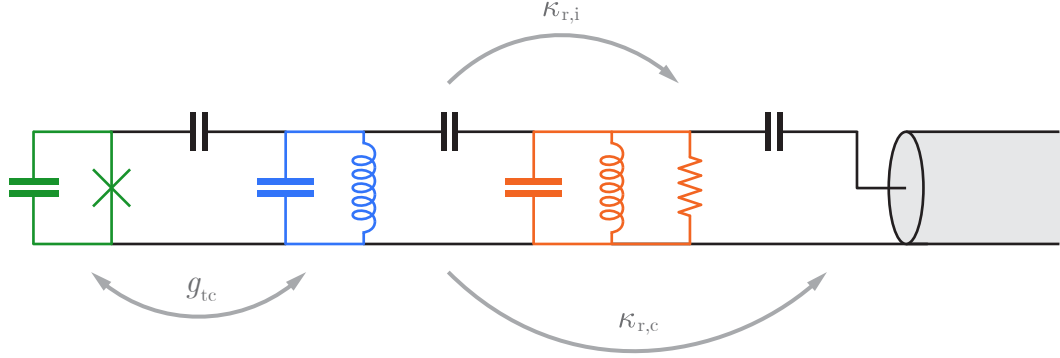


Figure 5.7: Resonant circuit model of a cavity attenuator (orange, “a”) coupled to a standard circuit QED module consisting of a transmon artificial atom (green, “t”) capacitively coupled to a superconducting readout cavity (blue, “c”). The linear coupling strength between the transmon and the superconducting readout cavity is denoted again using g_{tc} . The internal dissipation rate to the cold reservoir and the external coupling rate to the transmission of the *hybridized* readout mode (“r”) between the superconducting readout cavity and the dissipative cavity attenuator are labeled as $\kappa_{r,i}$ and $\kappa_{r,c}$, respectively.

of the output chain being the same. This problem could be solved by in situ quantum limited amplification, which will be discussed in Chapter 6.

It is worth noting that one of the ideas behind our experiment—introducing a cold dissipation source in the path of quantum signals—is similar to what has been introduced in Rigetti *et al.* [2012]; alternatively, the qubit dephasing can also be suppressed by reducing the coupling rate of the readout cavity to the output line [Sears *et al.*, 2012]. Compared to these strategies, our two-cavity modular approach provides more flexibility in experimental design. In addition, the cavity attenuator filters out off-resonance radiation and thus further suppresses the radiative decay of the qubit [Esteve *et al.*, 1986; Houck *et al.*, 2008], acting as an effective Purcell filter [Reed *et al.*, 2010a].

The two coupled linear resonant cavity modes—one in the cavity attenuator and

the other in the aluminum readout cavity—form two *uncoupled* eigenmodes after hybridization. Both of them are linearly coupled to the transmon and can thus be used for the qubit readout. Using the notations explained in the caption of Figure 5.7, if one of the hybridized readout modes is denoted by the bosonic operator \hat{r} , its dynamics is governed by the Heisenberg–Langevin equation—

$$\dot{\hat{r}} = -i(\omega_r - \chi_{\text{tr}}\hat{t}^\dagger\hat{t})\hat{r} - \frac{\kappa_r}{2}\hat{r} + \sqrt{\kappa_{r,c}}\hat{r}_{\text{in},c} + \sqrt{\kappa_{r,i}}\hat{r}_{\text{in},i}, \quad (5.4)$$

in which ω_r is the hybridized readout mode frequency; χ_{tr} is the dispersive frequency shift between the transmon and the readout mode; $\kappa_r = \kappa_{r,i} + \kappa_{r,c}$ is the total readout mode linewidth.

In the absence of any signal inputs, the population of the readout mode is subject to the thermal fluctuations of the internal dissipation and external coupling reservoirs—

$$\langle \hat{r}_{\text{in},i}^\dagger(t) \hat{r}_{\text{in},i}(t') \rangle = \bar{n}_{\text{th},i} \delta(t - t'), \quad (5.5)$$

$$\langle \hat{r}_{\text{in},c}^\dagger(t) \hat{r}_{\text{in},c}(t') \rangle = \bar{n}_{\text{th},c} \delta(t - t'), \quad (5.6)$$

or equivalently expressed in the frequency domain—

$$\langle (\hat{r}_{\text{in},i}[\omega])^\dagger \hat{r}_{\text{in},i}[\omega'] \rangle = 2\pi \bar{n}_{\text{th},i} \delta(\omega - \omega'), \quad (5.7)$$

$$\langle (\hat{r}_{\text{in},c}[\omega])^\dagger \hat{r}_{\text{in},c}[\omega'] \rangle = 2\pi \bar{n}_{\text{th},c} \delta(\omega - \omega'), \quad (5.8)$$

if the Fourier transform of an operator \hat{O} is defined as

$$\hat{O}[\omega] = \int \hat{O}(t) e^{i\omega t} dt. \quad (5.9)$$

In the above equation, the average thermal photon populations of the internal and

external reservoirs are denoted by $\bar{n}_{\text{th},i}$ and $\bar{n}_{\text{th},c}$, respectively. Therefore, one can write the thermal photon population in the readout mode—

$$\bar{n}_{\text{th}} = \langle \hat{r}^\dagger(t) \hat{r}(t) \rangle = \frac{1}{(2\pi)^2} \iint \langle (\hat{r}[\omega])^\dagger \hat{r}[\omega'] \rangle e^{i(\omega' - \omega)t} d\omega d\omega'. \quad (5.10)$$

In the absence of transmon dynamics, Equation (5.4) can be solved in the frequency domain—

$$\hat{r}[\omega] = \frac{\sqrt{\kappa_{r,c}} \hat{r}_{\text{in},c}[\omega] + \sqrt{\kappa_{r,i}} \hat{r}_{\text{in},i}[\omega]}{\frac{\kappa_r}{2} - i(\omega - \omega_r)}, \quad (5.11)$$

and hence Equation (5.10) can be computed as

$$\bar{n}_{\text{th}} = \frac{1}{2\pi} \int \frac{\bar{n}_{\text{th},c} \kappa_{r,c} + \bar{n}_{\text{th},i} \kappa_{r,i}}{\frac{\kappa_r^2}{4} + (\omega - \omega_r)^2} d\omega = \frac{\bar{n}_{\text{th},c} \kappa_{r,c} + \bar{n}_{\text{th},i} \kappa_{r,i}}{\kappa_r}. \quad (5.12)$$

This result is intuitively simple: the average thermal population of the readout mode is the weighted average of the thermal populations of its internal and external reservoirs. Therefore, to reduce $\langle \hat{r}^\dagger(t) \hat{r}(t) \rangle$ in the presence of a finite $\bar{n}_{\text{th},c}$ due to the residual thermal population in the cryogenic microwave circuitry, it is desirable that $\bar{n}_{\text{th},i} \ll \bar{n}_{\text{th},c}$ and meanwhile $\kappa_{r,i} \gg \kappa_{r,c}$ —namely, the readout mode is under-coupled to the external transmission line while being cooled by a well-thermalized internal reservoir.

We measured the 0.3 mm-gap brass cavity attenuator—described in the previous section—coupled to a transmon–aluminum readout cavity system. As presented in Figure 5.8, the reflected signal off the coupled system, measured using a VNA, shows two hybridized modes centered at 7.573 GHz and 7.719 GHz. Using the measured trace, we estimated using two-mode spectroscopy fitting that the mode centered at 7.57 GHz participates 79% in the aluminum cavity and 21% in the brass cavity, while

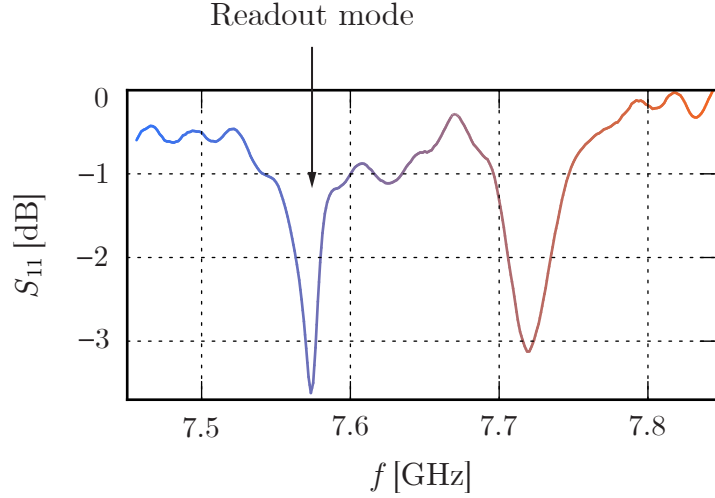


Figure 5.8: Reflection spectroscopy of a cavity attenuator coupled to a circuit QED module. The blue and orange colors show the relative participation of the aluminum readout cavity and the brass cavity attenuator, respectively. Among the two hybridized modes, the one with a lower resonant frequency and a larger participation in the aluminum cavity is employed as the readout mode in the following measurements.

the mode centered at 7.719 GHz participates 21% in the aluminum cavity and 79% in the brass cavity. We then used the mode at 7.573 GHz to readout the qubit since it participates more in the aluminum cavity and thus has a larger dispersive shift. The ratio of internal dissipation to external coupling for this readout mode is estimated to be $\kappa_{r,i}/\kappa_{r,c} \approx 6$. In our experimental system, $\bar{n}_{th,i} \ll \bar{n}_{th,c}$ since the brass cavity is in thermal equilibrium with the mixing chamber. Therefore, we obtain the residual thermal population of the readout mode to be $\bar{n}_{th} \approx \bar{n}_{th,c}/7$, indicating 85% of residual photons are dissipated in the cold cavity attenuator.

5.4 Improving qubit coherence times

We tested the performance of these cavity attenuators by coupling them to a circuit QED system and measuring the qubit coherence properties while varying the mixing

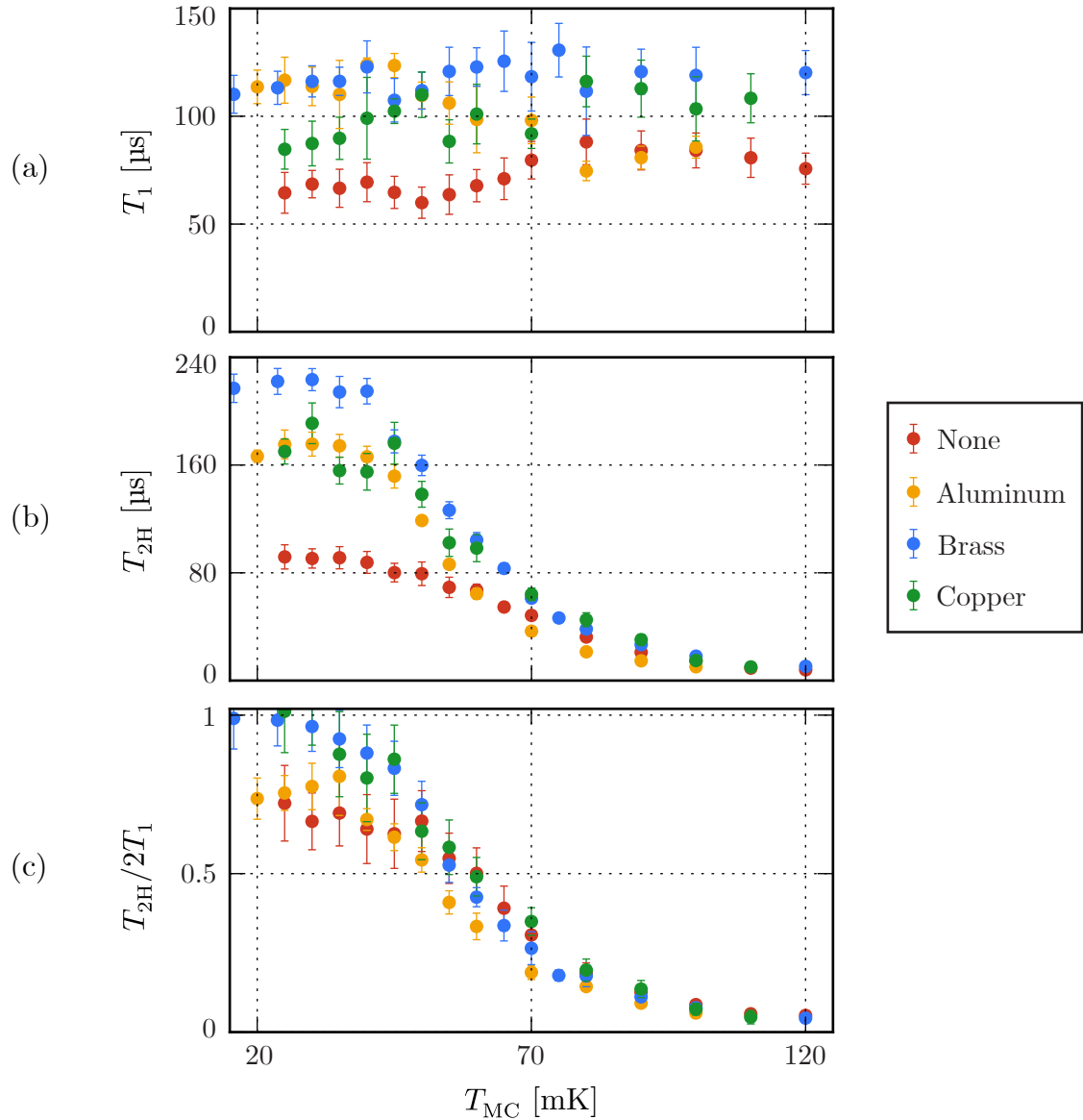


Figure 5.9: Qubit coherence times with and without cavity attenuators. (a) Energy relaxation time T_1 , (b) Hahn echo decoherence time T_{2H} , and (c) $T_{2H}/2T_1$ with and without cavity attenuators were measured with variable T_{MC} —the temperature of the mixing chamber of the dilution refrigerator. All the data are collected on transmon A. Error bars include both the measurement imprecision and the fluctuation of T_1 over the data acquisition time of one hour. Red circles: no attenuator. Yellow circles: aluminum cavity attenuator with a 0.08 mm gap. Blue circles: brass cavity attenuator with a 0.3 mm gap. Green circles: copper cavity attenuator with a 0.08 mm gap.

Transmon	f_t^{01} [GHz]	K_t [GHz]
A	4.75	0.25
B	5.09	0.25

Table 5.2: The 0–1 transition frequency f_t^{01} and anharmonicity $K_t = f_t^{01} - f_t^{12}$ of the two transmon qubits (A and B) in this experiment, measured using the standard two-tone and three-tone spectroscopy methods.

chamber (MC) temperature T_{MC} of the dilution refrigerator. Energy relaxation time T_1 and Hahn echo decoherence time T_{2H} were measured as a function of temperature for two transmon–cavity systems, labeled A and B, coupled with brass and copper cavity attenuators as well as without an attenuator. As a control experiment, we also measured an aluminum cavity filter with identical dimensions to the copper attenuator that however provides no attenuation on resonance. The transmon frequencies and anharmonicities are listed in Table 5.2. Data taken on transmon A are shown in Figures 5.9(a) and 5.9(b), with experimental conditions summarized in Table 5.3. Each T_1 and T_{2H} data point is the average of ten measurements performed over the course of around one hour.

From these results we can infer that cavity attenuators dissipate excess photons in the readout mode and suppress photon-induced qubit dephasing. We see in Figure 5.9(b) that T_{2H} for transmon A at base temperature is improved by more than a factor of two with cavity attenuators and can exceed 220 μs . Meanwhile, Ramsey T_{2R} (not shown) was also improved from 28–35 μs without a cavity attenuator to 41–43 μs with the brass attenuator and 35–40 μs with the copper attenuator. The difference between T_{2R} and T_{2H} indicates that low-frequency noise in our measurement setup is causing qubit dephasing. However, since the dephasing due to residual thermal photons cannot be filtered out by a single echo pulse [Sears *et al.*, 2012], we use T_{2H}

Attenuator	$T_{\text{MC}} = 25 \text{ mK}$							
Material	f_r	$\kappa_{r,i}/2\pi$	$\kappa_{r,c}/2\pi$	$\chi_{\text{tr}}/2\pi$	$T_{2\text{H}}/2T_1$	\bar{n}_{th}	T_{eff}	P_e
	[GHz]	[MHz]	[MHz]	[MHz]	[0–1]	$[\geq 0]$	[mK]	[0–1]
None	7.573	n/a	16.5	1.5	$0.72^{+0.12}_{-0.12}$	4×10^{-3}	65	0.01
Aluminum	7.847	n/a	0.24	1.1	$0.75^{+0.06}_{-0.06}$	1×10^{-3}	55	0.01
Brass	7.573	11.4	1.9	1.2	$0.98^{+0.02}_{-0.08}$	2×10^{-4}	43	0.005
Cu	7.857	7.1	0.9	1.1	$1.00^{+0.00}_{-0.12}$	2×10^{-4}	44	0.04

Table 5.3: Frequency f_r , rates $\kappa_{r,i}$ and $\kappa_{r,c}$ of the readout mode, dispersive shift χ_{tr} , $T_{2\text{H}}/2T_1$, estimated *upper bounds* of \bar{n}_{th} and T_{eff} at $T_{\text{MC}} = 25 \text{ mK}$, and transmon excited-state population P_e for each experiment in Figure 5.9. The values of $\kappa_{r,i}$ for the experimental rounds without an attenuator and with an aluminum filter are below fitting errors. The wire-EDM-cutting gaps of the aluminum, brass, and copper cavities are 0.08 mm, 0.3 mm, and 0.08 mm, respectively.

to inform us about the effect of the cavity attenuator on the residual thermal photon population.

An important figure of merit to quantify qubit dephasing is the dimensionless value $T_{2\text{H}}/2T_1 = T_\phi/(T_\phi + 2T_1)$, which is close to its unity upper limit when the dephasing time satisfies $T_\phi \gg T_1$. As shown in Figure 5.9(c), at base temperature we measured $T_{2\text{H}}/2T_1 = 0.98 (+0.02/-0.08)$ with the brass attenuator. This ratio is $1.00 (+0.00/-0.12)$ with the copper attenuator.³ In both experimental rounds, the average T_ϕ is close to 10 ms, much longer than T_1 , indicating qubit coherence is limited by relaxation rather than pure dephasing. If we attribute all the qubit dephasing to the residual thermal photon population in the fundamental mode of the readout cavity, according to Equation (5.1), the *upper bound* of \bar{n}_{th} is estimated to

³Here the error bars are asymmetric because $T_{2\text{H}}/2T_1$ cannot exceed 1 in principle.

be on the order of 10^{-4} , corresponding to an effective mode temperature of $T_{\text{eff}} \leq 40$ – 45 mK. As a comparison, in the absence of cavity attenuators, transmon A in the same measurement setup has $T_\phi \approx 0.3$ ms and $T_{2\text{H}}/2T_1 = 0.72 \pm 0.12$, indicating $\bar{n}_{\text{th}} \leq 4 \times 10^{-3}$ and $T_{\text{eff}} \leq 65$ mK. The transmon excited-state populations in these experiments were measured with the three-tone protocol reported in Geerlings *et al.* [2013]. The results are listed in Table 5.3.

To verify the efficacy of these cavity attenuators, we further performed two control experiments. First, in the same geometry as the 0.08 mm-gap copper attenuator, we machined an aluminum cavity. It becomes a lossless cavity filter below 1 K and thus should leave the thermal photon population of the readout mode unchanged. By coupling it to transmon A and performing the same temperature-dependent measurements, we acquired the yellow circles in Figure 5.9. At $T_{\text{MC}} = 25$ mK, we measured $T_{2\text{H}}/2T_1 = 0.75 \pm 0.06$, indicating $\bar{n}_{\text{th}} \leq 1 \times 10^{-3}$ and $T_{\text{eff}} \leq 55$ mK, which are between the no-attenuator and brass/copper-attenuator results. Therefore, we conclude that the enhancement of qubit coherence in our cavity attenuator experiments is not only due to lossless filtering, which rejects the incoming thermal photons that would populate the higher modes of the readout cavity. Dissipation is necessary for reducing high-frequency dephasing noise caused by residual thermal photons in the readout mode.

As a second control, we repeated the copper-attenuator experiment but added to the aluminum readout cavity a copper coaxial cable coupler with coupling rate to the readout mode around 5 kHz $\ll \kappa_c, \kappa_i$. This input line with 70 dB cold attenuation was terminated by a 50Ω load at room temperature (see Figure 5.5). At $T_{\text{MC}} = 25$ mK, we observed $T_1 = 100 \pm 8$ μs , $T_{2\text{H}} = 171 \pm 10$ μs , and obtained $T_{2\text{H}}/2T_1 = 0.86 \pm 0.09$, $\bar{n}_{\text{th}} \leq 1 \times 10^{-3}$, corresponding to $T_{\text{eff}} \leq 55$ mK (data not shown in the Figures). We conclude that even a weakly coupled port has non-negligible contribution to qubit dephasing if it is not directly thermalized to the mixing chamber. Based on this and

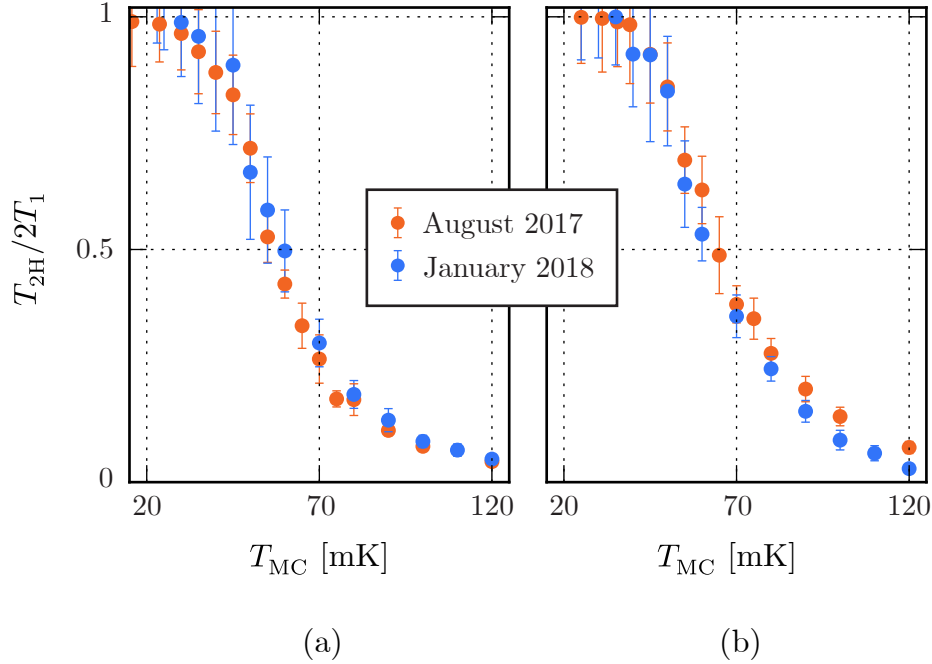


Figure 5.10: Repeatability test for qubit coherence time improvements. The consistency of $T_{2H}/2T_1$ across multiple samples and cooldowns when the qubits are protected by the 0.3 mm brass cavity attenuators has been verified. For transmon B, its energy relaxation time $T_1 \approx 50 \pm 10 \mu\text{s}$ when $T_{MC} \leq 100$ mK.

other experiments in our lab, we suspect—in particular—that the Teflon in the coaxial cable is a source of excess photons. Therefore, to achieve the best qubit coherence, ideally every coupling port on the readout cavity should be properly protected by a cold cavity attenuator.

We tested the consistency of the performance of cavity attenuators by conducting experiments on the two transmons A and B in multiple cooldowns. Plotted in Figure 5.10 are results with 300 mm-gap brass attenuators. These two cooldowns were separated by five months during which time the attenuators were removed from the setups. For both qubits, temperature-dependent measurements showed good reproducibility on $T_{2H}/2T_1$, which is close to one on average and larger than 0.9 within one

standard deviation at the base temperature. We believe that the reliable performance of these attenuators arises from their well-understood material properties, geometric structures, and fabrication processes.

5.5 Measuring thermal photon populations

Precisely measuring T_ϕ and \bar{n}_{th} becomes a challenging task when $T_2 \approx 2T_1$, as the fluctuation of T_1 over time causes the error bar of $\Gamma_\phi = 1/T_\phi$ to exceed the value of Γ_ϕ itself. In order to mitigate the impact of the T_1 fluctuation on the determination of the residual \bar{n}_{th} at base temperature, we performed noise-induced dephasing measurement on both transmons. Adopting a method similar to the one reported in Yan *et al.* [2016] and Yan *et al.* [2018], we amplitude-modulated broadband white noise at the IF frequency band (0–80 MHz in our situation) onto a continuous-wave microwave signal at the hybridized readout frequency using an IQ mixing setup similar to the chain shown in Figure 4.5: for white noise generation at RF frequencies, the IF noise generators should replace the deterministic analog outputs of the arbitrary waveform generator (AWG) at the mixer input ports, and the following preamplifier becomes optional if sufficient noise power can be delivered to the circuit QED module so as to induce significant qubit dephasing (see Section 3.3). The total average photon population in the readout mode becomes $\bar{n}_{\text{tot}} = \bar{n}_{\text{add}} + \bar{n}_{\text{th}}$, in which \bar{n}_{add} is proportional to the output power of the IF broadband noise generators. By measuring \bar{n}_{tot} as a function of the added noise power. The experimental results are shown in Figure 5.11. Finally, through linear regression, we obtained $\bar{n}_{\text{th}} = 2(+3/-2) \times 10^{-4}$ for transmon A and $\bar{n}_{\text{th}} = 2(+4/-2) \times 10^{-4}$ for transmon B when they are protected by copper cavity attenuators,⁴ corresponding to $T_{\text{eff}} \leq 44$ mK. These results are consistent with

⁴Here again the error bars of \bar{n}_{th} are asymmetric because the average thermal photon population has to be non-negative.

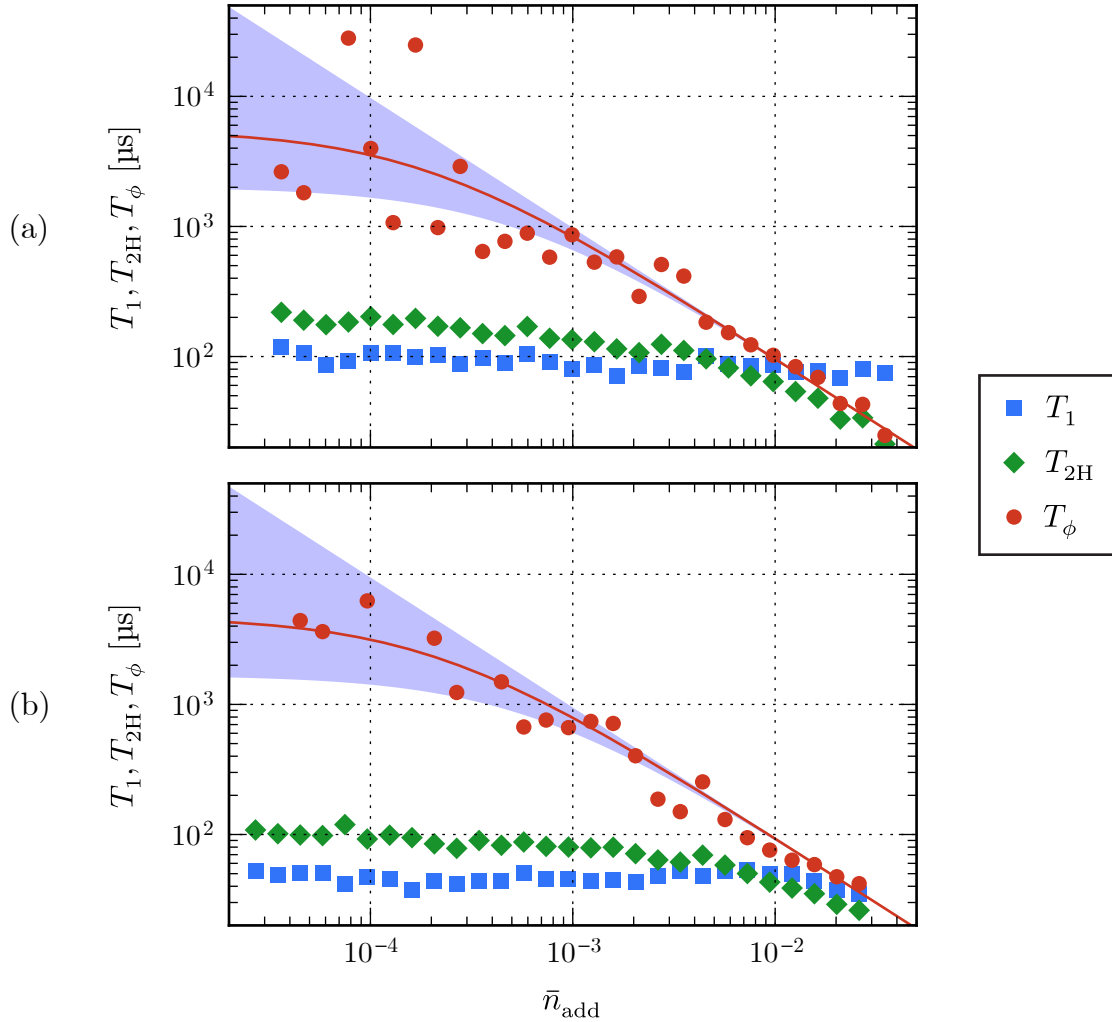


Figure 5.11: Noise-induced qubit dephasing measurement of the average thermal population \bar{n}_{th} in the hybridized readout mode. Data are collected from (a) transmon A protected by a 0.08 mm copper cavity attenuator, and (b) transmon B protected by a 0.13 mm copper cavity attenuator. In each subfigure, T_1 (blue squares) and T_{2H} (green diamonds) are plotted versus the average added thermal photon number \bar{n}_{add} . The extracted values of T_ϕ (red circles) are shown together with the fitting results (red curves). The purple shadows represent the error ranges of the linear regression within one standard deviation.

the order-of-magnitude estimate in Section 5.4, and lower than the values in two other recent reports [Yan *et al.*, 2018; Yeh *et al.*, 2017] that also aimed at reducing \bar{n}_{th} in circuit QED systems.

5.6 Conclusions and future directions

The results of our experiments have two important implications:

- (i) Cavity attenuators can reproducibly reduce \bar{n}_{th} of the readout cavity by an order of magnitude and extend $T_{2\text{H}}$ close to the $2T_1$ limit.
- (ii) The improvement of qubit coherence by cavity attenuators will nonetheless be impacted if the readout cavity has any direct coupling to the input and output lines, even if the coupling is very weak.

Our experiment suggests that excess thermal photons inevitably come from the commercial microwave components at the base temperature plate of the dilution refrigerator. Consequently, cavity attenuators should be employed as a standard device to create a cold black-body radiation environment for superconducting quantum circuits.

With these being said, two problems need to be solved before cavity attenuators can have broader applications in circuit QED experiments:

- (a) In the experiments reported in this paper, qubit control and readout tones share the same coupling aperture protected by a cavity attenuator centered near the readout frequency. As a result, qubit control pulses, which are by 2.5–3 GHz lower than the readout frequency—are mostly filtered out by the resonant cavity, which slows down the qubit state manipulation. This can be avoided by separating the qubit control and readout ports and protecting them with cavity attenuators centered at different frequencies. More desirably, it is

possible to design a *multi-pole* dissipative filter whose bandwidth covers a few qubits simultaneously.

- (b) In the current measurement setup, while excess thermal photons are dissipated in the cold reservoir, the cavity attenuator also attenuates the quantum signals at the sole port of the qubit readout cavity. Consequently, the measurement signal-to-noise ratio is not sufficient for the high-fidelity single-shot dispersive readout of qubit states. This problem can be addressed by moving the cavity attenuator to other locations in the cryogenic microwave circuitry—for instance, on the input line before the circulator, or at the output port of the quantum-limited amplifier. However, it can be inferred from our control experiments that these arrangements, while avoiding the extra attenuation of readout signals before the amplifier chain, will likely demonstrate less-than-ideal protections for the qubit compared to our experimental setup, by exposing the circuit QED module to the residual thermal photons from the circulator array and the microwave cables immediately connected to the readout cavity. Here we are facing the general conflict between coherence/protection and controllability/measurability in quantum information machines, which has been explained in this dissertation as early as Section 1.2.

A compact solution to the above issue (b) demands an in-situ quantum-limited amplification scheme inside the readout cavity, such that sufficient readout SNR can be obtained despite the reduction in the measurement efficiency of the external output line caused by the artificial cold dissipative device. In the next chapter, I will report our latest work on implementing the intra-cavity amplification of qubit readout signals through engineering multi-mode Josephson quantum circuits—namely, by inventing a new superconducting artificial molecule— Π -mon, which integrates the qubit and

the on-chip amplifier degrees of freedom. From complementary angles, the cavity attenuator and the Π -mon artificial molecule are designed to assist the protection and acquisition of quantum information in superconducting Josephson circuits. More promises of their combination will be discussed in Chapter 7.

Chapter 6

Π -mon:

An Artificial Molecule for the Intra-Cavity Amplification of Qubit Readout Signals

What sort of information is an instrument capable of giving us? To what extent is what the instrument gives us colored by the instrument itself, or is the instrument capable of revealing to us something “independent of the instrument”? We would not have asked this last question before the advent of quantum theory. We now know that this is a very important question indeed for a certain range of phenomena, and that in this range instrument-of-observation and object-of-observation cannot be separated from each other.

Percy Williams Bridgman [1959]

As I have argued in the ending paragraph of the previous chapter, the introduction of extra-cavity cold dissipative attenuators on the qubit readout circuitry is strongly motivating the implementation of intra-cavity amplification schemes to retain the level of measurement SNR required in a high-fidelity single-shot qubit readout. Meanwhile, even in the standard circuit QED measurement setup (as shown in Figure 3.6), a quantum-limited preamplifier inside the readout cavity will be able to recompense

the quantum electrical signals for their parasitic losses before the external Josephson parametric amplifier, which are—in practical systems—the leading constraint for the nonideal measurement efficiency of the output chain. Following the general principles summarized in Section 1.3.4, the physical realization of an intra-cavity preamplifier for quantum measurements again requires dissipation-free nonlinear circuit elements, for which Josephson junctions are the natural candidate. Moreover, this in-situ Josephson preamplifier will allow quantum circuit engineers to redesign the coupling scheme between the superconducting qubit and the microwave photons in the readout cavity, so as to pursue more ideal qubit coherence properties and readout performance.

In this chapter, I will present our novel design and preliminary characterization results of a superconducting artificial molecule— Π -mon, which integrates a transmon-like qubit mode and a Josephson junction array to achieve the in-situ amplification of quantum readout signals inside the circuit QED module. Following a brief review of the key motivations for intra-cavity preamplifiers in Section 6.1, I will outline the design principles of the Π -mon artificial molecule in Section 6.2 and analyze its circuit model and Hamiltonian in Section 6.3. The measurement setup and experimental parameters of our Π -mon sample will be introduced in Section 6.4. In the next three sections, I will report our preliminary experimental results: Section 6.5 on the nonlinear dynamics of the bright “preamplifier” mode; Section 6.6 on the coherence properties of the dark “qubit” mode; and Section 6.7 on the demonstrations of the intra-cavity gain and single-shot qubit readout. Finally, in Section 6.8, I will propose upcoming experimental directions in the search for higher intra-cavity gains and lower qubit measurement back-actions.

6.1 Preamble: purposes of intra-cavity preamplifiers

Despite not currently being the most standard tool in quantum circuit experiments, intra-cavity Josephson parametric preamplifiers for quantum measurements have been present for nearly two decades, with which single-shot microwave readouts of superconducting qubits were realized prior to those using linear circuit QED measurement systems. The earliest relevant example consists of a single driven Josephson junction in its nonlinear bifurcation regime [Siddiqi *et al.*, 2006b, 2005, 2004], which can be dispersively coupled to a quantonium artificial atom and read out its qubit state [Boulant *et al.*, 2007; Siddiqi *et al.*, 2006a], or be embedded in a microwave resonator [Manucharyan *et al.*, 2007] and read out the state of a quantonium [Metcalf *et al.*, 2007] or transmon qubit [Mallet *et al.*, 2009; Schmitt *et al.*, 2014]. Similar principles can be applied to read out a flux qubit by coupling it to a driven SQUID resonator in its nonlinear bifurcation regime [Krantz *et al.*, 2016; Lupaşcu *et al.*, 2006, 2007]. In two more recent experiments, a SQUID array is dispersively coupled to a transmon with linear [Eddins *et al.*, 2019] and cross-Kerr [Dassonneville *et al.*, 2020] interactions, respectively; both systems have demonstrated on-chip gains with the SQUID array in the non-bifurcation regime, which in principle should cause fewer measurement-induced qubit-state-transition events and preserve higher QND fidelities compared to the bifurcated latching readouts reported in earlier works.

Figure 6.1 depicts a generic circuit QED measurement setup involving a preamplifier inside the readout cavity to enhance the level of qubit readout signals before the external amplifier chain, which is composed of—in the standard order—a linear quantum-limited Josephson parametric amplifier (QLA), a semiconductor cryogenic low-noise amplifier (CLNA), and more semiconductor room-temperature amplifiers (RTA). Among those experiments cited in the previous paragraph, all but the last

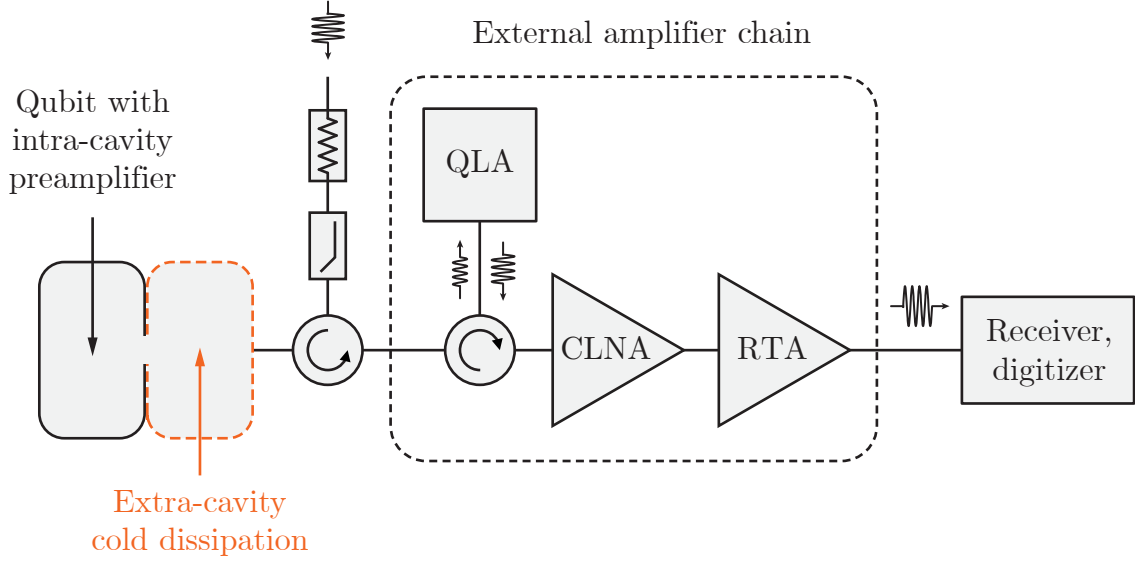


Figure 6.1: Idea of combining extra-cavity dissipation and intra-cavity amplification in the circuit QED measurement setup. Compared to the standard measurement setup shown in Figure 3.6, a pre-amplification scheme is introduced inside the circuit QED readout cavity to compensate for the parasitic loss channels for readout signals before the external quantum-limited amplifier (QLA), or if present, the purposefully installed extra-cavity cold dissipative reservoir—for instance, a cavity attenuator (colored in orange).

two were performed without the external linear QLA, in which photons from the non-linear readout resonator were directly sent to the semiconductor CLNA installed on the 4 K stage of the dilution refrigerator. However, the intra-cavity preamplifier can also be operated together with the external QLA on the base (mixing chamber) stage, as has been demonstrated in Eddins *et al.* [2019] and Dassonneville *et al.* [2020]. This arrangement has two major advantages:

- (i) With an intra-cavity pre-amplification stage, only a moderate level of parametric gain is required to be provided by the external QLA. Consequently, a larger gain bandwidth and a higher saturation power or dynamic range should be available at the external QLA, which have been serious goals for the optimization of

modular Josephson parametric amplifiers [Frattini *et al.*, 2018; Macklin *et al.*, 2015; O’Brien *et al.*, 2014; Planat *et al.*, 2020; Sivak *et al.*, 2019, 2020].

- (ii) The intra-cavity preamplifier can compensate for the parasitic dissipation of qubit readout signals between the readout cavity and the external QLA. These losses occur at the microwave coaxial cables, connectors, and in particular, the ferrite circulator array,¹ and often limit the overall measurement efficiency of the readout system. Boosting the readout SNR has been the most direct motivation for the in-situ implementation of parametric amplification schemes, which in principle minimizes added noise to the quantum signals and produces higher readout fidelities at a fixed readout power level.²

As derived from the above point (ii), an intra-cavity preamplifier would be particularly desirable if any artificial dissipative mechanism is introduced on purpose before the output amplifier chain—for instance, a resonant cavity attenuator as a cold thermal reservoir (see Chapter 5). In the particular arrangement depicted in Figure 6.1, the cavity attenuator is directly coupled to the circuit QED module to achieve the

¹Efforts have been made to replace these ferrite non-reciprocal devices with on-chip Josephson-circuit [Chapman *et al.*, 2016, 2017, 2019; Kerckhoff *et al.*, 2015; Lecocq *et al.*, 2020, 2017; Naaman *et al.*, 2016; Ranzani *et al.*, 2017; Rosenthal *et al.*, 2021; Sliwa *et al.*, 2015] and electromechanical realizations [Barzanjeh *et al.*, 2017; Bernier *et al.*, 2017; Mercier de Lépinay *et al.*, 2019; Peterson *et al.*, 2017].

²A slightly counterintuitive fact at first glance is that an intra-cavity preamplifier directly coupled to the qubit will not improve its overall measurement efficiency limited by external power-independent loss channels—for instance, the insertion loss of cables, connectors, and circulators as explained above. This can be understood from Equations (3.50) and (3.51): while the readout SNR is improved due to the in-situ amplification scheme, the measurement-induced qubit dephasing rate is also increased in proportion to SNR^2 , leaving η_m unchanged and still set by off-chip dissipation mechanisms. This situation is different from an external “modular” parametric amplifier, which improves the SNR but ideally induces no additional qubit dephasing due to the directionality of the output signal line, hence resulting in a higher η_m . Therefore, intra-cavity amplification should be more precisely understood as an effort to increase the measurement strength, rather than to add another modular stage prior to the output amplifier chain.

maximal protection for the superconducting artificial atom against residual thermal electromagnetic noise. An intra-cavity signal gain comparable to the added extra-cavity attenuation is then necessary so as to provide sufficient SNR for high-fidelity single-shot qubit readouts. The cavity attenuator was not installed in the measurement setup during the experimental rounds to be reported in this chapter, which are intended as proof-of-principle demonstrations for the new qubit readout scheme. But meanwhile, as will be shown in Section 6.4, our measurement system is compatible with add-on cavity attenuator or waveguide Purcell filter devices, which are designed to alter the electromagnetic environment of the circuit QED system for the improved protection of qubit coherence or encoded quantum information.

6.2 Design principles of the artificial molecule

The general approach of realizing intra-cavity amplification is to couple the superconducting artificial atom to nonlinear, low-dissipation microwave modes fabricated on the same solid-state chip. This multi-mode Josephson quantum circuit is often called a **superconducting artificial molecule**, wherein the most anharmonic degree of freedom serves as the qubit, and another degree of freedom with lower anharmonicity can be employed as the parametric amplifier. The output photons of this on-chip preamplifier can be directly released into a microwave transmission line connecting the off-chip amplifier chain. Alternatively, the on-chip preamplifier mode can be coupled—in the dispersive regime—to a linear microwave cavity, similar to the one in a standard circuit QED module. In this configuration, the different output states of the on-chip preamplifier will induce distinguishable shifts on the resonant frequency of the linear readout cavity, which can be detected through cavity reflection or transmission measurements as explained in Section 3.2.2.

In the current experiment, we are devising a two-step readout scheme involving

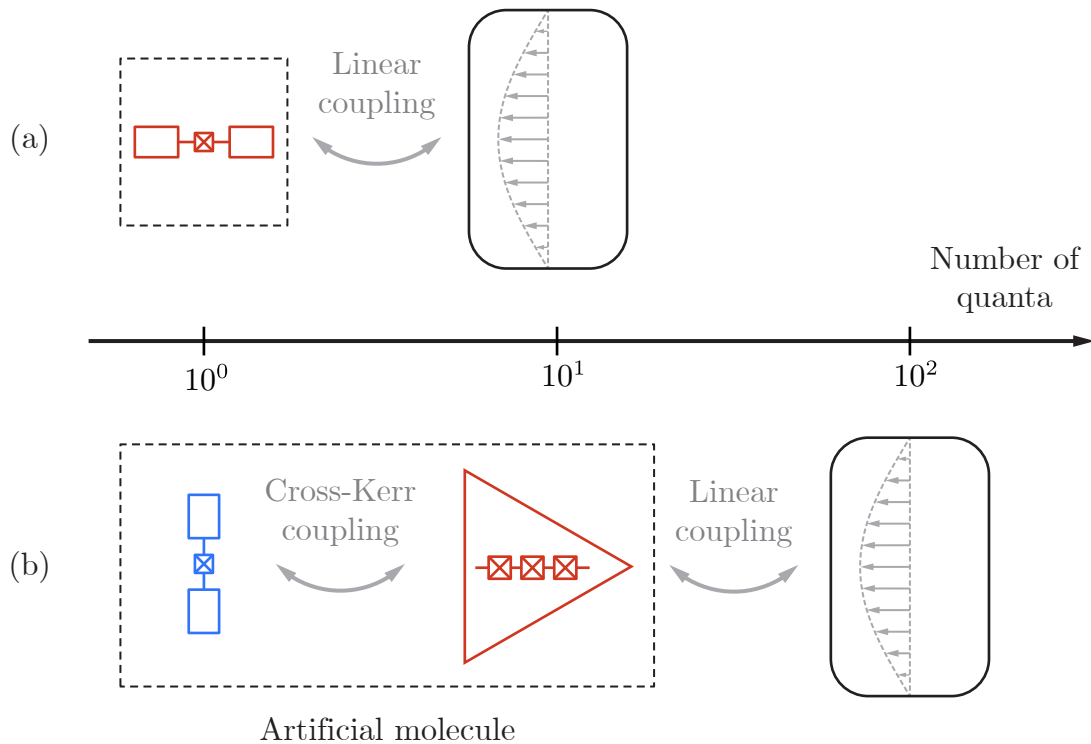


Figure 6.2: Illustration of the qubit readout scheme assisted by an intra-cavity preamplifier. (a) The standard circuit QED system wherein the qubit—represented here using a fixed-frequency transmon—is linearly coupled to the readout cavity. (b) A two-step readout scheme, in which the qubit is coupled to an on-chip Josephson preamplifier (represented as a Josephson-junction array inside a triangular amplifier symbol), the latter being coupled to a linear readout cavity. In this configuration, one wants to avoid the direct linear coupling between the transmon and the linear cavity. For experiments using 3D readout cavities, those on-chip components are enclosed in dashed black boxes, albeit the readout resonators can also be integrated on the solid-state chip using 2D planar technologies. The horizontal axis indicates—with an order-of-magnitude accuracy—the number of excitation quanta in each degree of freedom (a) most commonly adopted in experiments, and (b) conceived in our new measurement scheme. In the standard dispersive readout setup, although the cavity can be populated with a higher number of photons, it is generally not recommended due to excessive photon-induced qubit-state-transition events that are detrimental to the readout performance (see Section 3.4).

both an on-chip Josephson parametric preamplifier and a 3D superconducting linear readout cavity, as illustrated in the lower panel of Figure 6.2. This specific design is motivated by two major principles:

- (i) The system consists of a *strongly nonlinear* qubit oscillator, a *weakly nonlinear* on-chip preamplifier oscillator, and a *linear* cavity resonator. The on-chip preamplifier mode, with an intermediate degree of anharmonicity, is also going to be populated with an intermediate number of excitation quanta—on the order of 1–10, which is between that of the qubit (ideally limited to the $|0\rangle$ and $|1\rangle$ subspace) and the readout cavity (up to 10^2 or more photons).
- (ii) The on-chip preamplifier mode is designed to mediate the interaction between the qubit and the readout cavity, between which the direct linear coupling g_{tc} as in standard circuit QED modules (see Figure 1.5) ought to be avoided. A working mechanism is to linearly couple the preamplifier mode to the readout cavity, and meanwhile to perpendicularly arrange the electric dipole moments of the qubit and the preamplifier such that their leading interaction is of the cross-Kerr form (see Section 3.4). This layout is intended to minimize the spurious qubit-state transition events occurring in the midst of a measurement process while the readout cavity is populated with a large number of microwave photons, such that qubit readouts can be expected to show higher QND fidelities.

Combining (i) and (ii), in an ideal design, the artificial molecule is supposed to host both a high-coherence qubit mode that is decoupled from the readout cavity at the linear order, and a parametric preamplifier mode that provides a measurement interface between the qubit and readout photons. As an extra guideline, we are also refrained from building charge gates or flux loops in the artificial molecule circuit, such that the qubit mode is subject to fewer parasitic electromagnetic noise channels

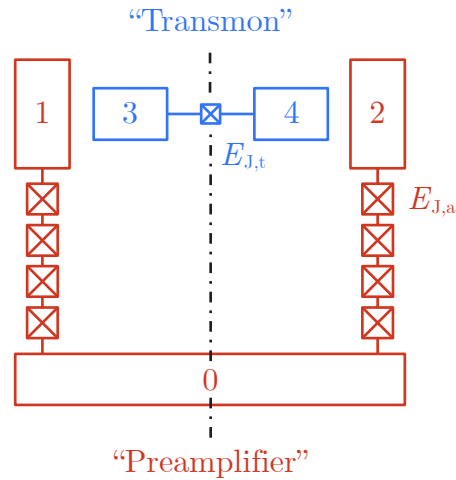


Figure 6.3: Introducing the Π -mon artificial molecule. The fixed-frequency transmon and the capacitively shunted Josephson junction arrays (“preamplifier”) are colored in blue and red, respectively. The dashed-dotted line at the center stands for the symmetric mirror. The numbers 0–4 label the five superconducting electrode pads, which will be used in the circuit analysis in the following section. The sizes of the electrode pads and their separations are not drawn in scale—see Figure 6.8 for the physical layout of the sample.

in pursuit of higher coherence times. And yet it is worth remarking on a constraint of the loop-free design: without an external magnetic flux, one will not have access to pure three-wave mixing elements in superconducting Josephson circuits [Fratini, 2021; Sivak *et al.*, 2019]. We will thus need to rely on the intrinsic four-wave mixing property of the Josephson nonlinearity to construct the integrated qubit–preamplifier subsystem.

6.3 Π -mon circuit: classical and quantum analysis

Following the guidelines listed above, our adopted design of the integrated qubit–preamplifier circuit—named the Π -mon because of the partial geometric resemblance—is presented in Figure 6.3. The artificial molecule consists of a standard fixed-

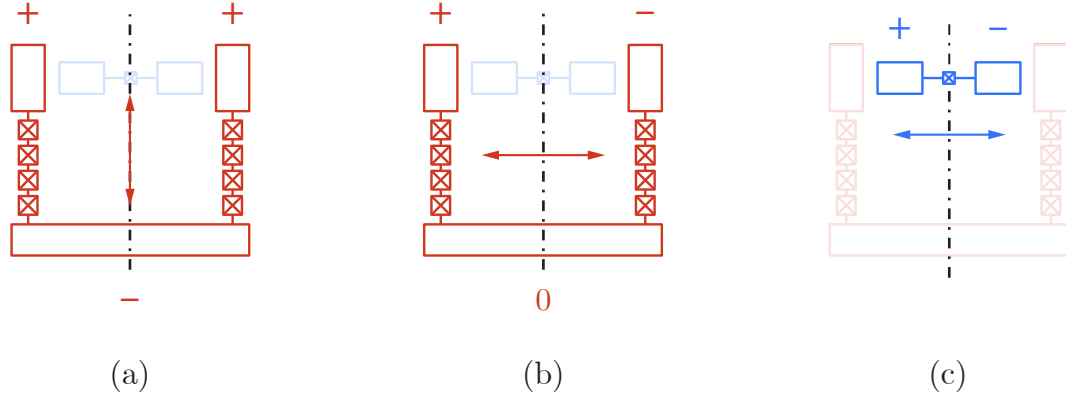


Figure 6.4: Three uncoupled linear modes in the Π -mon artificial molecule. Referred to the central vertical mirrors (dashed-dotted lines): (a) symmetric mode and (b) antisymmetric mode of the preamplifier oscillator; (c) antisymmetric mode of the transmon. The electric dipole moments of the three modes are shown using double-arrows in each drawing. “+”, “-”, and “0” denote the positive, negative, and neutral charge distributions on the electrode pads at a particular moment during the electromagnetic oscillation.

frequency transmon—a small Josephson junction (Josephson energy $E_{J,t}$) shunted by a coplanar capacitor (Coulomb charging energy $E_{C,t}$)—and two capacitively shunted Josephson junction arrays. Each array contains $N_J = 4$ identical Josephson junctions (Josephson energy $E_{J,a}$) in series. The two junction arrays are connected to their separate and yet identically sized upper electrode pads, while sharing the same lower electrode pad, forming an inversed “ Π ”-shape Josephson nonlinear oscillator. The planar circuit layout obeys a mirror symmetry, which is essential to its working principles. The transmon and the preamplifier oscillator are capacitively coupled without forming any closed Josephson-junction loop.

6.3.1 Bright, dark, and mediator modes

The three *uncoupled* linear modes in the Π -mon circuit can be easily identified. Their electric dipole moments, due to the reflection symmetry of the circuit layout, are

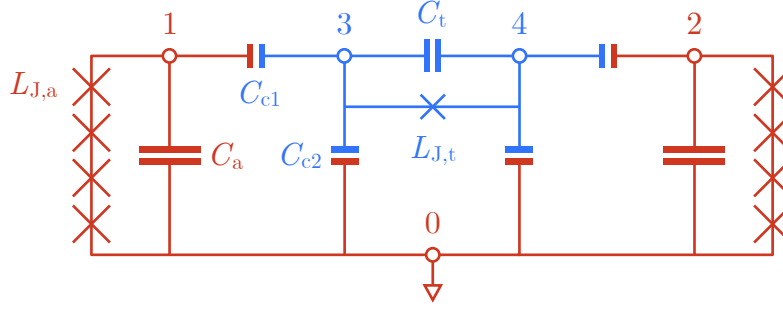


Figure 6.5: Lumped-element circuit model of the Π -mon. Nodes 0–4 correspond to the five superconducting electrode pads in the same order as they are labeled in Figure 6.3. Node 0 is assigned as the ground node.

either parallel or perpendicular to the mirror, as shown in Figure 6.4. The modified linear modes due to capacitive coupling can be obtained through a full circuit analysis.

Figure 6.5(a) presents a lumped-element circuit model of the Π -mon artificial molecule (see Figure 6.3): Each Josephson junction is replaced by an ideal Josephson element with a Josephson inductance $L_{J,t} = \phi_0^2/E_{J,t}$ (transmon junction) or $L_{J,a} = \phi_0^2/E_{J,a}$ (array junctions), here $\phi_0 = \hbar/2e$ being the reduced flux quantum. The mutual capacitor between Nodes n_1 and n_2 is denoted by $C_{n_1 n_2}$ ($n_1, n_2 = 0, 1, 2, 3, 4$). The junction capacitor of the transmon is included in $C_{34} = C_t$. The junction capacitors on the arrays are much smaller than $C_{10} = C_{20} = C_a$ and are thus omitted for simplicity. The coupling capacitors are $C_{13} = C_{24} = C_{c1}$ between the transmon electrodes and the upper electrodes of the arrays,³ and $C_{10} = C_{20} = C_{c2}$ between the upper and lower electrodes of the arrays.

Considering the mirror symmetry of the Π -mon circuits, we employ the method of **even–odd mode analysis** to visualize the coupled linear modes of this network.

³The cross-coupling capacitors C_{14} and C_{23} are small compared to the direct-coupling capacitors C_{13} and C_{24} , and are thus neglected in the circuit model.

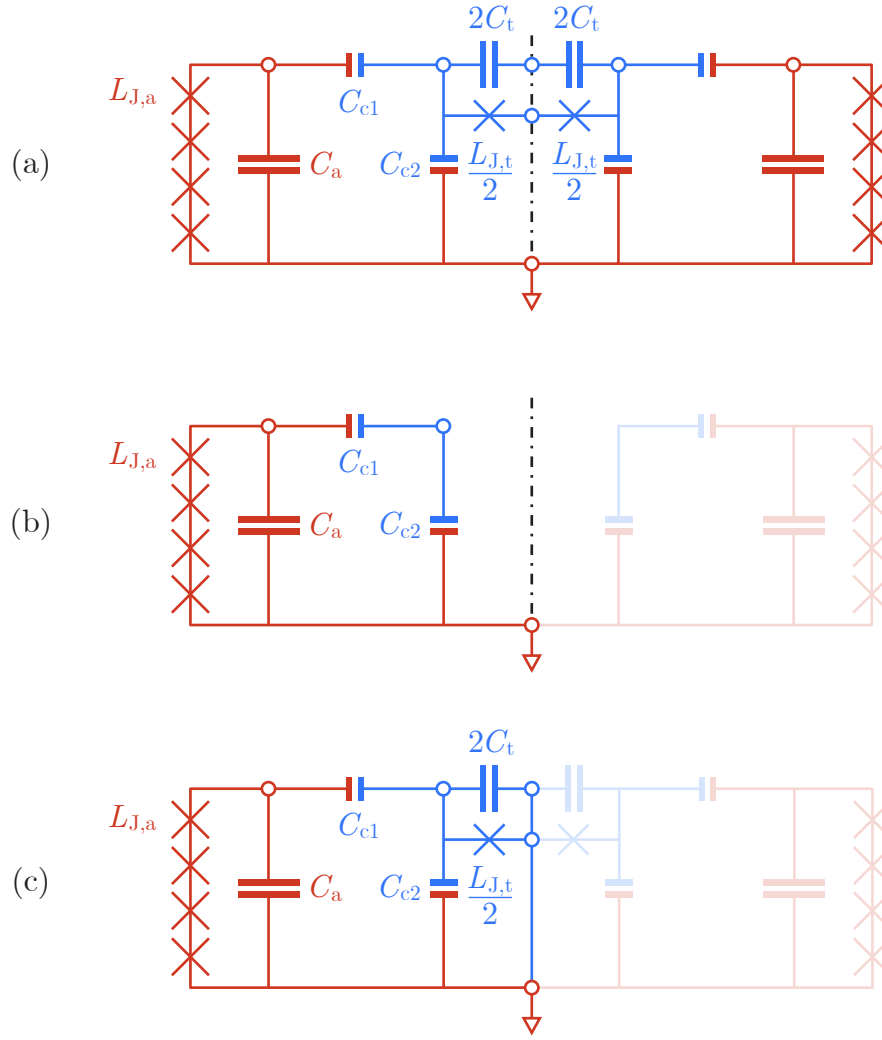


Figure 6.6: Even-odd mode analysis of the Π -mon circuit. (a) Preparation for the even-odd mode analysis. The transmon junction and its shunting capacitor are split into a pair of junctions and capacitors that are twice as large, such that the circuit can be bisected by its central mirror (dashed-dotted line). (b) Equivalent circuit for the even (common or symmetric) mode, obtained from (a) by assigning open circuits to the mirror nodes. The even-mode circuit contains one resonant mode based on the Josephson preamplifier oscillator, with the array capacitance C_a adjusted by C_{c1} and C_{c2} . (c) Equivalent circuit for the odd (differential or antisymmetric) modes, obtained from (a) by grounding the mirror nodes. This circuit shows the capacitive coupling (through C_{c1}) Josephson preamplifier oscillator and the transmon with its shunting capacitance adjusted by C_{c2} .

Figure 6.5(b) is a preparatory step in which the transmon junction is replaced by two identical junctions with Josephson energies $2E_{J,t}$ (Josephson inductances $L_{J,t}/2$) in series, and similarly, the shunting capacitor by two $2C_t$ series capacitors. The even (common or symmetric) circuit mode can then be acquired by assigning open circuits to the nodes on the mirror line, as shown in Figure 6.5(c). We name it the “bright” mode, whose linear frequency is given by

$$\omega_b = \frac{1}{\sqrt{N_J L_{J,a} \left(C_a + \frac{C_{c1} C_{c2}}{C_{c1} + C_{c2}} \right)}}, \quad (6.1)$$

in which the number of junctions in the array $N_J = 4$. The bright mode frequency ω_b is close to that of the fundamental linear mode of the uncoupled junction array oscillator $\omega_{b0} = 1/\sqrt{N_J L_{J,a} C_a}$ but modified by the coupling capacitors C_{c1} and C_{c2} .

The odd (differential or antisymmetric) modes of this network can be found if one short-circuiting the mirror nodes and the ground node 0. In Figure 6.5(d), one finds two capacitively coupled oscillators with uncoupled linear frequencies $\omega_{m0} = \omega_{b0} = 1/\sqrt{N_J L_{J,a} C_a}$ and $\omega_{d0} = 1/\sqrt{L_{J,t} (C_t + C_{c2}/2)}$. Due to the capacitive coupling, the linear mode frequencies are modified to be

$$\omega_m = \frac{1}{\sqrt{N_J L_{J,a} \left[C_a + \frac{C_{c1} (2C_t + C_{c2})}{2C_t + C_{c1} + C_{c2}} \right]}}, \quad (6.2)$$

$$\omega_d = \frac{1}{\sqrt{L_{J,t} \left[C_t + \frac{C_{c2}}{2} + \frac{C_a C_{c1}}{2(C_a + C_{c1})} \right]}}. \quad (6.3)$$

We then name the first mode at frequency ω_m , which chiefly resides in the junction array oscillator, as the “mediator” mode, and the second mode at frequency ω_d , which is mainly in the transmon, as the “dark mode.” The assignment of the names “bright” versus “dark” will become clear once we consider the readout setup by coupling the

Π -mon to a linear readout cavity, which is to be discussed in Section 6.4.

6.3.2 Effective circuit Hamiltonian

After obtaining the three coupled linear modes of the Π -mon circuit by considering its geometric symmetry, in this section I am going to continue with the nonlinear analysis using the Lagrangian and Hamiltonian formalisms of electrical circuits [Devoret, 1997; Vool and Devoret, 2017].

We start by assigning the flux variables of the four nodes— Φ_i ($i = 1, 2, 3, 4$) as the generalized position variables of the system, while again choosing Node 0 to be the ground node. The Lagrangian of the system has the general form

$$L_{\Pi} = K_{\Pi} - V_{\Pi}, \quad (6.4)$$

in which the kinetic energy

$$K_{\Pi} = \frac{C_t(\dot{\Phi}_3 - \dot{\Phi}_4)^2}{2} + \sum_{i=1,2} \frac{C_a \dot{\Phi}_i^2 + C_{c1}(\dot{\Phi}_i - \dot{\Phi}_{i+2})^2}{2} + \sum_{i=3,4} \frac{C_{c2} \dot{\Phi}_i^2}{2}, \quad (6.5)$$

and the potential energy

$$V_{\Pi} = -E_{J,t} \cos\left(\frac{\Phi_3 - \Phi_4}{\phi_0}\right) - \sum_{n=1,2} N_J E_{J,a} \cos\left(\frac{\Phi_n}{N_J \phi_0}\right). \quad (6.6)$$

Now consider a substitution of variables that defines four new common and differential

generalized position degrees of freedom—

$$\Phi_b = \Phi_1 + \Phi_2, \quad (6.7)$$

$$\Phi_m = \Phi_1 - \Phi_2, \quad (6.8)$$

$$\Phi_n = \Phi_3 + \Phi_4, \quad (6.9)$$

$$\Phi_d = \Phi_3 - \Phi_4. \quad (6.10)$$

The Lagrangian can then be rewritten as

$$\begin{aligned} L_{\Pi} = & \frac{C_t \dot{\Phi}_d^2}{2} + \frac{C_a \dot{\Phi}_b^2 + C_{c2} \dot{\Phi}_n^2 + C_{c1} (\dot{\Phi}_b - \dot{\Phi}_n)^2}{4} + \frac{C_a \dot{\Phi}_m^2 + C_{c2} \dot{\Phi}_d^2 + C_{c1} (\dot{\Phi}_m - \dot{\Phi}_d)^2}{4} \\ & + E_{J,t} \cos\left(\frac{\Phi_d}{\phi_0}\right) + N_J E_{J,a} \cos\left(\frac{\Phi_b + \Phi_m}{2N_J \phi_0}\right) + N_J E_{J,a} \cos\left(\frac{\Phi_b - \Phi_m}{2N_J \phi_0}\right), \end{aligned} \quad (6.11)$$

and the Hamiltonian can be obtained from the Legendre transformation [Goldstein *et al.*, 2002]—

$$H_{\Pi} = Q_b \dot{\Phi}_b + Q_n \dot{\Phi}_n + Q_m \dot{\Phi}_m + Q_d \dot{\Phi}_d - L_{\Pi}, \quad (6.12)$$

with the *canonical conjugate momenta* of the flux variables given by

$$Q_b = \frac{\partial L}{\partial \dot{\Phi}_b} = \frac{(C_a + C_{c1}) \dot{\Phi}_b - C_{c1} \dot{\Phi}_n}{2}, \quad (6.13)$$

$$Q_n = \frac{\partial L}{\partial \dot{\Phi}_n} = \frac{(C_{c2} + C_{c1}) \dot{\Phi}_n - C_{c1} \dot{\Phi}_b}{2}, \quad (6.14)$$

$$Q_m = \frac{\partial L}{\partial \dot{\Phi}_m} = \frac{(C_a + C_{c1}) \dot{\Phi}_m - C_{c1} \dot{\Phi}_d}{2}, \quad (6.15)$$

$$Q_d = \frac{\partial L}{\partial \dot{\Phi}_d} = \frac{(C_{c2} + C_{c1} + 2C_t) \dot{\Phi}_d - C_{c1} \dot{\Phi}_m}{2}. \quad (6.16)$$

After solving the above Equations (6.13)–(6.16), one can write down

$$H_{\Pi} = \frac{Q_b^2}{2C_b} + \frac{Q_n^2}{2C_n} + \frac{Q_b Q_n}{C_{bn}} + \frac{Q_m^2}{2C_m} + \frac{Q_d^2}{2C_d} + \frac{Q_m Q_d}{C_{md}} - E_{J,t} \cos\left(\frac{\Phi_d}{\phi_0}\right) - 2N_J E_{J,a} \cos\left(\frac{\Phi_b}{2N_J \phi_0}\right) \cos\left(\frac{\Phi_m}{2N_J \phi_0}\right), \quad (6.17)$$

in which C_b , C_n , C_m , and C_d are the effective self-capacitances, and C_{bn} and C_{md} are the coupling capacitances between the two even and odd modes, respectively. The values of these capacitances are given by

$$C_b = \frac{1}{2} \left(C_a + \frac{C_{c1} C_{c2}}{C_{c1} + C_{c2}} \right), \quad (6.18)$$

$$C_n = \frac{1}{2} \left(C_{c2} + \frac{C_{c1} C_a}{C_{c1} + C_a} \right), \quad (6.19)$$

$$C_m = \frac{1}{2} \left[C_a + \frac{C_{c1} (C_{c2} + 2C_t)}{C_{c1} + C_{c2} + 2C_t} \right], \quad (6.20)$$

$$C_d = \frac{1}{2} \left(2C_t + C_{c2} + \frac{C_{c1} C_a}{C_{c1} + C_a} \right), \quad (6.21)$$

$$C_{bn} = \frac{1}{2} \left(C_a + C_{c2} + \frac{C_a C_{c2}}{C_{c1}} \right), \quad (6.22)$$

$$C_{md} = \frac{1}{2} \left[C_a + 2C_t + C_{c2} + \frac{C_a (2C_t + C_{c2})}{C_{c1}} \right]. \quad (6.23)$$

Expanding the Josephson potential energies in Equation (6.17) up to the fourth order of flux variables and dropping all constant terms [Dassonneville *et al.*, 2020; Diniz *et al.*, 2013], one then obtain the effective quartic Hamiltonian

$$H_{\Pi, \text{eff}} = \frac{Q_b^2}{2C_b} + \frac{\Phi_b^2}{4N_J L_{J,a}} - \frac{E_{J,a}}{192N_J^3} \left(\frac{\Phi_b}{\phi_0} \right)^4 + \frac{Q_m^2}{2C_m} + \frac{\Phi_m^2}{4N_J L_{J,a}} - \frac{E_{J,a}}{192N_J^3} \left(\frac{\Phi_m}{\phi_0} \right)^4 + \frac{Q_d^2}{2C_d} + \frac{\Phi_d^2}{2L_{J,t}} + \frac{Q_m Q_d}{C_{md}} + \frac{Q_n^2}{2C_n} + \frac{Q_b Q_n}{C_{bn}} - \frac{E_{J,t}}{8N_J} \left(\frac{\Phi_b \Phi_m}{\phi_0^2} \right)^2 - \frac{E_{J,t}}{24} \left(\frac{\Phi_d}{\phi_0} \right)^4, \quad (6.24)$$

which contains three resonant modes, with linear frequencies

$$\omega_b = \frac{1}{\sqrt{2N_J L_{J,a} C_b}}, \quad (6.25)$$

$$\omega_m = \frac{1}{\sqrt{2N_J L_{J,a} C_m}}, \quad (6.26)$$

$$\omega_d = \frac{1}{\sqrt{L_{J,t} C_d}}. \quad (6.27)$$

These results are identical to Equations (6.1)–(6.3), showing the equivalence of the circuit diagram and the Lagrangian–Hamiltonian formulation presented in these two subsections.

6.3.3 Circuit quantization

Define the dimensionless Josephson phase and charge number variables $\varphi_j = \Phi_j/\phi_0$ and $n_j = Q_j/2e$ ($j = b, m, d$). After dropping the kinetic energy terms involving Q_n in Equation (6.24),⁴ this effective quartic Hamiltonian can be rewritten as

$$\begin{aligned} H_{\Pi,\text{eff}} = & 4E_{C,b}n_b^2 + \frac{E_{J,a}}{4N_J}\varphi_b^2 - \frac{E_{J,a}}{192N_J^3}\varphi_b^4 + 4E_{C,m}n_m^2 + \frac{E_{J,a}}{4N_J}\varphi_m^2 - \frac{E_{J,a}}{192N_J^3}\varphi_m^4 \\ & + 4E_{C,d}n_d^2 + \frac{E_{J,t}}{2}\varphi_d^2 - \frac{E_{J,t}}{24}\varphi_d^4 + 8E_{C,md}n_m n_d - \frac{E_{J,a}}{8N_J}\varphi_b^2\varphi_m^2, \end{aligned} \quad (6.28)$$

in which the Coulomb charging energies are defined as

$$E_{C,j} = \frac{e^2}{2C_j}, \quad (j = b, m, d), \quad (6.29)$$

$$E_{C,md} = \frac{e^2}{2C_{md}}. \quad (6.30)$$

⁴The uncoupled dynamics of the “n” degree of freedom is the same as that of a free particle. It therefore does not form a resonant mode like the other three degrees of freedom.

Following the **canonical quantization** protocol introduced in Section 1.3.2, we write

$$\varphi_j \rightarrow \hat{\varphi}_j = \varphi_{\text{ZPF},j}(\hat{j}^\dagger + \hat{j}), \quad (6.31)$$

$$n_j \rightarrow \hat{n}_j = i n_{\text{ZPF},j}(\hat{j}^\dagger - \hat{j}), \quad (6.32)$$

in which the bosonic operators obey the canonical commutation relations

$$[\hat{j}, \hat{j}^\dagger] = 1, \quad (j = b, m, d). \quad (6.33)$$

The zero-point fluctuations of the phase and charge number variables are given by

$$\varphi_{\text{ZPF},j} = \sqrt{2} \left(\frac{N_J E_{C,j}}{E_{J,a}} \right)^{\frac{1}{4}}, \quad (6.34)$$

$$n_{\text{ZPF},j} = \frac{1}{2\sqrt{2}} \left(\frac{E_{J,a}}{N_J E_{C,j}} \right)^{\frac{1}{4}}, \quad (6.35)$$

for the bright and mediator modes ($j = b, m$), and

$$\varphi_{\text{ZPF},d} = \frac{1}{\sqrt{2}} \left(\frac{8E_{C,d}}{E_{J,t}} \right)^{\frac{1}{4}}, \quad (6.36)$$

$$n_{\text{ZPF},d} = \frac{1}{\sqrt{2}} \left(\frac{E_{J,t}}{8E_{C,d}} \right)^{\frac{1}{4}} \quad (6.37)$$

for the dark mode. One can write the quantum Hamiltonian of the Π -mon—

$$\begin{aligned} \frac{\hat{H}_{\Pi,\text{eff}}}{\hbar} = & \omega_b^{01} \hat{b}^\dagger \hat{b} + \omega_m^{01} \hat{m}^\dagger \hat{m} + \omega_d^{01} \hat{d}^\dagger \hat{d} - \frac{K_b}{2} \hat{b}^{\dagger 2} \hat{b}^2 - \frac{K_m}{2} \hat{m}^{\dagger 2} \hat{m}^2 - \frac{K_d}{2} \hat{d}^{\dagger 2} \hat{d}^2 \\ & - g_{\text{md}} (\hat{m}^\dagger - \hat{m}) (\hat{d}^\dagger - \hat{d}) - g_{\text{bm}} (\hat{b}^\dagger + \hat{b})^2 (\hat{m}^\dagger + \hat{m})^2, \end{aligned} \quad (6.38)$$

in which the 0–1 transition frequencies are modified from the coupled linear frequencies of the bright, mediator, and dark modes,

$$\omega_j^{01} = \omega_j - K_j, \quad (j = \text{b, m, d}). \quad (6.39)$$

Their mode anharmonicities are given by

$$K_j = \frac{E_{C,j}}{\hbar} \frac{1}{4N_j^2}, \quad (j = \text{b, m}), \quad (6.40)$$

$$K_d = \frac{E_{C,d}}{\hbar}. \quad (6.41)$$

Equation (6.40) demonstrates again the conclusion we have obtained in the end of Section 1.3.2: The anharmonicity of the fundamental mode of a Josephson nonlinear resonator containing an array of N_j identical junctions are suppressed by a factor of N_j^2 . The weak nonlinearity of the two junction array modes thus makes them natural candidates for the on-chip parametric preamplifier, while the dark mode is to be employed as the qubit due to its strong, undiluted Josephson nonlinearity. During design iterations, different values of N_j can be used to adjust K_b and K_m without changing the geometric pattern of the sample.

More important features of the coupling schemes inside the Π -mon artificial molecule are shown on the second line of Equation (6.38):

- (i) The two antisymmetric modes—the mediator mode and the dark mode—are linearly coupled with a coupling coefficient

$$g_{\text{md}} = \frac{E_{C,\text{md}}}{\hbar} \left(\frac{2E_{J,\text{a}}E_{J,\text{t}}}{N_j E_{C,\text{m}} E_{C,\text{d}}} \right)^{\frac{1}{4}}, \quad (6.42)$$

in which $E_{C,\text{md}}$ is proportional to the coupling capacitance C_{c1} . The same conclusion can be obtained from Figure 6.6(c).

- (ii) The bright mode and the mediator mode are linearly decoupled due to their orthogonal electric dipole moments, whereas they are coupled in the cross-Kerr form, with a coupling strength

$$g_{\text{bm}} = \frac{1}{4\hbar} \sqrt{\frac{E_{\text{J,a}} \sqrt{E_{\text{C,b}} E_{\text{C,m}}}}{N_{\text{J}}}}. \quad (6.43)$$

Note that this cross-Kerr interaction is purely due to the Josephson nonlinearity of the junction arrays, where both the bright mode and the mediator mode have considerable energy participations.

The two interaction terms explained in (i) and (ii) together elucidate the essential role of the mediator mode, with which the bright mode and the dark mode, albeit having orthogonal electric dipole moments and primarily residing in physically separate Josephson oscillators, are indirectly coupled with avoided linear interaction. This is an exact realization of our design goal as illustrated in Figure 6.2. In the next section, we will consider the full readout scheme and introduce the experimental setup for demonstrating the intra-cavity amplification of qubit readout signals using a Π -mon in a modified circuit QED configuration.

6.4 Π -mon coupled to a linear readout cavity

Figure 6.7 depicts the measurement system of the Π -mon based on the circuit QED techniques, in which the bright mode of the artificial molecule is symmetrically aligned, and thus linearly coupled to the TE_{101} mode of a 3D linear cavity, which is employed for qubit readouts. In this arrangement, the dark mode has no direct linear interaction to the readout cavity, but as explained in the previous section, they are indirectly coupled with a cross-Kerr interaction mediated by the first antisymmetric mode of the preamplifier oscillator (“mediator”). The frequencies of the dark,

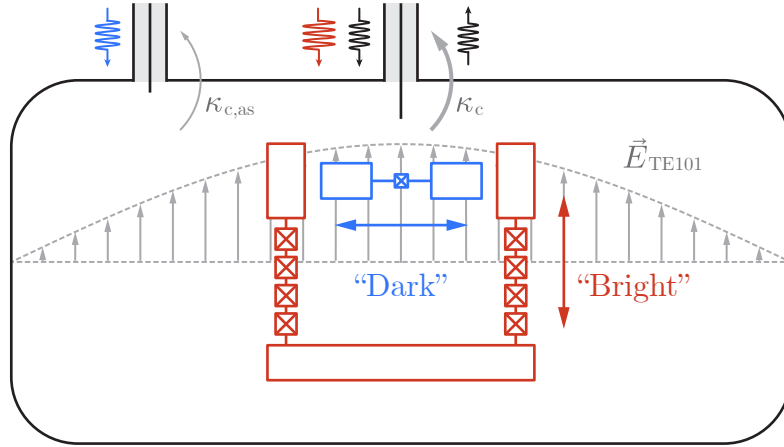


Figure 6.7: Cross-section drawing of a circuit QED module containing a Π -mon artificial molecule. The sample is housed symmetrically inside a linear readout cavity. The electric field of the cavity TE_{101} is aligned to the electric dipole moment of the bright mode (red double-arrow), and perpendicular to that of the dark mode (blue double-arrow). Microwave drives of the bright mode (red) and of the readout cavity drives (black) share the same symmetric coaxial cable (or waveguide aperture, not represented) coupled to the TE_{101} mode with a rate κ_c . The dark mode is driven through an asymmetric coaxial cable, whose coupling rate to the cavity TE_{101} mode is $\kappa_{c,\text{as}} \ll \kappa_c$. The majority of readout signals are therefore collected by the symmetric port and sent to a standard quantum-limited output amplifier chain (see Figure 6.1).

mediator, bright, and cavity modes are mutually detuned such that we can write the effective Hamiltonian of this circuit QED system in the dispersive regime—

$$\frac{\hat{H}_{\Pi-c}}{\hbar} = \tilde{\omega}_c \hat{c}^\dagger \hat{c} + \sum_{j=b,m,d} \left(\tilde{\omega}_j^{01} \hat{j}^\dagger \hat{j} - \frac{\tilde{K}_j}{2} \hat{j}^{\dagger 2} \hat{j}^2 \right) - \sum_{\substack{i,j=c,b,m,d \\ i \neq j}} \tilde{\chi}_{ij} \hat{i}^\dagger \hat{i} \hat{j}^\dagger \hat{j}. \quad (6.44)$$

Similar to Equation (3.4), here the operators and parameters under the tilde are modified from their uncoupled definitions due to the cavity– Π -mon interaction. In the rest of this chapter, we will drop these tildes for notational simplicity.

6.4.1 Control and measurement interfaces

In this system, the modes we will actively manipulate and measure are the bright mode (“b”) and dark mode (“d”) on the Π -mon chip, and the fundamental (TE_{101}) mode of the readout cavity (“c”). The $|0\rangle$ and $|1\rangle$ subspace of the strongly anharmonic dark mode is used as the qubit. The weakly anharmonic bright mode is employed as the on-chip parametric preamplifier. The bright mode and readout drives are delivered through the same symmetric cavity port (coupling rate κ_c), while the dark mode is at the first order insensitive to incoming radiation from the symmetric port in the vicinity of the dark mode frequency when the sample is correctly oriented, and thus has to be excited through an asymmetric port (coupling rate $\kappa_{c,\text{as}}$).⁵ The efficient collection of intra-cavity readout signals in a reflection measurement setup is guaranteed by $\kappa_c \gg \kappa_{c,\text{as}}$. A small $\kappa_{c,\text{as}}$ is also desirable for reducing the photon-induced qubit dephasing effect on the dark mode, as we have discussed in detail in Chapter 5.

Like in a standard circuit QED module, χ_{bc} and χ_{dc} quantify the dispersive interaction between the cavity photons and the bright and dark modes, respectively. While χ_{bc} is caused by the direct linear coupling between the bright mode and the cavity, a residual χ_{dc} can be observed due to the indirect interaction mediated by the mediator and bright modes, and is limiting the radiative protection or “darkness” of the dark mode as seen from the readout cavity or its symmetric port. In an optimal design, the ratio χ_{bc}/χ_{dc} should be maximized for improved qubit coherence properties relative to its measurability.

The cascade of the cross-Kerr interaction between the bright and the mediator modes and the linear interaction between the mediator and the dark modes result in

⁵Note that the cavity and the bright mode can also be driven from the asymmetric port.

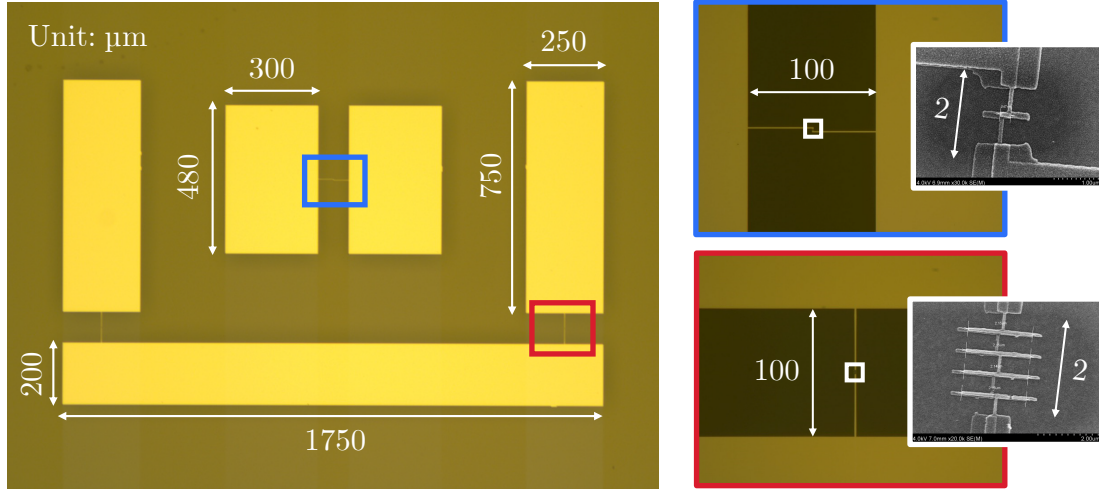


Figure 6.8: Left: optical micrograph of the Π -mon sample with which the experiments reported in this chapter are performed. The areas of the transmon and the preamplifier junction links (in the blue and red boxes) are zoomed in on the right. Insets: scanning electron micrographs of the transmon junction and the preamplifier junction array ($N_J = 4$).

χ_{bd} , which induces a dispersive frequency shift on the bright mode conditioned on the qubit (dark mode) state. Driving the bright mode at either ω_b^{01} or $(\omega_b^{01} - \chi_{bd})$, one will be able to observe its population change by monitoring the readout cavity frequency, which carries information of the qubit state. Such is the basic principle of the two-step qubit readout mediated by the on-chip bright mode (intra-cavity preamplifier). We will continue examining this measurement protocol in Section 6.7.

6.4.2 Experimental setup and parameters

The experimental data presented in the following sections were collected on the same Π -mon sample, whose optical and scanning electron micrographs are shown in Figure 6.8. The sample preparation followed the standard fabrication procedure of transmons, which has been described in Section 4.1. Probed at the room temperature

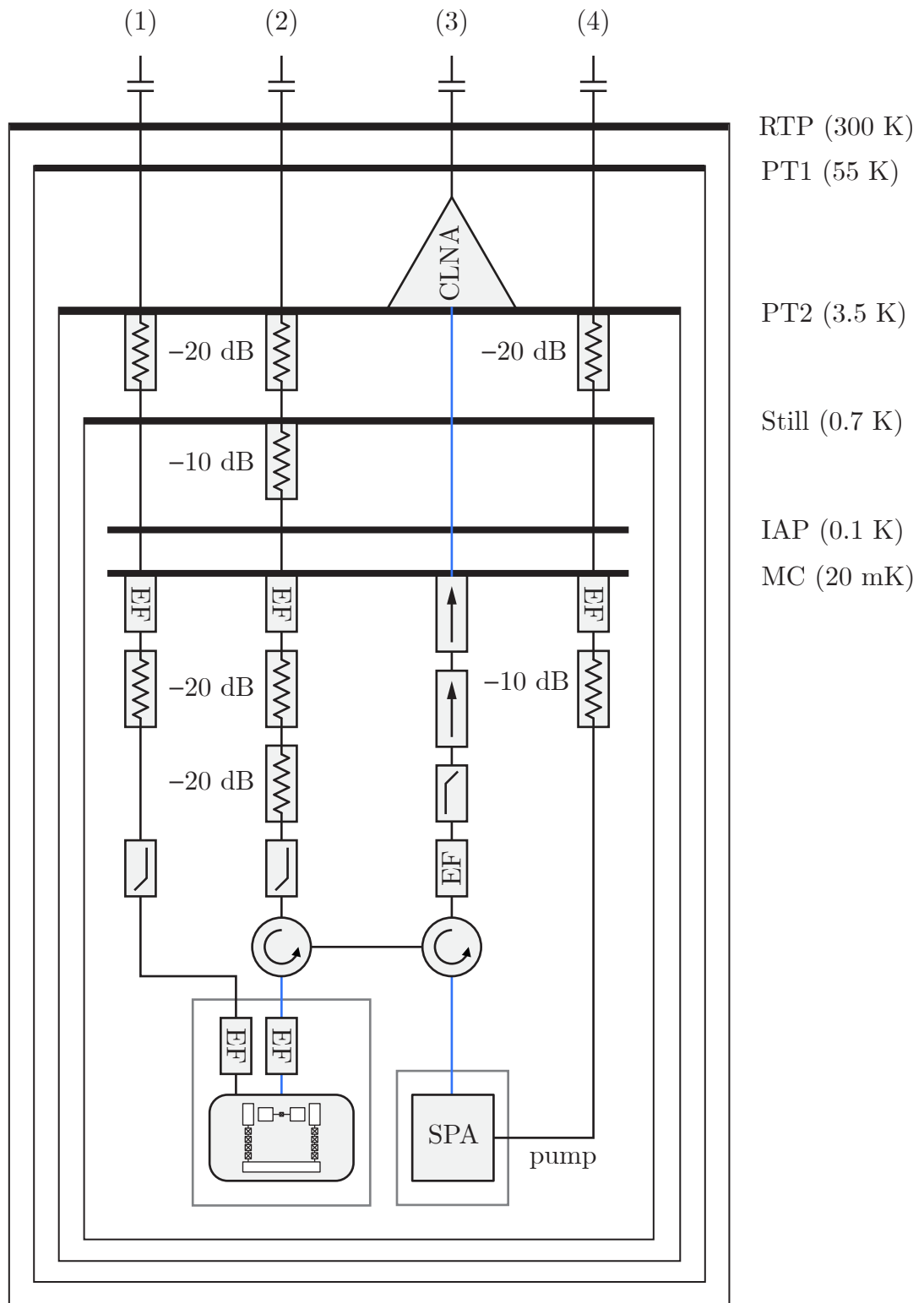


Figure 6.9: Cryogenic wiring diagram of the Π -mon experiment. Circuit symbols and notations are the same as those in Figures 4.4 and 5.5. The four lines at the top of the dilution refrigerator, from left to right, are for (1) dark mode drive, (2) bright mode and readout cavity drives, (3) readout output, and (4) parametric amplifier pump. The SPA was operated in the phase-preserving mode with 20–25 dB gain for all data collection cycles.

prior to cryogenic experiments, the normal resistances of the two Josephson junction arrays show a high degree of symmetry, with a relative uncertainty no larger than 10^{-3} .

The Π -mon sample was loaded into the central chip slot of a 3D aluminum (alloy 6061) readout cavity as shown in Figure 4.2. The alignment was done by hand under mechanical constraints, without further assistance.⁶ The cavity half with a coupling aperture on the flange is connected to a home-designed waveguide-to-coaxial-cable coupler, with a cross-section matching that of the WR-90 waveguide (22.86 mm \times 10.16 mm, see Figure 5.6) as the symmetric readout port. Its coupling rate $\kappa_c/2\pi = 3.0$ MHz is determined by the geometry of the aperture. To drive the dark mode, an asymmetric coaxial pin coupler is installed on the other half of the cavity, with a coupling rate $\kappa_{c,as}/2\pi = 5.7$ kHz $\approx 0.002\kappa_c$.

The low-temperature measurement setup is drawn in Figure 6.9, which has two special features compared to the setup of the cavity attenuator experiment (previously shown in Figure 5.5):

- (i) To compensate for the very small coupling rate $\kappa_{c,as}$ of the asymmetric cav-

⁶We have examined the ideality of the sample alignment by testing the “darkness” of the dark mode: no dark mode response was observed under continuous-wave spectroscopy drives through the symmetric port up to a maximum drive power that had significantly raised the mixing-chamber temperature of the dilution refrigerator. The effect of sampling alignment on the coherence times of the dark mode remains to be studied.

ity port, the total attenuation on its input line is reduced such that sufficient microwave power can be delivered for fast qubit gates. The impact of residual thermal radiation from this weakly-coupled input line on the dark mode (qubit) coherence times remains to be examined.

- (ii) Two Eccosorb filters (EF) are installed on both the symmetric and asymmetric cavity ports *inside* the high-magnetic-permeability mu-metal shield.⁷ Consequently, the energy relaxation times T_1 of both the dark and the bright modes have been improved by four to five times compared to the data from earlier experimental rounds when these two in-shield Eccosorb filters were not installed (see Table 6.4).

All parameters of the effective Hamiltonian in the dispersive regime—Equation (6.44) were measured using spectroscopy methods. The results are summarized in Tables 6.1 and 6.2. We find the values of K_d , K_m , and K_b decreasing each compared to the previous one by one order of magnitude, which is consistent with the increasing participations of these three modes on the Josephson junction array with diluted nonlinearity. The dark mode has a residual coupling rate $\chi_{dc}/2\pi = 31$ kHz to the readout cavity, with $\chi_{bc}/\chi_{dc} \approx 6$. From these data, we estimate $E_{J,a}/h = 62$ GHz (on average) and $E_{J,t}/h = 9.6$ GHz. The ratio $E_{J,t}/E_{C,t} = 54$ shows that the dark mode is in the standard transmon regime.

The design of this sample and its readout cavity was assisted by the 3D finite-element-method (FEM) electromagnetic solver **Ansys HFSS** for linear eigenmode simulations, and the Python-based open-source package **pyEPR** to compute the Kerr matrix following the energy participation ratio (EPR) method [Minev *et al.*, 2021a] (see Section 4.5). The numerical simulation results are listed in Table 6.3. The closeness

⁷As recommended in Serniak *et al.* [2019] and Diamond *et al.* [2022].

Unit: [GHz]	f_d^{01}	f_m^{01}	f_b^{01}	f_c
	4.0912	4.8658	5.8982	7.4678

Table 6.1: Frequencies of the dark (d), mediator (m), and bright (b) modes of the Π -mon (0–1 transitions) and the TE_{101} mode of the readout cavity. The frequencies of the on-chip modes were extracted from two-tone spectroscopy measurements. Over several experimental rounds, f_d^{01} , f_m^{01} , and f_b^{01} underwent minor down-drifts as a result of the oxidation of Josephson junctions between these cooldowns, while the sample was exposed to the atmosphere at the room temperature. The properties and overall performance of this sample were not influenced by these frequency shifts.

Unit: [MHz]	Dark (d)	Mediator (m)	Bright (b)	Cavity (c)
Dark (d)	179	109	3.0	0.031
Mediator (m)		24.4	10.0	0.11
Bright (b)			8.3	0.19
Cavity (c)				0.0012

Table 6.2: Kerr matrix of the Π -mon coupled to a linear readout cavity: experimental data. Diagonal elements stand for the mode anharmonicities: $K_j/2\pi$ ($j = \text{b, m, d, c}$). Off-diagonal elements stand for the cross-Kerr coupling coefficients: $\chi_{ij}/2\pi$ ($i, j = \text{b, m, d, c}$, $i \neq j$). Symmetric table elements in the lower triangle are omitted. K_c was measured using cavity reflection spectroscopy with variable power levels; χ_{bc} , χ_{mc} , and χ_{dc} were extracted in two-tone spectroscopy experiments; the rest of the table elements were measured using the three-tone spectroscopy method. The measurement values are subject to minor changes over multiple cooldowns.

Unit: [MHz]	Dark (d)	Mediator (m)	Bright (b)	Cavity (c)
Dark (d)	184	135	3.9	0.044
Mediator (m)		33.7	11.0	0.11
Bright (b)			7.9	0.18
Cavity (c)				0.0010

Table 6.3: Numerical simulation of the Kerr matrix based on the energy participation ratio (EPR) calculation. A symmetric device layout with four identical Josephson junctions in each junction array is used in both the linear and nonlinear simulations. The values of $E_{J,a}$ and $E_{J,t}$ in this circuit model are estimated from experimental data (see the main text). In the nonlinear calculation, the first eight energy levels are used to span the finite Hilbert space of each mode, and cosine functions are truncated at the order of seven. Dissipations are not included in the nonlinear simulation.

Mode	Eccosorb filters	T_1 [μ s]	T_{2R} [μ s]	T_{2H} [μ s]
Dark	No	17	5.4	19
	Yes	70	9.5	77
Bright	No	6.5	7.0	12
	Yes	32	18	51

Table 6.4: Energy relaxation time T_1 , Ramsey decoherence time T_{2R} , and Hahn echo decoherence time T_{2H} of the dark and bright modes. Four-time to five-time improvements on the T_1 of both modes have been observed after the two Eccosorb filters are installed at the symmetric and asymmetric cavity ports inside the high-magnetic-permeability mu-metal shield (see Figure 6.9).

of Tables 6.2 and 6.3 in most of their elements shows the practical reliability of this simulation method for nonlinear Josephson quantum circuits.

6.5 Nonlinear spectroscopy of the bright mode

Among the three on-chip nonlinear resonant modes formed by the Josephson oscillators, the dark mode and the bright mode are of direct interest for the purpose of this experiment, as the former will be employed as the qubit, and the latter as the intracavity parametric preamplifier. The mediator mode, as has been explained in the end of Section 6.3.3, despite not being directly driven in the qubit readout protocol, plays an indispensable role of linking the qubit and the on-chip preamplifier. A notable distinction between the dark and the bright modes are their anharmonicities— K_d and K_b —relative to their intrinsic linewidths set by $\Gamma_1 = 1/T_1$. Using the measurement values reported in Tables 6.2 and 6.4,⁸ one obtains $K_d/\Gamma_{1,d} \approx 8 \times 10^4 \gg K_b/\Gamma_{1,b} \approx 1.7 \times 10^3$. Therefore, the dark mode has a more “atom-like” spectrum with far-separated transitions in the frequency domain, whereas the bright mode transitions become less distinguishable when their linewidths are broadened by drive and readout tones in a spectroscopy measurement. In other words, the dark mode with a larger K/Γ_1 ratio is deeper in the quantum regime. On the contrary, the higher-level subspace of the bright mode is comparatively easier to be activated, and in this situation, a larger number of excitations will push the mode dynamics toward the semiclassical regime of standard Josephson parametric amplifiers [Andersen *et al.*, 2020a; Manucharyan *et al.*, 2007; Muppalla *et al.*, 2018]. However, here in the Π -mon artificial molecule, the ratio $K_b/\Gamma_{1,b} \gg 1$ indicates that coherent quantum dynamics can still be observed on the bright mode, albeit with a limited speed and fidelity.

⁸The longer T_1 values measured in the presence of those in-shield Eccosorb filters are used in this estimation.

The intermediacy of the bright mode with respect to its nonlinearity or “quantumness” (see Section 1.3.5) provides us an additional degree of freedom to operate the intra-cavity preamplifier in different power regimes.

Figure 6.10 presents the data of continuous-wave (CW) two-tone spectroscopy measurements, in which the bright mode was driven by a microwave drive with a varying frequency $f_{\text{spec,b}}$, and meanwhile the dispersive frequency shift of the readout cavity due to the bright mode population under the spectroscopy drive is monitored by a second microwave tone at f_c . The average number of excitations \bar{n}_b of the bright mode can be derived, provided the dispersive coupling strength χ_{bc} is already calibrated (see Table 6.2). In this figure, one can clearly identify the series of bright mode transitions spaced by its mode anharmonicity—

$$f_b^{\nu,\nu+1} = f_b^{01} - \nu K_b \quad (6.45)$$

and interceded by two-photon transitions at the middle frequencies—

$$\frac{f_b^{\nu,\nu+2}}{2} = f_b^{01} - \left(\nu + \frac{1}{2}\right) K_b. \quad (6.46)$$

The increase of the apparent linewidths of these transitions from their intrinsic values is a combination of the spectroscopy power broadening (due to $P_{\text{spec,b}}$) and the measurement-induced dephasing (due to \bar{n}_c) [Abragam, 1961; Schuster *et al.*, 2005]. The measured values of \bar{n}_b semi-quantitatively agree with the numerical simulation results of a driven quantum Kerr oscillator model, with the intrinsic relaxation and dephasing rates of the mode obtained from very-low-power spectroscopy measurements (data not shown in the figure).

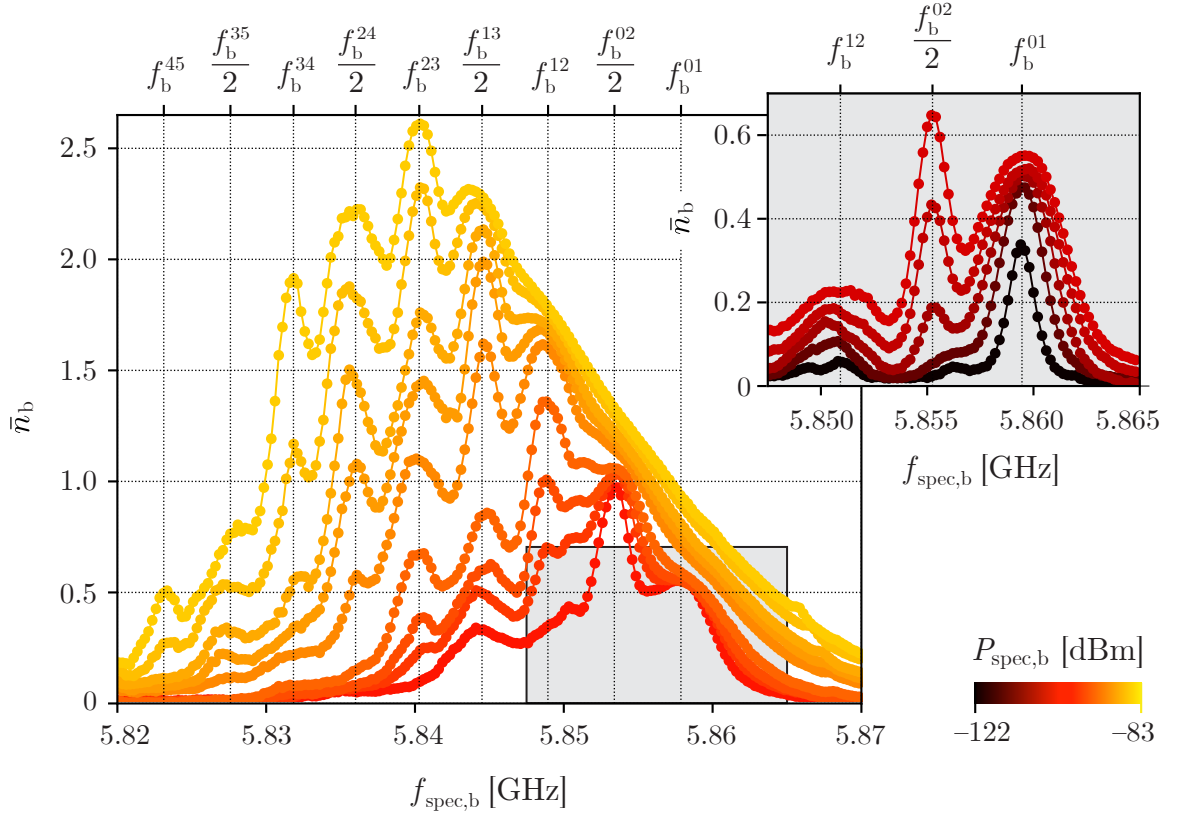


Figure 6.10: Continuous-wave (CW) bright mode two-tone spectroscopy with variable drive powers. During the measurements, the readout cavity was populated with \bar{n}_c photons by an on-resonance readout drive. Given $\bar{n}_b \chi_{bc} \ll \kappa_c$, the population change of the cavity mode conditioned on the bright mode state is negligible. The series of curves were measured with different bright mode drive powers $P_{\text{spec},b}$ at the input the symmetric cavity port, whose values are indicated by the color bar in the lower right corner. A group of low-power spectroscopy data—taken in the previous cooldown under the same experimental condition—are shown in the inset, whose axis ranges are indicated by the gray box in the main figure. Vertical dashed lines in both figures highlight the approximate frequencies of each transition, labeled above the top margin of the figure frames. Comparing the frequencies of the first three transitions, one can see a 2 MHz frequency down-drift due to the oxidation of the Π -mon sample in the latter experimental rounds (main figure).

6.6 Suppressing photon-induced qubit-state transitions

As has been stated in Section 6.2, one of the chief motivations for the Π -mon design is to alleviate the increased occurrence of qubit-state transition events in the midst of a readout sequence when the cavity is populated by a larger number of microwave photons. The data in Figure 6.6 provide evidence for the absence of such an effect with up to $\bar{n}_c \approx 200$ intra-cavity readout photons when the Π -mon is symmetrically coupled to the linear cavity as shown in Figure 6.7. The qubit-state-dependent cavity frequency shift is caused by the very small χ_{dc} , without the activation of the bright mode. This measurement was repeated on the same Π -mon sample in multiple cooldowns. The average dark mode T_1 measured without the cavity drive varied from 17 μs to 80 μs , depending on the different filtering conditions along the readout line; and yet in these cooldowns, the similar absence of T_1 reduction has always been observed. These results are consistent with our expectation, and also extend a previous experiment from our group performed with a “darkmon” sample that consists of two transmons with orthogonal electric dipole orientations [Minev, 2018; Minev *et al.*, 2019].⁹ All these positive outcomes are showing the effectiveness of this circuit layout strategy, and a higher QND fidelity should thus be expected in a circuit QED module with avoided linear coupling between the qubit and the cavity.

We repeated similar measurements on the bright mode of the Π -mon. No visible

⁹However, we would like to comment that unlike our current experiment, in Minev *et al.* [2019] the bright mode and the cavity are coupled in the strong dispersive regime ($\kappa_c < \chi_{db}$) and meanwhile the readout drive is fixed and calibrated at the frequency ($\omega_c - \chi_{db}$), which is detuned from the cavity frequencies when the system is in the dark-ground manifold. Because of this detuned cavity drive, the horizontal axis for the dark mode $T_1 - \bar{n}_c$ measurements in Supplementary Figure S2 is by a factor of 8 smaller than its labeled scale, and therefore the largest \bar{n}_c in these measurements was only around 6–7.

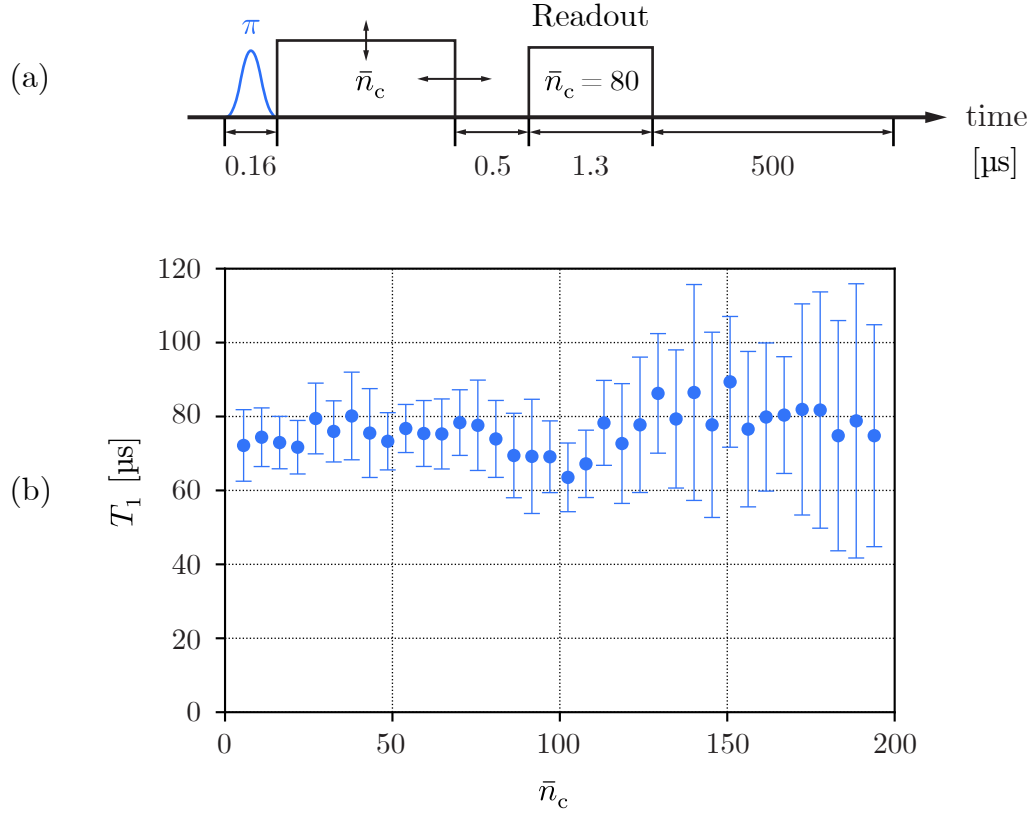


Figure 6.11: Cavity-photon-induced qubit relaxation measurement on the dark mode. (a) Microwave pulse sequence (time axis not in scale): during the waiting time between the qubit π pulse and the readout in a standard T_1 measurement sequence, the readout cavity is populated with a variable photon number \bar{n}_c —the horizontal axis in (b). The subsequent readout drive has a fixed power, corresponding to $\bar{n}_c = 80$. The readout pulse is preceded by a $0.5 \mu\text{s}$ time window for the cavity population due to the first cavity drive to decay out, such that the external amplifier chain will not be power-saturated. The qubit (dark mode) π pulse has a Gaussian envelope truncated at $\pm 2\sigma_t$, corresponding to a total pulse length $4\sigma_t = 160 \text{ ns}$. The speed of the single-qubit gate is limited by the weak coupling rate κ_{as} of the asymmetric cavity port. A $500 \mu\text{s}$ passive relaxation time window is inserted between two pulse cycles. (b) T_1 of the dark mode measured with a variable intra-cavity photon number \bar{n}_c . The error bars are contributed by both the measurement imprecision and the time-fluctuations of T_1 over the course of 10 hours.

decay of the bright mode T_1 was observed with $\bar{n}_c \lesssim 125$ (data not shown). These results set a safety zone for the applicable cavity photon number in a qubit readout sequence without introducing parasitic qubit-state transition errors. Hence as will be shown in the following section, we chose $\bar{n}_c = 80$ for the characterization of single-shot, bright-mode-assisted qubit readouts.

6.7 Demonstrations of the intra-cavity amplification

In the qubit coherence measurements reported in Figures 5.9–5.11 and Figure 6.11, the qubits are protected at the expense of the reduced accessibility of quantum information, either by adding artificial dissipations to the readout mode (as in the cavity attenuator experiment) or removing the linear qubit–cavity coupling through the redesigned circuit symmetry (as in the Π -mon artificial molecule). And yet there is an important difference between these two inventions: the cavity attenuator merely provides a passive cooling channel, whereas the Π -mon also supports an in-situ amplification mechanism of readout signals. The basic principles are illustrated in Figure 6.12: While a single qubit excitation only induces a small dispersive frequency shift χ_{dc} on the readout cavity mode, a bright mode excitation can be driven by a microwave pulse at the frequency $(\omega_b^{01} - \chi_{db})$ conditioned on the qubit being in its first excited state. The joint dark–bright mode excited state $|1, 1\rangle$ then shifts the cavity frequency by $(\chi_{dc} + \chi_{bc})$, in which χ_{bc} is large compared to χ_{dc} due to the direct linear coupling between the cavity and the bright mode. This bright-mode assisted readout scheme is depicted in the energy-level diagram in Figure 6.12(a), and the intra-cavity gain is illustrated in Figure 6.12(b).¹⁰ According to Equations (3.36) and (3.38), the

¹⁰It is worth remarking that parametric amplifications do not necessarily lead to a positive gain in the total signal power. For instance, consider a quantum-limited phase-sensitive amplifier introduced

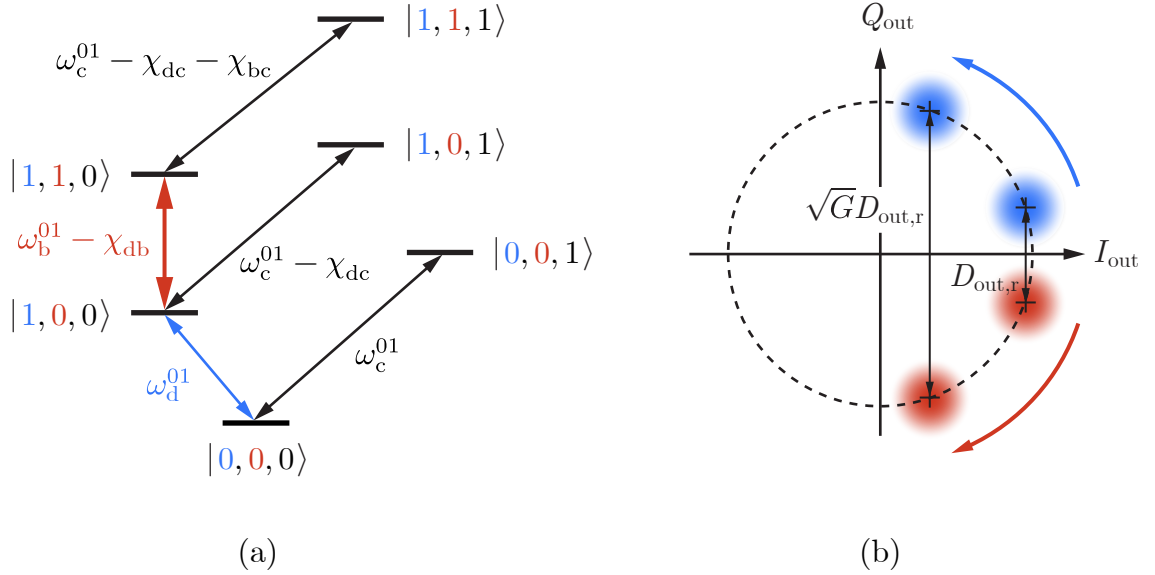


Figure 6.12: Principles of the intra-cavity dispersive gain. (a) Energy-level diagram of the two-step readout system, in which the three quantum numbers in a system state correspond to the excitation numbers of the dark (blue), bright (red), and cavity (black) modes, respectively. (b) The mechanism of intra-cavity amplification implemented in the current experiment: the selective parametric drive on the bright mode induces a larger dispersive frequency on the cavity frequency conditioned on the qubit (dark mode) state. Readout signals in the Q quadrature are amplified, and yet the power or photon number of the intra-cavity field remains unchanged. The notations in the IQ-plane representation of the output cavity field is the same as those in Figure 3.5.

in Section 1.3.4. The minimal possible output power given the input field components (I_{in}, Q_{in}) is

$$P_{out,min} = 2I_{in}Q_{in}, \quad \text{when } G_{PS} = \frac{I_{in}}{Q_{in}}.$$

It is easy to see from the inequality of arithmetic and geometric means that

$$P_{out,min} \leq P_{in} = I_{in}^2 + Q_{in}^2.$$

So the minimal output power of a quantum-limited phase-sensitive is no larger than its input power. The conclusion will be different for phase-preserving amplifiers whereby both input components as

separation of the output cavity states is amplified from

$$D_{\text{out,r}} = 2\sqrt{\bar{n}_c\kappa_c} \frac{\chi_{\text{dc}}}{\sqrt{\kappa_c^2 + \chi_{\text{dc}}^2}} \quad (6.47)$$

with only one dark mode excitation, to

$$\sqrt{G}D_{\text{out,r}} = 2\sqrt{\bar{n}_c\kappa_c} \frac{\chi_{\text{dc}} + \chi_{\text{bc}}}{\sqrt{\kappa_c^2 + (\chi_{\text{dc}} + \chi_{\text{bc}})^2}} \quad (6.48)$$

with both the dark and the bright modes in their first excited state. Therefore, we can write the intra-cavity dispersive gain of the measurement rate¹¹ as

$$G = \left(1 + \frac{\chi_{\text{bc}}}{\chi_{\text{dc}}}\right)^2 \frac{\kappa_c^2 + \chi_{\text{dc}}^2}{\kappa_c^2 + (\chi_{\text{dc}} + \chi_{\text{bc}})^2} \xrightarrow{\kappa_c \gg \chi_{\text{dc}}, \chi_{\text{bc}}} \left(1 + \frac{\chi_{\text{bc}}}{\chi_{\text{dc}}}\right)^2. \quad (6.49)$$

This conclusion can be tested using both the continuous-wave (CW) and the pulsed measurement protocols.

6.7.1 Steady-state intra-cavity gain

The data shown in Figure 6.13 were collected from three-tone CW spectroscopy measurements: the dark mode (qubit) 0–1 transition was continuously driven by an on-resonance saturation tone; the second tone with a variable power $P_{\text{spec,b}}$ was sent at the frequency $(\omega_{\text{b}}^{01} - \chi_{\text{db}})$, populating the first excited state of the bright mode provided the dark mode is in its first excited state; the dispersive shift of the readout cavity was monitored by the third tone at the frequency f_{c} . In the ideal situation, assuming the excited levels have infinite lifetimes, the steady-state population distri-

well as the total signal power are amplified by the same gain.

¹¹See the definition of the measurement rate in Equation (3.50).

bution of the Π -mon is

$$p_{0,0}^{\text{on}} = \frac{1}{2}, \quad (6.50)$$

$$p_{1,0}^{\text{on}} = \frac{1}{4}, \quad (6.51)$$

$$p_{1,1}^{\text{on}} = \frac{1}{4}. \quad (6.52)$$

In the above subscripts, the first and the second quantum numbers denote the excitation number of the dark and bright modes, respectively. In contrast, without the bright mode drive, the population distribution becomes

$$p_{0,0}^{\text{off}} = \frac{1}{2}, \quad (6.53)$$

$$p_{1,0}^{\text{off}} = \frac{1}{2}. \quad (6.54)$$

Therefore, the theoretical limit of the steady-state gain becomes

$$G_{\text{CW}} = \left[\frac{p_{1,0}^{\text{on}} \chi_{\text{dc}} + p_{1,1}^{\text{on}} (\chi_{\text{dc}} + \chi_{\text{bc}})}{p_{1,0}^{\text{off}} \chi_{\text{dc}}} \right]^2 = \left(1 + \frac{\chi_{\text{bc}}}{2\chi_{\text{dc}}} \right)^2, \quad (6.55)$$

which is smaller than the optimal gain given by Equation (6.49) in the pulsed readout protocol (to be described in the next subsection). We measured the steady-state intra-cavity gain (purple arrow) around the optimal bright mode drive power $P_{\text{spec,b}}$ close to the theoretical limit G_{CW} —shown as the top margin (black arrow) of Figure 6.13. The drop of steady-state gain beyond the optimal $P_{\text{spec,b}}$ can also be attributed to the parametric conversion process in this particular sample ($\omega_c + \omega_d^{01} \approx 2\omega_b^{01}$), whereby the chance increases when the dark mode dynamics is outside its two-level subspace under a strong bright mode drive. This accidental frequency alignment ought to be avoided in the future fabrication rounds.

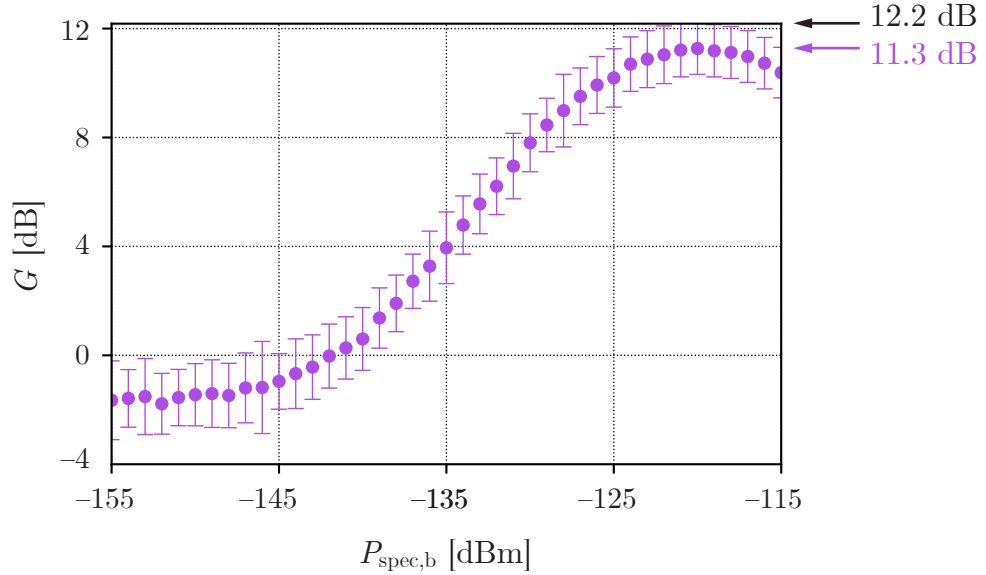


Figure 6.13: Intra-cavity gain measured using the three-tone continuous-wave (CW) spectroscopy method described in the main text. The horizontal axis corresponds to the estimated bright mode drive power at the cavity symmetric port. The top margin shows the theoretical CW gain limit derived in Equation (6.55).

6.7.2 Bright-mode-assisted single-shot qubit readout

Figure 6.14(a) shows the microwave pulse sequence for the bright-mode-assisted qubit readout protocol described by the energy-level diagram in Figure 6.12(a). The readout pulse—calibrated with $\bar{n}_c = 80$ intra-cavity photons—is preceded by a qubit-state-selective bright mode π conditioned on the dark mode being in $|1\rangle$ such that the dark mode (qubit) state $|0\rangle$ or $|1\rangle$ is mapped onto the joint dark–bright mode state $|0, 0\rangle$ or $|1, 1\rangle$. To achieve the frequency selectivity, the duration of the bright-mode Gaussian pulse in the time domain is constrained by $\sigma_t \gtrsim 1/\chi_{\text{db}}$, in which $\chi_{\text{db}}/2\pi = 3.0$ MHz. In practice, we chose $\sigma_t = 300$ ns.

Figures 6.14(b) and 6.14(c) display the readout histograms of the dark mode separately initialized in $|0\rangle$ (left) and $|1\rangle$ (right). The SNR along the Q_{out} axis is increased from 0.275 in Figure 6.14(b) without the bright mode drive to 1.729 in

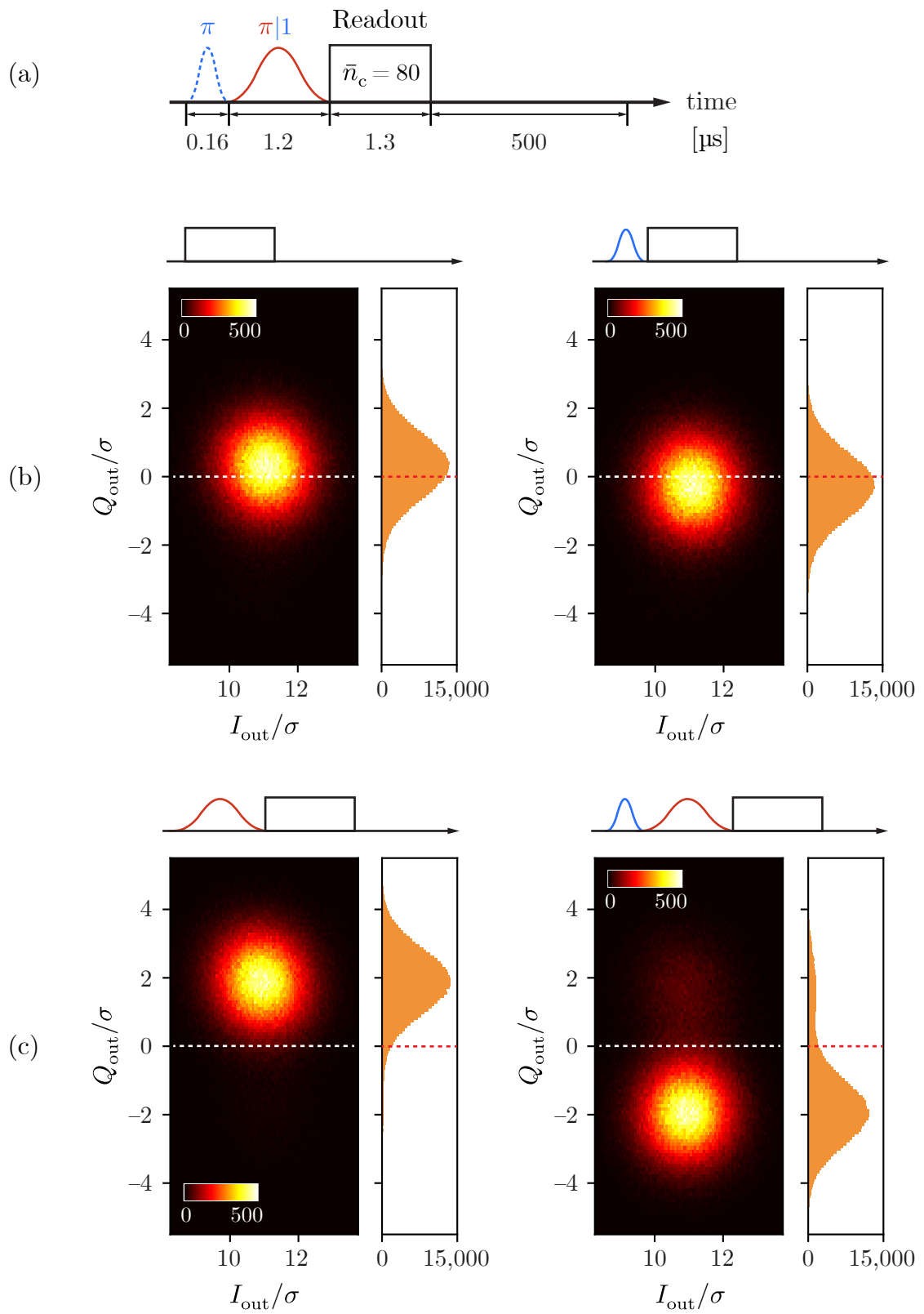


Figure 6.14: Bright-mode-assisted single-shot readout of the dark mode. (a) Microwave pulse sequence, with notations being the same as those in Figure 6.11(a). The σ_t of the dark mode π pulse (blue, center frequency at ω_d^{01}) and the qubit-state-selective bright mode π pulse on its 0–1 transition (red, center frequency at $\omega_b^{01} - \chi_{db}$) are 40 ns and 300 ns, respectively. The data acquisition (integration) time of the readout pulse is $T_m = 1 \mu\text{s}$. Modified copies of this pulse sequence are used in (b) and (c) to indicate the specific protocol of each measurement. (b) Qubit (dark mode) readout histograms without the bright mode drive. The $(I_{\text{out}}, Q_{\text{out}})$ coordinates are normalized by the standard deviation of the Gaussian distributions of the readout signals. Marginal (1D) histograms along the Q axis—the signal component—are shown on the right of each 2D histogram. The white and red dashed lines highlight the demarcation at $Q_{\text{out}} = 0$. (c) Qubit readout histograms assisted by the dark-mode-state selective bright mode drive. Notations are the same as those in (b). The number of shots are 400,000 in all histograms.

Figure 6.14(c) with the bright mode drive—or when the intra-cavity preamplifier is turned on. The enhancement of SNR by 6.3 times—equivalent to an intra-cavity gain of 16 dB—is consistent with the prediction in Equation (6.49) computed using the values of Kerr matrix elements in Table 6.2 within their measurement uncertainties. This agreement also proves the fidelity of the frequency-selective bright mode π pulse.

The readout fidelities of the single-shot qubit readout outcomes in Figure 6.14(c) calculated using Equations (2.17)–(2.19) are $\mathcal{F}_0 = 0.920$, $\mathcal{F}_1 = 0.724$, and $\mathcal{F}_{\text{tot}} = 0.822$. While \mathcal{F}_0 is apparently limited by the state distinguishability $\text{erf}(\text{SNR}/\sqrt{2}) = 0.916$ due to the limited readout SNR, the distribution tail above $Q_{\text{out}} = 0$ of the marginal histogram in the right panel of Figure 6.14(c)—as in the simulation results in Figure 2.7—shows the noticeable impact of dark mode and bright mode state-transition events on \mathcal{F}_1 .

Using Equation (3.49), one can obtain the measurement efficiency of the readout system $\eta_m = 0.24$. The inefficiency can be attributed to the microwave dissipations

between the readout cavity and the external parametric amplifier (SPA), especially the insertion loss of the Eccosorb filter at the symmetric cavity port inside the magnetic shield (see Figure 6.9).

6.8 Summary and upcoming steps

The results in Figure 6.14 are the first experimental evidence of the single-shot readout of the Π -mon qubit embedded in a two-step microwave readout setup, in which the qubit is linearly decoupled from the cavity. On the positive side, we have unambiguously demonstrated—using both the continuous-wave and the pulsed measurement protocols—the principle of the intra-cavity dispersive amplification scheme through a qubit-state-selective single-excitation drive on the bright mode. The intra-cavity gain of the measurement rate, which equals 16 dB in our experimental system with the current sample, agrees with the theoretical model. All these outcomes are proving our success in creating a new superconducting artificial molecule following the full quantum engineering procedure.

In Sections 6.5–6.7.2, we have reported the preliminary characterization of a Π -mon sample through several different measurements. The suppression of the photon-induced qubit-state transition phenomenon with intra-cavity photon numbers on the order of 10^2 is particularly encouraging. It shows the promise of achieving an improved QND fidelity under a relatively high readout power, which is one of the chief motivations of this research project. On the other hand, the fidelity and speed of the first single-shot readout data set are only comparable to those from the earliest demonstrations using transmon qubits in standard circuit QED modules, as listed in the first few rows of Table 3.2. The pursuit of higher readout performance will require simultaneous efforts in two lines:

- (a) **Improving coherence times:** For our current sample, the duration of the

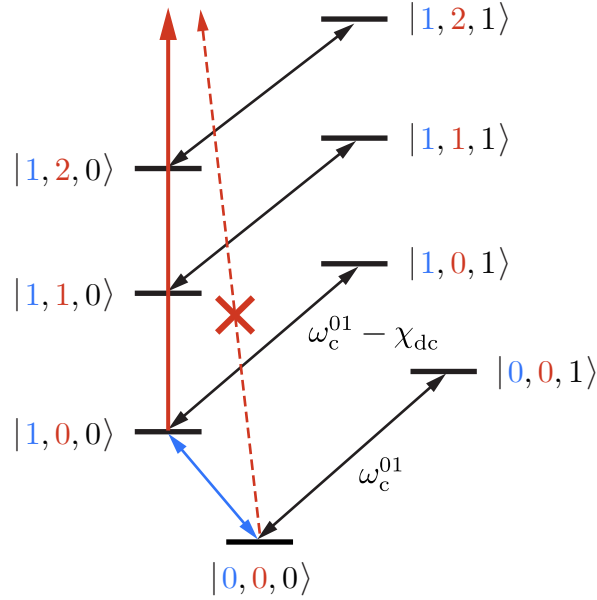


Figure 6.15: Illustration of a dark-mode-selective bright-mode drive in the combined energy-level diagram of the Π -mon-cavity system. The energy-level notations are the same as those in Figure 6.12(a). The forbidden transition is shown using a red dashed arrow with a red cross on its top.

frequency-selective bright mode π pulse on the order of $1 \mu\text{s}$ —limited by χ_{db} —is setting the lower bound of the measurement sequence length in the time domain. The bright mode $T_1 \sim 30 \mu\text{s}$ is therefore responsible for the majority of qubit-state transition events during the whose measurement process (including the bright mode π pulse). From FEM simulations, we obtained a radiative or Purcell limit of the bright mode T_1 to be on the same order of magnitude of the current measured values. Additional radiative protection, such as a waveguide Purcell filter [Narla, 2017] or a resonant cavity filter [Jeffrey *et al.*, 2014; Sete *et al.*, 2015; Walter *et al.*, 2017; Wang *et al.*, 2019] will then be instrumental in achieving a higher bright mode T_1 and fewer qubit-state transition errors in the single-shot readout.

(b) **Increasing the SNR:** A more intrinsic limitation on the readout fidelity and

speed is posted by the readout SNR. For its further improvement, not only the ratio χ_{bc}/χ_{dc} should be optimized in future sample designs, but also the value of χ_{bc} itself, which primarily sets the measurement rate when the intra-cavity preamplifier is turned on. Moreover, another applicable strategy is to populate the bright mode with a larger number of excitations such that the measurement strength and the SNR will be multiplied by another factor of $\bar{n}_b > 1$.¹² As explained in Figure 6.15, in a desired protocol, the bright mode is driven to its *higher* levels through a selective microwave pulse sequence conditioned on the dark mode being its first excited state. As an example, Figure 6.16 show the readout histogram data acquired from driving the conditional bright mode 0–2 transition through a two-photon process mediated by a virtual level, yielding a total readout fidelity of 0.912.

Considering the nonlinearity of the bright mode shown in Section 6.5, the conditional drive to its subspace $\{n_b \geq 2\}$ is not likely to be realized simply by increasing the power, but will need a combination of amplitude and frequency modulations. More sophisticated optimization protocols, such as machine learning [Niu *et al.*, 2019; Sivak *et al.*, 2022] may find their applications in this task.

¹²Compared to the results reported in Figure 6.14(c), a factor-of-two increase in the readout SNR will lead to a state distinguishability—the upper bound of \mathcal{F}_{tot} —as high as 0.9995.

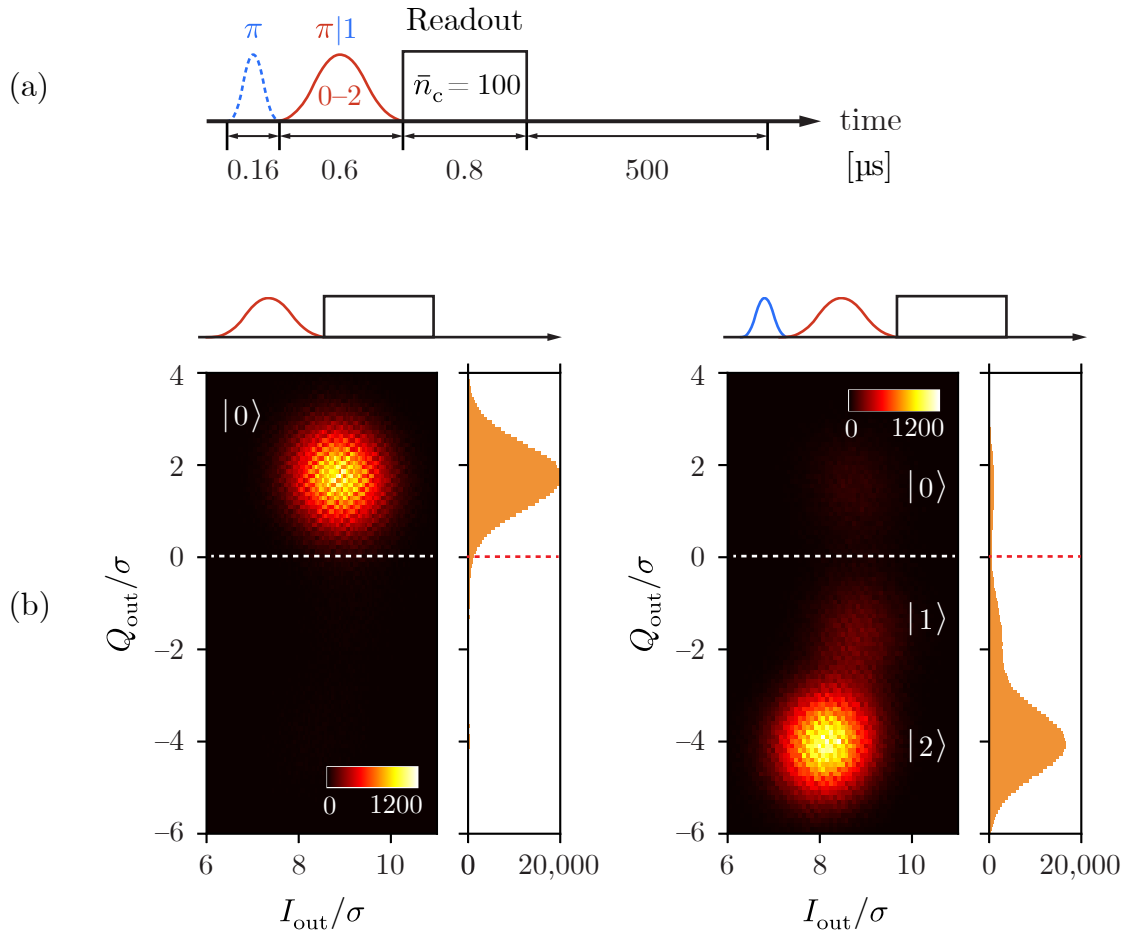


Figure 6.16: Single-shot readout of the dark mode assisted by the bright mode 0–2 transition. Graphic notations are the same as in Figure 6.14. In (a), the bright mode 0–2 transition is driven by a Gaussian pulse centered at frequency $(\omega_b^{01} - \chi_{\text{db}} - K_b/2)$. In (b), relevant bright mode number states are labeled by $|0\rangle$, $|1\rangle$, and $|2\rangle$. The number of shots are 500,000 in both histograms.

Chapter 7

Conclusions and Outlooks

The search will continue. Not until the empirical resources are exhausted, need we pass on to the dreamy realms of speculation.

Edwin Hubble [1936]

Throughout this dissertation, readers should have noticed the parallelism of two theoretical languages: one formalism for quantum mechanics and quantum optics that describes the dynamics and measurements of photons and atom-like excitations using operators, Hamiltonians, commutation relations, et cetera; the other language for microwave electrical circuits—transmission lines, resonators, antennae, mode couplings, and so forth. The mutual support of these two pictures, originally developed to depict very different divisions of the physical world, well exhibits the nature of research in superconducting quantum circuits—an interdisciplinary field aimed at constructing and operating artificial quantum coherent systems using engineering methods, in which major advances are achieved not merely through refined observations, but must involve creative designs and their effective implementations. The basic principles of quantum engineering stated at the beginning of Chapter 1 have been demonstrated in our original experiments. In this final chapter, I am going to conclude these reports by summarizing their main implications and proposing a few possible directions for further investigations.

Circuit QED systems—the starting point of the original works covered by this

dissertation—have been undergoing, in the past two decades, a rapid process of maturation and even standardization in many practical aspects. However, it is generally agreed that improvements at both the component and the system levels are still in need before this physical platform can support more sophisticated research tasks—for quantum computation and communication, and meanwhile toward more fundamental questions on quantum-enhanced sensing and simulation. These hardware optimizations should concentrate on the on-chip superconducting Josephson circuits as well as the off-chip microwave circuitry, both inside and outside the qubit–cavity module. Our two inventions—the cavity attenuator and the Π -mon artificial molecule—are addressing these two aspects separately: the former provides extra-cavity dissipations by modifying the electromagnetic environment of the qubit; the latter realizes the intra-cavity amplification of readout signals through a redesigned qubit–photon interface. As indicated in Figure 6.1, these two additions to the standard circuit QED toolkit are structurally compatible. Future researchers are invited to take the challenge to install them simultaneously in the measurement setup so as to combine their benefits in assisting the protection and acquisition of quantum information stored in superconducting circuits.

7.1 Qubit coherence versus measurability

Since the creation of this field, many efforts have been dedicated to optimizing single-qubit quantum circuits in the two-dimensional performance space of coherence times and measurability. The invention of circuit QED marks a key step in this odyssey: the microwave resonator filters out a broad spectrum of environment-induced qubit decoherence channels, and in the meantime, supports single-shot dispersive qubit readouts if connected to an output amplifier chain with near-quantum-limited efficiencies. To further advance the state of the art, attention has been naturally attracted to the

parasitic issues from this resonant readout mode. The two major concerns—cavity-photon-induced qubit dephasing and state-transition effects, as explained in Sections 3.3 and 3.4—are providing the direct motivations for our two experimental projects, both of which have demonstrated enhanced qubit protection against cavity photons: The resonant cavity attenuator, when carefully thermalized to the mixing chamber stage of the dilution refrigerator, provides a cold dissipative reservoir and can reduce the residual thermal photon population in the readout mode to the order of 10^{-4} , letting the qubit Hahn echo decoherence time be limited solely by the T_1 . The dark mode in the Π -mon artificial molecule shows no observable reduction in T_1 with 10^2 photons in the readout mode, thanks to its quadratic interactions to the bright mode and the readout cavity originating from the orthogonal electric-dipole arrangement and the circuit symmetry. Both measures have proved effective and at the same time, identify the leading physical causes of these measurement-induced qubit decoherence effects. These results will thus have long-term reference values for future investigators who attempt to solve these problems through different approaches.

However, in both cases, the gain in qubit coherence properties are obtained at the expense of reduced measurability: In the cavity attenuator experiment, the hybridized readout mode formed by the superconducting cavity and the resistive cavity attenuator is under-coupled to the coaxial transmission line; the readout signals are subject to the same loss rate as residual thermal radiation and thus fail to be efficiently collected by the output amplifier chain. The linear decoupling between the dark mode and the linear cavity mode in the Π -mon only leaves a residual dispersive shift on the order of 10 kHz, too weak to produce sufficient SNR for single-shot qubit readouts with 10^2 photons. This is why the intra-cavity preamplifier is needed in this readout scheme: by being linearly coupled to the cavity and entangled with the dark mode (qubit) under a selective drive, the bright mode amplified the dispersive measurement strength by one order of magnitude and enabled single-shot qubit read-

outs in our preliminary demonstrations. An even higher SNR will become available if the higher excitation levels of the weakly anharmonic bright mode can be selectively activated.

In this two-step qubit readout protocol, the bright mode effectively serves as a parametric switch, turning on the qubit–photon interaction only during the measurement window when the qubit information needs to be accessed. Such a high-selectivity switching mechanism is the key for breaking the general “antagonistic” relationship between the coherence and measurability of a physical qubit. In addition to the scheme demonstrated in Chapter 6 in which the bright mode is conditionally populated by a single near-resonance microwave drive and maps the qubit state onto the readout cavity field, more variations of intra-cavity amplification protocols in this physical system can be experimented, such as activating higher-order parametric processes in the nonlinear quantum Kerr oscillator through a combination of parametric drives and employing the multi-stability responses of the bright mode as the qubit-state indicator [Dykman, 2019; Lörch *et al.*, 2019; Venkatraman *et al.*, 2022]. These parametric resonances can potentially provide an even higher frequency selectivity and intra-cavity gain; in the meantime, investigations along this line will be able to further unveil the rich physics of driven nonlinear quantum oscillators.

In Sections 5.6 and 6.8, I have proposed two provisional approaches to improve the current performance and range of applicability of these two experimental systems. In the rest of this chapter, I will discuss more extended directions that connect our inventions to the research activities in quantum networks and quantum measurements, and eventually to a broader scope of problems in applied and fundamental quantum physics.

7.2 Microwave thermalization in hybrid quantum networks

Besides being a key method to improve qubit coherence times, the suppression of thermal noise at the microwave frequency band in the quantum regime is demanded in more types of artificial quantum systems than superconducting Josephson circuits. For instance, in several proposed protocols of quantum state transfer and entanglement generation between microwave and optical frequencies, microwave thermal noise is predicted to be detrimental to the fidelity of the quantum transduction process [Andrews *et al.*, 2014; Han *et al.*, 2021; Higginbotham *et al.*, 2018; Hill *et al.*, 2012], especially when this hybrid quantum system is installed on multiple cryogenic temperature stages for the optimal performance of its components and the isolation of the superconducting qubit from the laser power leakage [Zhong *et al.*, 2020]. As illustrated in Figure 7.1, a cavity attenuator, or its lossless cavity filter counterpart¹ can be installed on the microwave transmission line connecting the electro-optical or electro-optomechanical system and the circuit QED module. Provided the cavity attenuator or filter is well thermalized to the mixing chamber stage of the dilution refrigerator, we can expect a similar protection for the superconducting Josephson circuits against the thermal photons as well as other high-frequency radiation coming from the high-temperature stage of the microwave–optical converter. When planning this installation, one is supposed to be reminded of the competition between coherence and efficiency again: a dissipative circuit element on the signal channel will reduce the direct transduction efficiency in exchange for improved radiative protection and

¹See the control experiment described in Section 5.4.

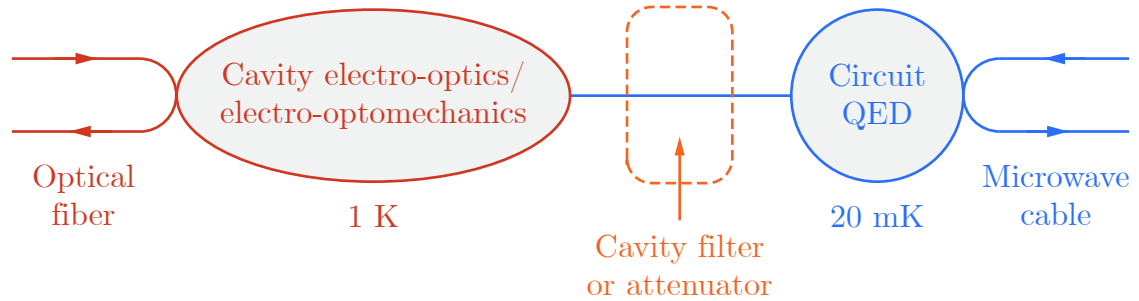


Figure 7.1: Modular diagram of a microwave–optical quantum transduction setup. Left: hybrid cavity quantum electro-optical or electro-optomechanical module (red) that couples microwave and optical modes through parametric processes. Right: superconducting circuit QED module (blue) as the microwave photon generator and analyzer. The two sub-systems are connected by a bi-directional channel (blue line) that transfers microwave excitations between the modules. The optical sub-system can be installed on a higher-temperature stage in a dilution refrigerator to mitigate the spurious laser heating effect, which is particularly harmful for the coherence times of superconducting qubits. In this multi-temperature configuration, the resonant cavity filter or attenuator can be a useful installation to block off-band electromagnetic noise or/and absorb in-band thermal photons so as to enhance the fidelity of quantum state transfer.

detection fidelity.² The exact choice in a preliminary demonstration should depend on the specific quantum state transfer or entanglement generation protocol that best fits the properties of the transducer device.

7.3 Multi-stage quantum measurement systems

In this final section, I am going to conclude this dissertation by revisiting the generic qubit–meter model of quantum measurements introduced in Figure 2.2. In this bi-

²It has been derived in the Supplemental Material of Wang *et al.* [2021] that for a circuit-QED-based quantum microwave radiometer, the residual qubit dephasing rate induced by parasitic photons can be converted to the dark count rate of an equivalent photon counting model.

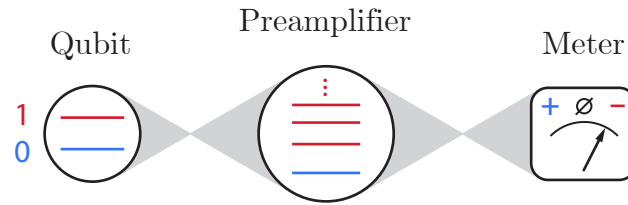


Figure 7.2: Multi-stage qubit–preamplifier–meter model for quantum measurements. The “preamplifier” degree of freedom in the middle is represented as a multi-level atom. The rest of the notations are the same as in Figure 2.2. In our Π -mon measurement setup, the “qubit,” the “preamplifier,” and the “meter” correspond to the dark mode, the bright mode, and the linear readout cavity connected to the output amplifier chain, respectively.

partite depiction, the quantum degree of freedom under observation is isolated as the “qubit,” while all other measurement equipment between the qubit and the human experimenter are summarized into an abstract “meter.” For the standard circuit QED readout setup presented in Figure 3.6, the meter consists of the microwave cavity and its multi-stage output amplifier chain. For the Π -mon measurement setup discussed in Chapter 6, the meter further includes the on-chip Josephson preamplifier (bright mode), which is the first physical object the qubit (dark mode) interacts with. However, one finds that in this configuration, the combined meter itself contains its own bipartite “qubit–meter” substructure, in which the population of the on-chip preamplifier oscillator is measured by a standard circuit QED setup in the dispersive regime. One can therefore expand the “qubit–meter” model into a tripartite one shown in Figure 7.2, in which the preamplifier is separately depicted as a multi-level quantum degree of freedom,³ rather than being incorporated into the classical meter. In our

³In fact, the readout cavity mode in the standard circuit QED system can be analogously modeled as a linear “preamplifier” degree of freedom with its low-energy subspace participating in the qubit readout. The mapping of the two qubit states different by one single excitation quantum to the two cavity states separated by several quanta—in the unit of $(\text{photon number})^{1/2}$ —in the phase space

preliminary demonstration, only the 0–1 subspace of the preamplifier participates in the single-shot qubit readout, whereas manipulating the higher preamplifier levels will be the immediate upcoming goal.

The intermediate quantum preamplifier introduces new problems for quantifying the performance of this two-step qubit readout protocol: For instance, the measurement error rate extracted in a readout fidelity measurement following the protocol described in Section 2.3.1 includes the contributions from the infidelities of the qubit–preamplifier mapping as well as the readout errors of the preamplifier state. Moreover, measurement back-actions on the qubit can be exerted by both the bright mode and the linear cavity (considering the non-negligible residual coupling rate χ_{dc} in the Kerr matrix). More complicated channel models thus need to be established for a full characterization of the qubit readout and QND fidelities.⁴ For further generalizations, one is encouraged to explore more sophisticated information theoretical tools for describing multi-stage quantum measurement systems under realistic experimental conditions.

already constitutes an in-situ amplification scheme on its own.

⁴See Sections 2.3.1 and 2.3.2

Bibliography

- Abdo, B., N. T. Bronn, O. Jinka, S. Olivadese, M. Brink, and J. M. Chow (2018), “Multi-path interferometric Josephson directional amplifier for qubit readout,” *Quantum Science and Technology* **3**, 024003.
- Abdo, B., K. Sliwa, L. Frunzio, and M. Devoret (2013), “Directional amplification with a Josephson circuit,” *Physical Review X* **3**, 031001.
- Abragam, A. (1961), *The Principles of Nuclear Magnetism* (Clarendon Press, Oxford).
- Agarwal, A., and J. H. Lang (2005), *Foundations of Analog and Digital Electronic Circuits* (Elsevier, Amsterdam).
- Aharonov, Y., and D. Rohrlich (2005), *Quantum Paradoxes: Quantum Theory for the Perplexed* (Wiley, Weinheim).
- Akkermans, E. (2010), *Mesoscopic Physics of Electrons and Photons* (Cambridge University Press, Cambridge, England).
- Albertinale, E., L. Balembois, E. Billaud, V. Ranjan, D. Flanigan, T. Schenkel, D. Estève, D. Vion, P. Bertet, and E. Flurin (2021), “Detecting spins by their fluorescence with a microwave photon counter,” *Nature* **600**, 434.
- Ambegaokar, V., and A. Baratoff (1963a), “Tunneling between superconductors,” *Physical Review Letters* **11**, 104.
- Ambegaokar, V., and A. Baratoff (1963b), “Tunneling between superconductors,” *Physical Review Letters* **10**, 486.
- Andersen, C. K., A. Kamal, N. A. Masluk, I. M. Pop, A. Blais, and M. H. Devoret (2020a), “Quantum versus classical switching dynamics of driven dissipative kerr resonators,” *Physical Review Applied* **13**, 044017.

- Andersen, C. K., A. Remm, S. Lazar, S. Krinner, J. Heinsoo, J.-C. Besse, M. Gabureac, A. Wallraff, and C. Eichler (2019), “Entanglement stabilization using ancilla-based parity detection and real-time feedback in superconducting circuits,” *npj Quantum Information* **5**, 69.
- Andersen, C. K., A. Remm, S. Lazar, S. Krinner, N. Lacroix, G. J. Norris, M. Gabureac, C. Eichler, and A. Wallraff (2020b), “Repeated quantum error detection in a surface code,” *Nature Physics* **16**, 875.
- Anderson, P. W., and J. M. Rowell (1963), “Probable observation of the Josephson superconducting tunneling effect,” *Physical Review Letters* **10**, 230.
- Andreev, A. F. (1964), “The thermal conductivity of the intermediate state in superconductors,” *Soviet Physics—Journal of Experimental and Theoretical Physics* **19**, 1228.
- Andrews, R. W., R. W. Peterson, T. P. Purdy, K. Cicak, R. W. Simmonds, C. A. Regal, and K. W. Lehnert (2014), “Bidirectional and efficient conversion between microwave and optical light,” *Nature Physics* **10**, 321.
- Annett, J. F. (2004), *Superconductivity, Superfluids and Condensates* (Oxford University Press, Oxford).
- Arthurs, E., and J. L. Kelly (1965), “On the simultaneous measurement of a pair of conjugate observables,” *Bell System Technical Journal* **44**, 725.
- Ashcroft, N. W., and N. D. Mermin (1976), *Solid State Physics* (Cengage, Boston).
- Asztalos, S. J., G. Carosi, C. Hagmann, D. Kinion, K. van Bibber, M. Hotz, L. J. Rosenberg, G. Rybka, J. Hoskins, J. Hwang, P. Sikivie, D. B. Tanner, R. Bradley, and J. Clarke (2010), “SQUID-based microwave cavity search for dark-matter axions,” *Physical Review Letters* **104**, 041301.
- Auerbach, F. (1923), *Entwicklungsgeschichte der modernen Physik: Zugleich eine Übersicht ihrer Tatsachen, Gesetze und Theorien* (Springer, Berlin).
- Axline, C. J., L. D. Burkhardt, W. Pfaff, M. Zhang, K. Chou, P. Campagne-Ibarcq, P. Reinhold, L. Frunzio, L. Jiang, M. H. Devoret, and R. J. Schoelkopf (2018), “On-demand quantum state transfer and entanglement between remote microwave cavity memories,” *Nature Physics* **14**, 705.

- Backes, K. M., D. A. Palken, S. A. Kenany, B. M. Brubaker, S. B. Cahn, A. Droster, G. C. Hilton, S. Ghosh, H. Jackson, S. K. Lamoreaux, A. F. Leder, K. W. Lehnert, S. M. Lewis, M. Malnou, R. H. Maruyama, N. M. Rapidis, M. Simanovskaia, S. Singh, D. H. Speller, I. Urdinaran, L. R. Vale, E. C. van Assendelft, K. van Bibber, and H. Wang (2021), “A quantum enhanced search for dark matter axions,” *Nature* **590**, 238.
- Balanis, C. A. (2016), *Antenna Theory: Analysis and Design*, 4th ed. (Wiley, Hoboken, New Jersey).
- Balian, R. (1982), *Du microscopique au macroscopique. Cours de physique statistique de l'École polytechnique*, Tome I (Ellipses, Paris); English translation by D. ter Haar and J. F. Gregg (1992), *From Microphysics to Macrophysics: Methods and Applications of Statistical Physics*, Vol. 1 (Springer, Berlin and Heidelberg).
- Bardeen, J., L. N. Cooper, and J. R. Schrieffer (1957), “Theory of superconductivity,” *Physical Review* **108**, 1175.
- Barends, R., J. Wenner, M. Lenander, Y. Chen, R. C. Bialczak, J. Kelly, E. Lucero, P. O'Malley, M. Mariantoni, D. Sank, H. Wang, T. C. White, Y. Yin, J. Zhao, A. N. Cleland, J. M. Martinis, and J. J. A. Baselmans (2011), “Minimizing quasiparticle generation from stray infrared light in superconducting quantum circuits,” *Applied Physics Letters* **99** (11), 113507.
- Barzanjeh, S., M. Wulf, M. Peruzzo, M. Kalaei, P. B. Dieterle, O. Painter, and J. M. Fink (2017), “Mechanical on-chip microwave circulator,” *Nature Communications* **8**, 953.
- Beenakker, C. W. J., and H. van Houten (1991), “Josephson current through a superconducting quantum point contact shorter than the coherence length,” *Physical Review Letters* **66**, 3056.
- Bell, M. T., and A. Samolov (2015), “Traveling-wave parametric amplifier based on a chain of coupled asymmetric SQUIDs,” *Physical Review Applied* **4**, 024014.
- Bergeal, N., F. Schackert, M. Metcalfe, R. Vijay, V. E. Manucharyan, L. Frunzio, D. E. Prober, R. J. Schoelkopf, S. M. Girvin, and M. H. Devoret (2010a), “Phase-preserving amplification near the quantum limit with a Josephson ring modulator,” *Nature* **465**, 64.

- Bergeal, N., R. Vijay, V. E. Manucharyan, I. Siddiqi, R. J. Schoelkopf, S. M. Girvin, and M. H. Devoret (2010b), “Analog information processing at the quantum limit with a Josephson ring modulator,” *Nature Physics* **6**, 296.
- Bernier, N. R., L. D. Tóth, A. Koottandavida, M. A. Ioannou, D. Malz, A. Nunnenkamp, A. K. Feofanov, and T. J. Kippenberg (2017), “Nonreciprocal reconfigurable microwave optomechanical circuit,” *Nature Communications* **8**, 604.
- Bernu, J., S. Deléglise, C. Sayrin, S. Kuhr, I. Dotsenko, M. Brune, J. M. Raimond, and S. Haroche (2008), “Freezing coherent field growth in a cavity by the quantum Zeno effect,” *Physical Review Letters* **101**, 180402.
- Bertet, P., I. Chiorescu, G. Burkard, K. Semba, C. J. P. M. Harmans, D. P. DiVincenzo, and J. E. Mooij (2005a), “Dephasing of a superconducting qubit induced by photon noise,” *Physical Review Letters* **95**, 257002.
- Bertet, P., I. Chiorescu, C. J. P. M. Harmans, and J. E. Mooij (2005b), “Dephasing of a flux-qubit coupled to a harmonic oscillator,” *arXiv:cond-mat/0507290*.
- Besse, J.-C., S. Gasparinetti, M. C. Collodo, T. Walter, P. Kurpiers, M. Pechal, C. Eichler, and A. Wallraff (2018), “Single-shot quantum nondemolition detection of individual itinerant microwave photons,” *Physical Review X* **8**, 021003.
- Billangeon, P.-M., J. S. Tsai, and Y. Nakamura (2015), “Circuit-QED-based scalable architectures for quantum information processing with superconducting qubits,” *Physical Review B* **91**, 094517.
- Blais, A., S. M. Girvin, and W. D. Oliver (2020), “Quantum information processing and quantum optics with circuit quantum electrodynamics,” *Nature Physics* **16**, 247.
- Blais, A., A. L. Grimsmo, S. M. Girvin, and A. Wallraff (2021), “Circuit quantum electrodynamics,” *Reviews of Modern Physics* **93**, 025005.
- Blais, A., R.-S. Huang, A. Wallraff, S. M. Girvin, and R. J. Schoelkopf (2004), “Cavity quantum electrodynamics for superconducting electrical circuits: An architecture for quantum computation,” *Physical Review A* **69**, 062320.
- Bloch, F. (1946), “Nuclear induction,” *Physical Review* **70**, 460.

- Bloch, F., W. W. Hansen, and M. Packard (1946), “The nuclear induction experiment,” *Physical Review* **70**, 474.
- Bloembergen, N., E. M. Purcell, and R. V. Pound (1948), “Relaxation effects in nuclear magnetic resonance absorption,” *Physical Review* **73**, 679.
- Boissonneault, M., J. M. Gambetta, and A. Blais (2008), “Nonlinear dispersive regime of cavity qed: The dressed dephasing model,” *Physical Review A* **77**, 060305.
- Boissonneault, M., J. M. Gambetta, and A. Blais (2009), “Dispersive regime of circuit QED: Photon-dependent qubit dephasing and relaxation rates,” *Physical Review A* **79**, 013819.
- Bouchiat, V., D. Vion, P. Joyez, D. Esteve, and M. H. Devoret (1998), “Quantum coherence with a single Cooper pair,” *Physica Scripta* **T76**, 165.
- Boulant, N., G. Ithier, P. Meeson, F. Nguyen, D. Vion, D. Esteve, I. Siddiqi, R. Vijay, C. Rigetti, F. Pierre, and M. Devoret (2007), “Quantum nondemolition readout using a Josephson bifurcation amplifier,” *Physical Review B* **76**, 014525.
- Boyle, R. (1661), *Two Essays, Concerning the Unsuccessfulness of Experiments, Containing divers Admonitions and Observations (chiefly Chymical) touching that Subject* (Henry Herringman, London).
- Braginsky, V. B. (1970), *Fizicheskiye Eksperimenty s Probnyimi Telami*, Физические эксперименты с пробными телами (Nauka, Moscow); English translation (1972), *Physical Experiments with Test Bodies* (NASA, Washington, D.C.).
- Braginsky, V. B., and F. Y. Khalili (1992), *Quantum Measurement* (Cambridge University Press, Cambridge, England).
- Braginsky, V. B., and F. Y. Khalili (1996), “Quantum nondemolition measurements: the route from toys to tools,” *Reviews of Modern Physics* **68**, 1.
- Braginsky, V. B., and Y. I. Vorontsov (1975), “Quantum-mechanical limitations in macroscopic experiments and modern experimental technique,” *Soviet Physics Uspekhi* **17**, 644.
- Braginsky, V. B., Y. I. Vorontsov, and K. S. Thorne (1980), “Quantum nondemolition measurements,” *Science* **209**, 547.

- Brecht, T., Y. Chu, C. Axline, W. Pfaff, J. Z. Blumoff, K. Chou, L. Krayzman, L. Frunzio, and R. J. Schoelkopf (2017), “Micromachined integrated quantum circuit containing a superconducting qubit,” *Physical Review Applied* **7**, 044018.
- Brecht, T., M. Reagor, Y. Chu, W. Pfaff, C. Wang, L. Frunzio, M. H. Devoret, and R. J. Schoelkopf (2015), “Demonstration of superconducting micromachined cavities,” *Applied Physics Letters* **107**, 192603.
- Bridgman, P. W. (1927), *The Logic of Modern Physics* (Macmillan, New York).
- Bridgman, P. W. (1959), *The Way Things Are* (Harvard University Press, Cambridge, Massachusetts).
- Brillouin, L. (1951a), “Maxwell’s demon cannot operate: Information and entropy. I,” *Journal of Applied Physics* **22**, 334.
- Brillouin, L. (1951b), “Physical entropy and information. II,” *Journal of Applied Physics* **22**, 338.
- Brillouin, L. (1953), “The negentropy principle of information,” *Journal of Applied Physics* **24**, 1152.
- Brillouin, L. (1956), *Science and Information Theory* (Academic Press, New York).
- Brubaker, B. M., L. Zhong, Y. V. Gurevich, S. B. Cahn, S. K. Lamoreaux, M. Simanovskaia, J. R. Root, S. M. Lewis, S. Al Kenany, K. M. Backes, I. Urdinanan, N. M. Rapidis, T. M. Shokair, K. A. van Bibber, D. A. Palken, M. Malnou, W. F. Kindel, M. A. Anil, K. W. Lehnert, and G. Carosi (2017), “First results from a microwave cavity axion search at 24 μeV ,” *Physical Review Letters* **118**, 061302.
- Brun, T. A. (2002), “A simple model of quantum trajectories,” *American Journal of Physics* **70**, 719.
- Bultink, C. C., M. A. Rol, T. E. O’Brien, X. Fu, B. C. S. Dikken, C. Dickel, R. F. L. Vermeulen, J. C. de Sterke, A. Bruno, R. N. Schouten, and L. DiCarlo (2016), “Active resonator reset in the nonlinear dispersive regime of circuit QED,” *Physical Review Applied* **6**, 034008.

- Bultink, C. C., B. Tarasinski, N. Haandbæk, S. Poletto, N. Haider, D. J. Michalak, A. Bruno, and L. DiCarlo (2018), “General method for extracting the quantum efficiency of dispersive qubit readout in circuit QED,” *Applied Physics Letters* **112**, 092601.
- Burkhart, L. D., J. D. Teoh, Y. Zhang, C. J. Axline, L. Frunzio, M. Devoret, L. Jiang, S. Girvin, and R. Schoelkopf (2021), “Error-detected state transfer and entanglement in a superconducting quantum network,” *PRX Quantum* **2**, 030321.
- Callen, H. B., and T. A. Welton (1951), “Irreversibility and generalized noise,” *Physical Review* **83**, 34.
- Campagne-Ibarcq, P., E. Zalys-Geller, A. Narla, S. Shankar, P. Reinhold, L. Burkhardt, C. Axline, W. Pfaff, L. Frunzio, R. J. Schoelkopf, and M. H. Devoret (2018), “Deterministic remote entanglement of superconducting circuits through microwave two-photon transitions,” *Physical Review Letters* **120**, 200501.
- Campbell, S. A. (2001), *The Science and Engineering of Microelectronic Fabrication*, 2nd ed. (Oxford University Press, New York and Oxford).
- Carmichael, H. J. (1993), *An Open Systems Approach to Quantum Optics* (Springer, Berlin and Heidelberg).
- Castellanos-Beltran, M. A., K. D. Irwin, G. C. Hilton, L. R. Vale, and K. W. Lehnert (2008), “Amplification and squeezing of quantum noise with a tunable Josephson metamaterial,” *Nature Physics* **4**, 929.
- Catelani, G., R. J. Schoelkopf, M. H. Devoret, and L. I. Glazman (2011), “Relaxation and frequency shifts induced by quasiparticles in superconducting qubits,” *Physical Review B* **84**, 064517.
- Caves, C. M. (1980), “Quantum-mechanical radiation-pressure fluctuations in an interferometer,” *Physical Review Letters* **45**, 75.
- Caves, C. M. (1981), “Quantum-mechanical noise in an interferometer,” *Physical Review D* **23**, 1693.
- Caves, C. M. (1982), “Quantum limits on noise in linear amplifiers,” *Physical Review D* **26**, 1817.

- Caves, C. M., K. S. Thorne, R. W. P. Drever, V. D. Sandberg, and M. Zimmermann (1980), “On the measurement of a weak classical force coupled to a quantum-mechanical oscillator. i. issues of principle,” *Reviews of Modern Physics* **52**, 341.
- Chambers, R. G. (1950), “Anomalous skin effect in metals,” *Nature* **165**, 239.
- Chapman, B. J., B. A. Moores, E. I. Rosenthal, J. Kerckhoff, and K. W. Lehnert (2016), “General purpose multiplexing device for cryogenic microwave systems,” *Applied Physics Letters* **108**, 222602.
- Chapman, B. J., E. I. Rosenthal, J. Kerckhoff, B. A. Moores, L. R. Vale, J. A. B. Mates, G. C. Hilton, K. Lalumière, A. Blais, and K. W. Lehnert (2017), “Widely tunable on-chip microwave circulator for superconducting quantum circuits,” *Physical Review X* **7**, 041043.
- Chapman, B. J., E. I. Rosenthal, and K. W. Lehnert (2019), “Design of an on-chip superconducting microwave circulator with octave bandwidth,” *Physical Review Applied* **11**, 044048.
- Chaudhuri, S., D. Li, K. D. Irwin, C. Bockstiegel, J. Hubmayr, J. N. Ullom, M. R. Vissers, and J. Gao (2017), “Broadband parametric amplifiers based on nonlinear kinetic inductance artificial transmission lines,” *Applied Physics Letters* **110**, 152601.
- Chiorescu, I., Y. Nakamura, C. J. P. M. Harmans, and J. E. Mooij (2003), “Coherent quantum dynamics of a superconducting flux qubit,” *Science* **299**, 1869.
- Chou, K. S., J. Z. Blumoff, C. S. Wang, P. C. Reinhold, C. J. Axline, Y. Y. Gao, L. Frunzio, M. H. Devoret, L. Jiang, and R. J. Schoelkopf (2018), “Deterministic teleportation of a quantum gate between two logical qubits,” *Nature* **561**, 368.
- Chow, J. M., A. D. Córcoles, J. M. Gambetta, C. Rigetti, B. R. Johnson, J. A. Smolin, J. R. Rozen, G. A. Keefe, M. B. Rothwell, M. B. Ketchen, and M. Steffen (2011), “Simple all-microwave entangling gate for fixed-frequency superconducting qubits,” *Physical Review Letters* **107**, 080502.
- Chow, J. M., J. M. Gambetta, A. W. Cross, S. T. Merkel, C. Rigetti, and M. Steffen (2013), “Microwave-activated conditional-phase gate for superconducting qubits,” *New Journal of Physics* **15**, 115012.

- Clarke, J., A. N. Cleland, M. H. Devoret, D. Esteve, and J. M. Martinis (1988), “Quantum mechanics of a macroscopic variable: The phase difference of a Josephson junction,” *Science* **239**, 992.
- Clarke, J., and F. K. Wilhelm (2008), “Superconducting quantum bits,” *Nature* **453**, 1031.
- Clerk, A. A., M. H. Devoret, S. M. Girvin, F. Marquardt, and R. J. Schoelkopf (2010), “Introduction to quantum noise, measurement, and amplification,” *Reviews of Modern Physics* **82**, 1155.
- Clerk, A. A., K. W. Lehnert, P. Bertet, J. R. Petta, and Y. Nakamura (2020), “Hybrid quantum systems with circuit quantum electrodynamics,” *Nature Physics* **16**, 257.
- Clerk, A. A., and D. W. Utami (2007), “Using a qubit to measure photon-number statistics of a driven thermal oscillator,” *Physical Review A* **75**, 042302.
- Cohadon, P.-F., J. Harris, F. Marquardt, and L. Cugliandolo, Eds. (2020), *Quantum Optomechanics and Nanomechanics*, École de Physique des Houches, Session CV (Oxford University Press, Oxford).
- Cohen-Tannoudji, C., B. Diu, and F. Laloë (1973), *Mécanique quantique*, Tome I (Hermann, Paris); English translation by S. R. Hemley, N. Ostrowsky, and D. Ostrowsky (1977), *Quantum Mechanics*, Vol. 1 (Wiley, New York).
- Cohen-Tannoudji, C., J. Dupont-Roc, and G. Grynberg (1987), *Photons et atomes. Introduction à l'électrodynamique quantique* (CNRS Éditions, Paris); English translation (1989), *Photons and Atoms: Introduction to Quantum Electrodynamics* (Wiley, New York).
- Cohen-Tannoudji, C., J. Dupont-Roc, and G. Grynberg (1988), *Processus d'interaction entre photons et atomes* (CNRS Éditions, Paris); English translation by P. Thickstun (1992), *Atom—Photon Interactions: Basic Process and Applications* (Wiley, New York).
- Cohen-Tannoudji, C., and D. Guéry-Odelin (2011), *Advances in Atomic Physics: An Overview* (World Scientific, Singapore).
- Cottet, A. (2002), *Implementation of a quantum bit in a superconducting circuit*, Ph.D. dissertation (Université Paris VI).

- Cover, T. M., and J. A. Thomas (2005), *Elements of Information Theory*, 2nd ed. (Wiley, Hoboken, New Jersey).
- d'Arsonval, A. (1888), *Notice sur les titres et travaux scientifiques de M. A. d'Arsonval* (La Lumière électrique, Paris).
- Dassonneville, R. (2019), *Qubit Readouts Using a Transmon Molecule in a 3D Circuit Quantum Electrodynamics Architecture*, Ph.D. dissertation (Université Grenoble Alpes).
- Dassonneville, R., T. Ramos, V. Milchakov, L. Planat, E. Dumur, F. Foroughi, J. Puertas, S. Leger, K. Bharadwaj, J. Delaforce, C. Naud, W. Hasch-Guichard, J. J. García-Ripoll, N. Roch, and O. Buisson (2020), “Fast high-fidelity quantum nondemolition qubit readout via a nonperturbative cross-kerr coupling,” *Physical Review X* **10**, 011045.
- Datta, S. (1995), *Electronic Transport in Mesoscopic Systems* (Cambridge University Press, Cambridge, England).
- de Gennes, P. G. (1966), *Superconductivity of Metals and Alloys* (Benjamin, New York).
- de Wolf, R. (2019), “Quantum computing: Lecture notes,” arXiv:1907.09415.
- d’Espagnat, B. (1976), *Conceptual Foundations of Quantum Mechanics*, 2nd ed. (Benjamin, New York).
- Devoret, M. H. (1997), “Quantum fluctuations in electrical circuits,” in *Quantum Fluctuations*, École de Physique des Houches, Session LXIII, edited by S. Reynaud, E. Giacobino, and J. Zinn-Justin (Elsevier, Amsterdam) pp. 351–386.
- Devoret, M. H. (2008), *De l’atome aux machines quantiques*, Leçons inaugurales du Collège de France (Collège de France/Fayard, Paris).
- Devoret, M. H., D. Esteve, C. Urbina, A. N. Cleland, J. M. Martinis, and J. Clarke (2003), “Macroscopic quantum mechanics of the current-biased Josephson junction,” in *Exploring the Quantum/Classical Frontier: Recent Advances in Macroscopic Quantum Phenomena*, edited by J. R. Friedman and S. Han (Nova, New York) pp. 1–34.

- Devoret, M. H., B. Huard, R. Schoelkopf, and L. F. Cugliandolo, Eds. (2011), *Quantum Machines: Measurement and Control of Engineered Quantum Systems*, École de Physique des Houches, Session XCVI (Oxford University Press, Oxford).
- Devoret, M. H., and J. M. Martinis (2004), “Superconducting qubits,” in *Quantum Entanglement and Information Processing*, École de Physique des Houches, Session LXXIX, edited by D. Esteve, J.-M. Raimond, and J. Dalibard (Elsevier, New York) pp. 443–485.
- Devoret, M. H., J. M. Martinis, and J. Clarke (1985), “Measurements of macroscopic quantum tunneling out of the zero-voltage state of a current-biased Josephson junction,” *Physical Review Letters* **55**, 1908.
- Devoret, M. H., and R. J. Schoelkopf (2013), “Superconducting circuits for quantum information: An outlook,” *Science* **339**, 1169.
- Dial, O., D. T. McClure, S. Poletto, G. A. Keefe, M. B. Rothwell, J. M. Gambetta, D. W. Abraham, J. M. Chow, and M. Steffen (2016), “Bulk and surface loss in superconducting transmon qubits,” *Superconductor Science and Technology* **29** (4), 044001.
- Diamond, S., V. Fatemi, M. Hays, H. Nho, P. D. Kurilovich, T. Connolly, V. R. Joshi, K. Serniak, L. Frunzio, L. I. Glazman, and M. H. Devoret (2022), “Distinguishing parity-switching mechanisms in a superconducting qubit,” arXiv:2204.07458.
- DiCarlo, L., J. M. Chow, J. M. Gambetta, L. S. Bishop, B. R. Johnson, D. I. Schuster, J. Majer, A. Blais, L. Frunzio, S. M. Girvin, and R. J. Schoelkopf (2009), “Demonstration of two-qubit algorithms with a superconducting quantum processor,” *Nature* **460**, 240.
- Didier, N., J. Bourassa, and A. Blais (2015), “Fast quantum nondemolition readout by parametric modulation of longitudinal qubit-oscillator interaction,” *Physical Review Letters* **115**, 203601.
- Dillon, A., K. McCusker, J. V. Dyke, B. Isler, and M. Christiansen (2017), “Thermal interface material characterization for cryogenic electronic packaging solutions,” *IOP Conference Series: Materials Science and Engineering* **278**, 012054.

- Diniz, I., E. Dumur, O. Buisson, and A. Auffèves (2013), “Ultrafast quantum non-demolition measurements based on a diamond-shaped artificial atom,” *Physical Review A* **87**, 033837.
- Dirac, P. A. M. (1930), *The Principles of Quantum Mechanics* (Clarendon Press, Oxford).
- DiVincenzo, D. P. (2000), “The physical implementation of quantum computation,” *Fortschritte der Physik* **48**, 771.
- Dixit, A. V., S. Chakram, K. He, A. Agrawal, R. K. Naik, D. I. Schuster, and A. Chou (2021), “Searching for dark matter with a superconducting qubit,” *Physical Review Letters* **126**, 141302.
- Dolan, G. J. (1977), “Offset masks for lift-off photoprocessing,” *Applied Physics Letters* **31**, 337.
- Dowling, J. P., and G. J. Milburn (2003), “Quantum technology: the second quantum revolution,” *Philosophical Transactions of the Royal Society A* **361**, 1655.
- Du, N., N. Force, R. Khatiwada, E. Lentz, R. Ottens, L. J. Rosenberg, G. Rybka, G. Carosi, N. Woollett, D. Bowering, A. S. Chou, A. Sonnenschein, W. Wester, C. Boutan, N. S. Oblath, R. Bradley, E. J. Daw, A. V. Dixit, J. Clarke, S. R. O’Kelley, N. Crisosto, J. R. Gleason, S. Jois, P. Sikivie, I. Stern, N. S. Sullivan, D. B. Tanner, and G. C. Hilton (ADMX Collaboration) (2018), “Search for invisible axion dark matter with the axion dark matter experiment,” *Physical Review Letters* **120**, 151301.
- Dunoyer, L. (1913), “Expérience de résonance optique sur un gaz à une dimension. L’amortissement des vibreurs lumineux,” *Comptes Rendus de l’Académie des sciences* **157**, 1068.
- Dunsworth, A., A. Megrant, C. Quintana, Z. Chen, R. Barends, B. Burkett, B. Foxen, Y. Chen, B. Chiaro, A. Fowler, R. Graff, E. Jeffrey, J. Kelly, E. Lucero, J. Y. Mutus, M. Neeley, C. Neill, P. Roushan, D. Sank, A. Vainsencher, J. Wenner, T. C. White, and J. M. Martinis (2017), “Characterization and reduction of capacitive loss induced by sub-micron Josephson junction fabrication in superconducting qubits,” *Applied Physics Letters* **111**, 022601.

- Dykman, M. I. (2019), “Coherent multiple-period states of periodically modulated qubits,” *Physical Review A* **100**, 042101.
- Eddins, A., J. M. Kreikebaum, D. M. Toyli, E. M. Levenson-Falk, A. Dove, W. P. Livingston, B. A. Levitan, L. C. G. Govia, A. A. Clerk, and I. Siddiqi (2019), “High-efficiency measurement of an artificial atom embedded in a parametric amplifier,” *Physical Review X* **9**, 011004.
- Eddins, A., S. Schreppler, D. M. Toyli, L. S. Martin, S. Hacoheh-Gourgy, L. C. G. Govia, H. Ribeiro, A. A. Clerk, and I. Siddiqi (2018), “Stroboscopic qubit measurement with squeezed illumination,” *Physical Review Letters* **120**, 040505.
- Eichler, C., Y. Salathe, J. Mlynek, S. Schmidt, and A. Wallraff (2014), “Quantum-limited amplification and entanglement in coupled nonlinear resonators,” *Physical Review Letters* **113**, 110502.
- Esteve, D., M. H. Devoret, and J. M. Martinis (1986), “Effect of an arbitrary dissipative circuit on the quantum energy levels and tunneling of a Josephson junction,” *Physical Review B* **34**, 158.
- Esteve, D., J.-M. Raimond, and J. Dalibard, Eds. (2004), *Quantum Entanglement and Information Processing*, École de Physique des Houches, Session LXXIX (Elsevier, New York).
- Facchi, P., V. Gorini, G. Marmo, S. Pascazio, and E. Sudarshan (2000), “Quantum Zeno dynamics,” *Physics Letters A* **275** (1), 12.
- Facchi, P., and S. Pascazio (2002), “Quantum Zeno subspaces,” *Physical Review Letters* **89**, 080401.
- Facchi, P., and S. Pascazio (2008), “Quantum Zeno dynamics: mathematical and physical aspects,” *Journal of Physics A: Mathematical and Theoretical* **41**, 493001.
- Feynman, R. P., R. B. Leighton, and M. L. Sands (1964), *The Feynman Lectures on Physics*, Vol. 2: Mainly Electromagnetism and Matter (Addison-Wesley, Reading, Massachusetts and Palo Alto).
- Filipp, S., M. Göppl, J. M. Fink, M. Baur, R. Bianchetti, L. Steffen, and A. Wallraff (2011), “Multimode mediated qubit-qubit coupling and dark-state symmetries in circuit quantum electrodynamics,” *Physical Review A* **83**, 063827.

- Flurin, E., N. Roch, F. Mallet, M. H. Devoret, and B. Huard (2012), “Generating entangled microwave radiation over two transmission lines,” *Physical Review Letters* **109**, 183901.
- Forn-Díaz, P., J. Lisenfeld, D. Marcos, J. J. García-Ripoll, E. Solano, C. J. P. M. Harmans, and J. E. Mooij (2010), “Observation of the bloch-siegert shift in a qubit-oscillator system in the ultrastrong coupling regime,” *Physical Review Letters* **105**, 237001.
- Fox, M. (2006), *Quantum Optics: An Introduction* (Oxford University Press, Oxford).
- Frattini, N. E. (2021), *Three-Wave Mixing in Superconducting Circuits: Stabilizing Cats with SNAILs*, Ph.D. dissertation (Yale University).
- Frattini, N. E., V. V. Sivak, A. Lingenfelter, S. Shankar, and M. H. Devoret (2018), “Optimizing the nonlinearity and dissipation of a SNAIL parametric amplifier for dynamic range,” *Physical Review Applied* **10**, 054020.
- Frattini, N. E., U. Vool, S. Shankar, A. Narla, K. M. Sliwa, and M. H. Devoret (2017), “3-wave mixing Josephson dipole element,” *Applied Physics Letters* **110**, 222603.
- Friedman, J. R., V. Patel, W. Chen, S. K. Tolpygo, and J. E. Lukens (2000), “Quantum superposition of distinct macroscopic states,” *Nature* **406**, 43.
- Frisk Kockum, A., A. Miranowicz, S. De Liberato, S. Savasta, and F. Nori (2019), “Ultrastrong coupling between light and matter,” *Nature Reviews Physics* **1**, 19.
- Fröwis, F., P. Sekatski, W. Dür, N. Gisin, and N. Sangouard (2018), “Macroscopic quantum states: Measures, fragility, and implementations,” *Reviews of Modern Physics* **90**, 025004.
- Furusaki, A., and M. Tsukada (1991), “Current-carrying states in Josephson junctions,” *Physical Review B* **43**, 10164.
- Gambetta, J., A. Blais, M. Boissonneault, A. A. Houck, D. I. Schuster, and S. M. Girvin (2008), “Quantum trajectory approach to circuit QED: Quantum jumps and the Zeno effect,” *Physical Review A* **77**, 012112.

- Gambetta, J., A. Blais, D. I. Schuster, A. Wallraff, L. Frunzio, J. Majer, M. H. Devoret, S. M. Girvin, and R. J. Schoelkopf (2006), “Qubit–photon interactions in a cavity: Measurement-induced dephasing and number splitting,” *Physical Review A* **74**, 042318.
- Gambetta, J., W. A. Braff, A. Wallraff, S. M. Girvin, and R. J. Schoelkopf (2007), “Protocols for optimal readout of qubits using a continuous quantum nondemolition measurement,” *Physical Review A* **76**, 012325.
- Gao, Y. Y., B. J. Lester, K. S. Chou, L. Frunzio, M. H. Devoret, L. Jiang, S. M. Girvin, and R. J. Schoelkopf (2019), “Entanglement of bosonic modes through an engineered exchange interaction,” *Nature* **566**, 509.
- Gao, Y. Y., B. J. Lester, Y. Zhang, C. Wang, S. Rosenblum, L. Frunzio, L. Jiang, S. M. Girvin, and R. J. Schoelkopf (2018), “Programmable interference between two microwave quantum memories,” *Physical Review X* **8**, 021073.
- Gao, Y. Y., M. A. Rol, S. Touzard, and C. Wang (2021), “Practical guide for building superconducting quantum devices,” *PRX Quantum* **2**, 040202.
- Geerlings, K., Z. Leghtas, I. M. Pop, S. Shankar, L. Frunzio, R. J. Schoelkopf, M. Mirrahimi, and M. H. Devoret (2013), “Demonstrating a driven reset protocol for a superconducting qubit,” *Physical Review Letters* **110**, 120501.
- Gerlach, W., and O. Stern (1922), “Der experimentelle nachweis der richtungsquantelung im magnetfeld,” *Zeitschrift für Physik* **9**, 349.
- Girvin, S. M. (2014), “Circuit QED: superconducting qubits coupled to microwave photons,” in *Quantum Machines: Measurement and Control of Engineered Quantum Systems*, École de Physique des Houches, Session XCVI, edited by M. Devoret, B. Huard, R. Schoelkopf, and L. F. Cugliandolo (Oxford University Press, Oxford) pp. 113–255.
- Girvin, S. M., M. H. Devoret, and R. J. Schoelkopf (2009), “Circuit QED and engineering charge-based superconducting qubits,” *Physica Scripta* **T137**, 014012.
- Gisin, N. (2002), “Sundays in a quantum engineer’s life,” in *Quantum [Un]speakable*, edited by R. A. Bertlmann and A. Zeilinger (Springer, Berlin) pp. 199–208.

- Glauber, R. J. (1963), “The quantum theory of optical coherence,” *Physical Review* **130**, 2529.
- Gleyzes, S., and J.-M. Raimond (2016), “Quantum Zeno dynamics in atoms and cavities,” *Comptes Rendus Physique* **17**, 685.
- Goetz, J., S. Pogorzalek, F. Deppe, K. G. Fedorov, P. Eder, M. Fischer, F. Wulschner, E. Xie, A. Marx, and R. Gross (2017), “Photon statistics of propagating thermal microwaves,” *Physical Review Letters* **118**, 103602.
- Goldstein, H., C. P. Poole, and J. L. Safko (2002), *Classical Mechanics*, 3rd ed. (Addison-Wesley, New York).
- Grabert, H., and M. H. Devoret, Eds. (1992), *Single Charge Tunneling: Coulomb Blockade Phenomena in Nanostructures* (Springer, New York).
- Griffiths, R. B. (2002), *Consistent Quantum Theory* (Cambridge University Press, Cambridge, England).
- Grynberg, G., A. Aspect, and C. Fabre (2010), *Introduction to Quantum Optics: From the Semi-Classical Approach to Quantized Light* (Cambridge University Press, Cambridge, England).
- Gu, X., A. F. Kockum, A. Miranowicz, Y. Liu, and F. Nori (2017), “Microwave photonics with superconducting quantum circuits,” *Physics Reports* **718–719**, 1.
- Hacohen-Gourgy, S., L. S. Martin, E. Flurin, V. V. Ramasesh, K. B. Whaley, and I. Siddiqi (2016), “Quantum dynamics of simultaneously measured non-commuting observables,” *Nature* **538**, 491.
- Halpern, M., H. P. Gush, E. Wishnow, and V. D. Cosmo (1986), “Far infrared transmission of dielectrics at cryogenic and room temperatures: glass, fluorogold, eccosorb, stycast, and various plastics,” *Applied Optics* **25**, 565.
- Han, X., W. Fu, C.-L. Zou, L. Jiang, and H. X. Tang (2021), “Microwave-optical quantum frequency conversion,” *Optica* **8** (8), 1050.
- Haroche, S., M. Brune, and J.-M. Raimond (2020), “From cavity to circuit quantum electrodynamics,” *Nature Physics* **16**, 243.

- Haroche, S., and J.-M. Raimond (2006), *Exploring the Quantum: Atoms, Cavities, and Photons* (Oxford University Press, Oxford).
- Hatridge, M., S. Shankar, M. Mirrahimi, F. Schackert, K. Geerlings, T. Brecht, K. M. Sliwa, B. Abdo, L. Frunzio, S. M. Girvin, R. J. Schoelkopf, and M. H. Devoret (2013), “Quantum back-action of an individual variable-strength measurement,” *Science* **339**, 178.
- Hatridge, M., R. Vijay, D. H. Slichter, J. Clarke, and I. Siddiqi (2011), “Dispersive magnetometry with a quantum limited SQUID parametric amplifier,” *Physical Review B* **83**, 134501.
- Haus, H. A., and J. A. Mullen (1962), “Quantum noise in linear amplifiers,” *Physical Review* **128**, 2407.
- Hays, M. (2021), *Realizing an Andreev Spin Qubit: Exploring Sub-Gap Structure in Josephson Nanowires Using Circuit QED*, Ph.D. dissertation (Yale University) (Springer, Cham).
- Heinsoo, J., C. K. Andersen, A. Remm, S. Krinner, T. Walter, Y. Salathé, S. Gasparinetti, J.-C. Besse, A. Potočnik, A. Wallraff, and C. Eichler (2018), “Rapid high-fidelity multiplexed readout of superconducting qubits,” *Physical Review Applied* **10**, 034040.
- Heisenberg, W. (1930), *The Physical Principles of the Quantum Theory* (University of Chicago Press, Chicago).
- Heisenberg, W. (1955), *Das Naturbild der heutigen Physik* (Rowohlt, Hamburg); English translation by A. J. Pomerans (1958), *The Physicist’s Conception of Nature* (Hutchinson, London).
- Higginbotham, A. P., P. S. Burns, M. D. Urmey, R. W. Peterson, N. S. Kampel, B. M. Brubaker, G. Smith, K. W. Lehnert, and C. A. Regal (2018), “Harnessing electro-optic correlations in an efficient mechanical converter,” *Nature Physics* **14**, 1038.
- Hill, J. T., A. H. Safavi-Naeini, J. Chan, and O. Painter (2012), “Coherent optical wavelength conversion via cavity optomechanics,” *Nature Communications* **3**, 1196.

- Ho, K. H., S. T. Newman, S. Rahimifard, and R. D. Allen (2004), “State of the art in wire electrical discharge machining (WEDM),” *International Journal of Machine Tools and Manufacture* **44**, 1247.
- Ho Eom, B., P. K. Day, H. G. LeDuc, and J. Zmuidzinas (2012), “A wideband, low-noise superconducting amplifier with high dynamic range,” *Nature Physics* **8**, 623.
- Houck, A. A., J. A. Schreier, B. R. Johnson, J. M. Chow, J. Koch, J. M. Gambetta, D. I. Schuster, L. Frunzio, M. H. Devoret, S. M. Girvin, and R. J. Schoelkopf (2008), “Controlling the spontaneous emission of a superconducting transmon qubit,” *Physical Review Letters* **101**, 080502.
- Houck, A. A., D. I. Schuster, J. M. Gambetta, J. A. Schreier, B. R. Johnson, J. M. Chow, L. Frunzio, J. Majer, M. H. Devoret, S. M. Girvin, and R. J. Schoelkopf (2007), “Generating single microwave photons in a circuit,” *Nature* **449**, 328.
- Houck, A. A., H. E. Türeci, and J. Koch (2012), “On-chip quantum simulation with superconducting circuits,” *Nature Physics* **8**, 292.
- Houzet, M., K. Serniak, G. Catelani, M. H. Devoret, and L. I. Glazman (2019), “Photon-assisted charge-parity jumps in a superconducting qubit,” *Physical Review Letters* **123**, 107704.
- Hover, D., Y.-F. Chen, G. J. Ribeill, S. Zhu, S. Sendelbach, and R. McDermott (2012), “Superconducting low-inductance undulatory galvanometer microwave amplifier,” *Applied Physics Letters* **100**, 063503.
- Hubble, E. (1936), *The Realm of the Nebulae* (Yale University Press, New Haven).
- Imry, Y. (1997), *Introduction to Mesoscopic Physics* (Oxford University Press, New York and Oxford).
- Inguscio, M., W. Ketterle, S. Stringari, and G. Roati, Eds. (2016), *Quantum Matter at Ultralow Temperatures*, *Rendiconti della Scuola Internazionale di Fisica “Enrico Fermi”*, CXCI Corso (Società Italiana di Fisica, Bologna).
- Inomata, K., Z. Lin, K. Koshino, W. D. Oliver, J.-S. Tsai, T. Yamamoto, and Y. Nakamura (2016), “Single microwave-photon detector using an artificial L-type three-level system,” *Nature Communications* **7**, 12303.

- Itano, W. M., D. J. Heinzen, J. J. Bollinger, and D. J. Wineland (1990), "Quantum Zeno effect," *Physical Review A* **41**, 2295.
- Jammer, M. (1966), *The Conceptual Development of Quantum Mechanics* (McGraw-Hill, New York).
- Jaynes, E. T. (1957a), "Information theory and statistical mechanics," *Physical Review* **106**, 620.
- Jaynes, E. T. (1957b), "Information theory and statistical mechanics. II," *Physical Review* **108**, 171.
- Jeffrey, E., D. Sank, J. Y. Mutus, T. C. White, J. Kelly, R. Barends, Y. Chen, Z. Chen, B. Chiaro, A. Dunsworth, A. Megrant, P. J. J. O'Malley, C. Neill, P. Roushan, A. Vainsencher, J. Wenner, A. N. Cleland, and J. M. Martinis (2014), "Fast accurate state measurement with superconducting qubits," *Physical Review Letters* **112**, 190504.
- Johnson, B. R., M. D. Reed, A. A. Houck, D. I. Schuster, L. S. Bishop, E. Ginossar, J. M. Gambetta, L. DiCarlo, L. Frunzio, S. M. Girvin, and R. J. Schoelkopf (2010), "Quantum non-demolition detection of single microwave photons in a circuit," *Nature Physics* **6**, 663.
- Johnson, J. B. (1928), "Thermal agitation of electricity in conductors," *Physical Review* **32**, 97.
- Johnson, J. E., C. Macklin, D. H. Slichter, R. Vijay, E. B. Weingarten, J. Clarke, and I. Siddiqi (2012), "Heralded state preparation in a superconducting qubit," *Physical Review Letters* **109**, 050506.
- Joos, E., H. D. Zeh, C. Kiefer, D. Giulini, J. Kupsch, and I.-O. Stamatescu (2003), *Decoherence and the Appearance of a Classical World in Quantum Theory*, 2nd ed. (Springer, Berlin and Heidelberg).
- Josephson, B. (1962), "Possible new effects in superconductive tunnelling," *Physics Letters* **1**, 251.
- Josephson, B. D. (1964), "Coupled superconductors," *Reviews of Modern Physics* **36**, 216.

- Kaiser, D. (2011), *How the Hippies Saved Physics: Science, Counterculture, and the Quantum Revival* (W. W. Norton, New York and London).
- Kamal, A., J. Clarke, and M. H. Devoret (2011), “Noiseless non-reciprocity in a parametric active device,” *Nature Physics* **7**, 311.
- Kamal, A., J. Clarke, and M. H. Devoret (2012), “Gain, directionality, and noise in microwave SQUID amplifiers: Input-output approach,” *Physical Review B* **86**, 144510.
- Kapitsa, P. L. (1940), “Проблемы жидкого гелия,” in *Эксперимент, теория, практика: Статьи выступления* (Nauka, Moscow); English translation (1980), “Problems of liquid helium,” in *Experiment, Theory, Practice: Articles and Addresses* (D. Reidel, Dordrecht, Boston, and London).
- Kerckhoff, J., K. Lalumière, B. J. Chapman, A. Blais, and K. W. Lehnert (2015), “On-chip superconducting microwave circulator from synthetic rotation,” *Physical Review Applied* **4**, 034002.
- Kerman, A. J. (2013), “Quantum information processing using quasiclassical electromagnetic interactions between qubits and electrical resonators,” *New Journal of Physics* **15**, 123011.
- Kjaergaard, M., M. E. Schwartz, J. Braumüller, P. Krantz, J. I.-J. Wang, S. Gustavsson, and W. D. Oliver (2020), “Superconducting qubits: Current state of play,” *Annual Review of Condensed Matter Physics* **11**, 369.
- Koch, J., T. M. Yu, J. Gambetta, A. A. Houck, D. I. Schuster, J. Majer, A. Blais, M. H. Devoret, S. M. Girvin, and R. J. Schoelkopf (2007), “Charge-insensitive qubit design derived from the Cooper pair box,” *Physical Review A* **76**, 042319.
- Kono, S., K. Koshino, Y. Tabuchi, A. Noguchi, and Y. Nakamura (2018), “Quantum non-demolition detection of an itinerant microwave photon,” *Nature Physics* **14**, 546.
- Koolstra, G., G. Yang, and D. I. Schuster (2019), “Coupling a single electron on superfluid helium to a superconducting resonator,” *Nature Communications* **10**, 5323.

- Krantz, P., A. Bengtsson, M. Simoen, S. Gustavsson, V. Shumeiko, W. D. Oliver, C. M. Wilson, P. Delsing, and J. Bylander (2016), “Single-shot read-out of a superconducting qubit using a Josephson parametric oscillator,” *Nature Communications* **7**, 11417.
- Krantz, P., M. Kjaergaard, F. Yan, T. P. Orlando, S. Gustavsson, and W. D. Oliver (2019), “A quantum engineer’s guide to superconducting qubits,” *Applied Physics Reviews* **6**, 021318.
- Kubo, R. (1966), “The fluctuation-dissipation theorem,” *Reports on Progress in Physics* **29**, 255.
- Kurpiers, P., P. Magnard, T. Walter, B. Royer, M. Pechal, J. Heinsoo, Y. Salathé, A. Akin, S. Storz, J.-C. Besse, S. Gasparinetti, A. Blais, and A. Wallraff (2018), “Deterministic quantum state transfer and remote entanglement using microwave photons,” *Nature* **558**, 264.
- Kurpiers, P., M. Pechal, B. Royer, P. Magnard, T. Walter, J. Heinsoo, Y. Salathé, A. Akin, S. Storz, J.-C. Besse, S. Gasparinetti, A. Blais, and A. Wallraff (2019), “Quantum communication with time-bin encoded microwave photons,” *Physical Review Applied* **12**, 044067.
- Laloë, F. (2012), *Do We Really Understand Quantum Mechanics?* (Cambridge University Press, Cambridge, England).
- Lamb, W. E. (1969), “An operational interpretation of nonrelativistic quantum mechanics,” *Physics Today* **22**, 23.
- Lamb, W. E. (1986), “Quantum theory of measurement,” *Annals of the New York Academy of Sciences* **480**, 407.
- Landauer, R. (1991), “Information is physical,” *Physics Today* **44**, 23.
- Landauer, R. (1996), “The physical nature of information,” *Physics Letters A* **217**, 188.
- Landauer, R. (1999), “Information is a physical entity,” *Physica A: Statistical Mechanics and its Applications* **263**, 63.

- Langevin, P. (1935), “Statistique et déterminisme,” in *La statistique, ses applications, les problèmes qu’elles soulèvent* (Presses universitaires de France, Paris) pp. 245–295.
- Laplace, P.-S. (1814), *Essai philosophique sur les probabilités* (Courcier, Paris); English translation by F. W. Truscott and F. L. Emory (1902), *A Philosophical Essay on Probabilities* (Chapman & Hall, London and Wiley, New York).
- Lecocq, F., I. M. Pop, Z. Peng, I. Matei, T. Crozes, T. Fournier, C. Naud, W. Guichard, and O. Buisson (2011), “Junction fabrication by shadow evaporation without a suspended bridge,” *Nanotechnology* **22** (31), 315302.
- Lecocq, F., L. Ranzani, G. Peterson, K. Cicak, A. Metelmann, S. Kotler, R. Simmonds, J. Teufel, and J. Aumentado (2020), “Microwave measurement beyond the quantum limit with a nonreciprocal amplifier,” *Physical Review Applied* **13**, 044005.
- Lecocq, F., L. Ranzani, G. A. Peterson, K. Cicak, R. W. Simmonds, J. D. Teufel, and J. Aumentado (2017), “Nonreciprocal microwave signal processing with a field-programmable Josephson amplifier,” *Physical Review Applied* **7**, 024028.
- Leggett, A. J. (1980), “Macroscopic quantum systems and the quantum theory of measurement,” *Progress of Theoretical Physics Supplement* **69**, 80.
- Leggett, A. J. (1987), “Quantum mechanics at the macroscopic level,” in *Chance and Matter*, École de Physique des Houches, Session XLVI, edited by J. Souletie, J. Vanniménus, and R. Stora (Elsevier, Amsterdam) pp. 395–506.
- Leggett, A. J. (2006), *Quantum Liquids: Bose Condensation and Cooper Pairing in Condensed-matter Systems* (Oxford University Press, Oxford).
- Lescanne, R., S. Deléglise, E. Albertinale, U. Réglade, T. Capelle, E. Ivanov, T. Jacqmin, Z. Leghtas, and E. Flurin (2020), “Irreversible qubit-photon coupling for the detection of itinerant microwave photons,” *Physical Review X* **10**, 021038.
- Lescanne, R., L. Verney, Q. Ficheux, M. H. Devoret, B. Huard, M. Mirrahimi, and Z. Leghtas (2019), “Escape of a driven quantum Josephson circuit into unconfined states,” *Physical Review Applied* **11**, 014030.

- Leung, N., Y. Lu, S. Chakram, R. K. Naik, N. Earnest, R. Ma, K. Jacobs, A. N. Cleland, and D. I. Schuster (2019), “Deterministic bidirectional communication and remote entanglement generation between superconducting qubits,” *npj Quantum Information* **5**, 18.
- Likharev, K. K. (1979), “Superconducting weak links,” *Reviews of Modern Physics* **51**, 101.
- Lin, Z. R., K. Inomata, W. D. Oliver, K. Koshino, Y. Nakamura, J. S. Tsai, and T. Yamamoto (2013), “Single-shot readout of a superconducting flux qubit with a flux-driven Josephson parametric amplifier,” *Applied Physics Letters* **103**, 132602.
- Liu, G., X. Cao, T. C. Chien, C. Zhou, P. Lu, and M. Hatridge (2020), “Noise reduction in qubit readout with a two-mode squeezed interferometer,” arXiv:2007.15460.
- Liu, Y., S. J. Srinivasan, D. Hover, S. Zhu, R. McDermott, and A. A. Houck (2014), “High fidelity readout of a transmon qubit using a superconducting low-inductance undulatory galvanometer microwave amplifier,” *New Journal of Physics* **16**, 113008.
- Lörch, N., Y. Zhang, C. Bruder, and M. I. Dykman (2019), “Quantum state preparation for coupled period tripling oscillators,” *Physical Review Research* **1**, 023023.
- Louisell, W. H. (1973), *Quantum Statistical Properties of Radiation* (Wiley, New York).
- Lounasmaa, O. V. (1974), *Experimental Principles and Methods Below 1 K* (Academic Press, London and New York).
- Lupaşcu, A., E. F. C. Driessen, L. Roschier, C. J. P. M. Harmans, and J. E. Mooij (2006), “High-contrast dispersive readout of a superconducting flux qubit using a nonlinear resonator,” *Physical Review Letters* **96**, 127003.
- Lupaşcu, A., S. Saito, T. Picot, P. C. de Groot, C. J. P. M. Harmans, and J. E. Mooij (2007), “Quantum non-demolition measurement of a superconducting two-level system,” *Nature Physics* **3**, 119.
- Ma, W.-L., S. Puri, R. J. Schoelkopf, M. H. Devoret, S. Girvin, and L. Jiang (2021), “Quantum control of bosonic modes with superconducting circuits,” *Science Bulletin* **66**, 1789.

- Macklin, C., K. O'Brien, D. Hover, M. E. Schwartz, V. Bolkhovskiy, X. Zhang, W. D. Oliver, and I. Siddiqi (2015), "A near-quantum-limited Josephson traveling-wave parametric amplifier," *Science* **350**, 307.
- Magesan, E., J. M. Gambetta, A. D. Córcoles, and J. M. Chow (2015), "Machine learning for discriminating quantum measurement trajectories and improving readout," *Physical Review Letters* **114**, 200501.
- Majer, J., J. M. Chow, J. M. Gambetta, J. Koch, B. R. Johnson, J. A. Schreier, L. Frunzio, D. I. Schuster, A. A. Houck, A. Wallraff, A. Blais, M. H. Devoret, S. M. Girvin, and R. J. Schoelkopf (2007), "Coupling superconducting qubits via a cavity bus," *Nature* **449**, 443.
- Makhlin, Y., G. Schön, and A. Shnirman (2001), "Quantum-state engineering with josephson-junction devices," *Reviews of Modern Physics* **73**, 357.
- Mallet, F., F. R. Ong, A. Palacios-Laloy, F. Nguyen, P. Bertet, D. Vion, and D. Esteve (2009), "Single-shot qubit readout in circuit quantum electrodynamics," *Nature Physics* **5**, 791.
- Manucharyan, V. E., E. Boaknin, M. Metcalfe, R. Vijay, I. Siddiqi, and M. Devoret (2007), "Microwave bifurcation of a josephson junction: Embedding-circuit requirements," *Physical Review B* **76**, 014524.
- Manucharyan, V. E., J. Koch, M. Brink, L. I. Glazman, and M. H. Devoret (2009a), "Coherent oscillations between classically separable quantum states of a superconducting loop," arXiv:0910.3039.
- Manucharyan, V. E., J. Koch, L. I. Glazman, and M. H. Devoret (2009b), "Fluxonium: Single cooper-pair circuit free of charge offsets," *Science* **326**, 113.
- Marshak, H. (1983), "Nuclear orientation thermometry," *Journal of Research of the National Bureau of Standards* **88**, 175.
- Martinis, J. M. (2004), "Superconducting qubits and the physics of Josephson junctions," in *Quantum Entanglement and Information Processing*, École de Physique des Houches, Session LXXIX, edited by D. Esteve, J.-M. Raimond, and J. Dalibard (Elsevier, New York) pp. 487–520.

- Martinis, J. M., M. Ansmann, and J. Aumentado (2009), “Energy decay in superconducting Josephson-junction qubits from nonequilibrium quasiparticle excitations,” *Physical Review Letters* **103**, 097002.
- Martinis, J. M., M. H. Devoret, and J. Clarke (1985), “Energy-level quantization in the zero-voltage state of a current-biased Josephson junction,” *Physical Review Letters* **55**, 1543.
- Martinis, J. M., M. H. Devoret, and J. Clarke (2020), “Quantum Josephson junction circuits and the dawn of artificial atoms,” *Nature Physics* **16**, 234.
- Martinis, J. M., S. Nam, J. Aumentado, and C. Urbina (2002), “Rabi oscillations in a large Josephson-junction qubit,” *Physical Review Letters* **89**, 117901.
- Masluk, N. A., I. M. Pop, A. Kamal, Z. K. Mineev, and M. H. Devoret (2012), “Microwave characterization of Josephson junction arrays: Implementing a low loss superinductance,” *Physical Review Letters* **109**, 137002.
- Mazenko, G. F. (2006), *Nonequilibrium Statistical Mechanics* (Wiley, Weinheim).
- McClure, D. T., H. Paik, L. S. Bishop, M. Steffen, J. M. Chow, and J. M. Gambetta (2016), “Rapid driven reset of a qubit readout resonator,” *Physical Review Applied* **5**, 011001.
- Mercier de Lépinay, L., E. Damskäg, C. F. Ockeloen-Korppi, and M. A. Sillanpää (2019), “Realization of directional amplification in a microwave optomechanical device,” *Physical Review Applied* **11**, 034027.
- Merli, P. G., G. F. Missiroli, and G. Pozzi (1976), “On the statistical aspect of electron interference phenomena,” *American Journal of Physics* **44**, 306.
- Mermin, N. D. (2007), *Quantum Computer Science: An Introduction* (Cambridge University Press, Cambridge, England).
- Metcalf, M., E. Boaknin, V. Manucharyan, R. Vijay, I. Siddiqi, C. Rigetti, L. Frunzio, R. J. Schoelkopf, and M. H. Devoret (2007), “Measuring the decoherence of a qutrit qubit with the cavity bifurcation amplifier,” *Physical Review B* **76**, 174516.
- Meystre, P., and M. O. Scully, Eds. (1983), *Quantum Optics, Experimental Gravity, and Measurement Theory* (Springer, Boston).

- Miller, R., T. E. Northup, K. M. Birnbaum, A. Boca, A. D. Boozer, and H. J. Kimble (2005), “Trapped atoms in cavity QED: coupling quantized light and matter,” *Journal of Physics B: Atomic, Molecular and Optical Physics* **38**, S551.
- Mineev, Z. K. (2018), “Catching and reversing a quantum jump mid-flight,” Ph.D. dissertation (Yale University), arXiv:1902.10355.
- Mineev, Z. K., Z. Leghtas, S. O. Mundhada, L. Christakis, I. M. Pop, and M. H. Devoret (2021a), “Energy-participation quantization of josephson circuits,” *npj Quantum Information* **7**, 131.
- Mineev, Z. K., Z. Leghtas, P. Reinhold, S. O. Mundhada, A. Diringer, D. C. Hillel, D. Z.-R. Wang, M. Facchini, P. A. Shah, and M. Devoret (2021b), “pyEPR: The energy-participation-ratio (EPR) open-source framework for quantum device design,” <https://github.com/zlatko-mineev/pyEPR>; <https://pyepdocs.readthedocs.io/en/latest/>.
- Mineev, Z. K., S. O. Mundhada, S. Shankar, P. Reinhold, R. Gutiérrez-Jáuregui, R. J. Schoelkopf, M. Mirrahimi, H. J. Carmichael, and M. H. Devoret (2019), “To catch and reverse a quantum jump mid-flight,” *Nature* **570**, 200.
- Misra, B., and E. C. G. Sudarshan (1977), “The zeno’s paradox in quantum theory,” *Journal of Mathematical Physics* **18**, 756.
- Muppalla, P. R., O. Gargiulo, S. I. Mirzaei, B. P. Venkatesh, M. L. Juan, L. Grünhaupt, I. M. Pop, and G. Kirchmair (2018), “Bistability in a mesoscopic josephson junction array resonator,” *Physical Review B* **97**, 024518.
- Murch, K. W., S. J. Weber, C. Macklin, and I. Siddiqi (2013), “Observing single quantum trajectories of a superconducting quantum bit,” *Nature* **502**, 211.
- Mutus, J. Y., T. C. White, R. Barends, Y. Chen, Z. Chen, B. Chiaro, A. Dunsworth, E. Jeffrey, J. Kelly, A. Megrant, C. Neill, P. J. J. O’Malley, P. Roushan, D. Sank, A. Vainsencher, J. Wenner, K. M. Sundqvist, A. N. Cleland, and J. M. Martinis (2014), “Strong environmental coupling in a Josephson parametric amplifier,” *Applied Physics Letters* **104**, 263513.
- Naaman, O., M. O. Abutaleb, C. Kirby, and M. Rennie (2016), “On-chip Josephson junction microwave switch,” *Applied Physics Letters* **108**, 112601.

- Nakamura, Y., Y. A. Pashkin, and J. S. Tsai (1999), “Coherent control of macroscopic quantum states in a single-Cooper-pair box,” *Nature* **398**, 786.
- Narla, A. (2017), *Flying Qubit Operations in Superconducting Circuits*, Ph.D. dissertation (Yale University).
- Narla, A., S. Shankar, M. Hatridge, Z. Leghtas, K. M. Sliwa, E. Zolys-Geller, S. O. Mundhada, W. Pfaff, L. Frunzio, R. J. Schoelkopf, and M. H. Devoret (2016), “Robust concurrent remote entanglement between two superconducting qubits,” *Physical Review X* **6**, 031036.
- Nazarov, Y. V., and Y. M. Blanter (2009), *Quantum Transport: Introduction to Nanoscience* (Cambridge University Press, Singapore).
- Nielsen, M. A., and I. L. Chuang (2000), *Quantum Computation and Quantum Information* (Cambridge University Press, Cambridge, England).
- Niemczyk, T., F. Deppe, H. Huebl, E. P. Menzel, F. Hocke, M. J. Schwarz, J. J. Garcia-Ripoll, D. Zueco, T. Hümmer, E. Solano, A. Marx, and R. Gross (2010), “Circuit quantum electrodynamics in the ultrastrong-coupling regime,” *Nature Physics* **6**, 772.
- Niemeyer, J., and V. Kose (1976), “Observation of large dc supercurrents at nonzero voltages in Josephson tunnel junctions,” *Applied Physics Letters* **29**, 380.
- Niepcz, D., J. Burnett, and J. Bylander (2019), “High kinetic inductance NbN nanowire superinductors,” *Physical Review Applied* **11**, 044014.
- Nigg, S. E., H. Paik, B. Vlastakis, G. Kirchmair, S. Shankar, L. Frunzio, M. H. Devoret, R. J. Schoelkopf, and S. M. Girvin (2012), “Black-box superconducting circuit quantization,” *Physical Review Letters* **108**, 240502.
- Niu, M. Y., S. Boixo, V. N. Smelyanskiy, and H. Neven (2019), “Universal quantum control through deep reinforcement learning,” *npj Quantum Information* **5**, 33.
- Nyquist, H. (1928), “Thermal agitation of electric charge in conductors,” *Physical Review* **32**, 110.
- O’Brien, K., C. Macklin, I. Siddiqi, and X. Zhang (2014), “Resonant phase matching of Josephson junction traveling wave parametric amplifiers,” *Physical Review Letters* **113**, 157001.

- O’Connell, A. D., M. Hofheinz, M. Ansmann, R. C. Bialczak, M. Lenander, E. Lucero, M. Neeley, D. Sank, H. Wang, M. Weides, J. Wenner, J. M. Martinis, and A. N. Cleland (2010), “Quantum ground state and single-phonon control of a mechanical resonator,” *Nature* **464**, 697.
- Onnes, H. K. (1882), *De beteekenis van het quantitatief onderzoek in de natuurkunde* (Brill, Leiden); English translation by A. Laesecke (2002), “Through Measurement to Knowledge: The Inaugural Lecture of Heike Kamerlingh Onnes (1882),” *Journal of Research of the National Institute of Standards and Technology* **107**, 261.
- Orlando, T. P., and K. A. Delin (1991), *Foundations of Applied Superconductivity* (Addison-Wesley, Reading, Massachusetts).
- Paik, H., A. Mezzacapo, M. Sandberg, D. T. McClure, B. Abdo, A. D. Córcoles, O. Dial, D. F. Bogorin, B. L. T. Plourde, M. Steffen, A. W. Cross, J. M. Gambetta, and J. M. Chow (2016), “Experimental demonstration of a resonator-induced phase gate in a multiqubit circuit-QED system,” *Physical Review Letters* **117**, 250502.
- Paik, H., D. I. Schuster, L. S. Bishop, G. Kirchmair, G. Catelani, A. P. Sears, B. R. Johnson, M. J. Reagor, L. Frunzio, L. I. Glazman, S. M. Girvin, M. H. Devoret, and R. J. Schoelkopf (2011), “Observation of high coherence in Josephson junction qubits measured in a three-dimensional circuit QED architecture,” *Physical Review Letters* **107**, 240501.
- Pathria, R. K., and P. Beale (2021), *Statistical Mechanics*, 4th ed. (Academic Press, Cambridge, England).
- Peres, A. (1993), *Quantum Theory: Concepts and Methods* (Kluwer Academic Publishers, Dordrecht).
- Perrin, J. (1913), *Les Atomes* (Félix Alcan, Paris); English translation by D. Ll. Hammick (1916), *Atoms* (D. Van Nostrand, New York).
- Peterson, G. A., F. Lecocq, K. Cicak, R. W. Simmonds, J. Aumentado, and J. D. Teufel (2017), “Demonstration of efficient nonreciprocity in a microwave optomechanical circuit,” *Physical Review X* **7**, 031001.
- Picot, T., A. Lupaşcu, S. Saito, C. J. P. M. Harmans, and J. E. Mooij (2008), “Role of relaxation in the quantum measurement of a superconducting qubit using a nonlinear oscillator,” *Physical Review B* **78**, 132508.

- Pippard, A. B. (1947), “The surface impedance of superconductors and normal metals at high frequencies II. the anomalous skin effect in normal metals,” *Proceedings of the Royal Society A* **191** (1026), 385.
- Pippard, A. B. (1954), “Metallic conduction at high frequencies and low temperatures,” in *Advances in Electronics and Electron Physics*, Vol. 6, edited by L. Marton (Academic Press, New York) p. 1.
- Place, A. P. M., L. V. H. Rodgers, P. Mundada, B. M. Smitham, M. Fitzpatrick, Z. Leng, A. Premkumar, J. Bryon, A. Vrajitoarea, S. Sussman, G. Cheng, T. Madhavan, H. K. Babla, X. H. Le, Y. Gang, B. Jäck, A. Gyenis, N. Yao, R. J. Cava, N. P. de Leon, and A. A. Houck (2021), “New material platform for superconducting transmon qubits with coherence times exceeding 0.3 milliseconds,” *Nature Communications* **12**, 1779.
- Planat, L., A. Ranadive, R. Dassonneville, J. Puertas Martínez, S. Léger, C. Naud, O. Buisson, W. Hasch-Guichard, D. M. Basko, and N. Roch (2020), “Photonic-crystal Josephson traveling-wave parametric amplifier,” *Physical Review X* **10**, 021021.
- Platzman, P. M., and M. I. Dykman (1999), “Quantum computing with electrons floating on liquid helium,” *Science* **284**, 1967.
- Pobell, F. (2007), *Matter and Methods at Low Temperatures*, 3rd ed. (Springer, Berlin and Heidelberg).
- Poincaré, H. (1905), *La Valeur de la Science* (Flammarion, Paris); English translation by G. B. Halsted (1907), *The Value of Science* (The Science Press, New York).
- Pop, I. M., T. Fournier, T. Crozes, F. Lecocq, I. Matei, B. Pannetier, O. Buisson, and W. Guichard (2012), “Fabrication of stable and reproducible submicron tunnel junctions,” *Journal of Vacuum Science & Technology B* **30**, 010607.
- Pop, I. M., K. Geerlings, G. Catelani, R. J. Schoelkopf, L. I. Glazman, and M. H. Devoret (2014), “Coherent suppression of electromagnetic dissipation due to superconducting quasiparticles,” *Nature* **508**, 369.
- Pozar, D. M. (2012), *Microwave Engineering*, 4th ed. (Wiley, Hoboken, New Jersey).

- Purcell, E. M. (1946), “Spontaneous emission probabilities at radio frequencies,” *Physical Review* **69**, 681.
- Purcell, E. M., H. C. Torrey, and R. V. Pound (1946), “Resonance absorption by nuclear magnetic moments in a solid,” *Physical Review* **69**, 37.
- Ramsey, N. F. (1956), *Molecular Beams* (Clarendon Press, Oxford).
- Ranzani, L., M. Bal, K. C. Fong, G. Ribeill, X. Wu, J. Long, H.-S. Ku, R. P. Erickson, D. Pappas, and T. A. Ohki (2018), “Kinetic inductance traveling-wave amplifiers for multiplexed qubit readout,” *Applied Physics Letters* **113**, 242602.
- Ranzani, L., S. Kotler, A. J. Sirois, M. P. DeFeo, M. Castellanos-Beltran, K. Cicak, L. R. Vale, and J. Aumentado (2017), “Wideband isolation by frequency conversion in a josephson-junction transmission line,” *Physical Review Applied* **8**, 054035.
- Read, A. P., B. J. Chapman, C. U. Lei, J. C. Curtis, S. Ganjam, L. Krayzman, L. Frunzio, and R. J. Schoelkopf (2022), “Precision measurement of the microwave dielectric loss of sapphire in the quantum regime with parts-per-billion sensitivity,” arXiv:2206.14334.
- Reagor, M., W. Pfaff, C. Axline, R. W. Heeres, N. Ofek, K. Sliwa, E. Holland, C. Wang, J. Blumoff, K. Chou, M. J. Hatridge, L. Frunzio, M. H. Devoret, L. Jiang, and R. J. Schoelkopf (2016), “Quantum memory with millisecond coherence in circuit qed,” *Physical Review B* **94**, 014506.
- Reed, M. D., L. DiCarlo, B. R. Johnson, L. Sun, D. I. Schuster, L. Frunzio, and R. J. Schoelkopf (2010a), “High-fidelity readout in circuit quantum electrodynamics using the jaynes-cummings nonlinearity,” *Physical Review Letters* **105**, 173601.
- Reed, M. D., B. R. Johnson, A. A. Houck, L. DiCarlo, J. M. Chow, D. I. Schuster, L. Frunzio, and R. J. Schoelkopf (2010b), “Fast reset and suppressing spontaneous emission of a superconducting qubit,” *Applied Physics Letters* **96**, 203110.
- Reinhold, P. (2019), *Controlling Error-Correctable Bosonic Qubits*, PhD dissertation (Yale University).
- Ribeill, G. J., D. Hover, Y.-F. Chen, S. Zhu, and R. McDermott (2011), “Superconducting low-inductance undulatory galvanometer microwave amplifier: Theory,” *Journal of Applied Physics* **110**, 103901.

- Rigetti, C., J. M. Gambetta, S. Poletto, B. L. T. Plourde, J. M. Chow, A. D. Córcoles, J. A. Smolin, S. T. Merkel, J. R. Rozen, G. A. Keefe, M. B. Rothwell, M. B. Ketchen, and M. Steffen (2012), “Superconducting qubit in a waveguide cavity with a coherence time approaching 0.1 ms,” *Physical Review B* **86**, 100506.
- Ristè, D., M. Dukalski, C. A. Watson, G. de Lange, M. J. Tiggelman, Y. M. Blanter, K. W. Lehnert, R. N. Schouten, and L. DiCarlo (2013), “Deterministic entanglement of superconducting qubits by parity measurement and feedback,” *Nature* **502**, 350.
- Ristè, D., J. G. van Leeuwen, H.-S. Ku, K. W. Lehnert, and L. DiCarlo (2012), “Initialization by measurement of a superconducting quantum bit circuit,” *Physical Review Letters* **109**, 050507.
- Roch, N., E. Flurin, F. Nguyen, P. Morfin, P. Campagne-Ibarcq, M. H. Devoret, and B. Huard (2012), “Widely tunable, nondegenerate three-wave mixing microwave device operating near the quantum limit,” *Physical Review Letters* **108**, 147701.
- Roch, N., M. E. Schwartz, F. Motzoi, C. Macklin, R. Vijay, A. W. Eddins, A. N. Korotkov, K. B. Whaley, M. Sarovar, and I. Siddiqi (2014), “Observation of measurement-induced entanglement and quantum trajectories of remote superconducting qubits,” *Physical Review Letters* **112**, 170501.
- Rose-Innes, A. C., and E. H. Rhoderick (1978), *Introduction to Superconductivity*, 2nd ed. (Pergamon, Oxford).
- Rosenblum, S., Y. Y. Gao, P. Reinhold, C. Wang, C. J. Axline, L. Frunzio, S. M. Girvin, L. Jiang, M. Mirrahimi, M. H. Devoret, and R. J. Schoelkopf (2018), “A cnot gate between multiphoton qubits encoded in two cavities,” *Nature Communications* **9**, 652.
- Rosenthal, E. I., C. M. F. Schneider, M. Malnou, Z. Zhao, F. Leditzky, B. J. Chapman, W. Wustmann, X. Ma, D. A. Palken, M. F. Zanner, L. R. Vale, G. C. Hilton, J. Gao, G. Smith, G. Kirchmair, and K. W. Lehnert (2021), “Efficient and low-backaction quantum measurement using a chip-scale detector,” *Physical Review Letters* **126**, 090503.
- Roukes, M. L., M. R. Freeman, R. S. Germain, R. C. Richardson, and M. B. Ketchen (1985), “Hot electrons and energy transport in metals at millikelvin temperatures,” *Physical Review Letters* **55**, 422.

- Roy, A., and M. Devoret (2016), “Introduction to parametric amplification of quantum signals with Josephson circuits,” *Comptes Rendus Physique* **17**, 740.
- Sakurai, J. J., and J. Napolitano (2021), *Modern Quantum Mechanics*, 3rd ed. (Cambridge University Press).
- Samkharadze, N., A. Bruno, P. Scarlino, G. Zheng, D. P. DiVincenzo, L. DiCarlo, and L. M. K. Vandersypen (2016), “High-kinetic-inductance superconducting nanowire resonators for circuit qed in a magnetic field,” *Physical Review Applied* **5**, 044004.
- Sank, D., Z. Chen, M. Khezri, J. Kelly, R. Barends, B. Campbell, Y. Chen, B. Chiaro, A. Dunsworth, A. Fowler, E. Jeffrey, E. Lucero, A. Megrant, J. Mutus, M. Neeley, C. Neill, P. J. J. O’Malley, C. Quintana, P. Roushan, A. Vainsencher, T. White, J. Wenner, A. N. Korotkov, and J. M. Martinis (2016), “Measurement-induced state transitions in a superconducting qubit: Beyond the rotating wave approximation,” *Physical Review Letters* **117**, 190503.
- Schawlow, A. L., and C. H. Townes (1958), “Infrared and optical masers,” *Physical Review* **112**, 1940.
- Schlosshauer, M. (2005), “Decoherence, the measurement problem, and interpretations of quantum mechanics,” *Reviews of Modern Physics* **76**, 1267.
- Schlosshauer, M. A. (2007), *Decoherence and the Quantum-to-Classical Transition* (Springer, Berlin and Heidelberg).
- Schmidt-Böcking, H., L. Schmidt, H. J. Lüdde, W. Trageser, A. Templeton, and T. Sauer (2016), “The Stern-Gerlach experiment revisited,” *European Physical Journal H* **41**, 327.
- Schmitt, V., X. Zhou, K. Juliusson, B. Royer, A. Blais, P. Bertet, D. Vion, and D. Esteve (2014), “Multiplexed readout of transmon qubits with Josephson bifurcation amplifiers,” *Physical Review A* **90**, 062333.
- Schoelkopf, R. J., and S. M. Girvin (2008), “Wiring up quantum systems,” *Nature* **451**, 664.
- Schreier, J. A., A. A. Houck, J. Koch, D. I. Schuster, B. R. Johnson, J. M. Chow, J. M. Gambetta, J. Majer, L. Frunzio, M. H. Devoret, S. M. Girvin, and R. J. Schoelkopf (2008), “Suppressing charge noise decoherence in superconducting charge qubits,” *Physical Review B* **77**, 180502.

- Schrödinger, E. (1935), “Die gegenwärtige Situation in der Quantenmechanik,” *Naturwissenschaften* **23**, 807, English translation by J. D. Trimmer (1980), “The present situation in quantum mechanics,” *Proceedings of the American Philosophical Society* **124**, 323.
- Schrödinger, E. (1952a), “Are there quantum jumps? Part I,” *The British Journal for the Philosophy of Science* **3**, 109.
- Schrödinger, E. (1952b), “Are there quantum jumps? Part II,” *The British Journal for the Philosophy of Science* **3**, 233.
- Schuster, D. I. (2007), *Circuit Quantum Electrodynamics*, Ph.D. dissertation (Yale University).
- Schuster, D. I., A. Fragner, M. I. Dykman, S. A. Lyon, and R. J. Schoelkopf (2010), “Proposal for manipulating and detecting spin and orbital states of trapped electrons on helium using cavity quantum electrodynamics,” *Physical Review Letters* **105**, 040503.
- Schuster, D. I., A. A. Houck, J. A. Schreier, A. Wallraff, J. M. Gambetta, A. Blais, L. Frunzio, J. Majer, B. Johnson, M. H. Devoret, S. M. Girvin, and R. J. Schoelkopf (2007), “Resolving photon number states in a superconducting circuit,” *Nature* **445**, 515.
- Schuster, D. I., A. Wallraff, A. Blais, L. Frunzio, R.-S. Huang, J. Majer, S. M. Girvin, and R. J. Schoelkopf (2005), “ac Stark shift and dephasing of a superconducting qubit strongly coupled to a cavity field,” *Physical Review Letters* **94**, 123602.
- Scigliuzzo, M., A. Bengtsson, J.-C. Besse, A. Wallraff, P. Delsing, and S. Gasparinetti (2020), “Primary thermometry of propagating microwaves in the quantum regime,” *Physical Review X* **10**, 041054.
- Scully, M. O., and M. S. Zubairy (1997), *Quantum Optics* (Cambridge University Press, Cambridge, England).
- Sears, A. P., A. Petrenko, G. Catelani, L. Sun, H. Paik, G. Kirchmair, L. Frunzio, L. I. Glazman, S. M. Girvin, and R. J. Schoelkopf (2012), “Photon shot noise dephasing in the strong-dispersive limit of circuit QED,” *Physical Review B* **86**, 180504.

- Serniak, K. (2019), *Nonequilibrium Quasiparticles in Superconducting Qubits*, Ph.D. dissertation (Yale University).
- Serniak, K., S. Diamond, M. Hays, V. Fatemi, S. Shankar, L. Frunzio, R. Schoelkopf, and M. Devoret (2019), “Direct dispersive monitoring of charge parity in offset-charge-sensitive transmons,” *Physical Review Applied* **12**, 014052.
- Serniak, K., M. Hays, G. de Lange, S. Diamond, S. Shankar, L. D. Burkhardt, L. Frunzio, M. Houzet, and M. H. Devoret (2018), “Hot nonequilibrium quasiparticles in transmon qubits,” *Physical Review Letters* **121**, 157701.
- Sete, E. A., J. M. Martinis, and A. N. Korotkov (2015), “Quantum theory of a bandpass purcell filter for qubit readout,” *Physical Review A* **92**, 012325.
- Shannon, C. E. (1948), “A mathematical theory of communication,” *Bell Labs Technical Journal* **27**, 379.
- Shearrow, A., G. Koolstra, S. J. Whiteley, N. Earnest, P. S. Barry, F. J. Heremans, D. D. Awschalom, E. Shirokoff, and D. I. Schuster (2018), “Atomic layer deposition of titanium nitride for quantum circuits,” *Applied Physics Letters* **113**, 212601.
- Shimoda, K., H. Takahasi, and C. H. Townes (1957), “Fluctuations in amplification of quanta with application to maser amplifiers,” *Journal of the Physical Society of Japan* **12**, 686.
- Siddiqi, I. (2021), “Engineering high-coherence superconducting qubits,” *Nature Reviews Materials* **6**, 875.
- Siddiqi, I., R. Vijay, M. Metcalfe, E. Boaknin, L. Frunzio, R. J. Schoelkopf, and M. H. Devoret (2006a), “Dispersive measurements of superconducting qubit coherence with a fast latching readout,” *Physical Review B* **73**, 054510.
- Siddiqi, I., R. Vijay, F. Pierre, C. M. Wilson, L. Frunzio, M. Metcalfe, C. Rigetti, and M. H. Devoret (2006b), “The josephson bifurcation amplifier for quantum measurements,” in *Quantum Computing in Solid State Systems*, edited by B. Ruggiero, P. Delsing, C. Granata, Y. Pashkin, and P. Silvestrini (Springer, New York) pp. 28–37.

- Siddiqi, I., R. Vijay, F. Pierre, C. M. Wilson, L. Frunzio, M. Metcalfe, C. Rigetti, R. J. Schoelkopf, M. H. Devoret, D. Vion, and D. Esteve (2005), “Direct observation of dynamical bifurcation between two driven oscillation states of a josephson junction,” *Physical Review Letters* **94**, 027005.
- Siddiqi, I., R. Vijay, F. Pierre, C. M. Wilson, M. Metcalfe, C. Rigetti, L. Frunzio, and M. H. Devoret (2004), “Rf-driven josephson bifurcation amplifier for quantum measurement,” *Physical Review Letters* **93**, 207002.
- Silveri, M., E. Zalus-Geller, M. Hatridge, Z. Leghtas, M. H. Devoret, and S. M. Girvin (2016), “Theory of remote entanglement via quantum-limited phase-preserving amplification,” *Physical Review A* **93**, 062310.
- Sivak, V. V., A. Eickbusch, H. Liu, B. Royer, I. Tsioutsios, and M. H. Devoret (2022), “Model-free quantum control with reinforcement learning,” *Physical Review X* **12**, 011059.
- Sivak, V. V., N. E. Frattini, V. R. Joshi, A. Lingenfelter, S. Shankar, and M. H. Devoret (2019), “Kerr-free three-wave mixing in superconducting quantum circuits,” *Physical Review Applied* **11**, 054060.
- Sivak, V. V., S. Shankar, G. Liu, J. Aumentado, and M. H. Devoret (2020), “Josephson array-mode parametric amplifier,” *Physical Review Applied* **13**, 024014.
- Slichter, D. H. (2011), *Quantum Jumps and Measurement Backaction in a Superconducting Qubit*, Ph.D. dissertation (University of California, Berkeley).
- Slichter, D. H., C. Müller, R. Vijay, S. J. Weber, A. Blais, and I. Siddiqi (2016), “Quantum zeno effect in the strong measurement regime of circuit quantum electrodynamics,” *New Journal of Physics* **18**, 053031.
- Slichter, D. H., R. Vijay, S. J. Weber, S. Boutin, M. Boissonneault, J. M. Gambetta, A. Blais, and I. Siddiqi (2012), “Measurement-induced qubit state mixing in circuit QED from up-converted dephasing noise,” *Physical Review Letters* **109**, 153601.
- Sliwa, K. M., M. Hatridge, A. Narla, S. Shankar, L. Frunzio, R. J. Schoelkopf, and M. H. Devoret (2015), “Reconfigurable Josephson circulator/directional amplifier,” *Physical Review X* **5**, 041020.

- Smith, W. C. (2019), *Design of Protected Superconducting Qubits*, Ph.D. dissertation (Yale University).
- Sohn, L. L., L. P. Kouwenhoven, and G. Schön, Eds. (1997), *Mesoscopic Electron Transport* (Springer, Dordrecht).
- Steffen, M., S. Kumar, D. P. DiVincenzo, J. R. Rozen, G. A. Keefe, M. B. Rothwell, and M. B. Ketchen (2010), “High-coherence hybrid superconducting qubit,” *Physical Review Letters* **105**, 100502.
- Stern, M., G. Catelani, Y. Kubo, C. Grezes, A. Bienfait, D. Vion, D. Esteve, and P. Bertet (2014), “Flux qubits with long coherence times for hybrid quantum circuits,” *Physical Review Letters* **113**, 123601.
- Stone, A. D. (2013), *Einstein and the Quantum: The Quest of the Valiant Swabian* (Princeton University Press, Princeton).
- Suri, B., Z. K. Keane, R. Ruskov, L. S. Bishop, C. Tahan, S. Novikov, J. E. Robinson, F. C. Wellstood, and B. S. Palmer (2013), “Observation of Autler–Townes effect in a dispersively dressed Jaynes–Cummings system,” *New Journal of Physics* **15**, 125007.
- Szilard, L. (1929), “Über die entropieverminderung in einem thermodynamischen system bei eingriffen intelligenter wesen,” *Zeitschrift für Physik* **53**, 840, English translation by A. Rapoport and M. Knoller (1964), “On the decrease of entropy in a thermodynamic system by the intervention of intelligent beings,” *Systems Research* **9**, 301.
- Sólyom, J. (2003), *A modern szilárdtestfizika alapjai*, III. kötet. Kölcsönhatás az elektronok között (ELTE Eötvös Kiadó, Budapest); English translation (2010), *Fundamentals of the Physics of Solids*, Vol. 3: Normal, Broken-Symmetry, and Correlated Systems (Springer, Berlin and Heidelberg).
- Tabuchi, Y., S. Ishino, T. Ishikawa, R. Yamazaki, K. Usami, and Y. Nakamura (2014), “Hybridizing ferromagnetic magnons and microwave photons in the quantum limit,” *Physical Review Letters* **113**, 083603.
- Tabuchi, Y., S. Ishino, A. Noguchi, T. Ishikawa, R. Yamazaki, K. Usami, and Y. Nakamura (2015), “Coherent coupling between a ferromagnetic magnon and a superconducting qubit,” *Science* **349**, 405.

- Terhal, B. M., J. Conrad, and C. Vuillot (2020), “Towards scalable bosonic quantum error correction,” *Quantum Science and Technology* **5**, 043001.
- Tinkham, M. (1996), *Introduction to Superconductivity*, 2nd ed. (McGraw-Hill, New York).
- Tonomura, A., J. Endo, T. Matsuda, T. Kawasaki, and H. Ezawa (1989), “Demonstration of single-electron buildup of an interference pattern,” *American Journal of Physics* **57**, 117.
- Touzard, S., A. Grimm, Z. Leghtas, S. O. Mundhada, P. Reinhold, C. Axline, M. Reagor, K. Chou, J. Blumoff, K. M. Sliwa, S. Shankar, L. Frunzio, R. J. Schoelkopf, M. Mirrahimi, and M. H. Devoret (2018), “Coherent oscillations inside a quantum manifold stabilized by dissipation,” *Physical Review X* **8**, 021005.
- Touzard, S., A. Kou, N. E. Frattini, V. V. Sivak, S. Puri, A. Grimm, L. Frunzio, S. Shankar, and M. H. Devoret (2019), “Gated conditional displacement readout of superconducting qubits,” *Physical Review Letters* **122**, 080502.
- Toyli, D. M., A. W. Eddins, S. Boutin, S. Puri, D. Hover, V. Bolkhovskiy, W. D. Oliver, A. Blais, and I. Siddiqi (2016), “Resonance fluorescence from an artificial atom in squeezed vacuum,” *Physical Review X* **6**, 031004.
- Tucker, J. R., and M. J. Feldman (1985), “Quantum detection at millimeter wavelengths,” *Reviews of Modern Physics* **57**, 1055.
- Venkatraman, J., X. Xiao, R. G. Cortiñas, A. Eickbusch, and M. H. Devoret (2022), “Static effective hamiltonian of a rapidly driven nonlinear system,” *Physical Review Letters* **129**, 100601.
- Verney, L., R. Lescanne, M. H. Devoret, Z. Leghtas, and M. Mirrahimi (2019), “Structural instability of driven Josephson circuits prevented by an inductive shunt,” *Physical Review Applied* **11**, 024003.
- Vijay, R., D. H. Slichter, and I. Siddiqi (2011), “Observation of quantum jumps in a superconducting artificial atom,” *Physical Review Letters* **106**, 110502.
- Vion, D., A. Aassime, A. Cottet, P. Joyez, H. Pothier, C. Urbina, D. Esteve, and M. H. Devoret (2002), “Manipulating the quantum state of an electrical circuit,” *Science* **296**, 886.

- Vissers, M. R., R. P. Erickson, H.-S. Ku, L. Vale, X. Wu, G. C. Hilton, and D. P. Pappas (2016), “Low-noise kinetic inductance traveling-wave amplifier using three-wave mixing,” *Applied Physics Letters* **108**, 012601.
- von Neumann, J. (1932), *Mathematische Grundlagen der Quantenmechanik* (Springer, Berlin); English translation by R. T. Beyer (1955), *Mathematical Foundations of Quantum Mechanics* (Princeton University Press, Princeton).
- Vool, U. (2017), *Engineering Synthetic Quantum Operations*, Ph.D. dissertation (Yale University).
- Vool, U., and M. Devoret (2017), “Introduction to quantum electromagnetic circuits,” *International Journal Circuit Theory and Applications* **45**, 897.
- Wallraff, A., D. I. Schuster, A. Blais, L. Frunzio, R.-S. Huang, J. Majer, S. Kumar, S. M. Girvin, and R. J. Schoelkopf (2004), “Strong coupling of a single photon to a superconducting qubit using circuit quantum electrodynamics,” *Nature* **431**, 162.
- Wallraff, A., D. I. Schuster, A. Blais, L. Frunzio, J. Majer, M. H. Devoret, S. M. Girvin, and R. J. Schoelkopf (2005), “Approaching unit visibility for control of a superconducting qubit with dispersive readout,” *Physical Review Letters* **95**, 060501.
- Walls, D. F., and G. J. Milburn (2008), *Quantum Optics*, 2nd ed. (Springer, Berlin and Heidelberg).
- Walter, T., P. Kurpiers, S. Gasparinetti, P. Magnard, A. Potočnik, Y. Salathé, M. Pechal, M. Mondal, M. Oppliger, C. Eichler, and A. Wallraff (2017), “Rapid high-fidelity single-shot dispersive readout of superconducting qubits,” *Physical Review Applied* **7**, 054020.
- Walther, H., B. T. H. Varcoe, B.-G. Englert, and T. Becker (2006), “Cavity quantum electrodynamics,” *Reports on Progress in Physics* **69**, 1325.
- Wang, C., C. Axline, Y. Y. Gao, T. Brecht, Y. Chu, L. Frunzio, M. H. Devoret, and R. J. Schoelkopf (2015), “Surface participation and dielectric loss in superconducting qubits,” *Applied Physics Letters* **107**, 162601.
- Wang, C., Y. Y. Gao, I. M. Pop, U. Vool, C. Axline, T. Brecht, R. W. Heeres, L. Frunzio, M. H. Devoret, G. Catelani, L. I. Glazman, and R. J. Schoelkopf

- (2014), “Measurement and control of quasiparticle dynamics in a superconducting qubit,” *Nature Communications* **5**, 5836.
- Wang, W., Z.-J. Chen, X. Liu, W. Cai, Y. Ma, X. Mu, X. Pan, Z. Hua, L. Hu, Y. Xu, H. Wang, Y. P. Song, X.-B. Zou, C.-L. Zou, and L. Sun (2022), “Quantum-enhanced radiometry via approximate quantum error correction,” *Nature Communications* **13** (1), 3214.
- Wang, Z., S. Shankar, Z. K. Mineev, P. Campagne-Ibarcq, A. Narla, and M. H. Devoret (2019), “Cavity attenuators for superconducting qubits,” *Physical Review Applied* **11**, 014031.
- Wang, Z., M. Xu, X. Han, W. Fu, S. Puri, S. M. Girvin, H. X. Tang, S. Shankar, and M. H. Devoret (2021), “Quantum microwave radiometry with a superconducting qubit,” *Physical Review Letters* **126**, 180501.
- Weber, S. J., K. W. Murch, M. E. Kimchi-Schwartz, N. Roch, and I. Siddiqi (2016), “Quantum trajectories of superconducting qubits,” *Comptes Rendus Physique* **17**, 766.
- Weinreb, S. (1980), “Low-noise cooled GASFET amplifiers,” *IEEE Trans. Micro. Theory Tech.* **28**, 1041.
- Wellstood, F. C., C. Urbina, and J. Clarke (1994), “Hot-electron effects in metals,” *Physical Review B* **49**, 5942.
- Wendin, G. (2017), “Quantum information processing with superconducting circuits: a review,” *Reports on Progress in Physics* **80**, 106001.
- Wendin, G., and V. S. Shumeiko (2007), “Quantum bits with Josephson junctions,” *Low Temperature Physics* **33**, 724.
- Wheeler, J. A., and W. H. Zurek, Eds. (1983), *Quantum Theory and Measurement* (Princeton University Press, Princeton).
- Whittle, C., E. D. Hall, S. Dwyer, N. Mavalvala, V. Sudhir, and members of the LIGO Scientific Collaboration (2021), “Approaching the motional ground state of a 10-kg object,” *Science* **372**, 1333.
- Wilkinson, E. (1960), “An n-way hybrid power divider,” *IRE Transactions on Microwave Theory and Techniques* **8**, 116.

- Winkel, P., K. Borisov, L. Grünhaupt, D. Rieger, M. Spiecker, F. Valenti, A. V. Ustinov, W. Wernsdorfer, and I. M. Pop (2020), “Implementation of a transmon qubit using superconducting granular aluminum,” *Physical Review X* **10**, 031032.
- Wiseman, H. M., and G. J. Milburn (2009), *Quantum Measurement and Control* (Cambridge University Press, Cambridge, England).
- Yamamoto, T., K. Inomata, M. Watanabe, K. Matsuba, T. Miyazaki, W. D. Oliver, Y. Nakamura, and J. S. Tsai (2008), “Flux-driven Josephson parametric amplifier,” *Applied Physics Letters* **93**, 042510.
- Yan, F., D. Campbell, P. Krantz, M. Kjaergaard, D. Kim, J. L. Yoder, D. Hover, A. Sears, A. J. Kerman, T. P. Orlando, S. Gustavsson, and W. D. Oliver (2018), “Distinguishing coherent and thermal photon noise in a circuit quantum electrodynamical system,” *Physical Review Letters* **120**, 260504.
- Yan, F., S. Gustavsson, A. Kamal, J. Birenbaum, A. P. Sears, D. Hover, T. J. Gudmundsen, D. Rosenberg, G. Samach, S. Weber, J. L. Yoder, T. P. Orlando, J. Clarke, A. J. Kerman, and W. D. Oliver (2016), “The flux qubit revisited to enhance coherence and reproducibility,” *Nature Communications* **7**, 12964.
- Yariv, A., and P. Yeh (2006), *Photonics: Optical Electronics in Modern Communications* (Oxford University Press, Oxford).
- Yeh, J.-H., J. LeFebvre, S. Premaratne, F. C. Wellstood, and B. S. Palmer (2017), “Microwave attenuators for use with quantum devices below 100 mK,” *Journal of Applied Physics* **121**, 224501.
- Yoshihara, F., T. Fuse, S. Ashhab, K. Kakuyanagi, S. Saito, and K. Semba (2017), “Superconducting qubit–oscillator circuit beyond the ultrastrong-coupling regime,” *Nature Physics* **13**, 44.
- You, J. Q., X. Hu, S. Ashhab, and F. Nori (2007), “Low-decoherence flux qubit,” *Physical Review B* **75**, 140515.
- Yu, H., L. McCuller, M. Tse, N. Kijbunchoo, L. Barsotti, N. Mavalvala, and members of the LIGO Scientific Collaboration (2020), “Quantum correlations between light and the kilogram-mass mirrors of LIGO,” *Nature* **583**, 43.

- Yu, Y., S. Han, X. Chu, S.-I. Chu, and Z. Wang (2002), “Coherent temporal oscillations of macroscopic quantum states in a Josephson junction,” *Science* **296**, 889.
- Yurke, B., L. R. Corruccini, P. G. Kaminsky, L. W. Rupp, A. D. Smith, A. H. Silver, R. W. Simon, and E. A. Whittaker (1989), “Observation of parametric amplification and deamplification in a Josephson parametric amplifier,” *Physical Review A* **39**, 2519.
- Yurke, B., P. G. Kaminsky, R. E. Miller, E. A. Whittaker, A. D. Smith, A. H. Silver, and R. W. Simon (1988), “Observation of 4.2-K equilibrium-noise squeezing via a Josephson-parametric amplifier,” *Physical Review Letters* **60**, 764.
- Zagoskin, A. M. (2011), *Quantum Engineering: Theory and Design of Quantum Coherent Structures* (Cambridge University Press, Cambridge, England).
- Zhong, C., Z. Wang, C. Zou, M. Zhang, X. Han, W. Fu, M. Xu, S. Shankar, M. H. Devoret, H. X. Tang, and L. Jiang (2020), “Proposal for heralded generation and detection of entangled microwave–optical-photon pairs,” *Physical Review Letters* **124**, 010511.
- Zhong, L., S. Al Kenany, K. M. Backes, B. M. Brubaker, S. B. Cahn, G. Carosi, Y. V. Gurevich, W. F. Kindel, S. K. Lamoreaux, K. W. Lehnert, S. M. Lewis, M. Malnou, R. H. Maruyama, D. A. Palken, N. M. Rapidis, J. R. Root, M. Simanovskaia, T. M. Shokair, D. H. Speller, I. Urdinaran, and K. A. van Bibber (2018), “Results from phase 1 of the HAYSTAC microwave cavity axion experiment,” *Physical Review D* **97**, 092001.
- Zhou, X., G. Koolstra, X. Zhang, G. Yang, X. Han, B. Dizdar, X. Li, R. Divan, W. Guo, K. W. Murch, D. I. Schuster, and D. Jin (2022), “Single electrons on solid neon as a solid-state qubit platform,” *Nature* **605**, 46.
- Zorin, A. B. (2016), “Josephson traveling-wave parametric amplifier with three-wave mixing,” *Physical Review Applied* **6**, 034006.
- Zurek, W. H. (1981), “Pointer basis of quantum apparatus: Into what mixture does the wave packet collapse?” *Physical Review D* **24**, 1516.
- Zurek, W. H., Ed. (1990), *Complexity, Entropy and the Physics of Information* (Addison-Wesley, Redwood City, California).

-
- Zurek, W. H. (1991), "Decoherence and the transition from quantum to classical," *Physics Today* **44**, 36.
- Zurek, W. H. (2003), "Decoherence, einselection, and the quantum origins of the classical," *Reviews of Modern Physics* **75**, 715.